Instrument Development for the Next-Generation Astroparticle Detectors: Einstein Telescope and CTAO

Entwicklung von Instrumenten für die nächste Generation an Astroteilchen-Detektoren: Einstein-Teleskop und CTAO.

Vorgelegt von
Benjamin Schwab
aus Nürnberg

Der Naturwissenschaftlichen Fakultät
der Friedrich-Alexander-Universität Erlangen-Nürnberg
zur Erlangung des Doktorgrades Dr. rer. nat.

Als Dissertation genehmigt von der Naturwissenschaftlichen Fakultät der Friedrich-Alexander-Universität Erlangen-Nürnberg

Tag der mündlichen Prüfung:	02.02.2026
Gutachter:	Prof. Dr. Anna Nelles Prof. Dr. Stefan Funk Prof. Dr. Hanno Sahlmann

Abstract

The Einstein Telescope and the Cherenkov Telescope Array Observatory (CTAO) are two next-generation instruments currently in the design and construction phase to advance the field of astroparticle physics. Although they explore different aspects of it, gravitational waves and gamma rays, both face similar instrumentation challenges. In this thesis, specialised high-speed cameras are developed for each experiment, which are related by their shared utilisation of high-speed amplification and digitisation.

In the first part of this thesis, a monitoring tool for the Einstein Telescope is developed: A 56-pixel proof-of-concept phase camera capable of simultaneously measuring the spatial phase and amplitude of different radio-frequency components of a laser. Such a phase camera allows the determination of the mode content and wavefront aberrations caused by misalignment in the interferometer. A key innovation of the prototype is the introduction of a multimode fibre array, which significantly improves image quality by stabilising the phase relation between the pixels at higher frame rates. High-gain, high-bandwidth, low-noise amplification is developed to enable the digital demodulation to acquire the phase and amplitude information of the different radio frequency components. The complete signal chain is designed, built, and characterised with an in-depth study of the acquisition of phase and amplitude noise. To scale up the camera, the CTC digitising ASIC from the SST Camera is adapted and integrated into the system. Finally, a commissioning study of the phase camera at the ET Pathfinder is conducted to verify the performance and ability to observe and characterise the mode content.

In the second part, the front-end electronics for the SST, an Imaging Air Cherenkov Telescope (IACT) of CTAO, are characterised and optimised, with particular focus on the TARGET ASIC pair CTC and CT5TEA, the heart of the SST Camera. Throughout this thesis, a standardised calibration chain is developed for large-scale production of the camera, focusing on the digitisation ASIC CTC, refining established routines and introducing new ones. Special emphasis is placed on its temperature-stable performance, with in-situ recalibration techniques in the camera for temperature-sensitive calibration steps. Additionally, comprehensive evaluation and tuning of the Wilkinson ADC in the CTC are conducted to ensure meeting the specific performance criteria. The validation and verification results demonstrate that the CTC is suitable for IACTs and meets the CTAO's performance requirements.

Zusammenfassung

Das Einstein-Teleskop und das Cherenkov Telescope Array Observatory (CTAO) sind zwei Astroteilchendetektoren der nächsten Generation, die sich gerade in der Entwurfs- und Konstruktionsphase befinden, um das Feld der Astroteilchenphysik in Zukunft voranzubringen. Obwohl beide unterschiedliche Aspekte erforschen, nämlich Gravitationswellen und Gammastrahlen, stehen beide vor ähnlichen instrumentellen Herausforderungen. In dieser Arbeit wird für jedes Experiment jeweils eine spezialisierte Hochgeschwindigkeitskamera entwickelt, deren gemeinsame Nutzung von Hochgeschwindigkeits-Verstärkern und Digitalisierern sie eint.

Im ersten Teil dieser Arbeit wird eine Phasenkamera zur Überwachung der Wellenfront eines Lasers im Rahmen des Einstein-Teleskops entwickelt. Als Konzeptnachweis wird ein Prototyp mit 56 Pixeln konstruiert, der in der Lage ist, die räumliche Phase und Amplitude der Wellenfront aller Radiofrequenzkomponenten des Lasers gleichzeitig zu messen. Damit lassen sich der Modengehalt und Wellenfrontaberrationen darstellen, die zum Beispiel durch Fehlstellungen des Lasers im Interferometer entstehen. Innovativ ist hierbei die Einführung eines Multimodenlichtwellenleiters als bildgebender Sensor, der die Bildqualität signifikant verbessert, durch eine stabile Beziehung der gemessenen Phasen zwischen den Pixeln bei höheren Bildraten. Dazu wurde ein Verstärker mit hoher Bandbreite, hohem Verstärkungsfaktor und geringem Rauschen entwickelt, um die digitale Demodulation zu ermöglichen, mit der die Phasen beziehungsweise Amplituden der verschiedenen Radiofrequenzkomponenten berechnet werden. Die komplette Signalkette wurde entworfen, gebaut und charakterisiert mit einer eingehenden Studie zum Phasen- und Amplitudenrauschen. Um die Skalierung der Kamera auf eine Großzahl von Pixeln zu gewährleisten, wurde der Digitalisierungs-ASIC CTC adaptiert, welcher ursprünglich für die SST-Kamera entwickelt worden ist. Mit der Inbetriebnahme der Phasenkamera am ET Pathfinder wurde die Performance und Fähigkeit zur Abbildung und Charakterisierung des Modengehalts belegt.

Im zweiten Teil dieser Arbeit wird die Front-End-Elektronik für das SST, ein bildgebendes Cherenkov-Teleskope (IACT) von CTAO, charakterisiert und optimiert, mit speziellem Fokus auf das ASIC-Paar CTC und CT5TEA, dem Herzen der Kamera. Im Rahmen dieser Arbeit wird eine standardisierte Kalibrierungskette für die Serienfertigung der Kamera entwickelt, wobei der Schwerpunkt auf dem Digitalisierungs-ASIC CTC liegt. Dafür wurden verschiedene etablierte Kalibrierungsschritte weiterentwickelt und neue hinzugefügt. Besonderes Augenmerk wird auf die Temperaturstabilität der Performance gelegt, mit in-situ-Kalibrierungen, die jederzeit in der Kamera wiederholt werden können, um auf Temperaturschwankungen reagieren zu können. Darüber hinaus wird der Wilkinson ADC von CTC

im Detail evaluiert und optimiert, um spezifische Performancekriterien zu erfüllen. Schlussendlich zeigen die Validierungsergebnisse, dass CTC für die Benutzung in bildgebenden Cherenkov Teleskopen geeignet ist und die Performanceanforderungen von CTAO erfüllt.

Contents

Chapter I.
Phase Camera for the Einstein Telescope

1. Introduction

Nearly exactly 100 years after their prediction by Albert Einstein [1, 2], gravitational waves were directly measured on 14 September 2015 by the LIGO collaboration [3] and paved the way for a new era of multi-messenger astronomy [4, 5, 6]. Two black holes of 36^{+5}_{-4} and 29^{+4}_{-4} solar masses merged 410^{+160}_{-180} Mpc away, creating one of the most violent events in the cosmos. So violent that the ripples it left in space-time were measurable here on Earth. Major advancements in laser interferometry were needed to measure the length differences as small as 1000th of an atomic nucleus. Since then, the topic of gravitational waves has evolved into a prospering branch of physics, progressing the fields of gravitational physics [7, 8, 9], astrophysics [10, 11], cosmology [12], and nuclear physics [13], for example. With the Einstein Telescope [14, 15], a third-generation instrument that extends the frequency response and pushes the sensitivity to new limits in the design phase, it is now our time as the next generation of scientists to contribute to such an amazing enterprise.

To achieve the sensitivity required for the detection of gravitational waves, different sensing and control techniques have to be implemented to keep the interferometer within its operational range. An important example of such control techniques is the Pound–Drever–Hall (PDH) technique to stabilise the length of optical cavities or the frequency of a laser [16]. Here, the optical modulation of sidebands to the primary laser frequency is implemented, creating radio-frequency beatings in laser intensity between all frequency components. By demodulating these signals, an error signal can be generated to align the mirrors accordingly.
With their radio-frequency shifted wavelength, the sidebands can be treated as superimposed beams with their own wavefronts. Changes due to aberrations caused by thermal lensing, mirror surface roughness, or misalignment, for example, act individually on each radio-frequency component. These wavefront deformations can then deteriorate the response of control techniques or of the interferometer in general. An imbalance between the sidebands, for example, can cause problems for the length locking of cavities [17].

Therefore, a new class of imaging sensors has been developed, capable of imaging these individual wavefronts [18]. One of the most promising is the phase camera [19], which measures the optical beating between the different radio-frequency components using regular photodiodes. To separate the different frequency components, an additional reference frequency is superimposed on the beam for heterodyne detection. Via digital I-Q demodulation [20], the spatial phase and amplitude of the beam can be determined simultaneously for all available radio-frequency components. To spatially probe the wavefront, established systems scan the beam over a single photodiode for imaging. Hence, the images lack a stable phase relation

between pixels, which hampers the analysis of the phase image [19].
In this work, a phase camera with the novel concept of a multimode fibre array as a static 2D image sensor is introduced. The promised advantage is a stable phase relationship between pixels at higher frame rates, improving image quality. This is made possible by the availability of the cost-efficient Cherenkov-TARGET-C (CTC) Application Specific Integrated Circuit (ASIC) [21] developed for the Small-Sized Telescope (SST) Camera of Cherenkov Telescope Array Observatory (CTAO), which allows for equipping a large number of pixels, as the digital demodulation of all radio-frequency components in parallel requires $> 500\,\mathrm{MSa/\,s}$ digitising. As a proof-of-concept study, a 56-pixel fibre-based phase camera is designed from scratch and commissioned at the Einstein Telescope (ET) Pathfinder [22].

The first part of this thesis is organised as follows. Section 1 starts with the introduction of gravitational wave generation and the applied research on it. The laser interferometer for detection is presented in Section 3. Emphasis is put on the operation of Fabry–Pérot cavities [23] and how higher orders of Gaussian modes [24] are created by misalignment. The latter will be important for verifying the camera in Section 7. The concept behind and design of the fibre-based phase camera is described in detail in Section 4. In Section 5, the signal chain of the phase camera is defined and verified in terms of measured noise and how different kinds of noise sources can couple into the system. To facilitate the production of a large-scale version of the 56-pixel proof-of-concept camera, the CTC ASIC [21] is introduced as a performant and cost-efficient digitiser. The steps needed to implement the ASIC developed for photon pulse detection into the phase camera are described in-depth in Section 6. To demonstrate that the developed fibre-based phase camera is capable of detecting and characterising higher-order Gaussian modes, a measurement campaign at the ET pathfinder [25], the infrastructure for testing future technologies for the Einstein Telescope, is conducted. The methods and image analysis are presented in Section 7. A summary and a respective outlook are given in Section 8.

2. Introduction to Gravitational Waves

In this Section, the description of gravitational waves is introduced together with their detection properties. An overview of the different topics that can be studied with gravitational waves is provided.

2.1. Gravitational Waves and Einstein Field Equation

For the derivation of gravitational waves, the Einstein field equation has to be solved [26, 27, 28], which links the energy and momentum of matter to the curvature of space-time

$$R_{\mu\nu} - \frac{1}{2} g_{\mu\nu} R = \frac{8\pi G}{c^4} T_{\mu\nu} \ , \tag{2.1}$$

with $R_{\mu\nu}$ the Ricci tensor, $g_{\mu\nu}$ the metric, R the Ricci scalar, G the gravitational constant, c the speed of light in vacuum and $T_{\mu\nu}$ the energy momentum tensor. The Ricci tensor describes the change of a volume element across a curvature, while the Ricci scalar describes the overall curvature. The definition of both can be found in Appendix A, where the tensor calculus used in general relativity is also listed. As this equation represents 10 highly non-linear inter-coupled equations, it is not easily solved analytically without approximations or specific symmetries of the given problem. For the derivation of gravitational waves, the approximation of linearised gravity is used assuming a flat metric $\eta_{\mu\nu} = \text{diag}(-1, +1, +1, +1)$ with small ripples $|h_{\mu\nu}| \ll 1$ called strain, expressed as $g_{\mu\nu} \approx \eta_{\mu\nu} + h_{\mu\nu}$. This breaks the invariance under coordinate transformations as a reference frame is chosen. But one can choose a frame where certain gauge symmetries still hold as coordinate translation

$$x^\mu \to x'^\mu = x^\mu + \xi^\mu(x) \tag{2.2}$$

in first order if $|\partial_\mu \xi^\mu|$ is of the same magnitude as $|h_{\mu\nu}|$ which leads to the transformation of

$$h_{\mu\nu}(x) \to h'_{\mu\nu}(x') = h_{\mu\nu}(x) - (\partial_\mu \xi_\nu + \partial_\nu \xi_\mu) \tag{2.3}$$

that preserves $|h_{\mu\nu}| \ll 1$, and Lorentz transformations $x^\mu \to \Lambda^\mu{}_\nu x^\nu$. These gauge freedoms will later be important. Before solving the Einstein field equation with the linearised metric,

$$h = \eta^{\mu\nu} h_{\mu\nu} \quad \text{and} \quad \bar{h} = h_{\mu\nu} - \frac{1}{2} \eta^{\mu\nu} h \tag{2.4}$$

are defined to simplify the Equation. This leads to

$$\Box\bar{h}_{\mu\nu} + \eta_{\mu\nu}\partial^\rho\partial^\sigma\bar{h}_{\rho\sigma} - \partial^\rho\partial_\nu\bar{h}_{\mu\rho} - \partial^\rho\partial_\mu\bar{h}_{\nu\rho} = -\frac{16\pi G}{c^4}T_{\mu\nu} \tag{2.5}$$

with $\Box = \eta_{\mu\nu}\partial^\mu\partial^\nu$. Using the Lorenz gauge $\partial^\mu\bar{h}_{\mu\nu} = 0$, which can be derived from the translation freedom introduced in Equation 2.3, the Equation simplifies to

$$\Box\bar{h}_{\mu\nu} = -\frac{16\pi G}{c^4}T_{\mu\nu} \tag{2.6}$$

which reassembles a wave equation with six degrees of freedom instead of ten. As one is interested in the propagation of gravitational waves outside the source, the energy-momentum tensor is set to zero ($T_{\mu\nu} = 0$).
To further reduce the degrees of freedom, the Transverse-Traceless gauge (TT gauge) can be chosen. It can be directly derived from the Lorentz gauge. Taking a look on how $\bar{h}_{\mu\nu}$ changes under coordinate translation

$$\bar{h}_{\mu\nu}(x) \to \bar{h}'_{\mu\nu}(x') = \bar{h}_{\mu\nu}(x) - (\partial_\mu\xi_\nu + \partial_\nu\xi_\mu - \eta_{\mu\nu}\partial_\rho\xi^\rho) \equiv \partial^\nu\bar{h}_{\mu\nu} - \xi_{\mu\nu}, \tag{2.7}$$

the Lorentz gauge transforms as

$$\partial^\nu\bar{h}_{\mu\nu} \to (\partial^\nu\bar{h}_{\mu\nu})' = \partial^\nu\bar{h}_{\mu\nu} - \Box\xi_\mu \ . \tag{2.8}$$

As $\partial^\mu\bar{h}_{\mu\nu} = 0$, it can be follows that $\Box\xi_\mu = 0$ and $\Box\xi_{\mu\nu} = 0$. Therefore, Equation 2.7 shows that the six degrees of freedom of $\bar{h}_{\mu\nu}$ can be reduced to two by constructing a suitable ξ_μ that obeys the translation of coordinates. The use of this specially constructed ξ_μ is called TT gauge. First, ξ^0 is chosen so that the trace of $\bar{h}$ is zero, which leads to $\bar{h}_{\mu\nu} = h_{\mu\nu}$. The spatial part ξ^i is then chosen so that $h^{0i} = 0$. Expressed in terms of h, this leads to the following gauging condition:

$$h^{0\mu} = 0, \quad h^i_i = 0, \quad \partial^j h_{ij} = 0\,. \tag{2.9}$$

which only yields for $T_{\mu\nu} = 0$ and, therefore, only outside the source. Solving the wave equation (Equation 2.6) with a planar wave Ansatz together with the TT gauge yields

$$h^{TT}_{ij}(t,z) = \begin{pmatrix} h_+ & h_\times & 0 \\ h_\times & -h_+ & 0 \\ 0 & 0 & 0 \end{pmatrix}_{ij} \cos(\omega t_r) \tag{2.10}$$

assuming the wave propagating along the z-axis with h_+ and $h_\times$ the plus and cross polarisation of the transversal quadrupolar wave, ω the angular frequency of the gravitational wave and $t_r = t - \frac{z}{c}$ the retarded time. For each polarisation, space-time is squeezed in one dimension and then stretched in the perpendicular one per period ω. An illustration is given in Figure 1.

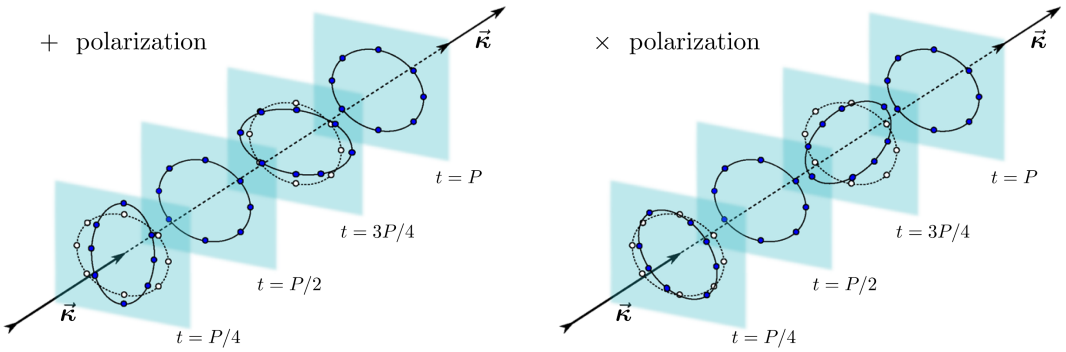

Figure 1: The propagation of a '+' and '×' polarised gravitational wave along the propagation vector $\vec{\kappa}$. The squeezing and stretching of space-time is illustrated by a ring of test masses. Image taken from [29].

2.2. The Challenge of Detecting Gravitational Waves

The planar wave Ansatz is useful for establishing gravitational waves in vacuum for non-realistic objects, but the amplitudes of the different polarisation modes h_+ and $h_\times$ are still not solved. From Equation 2.6, it becomes evident that the amplitude of gravitational waves is very small as $\frac{16\pi G}{c^4} \approx 10^{-43}\,\mathrm{s}^2/\mathrm{kgm}$. To calculate them, Equation 2.10 is solved by using a Green function following the methods of [30, 27]. This yields

$$\bar{h}_{ij} = \frac{2G}{r}\frac{d^2 I_{ij}}{dt^2}(t_r) \tag{2.11}$$

with r the distance to the source, $t_r = t - \frac{r}{c}$ the retarded time and

$$I_{ij} = \int y^i y^j T^{00}(t, \vec{y}) d^3 y \tag{2.12}$$

the quadrupole moment tensor of the energy density of the source. To explore the strain amplitudes of gravitational waves, an example of two orbiting black holes of equal mass M orbiting each other with distance $2R$ at angular frequency ω is presented, which yields

$$\bar{h}_{ij} = \frac{2GM}{r}\omega^2 R^2 \begin{pmatrix} -\cos(2\omega t_r) & -\sin(2\omega t_r) & 0 \\ -\sin(2\omega t_r) & \cos(2\omega t_r) & 0 \\ 0 & 0 & 0 \end{pmatrix}_{ij} \tag{2.13}$$

for the strain amplitude. In linearised gravity, one can approximate the orbiting speed and, therefore, angular frequency of the binary system in the Newtonian limit

$$\frac{Mv^2}{R} = \frac{GM^2}{(2R)^2}\ , \tag{2.14}$$

which leads to

$$\omega = \sqrt{\frac{GM}{2R^3}} \ . \tag{2.15}$$

The strain amplitude h can then be calculated by inserting ω in Equation 2.13. For two black holes of ten solar masses each, orbiting at the ten times the Schwarzschild radius at 100 Mpc distance to the observer, the strain amplitude is of magnitude $h \approx 10^{-21}$ at a frequency of $\nu \approx 100\,\mathrm{Hz}$ using Equation 2.13 and 2.15. To understand the dimensions of this minuscule amplitude strain, h can be approximated as $h \approx \frac{\delta l}{L}$ with L the proper distance between two space-time points and δl the length change due to the strain caused by the gravitational wave. Two test masses at a proper distance of $L = 1\,\mathrm{km}$ change by $\delta l \approx 10^{-18}\,\mathrm{m}$, one thousand times smaller than the size of a nucleus of an atom. A challenging but not impossible task, as the first ever observation of gravitational waves with a laser interferometer showed [31].

2.3. Astronomy with Gravitational Waves

As a new messenger in astronomy, gravitational waves unlock a new "window" to observe the universe. The applications are vast and diverse ranging from testing fundamental physics to addressing a wide range of astrophysical and cosmological problems. A brief summary is given here, following [15, 32, 33]. Unique features are the direct imprints of the gravitational field, physical environment and characteristics of the source in the gravitational wave itself. Therefore, a strong gravitational field with large curvatures could directly be observed to test violations of general relativity by Lorentz invariance violations [34] or violations of the strong equivalence principle [35]. In the same vein, signatures of quantum gravity could be found by parity violations that lead to certain polarisation states or birefringence along wave propagation [36].
As the observed amplitude of gravitational waves from compact binaries depends only on a handful of parameters and the distance to the observer, they are ideally suited to determine cosmological parameters such as the Hubble parameter [37], dark matter [38, 39] or dark energy densities [40]. Only the redshifts have to be measured by follow-up electromagnetic observations. From observations of a stochastic gravitational background, the formation histories of binary black holes, neutron stars, and their progenitor stars can be revealed. The large-scale distribution of galaxies and their clusters can be studied [41]. If there is a stochastic background created by the early universe, the observed phase transitions would also probe the standard model in energy ranges unattainable for contemporary experiments [42].

The equation of state of neutron star cores and the creation of their strong magnetic field is still a puzzle. By the observation of neutron star binaries, the tidal deformations of them are imprinted in the gravitational wave signal and are dictated by the internal structure of the neutron star, which directly relates to the introduced puzzles of neutron stars [43]. Together with follow-up observations in the electromagnetic spectrum, the mechanics of gamma-ray bursts from neutron star mergers or pulsar glitches could be constrained [44]. Neutron star mergers are generally linked to the stellar abundance of heavy elements. Combined studies could investigate if these mergers are sufficient for the population or if other astrophysical events, such as supernovae, also play a part [45].
Population studies of stellar-mass black holes via black hole binary mergers could also reveal primordial black holes as, among other things, a possible dark matter candidate [46] and how black holes of ~ 85 solar mass form, as they are too heavy to form via a progenitor star [47]. The measurement of the merger rates of these events as a function of redshift could also be used to constrain the metallicity-dependent stellar formation rate [48].

3. Gravitational Wave Detection with Laser Interferometers

In this Section, the fundamentals of detecting gravitational waves with a laser interferometer are introduced. An exemplary schematic of an instrument can be seen in Figure 2 with all the major components highlighted. Starting with the fundamentals of paraxial optics to describe laser beams, the Michelson interferometer is introduced as the baseline instrument of gravitational wave detection. The operation in nulled lock-in detection mode is discussed in terms of the expected signal and its advantages. To further increase the SNR of the interferometer, Fabry–Pérot cavity arms (ITM + ETM) and power recycling (PRM + SRM) are introduced as an extension of the detector. Then the mode cleaners (IMC + OMC) are discussed to suppress non-uniformities of the laser beam and pointing errors. The quantum noise suppression seen in Figure 2 in the form of the injection of squeezed light is skipped as it is not relevant for this work. For further, information see [50]. How noise can then couple to the interferometer is discussed in Section 3.8 with the emphasis on wavefront deformations that are investigated with the presented fibre-based phase camera. If not stated otherwise, all Subsections follow the example of [26, 51, 52]. In Section 3.1 to 3.1.2 the work of [51, 53, 54, 55] are used as reference. The calculation from Section 3.2 to 3.6 follows directly the methods of E. D. Black and R. N. Gutenkunst [56].

3.1. Paraxial Wave Optic

To describe and understand complex interferometers to detect gravitational waves, the fundamentals of light propagation must be understood. To be more precise, the propagation of laser light, which is concentrated near the propagation axis with non uniform intensity distributions [57]. Starting with the Maxwell equations in vacuum

$$\begin{aligned} \nabla \cdot \vec{E} = 0 \quad (i) \qquad & \nabla \times \vec{E} = -\partial_t \vec{B} \qquad (ii) \\ \nabla \cdot \vec{B} = 0 \quad (ii) \qquad & \nabla \times \vec{B} = \mu_0 \varepsilon_0 \partial_t \vec{E} \quad (iv) \end{aligned} \tag{3.1}$$

with $\mu_0 = 4 \times 10^{-7}\,\mathrm{H\,m^{-1}}$ the vacuum permeability and $\varepsilon_0 = 8.86 \times 10^{-12}\,\mathrm{F\,m^{-1}}$ the vacuum permittivity, the wave equation for electromagnetic waves can then be derived by taking the partial derivative in time of (ii) and then inserting (iv) to the left-hand side. Applying (i) after using the Graßmann-identity, leads to

$$\Delta \vec{E} - \frac{1}{c^2} \partial_t^2 \vec{E} = 0 \ , \tag{3.2}$$

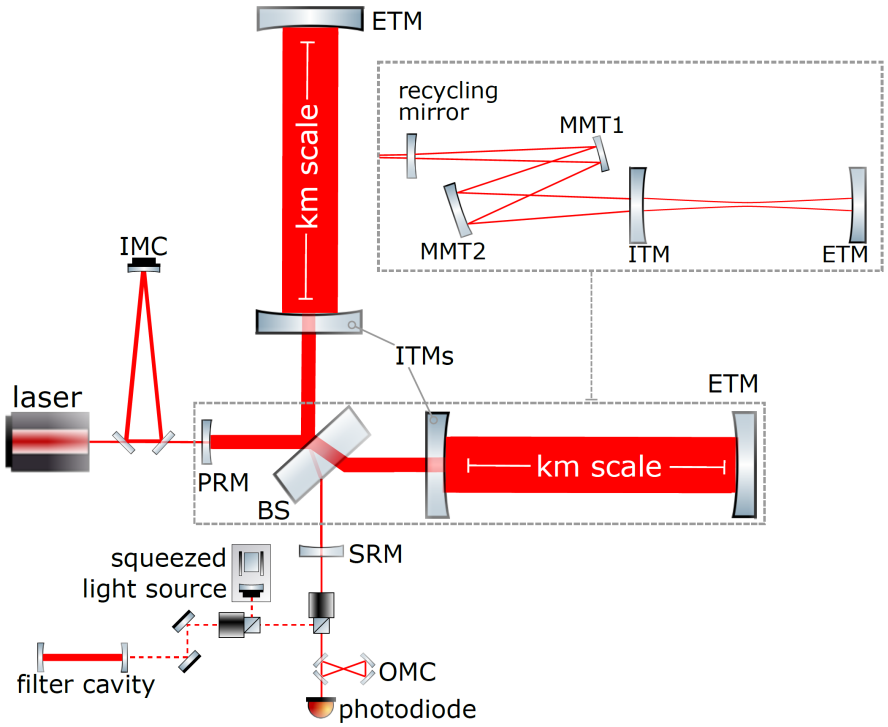

Figure 2: Illustration of a typical laser interferometer based on a Michelson interferometer. Starting with the laser source on the left, the mode content of the laser is cleaned in the input mode cleaner (IMC) and distributed into two interferometer arms by the beams splitter (BS). To virtually increase the arm length, Fabry–Pérot cavities (ITM + ETM) are used to fold the optical path. To match the normal modes of the cavity with the modes of the input beam, several telescopes are used (MMT1 + MMT2). The reflection of the interferometer arms is then recombined at the beam splitter (BS). The south port containing the signal is then filtered with squeezed light and the output mode cleaner (OMC) before being detected by a photodiode. To increase the Signal-to-Noise Ratio (SNR) of the interferometer, recycling mirrors are applied at both ports of the beam splitter (PRM + SRM). All concepts are in-depth described in the following Sections. Image taken from [49].

the electromagnetic wave equation described in terms of the electric field, with $\frac{1}{c^2} = \mu_0 \varepsilon_0$ the inverse square of the speed of light. To solve the equation, a separation of the variables is used, splitting the spatial component from the temporal one: $\vec{E} \equiv E(x, y, z, t) = U(x, y, z)V(t)$, leading to

$$\frac{\Delta U}{U} = \frac{1}{c^2} \frac{\partial_t^2 V}{V} = const \ . \tag{3.3}$$

As the left hand side is independent of the right side, the time dependent part can then be solved using a harmonic oscillator Ansatz $e^{-i\omega t}$ with ω the angular frequency, leading to the dispersion relation of light

$$\frac{\omega}{k} = c \ , \tag{3.4}$$

by wisely choosing the constant term in Equation 3.3 to be $-k^2$. By analysing the dimensions of the constant, it can be concluded that k is the free space wave number. The spatial part then gives rise to the Helmholtz equation

$$\Delta U + k^2 U = 0 \ . \tag{3.5}$$

For a electromagnetic wave propagating along the z-axis, the solution is of form

$$U(x, y, z) = u(x, y, z) \cdot e^{ikz} \ , \tag{3.6}$$

with e^{ikz}, a plane wave propagating along the z-axis, and $u(x, y, z)$ the beam shape. To introduce a description for $u(x, y, z)$, the solution is substituted into the wave equation leading to following differential equation

$$\left(\partial_x^2 u + \partial_y^2 u + \partial_z^2 u + 2ik\partial_z u\right) e^{ikz} = 0 \ . \tag{3.7}$$

Taking the paraxial nature of a laser beam into account, $u(x, y, z)$ will only vary slowly with z and, therefore, $2ik\partial_z u$ will be small and $\partial_z^2 u$ even smaller, which leads to the paraxial wave equation

$$\Delta_T u + 2ik\partial_z u = 0 \ , \tag{3.8}$$

with $\Delta_T = \partial_x^2 + \partial_y^2$, the transverse Laplace operator.

3.1.1. Gaussian Beam

A solution to the paraxial wave equations are Gaussian beams. Depending on the geometrical boundaries of the optical setup, they come in different flavours as Hermite-Gaussian modes for rectangular symmetries and Laguerre-Gaussian modes

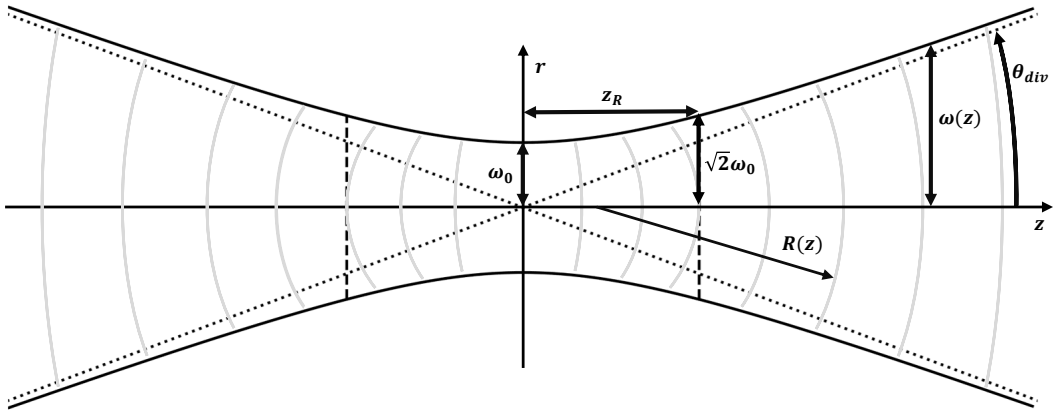

Figure 3: Illustration of a Gaussian beam with the most relevant parameter and observables marked.

for cylindric symmetries. Both span a complete set of modes capable of describing arbitrary laser beams and share the same fundamental mode, the TEM_{00} mode [51]. If a Gaussian beam is mentioned and the mode contend is not specified, the TEM_{00} mode is meant.
To understand the fundamentals of the propagation of Gaussian beams and their respective Higher Order Modes (HOMs) lets first have a look at the fundamental mode propagating along the optical axis z. An illustration is given in Figure 3 and it is described by

$$\vec{E}(r,z) = E_0 \frac{w_0}{w(z)} \exp\left(\frac{-r^2}{w(z)^2}\right) \exp\left(-i\left(kz + k\frac{r^2}{2R(z)} - \psi(z)\right)\right)\vec{\epsilon}\,, \tag{3.9}$$

with E_0 the E-field amplitude of the beam, z the coordinate along the optical axis, $r = \sqrt{x^2+y^2}$ the coordinate or distance perpendicular to the optical axis z, k the wave number, $\vec{\epsilon}$ the polarisation of the E-field, and the specific beam parameters $R(z)$ for the curvature, $w(z)$ the waist size, and ψ the Gouy phase, which are defined as

$$w(z) = w_0\sqrt{1+\left(\frac{z}{z_R}\right)}\,,\; R(z) = z\left(1+\left(\frac{z_R}{z}\right)^2\right)\,, \tag{3.10}$$

$$\psi(z) = \arctan\left(\frac{z}{z_R}\right)\,, \tag{3.11}$$

with $z_R = \frac{1}{2}kw_0^2$, the Rayleigh range [55, 51, 53]. The waist size $w(z)$ gives the radius of the transversal profile of them beam. It is Gaussian shaped as it follows from $\exp\left(\frac{-r^2}{w(z)^2}\right)$ in Equation 3.9. Therefore, the radius of the beam is defined as

where the E-field amplitude drops to the fraction of e^{-1}. The waist varies over the propagation along the z-axis, is minimal at $w_0 \equiv w(0)$, and diverges with $\Theta = \frac{w_0}{z_R}$. To compensate the divergence of the beam, the wavefront is curved, which is described by the curvature $R(z)$. For $z \ll z_R$, the curvature can be approximated by a planar wave while for $z \ll z_R$, the curvature reassembles the one of a spherical wave. At the focal region ($z = 0$), the curvature flips in sign.
An additional factor is the Gouy phase shift ψ ranging from $-\frac{\pi}{2}$ to $\frac{\pi}{2}$ with the largest increase in the Rayleigh range. The most intuitive way of interpreting this additional phase shift is treating it as light path difference between the actual one and the by geometric optic predicted path. Therefore, the Gouy phase is not solely an attribute of Gaussian beam, but of every focused wave [58].
Although the description of Gaussian beams seems rather extensive, the entire description of them is possible by knowing three parameters: The wavelength and, therefore, wave number k, the positions of the waist z_0 (for $z \to z - z_0$), and the minimal extension of the waist w_0. From there on, every other observable can be derived.
Going one step further, one can define the complex beam parameter q

$$\frac{1}{q(z)} = \frac{1}{R(z)} - \frac{i\lambda}{\pi w^2(z)} \ , \tag{3.12}$$

which fully describes the beam at position z. With it, the transfer matrix calculus of ray optics can be restored [59] by using

$$\begin{pmatrix} x \\ \Theta \end{pmatrix} \to \begin{pmatrix} q(z) \\ 1 \end{pmatrix} \ . \tag{3.13}$$

For HOMs, the curvature $R(z)$, waist size $w(z)$ stay the same. What changes is the perpendicular cross-section of the beam and additional accumulation of Gouy phase depending on the order of the mode, which will be introduced on the example of Hermite-Gaussian modes.

3.1.2. Hermite-Gaussian Modes

The Hermite-Gaussian modes are complete set of solutions to the paraxial wave equation in Cartesian coordinates described as

$$\begin{aligned} \mathrm{HG}_{nm}(x,y,z) = \frac{1}{\sqrt{2^{n+m-1} n! m! \pi}} \frac{w_0}{w(z)} H_n\left(\frac{\sqrt{2}x}{w(z)}\right) H_m\left(\frac{\sqrt{2}y}{w(z)}\right) \times \\ \times \exp\left(-\frac{r^2}{w^2(z)}\right) \exp\left(-ik\frac{r^2}{2R(z)} + i(l+m+1)\psi(z)\right) \ , \end{aligned} \tag{3.14}$$

with $H_n(x)$ the Hermite polynomials of nth order and define the spatial characteristics of the light field [51, 53]. Any laser beam can be described as the following sum:

$$\vec{E}(t,x,y,z) = \sum_j \sum_{n,m} E_0 \vec{\epsilon} HG_{nm}(x,y,z) \exp\left(-ikz + i\omega t\right) . \tag{3.15}$$

As seen in Equation 3.14, models a Hermite polynom in x- and y- dimension the amplitude allocation of the cross section. This amplitude cross section is fixed and scales only in size dependent on the waist size $w(z)$. An example is given in Figure 4 for different modes with the amplitude cross section on top and the associated phases on the bottom. The concentric features in phase are due to the curvature of the wavefront while the sharp phase jumps are due to the sign change in the Hermite polynomial. The sum $(n+m)$ gives the order of mode and the additional Gouy phase that accumulates. Therefore, two first order modes are presented on the left and one second order on the right.

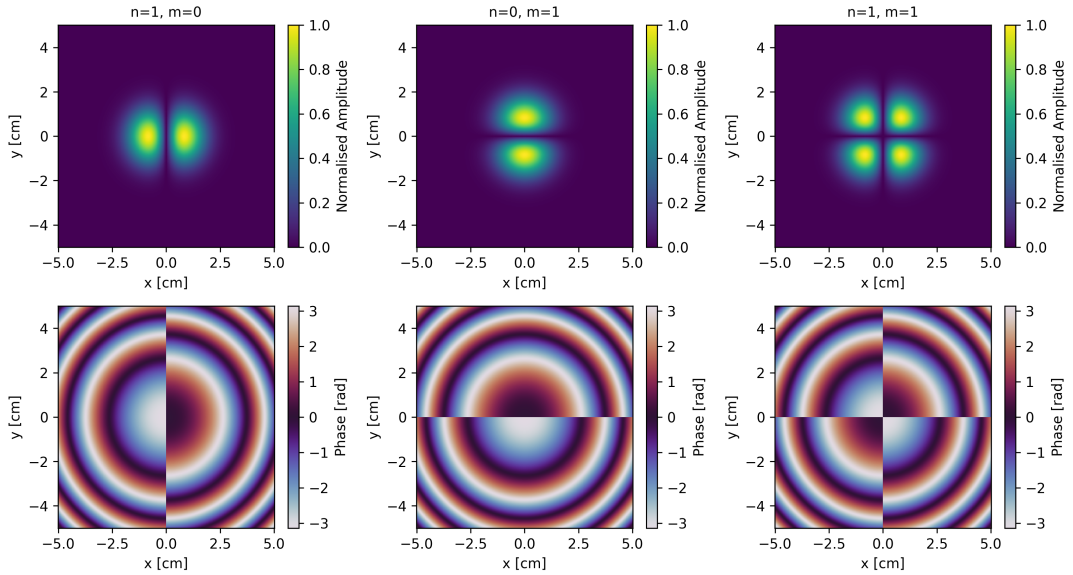

Figure 4: Top: Amplitude cross section of Hermite-Gaussian modes for different modes. Bottom: The associated phase.

3.2. Michelson Interferometer

Because of the quadrupole moment of gravitational waves, Michelson interferometers are a natural fit as a gravitational wave detector. Here, a laser beam is split into

two reflective arms in x- and y-direction[1] at a beam splitter. The reflected signal is then recombined at the beam splitter and read out with a photodiode at the reflective port, giving a measurement of the difference in arm length. Assuming lossless mirrors, the electric field at the photodiode can be described as

$$E_{out} = \frac{1}{2}\left(r_x e^{ik2L_x} - r_y e^{ik2L_y}\right) E_{in} \ , \tag{3.16}$$

with the detected signal power being

$$P_{out} = |E_{out}|^2 = P_{in}\cos^2\left[k(L_x - L_y)\right] \ , \tag{3.17}$$

with E_{in} and E_{out} the respective in- and output E-field, r_x and r_y the reflection coefficient of the mirrors at the end of the arms, k the wavenumber of the used laser, $L_{x/y}$ the respective length of each arm and P_{out} and P_{in} the in- and output power measured with the photodiode. For simplicity is r_x and r_y are set to -1 for full reflection.
Adding the presence of a gravitational wave yields an additional length change in both arms $\delta L_{x/y}$ depending on the induced strain $h \equiv \frac{\delta L_x - \delta L_y}{L}$, which leads to

$$P_{out} = P_{in}\cos^2\left[k(\Delta L + Lh)\right] \ , \tag{3.18}$$

with $\Delta L = L_x - L_y$ and $L = \frac{L_x + L_y}{2}$, where one can assume that $k\Delta L \ll 1$. Intuitively, one would suggest $k\Delta L = \frac{\pi}{4}$ as interferometer configuration to be the most sensitive to h as the derivative is here at maximum. However, one is also most sensitive to power, seismic or other ΔL influencing fluctuations, which are indistinguishable from gravitational wave in signal.

Nevertheless, a few key points of gravitational detection with Michelson interferometer can be derived from Equation 3.18. As δL grows with increasing L, the SNR can be increased by longer arms. The interferometer has to be decoupled from any noise that influences ΔL, such as seismic noise or fluctuations of the refractive index of air, for example. Further, the SNR can be increased by larger laser power as the intensity noise scales with $\sqrt{P}$. To decouple the measurement result from the present power measurement fluctuations, it is possible to run it in dark fringe mode. Here, the phase between both arms are π apart and, therefore, negatively interfere, resulting in no power at the read-out photodiode. But the detected signal for a gravitational wave signal scales then with $P_{out} \propto h^2$ in first order. For the expected strain of $h = 10^{-21}$, this is nearly impossible to detect. Therefore, the detection has to be enhanced by another technique, the nulled lock-in detection.

[1] Any configuration is possible as long as the two arms can span a 2D coordinate system

3.3. Nulled Lock-In Detection

The nulled lock-in detection restores the linear dependency of the output power in h by applying a lock-in detection. At dark fringe, the power and the derivative are zero, while the presence of a gravitational wave results in a second-order change in signal. By modulating the signal and comparing the modulation to the response of the instrument, the derivative of the instrument response is measured. Here, the second-order effect is reduced to a first-order effect.
To modulate the signal beam, an Electro-Optic Modulator (EOM) is used to modulate the phase of the laser beam with frequency Ω. It consists of a Pockels cell, a dielectric substrate whose refractive index changes proportionally to the applied voltage [60]. The resulting E-field can be expressed as

$$E_{in} = E_0 e^{i(\omega t + \beta \sin \Omega t)} \approx E_0 \left[J_0(\beta) e^{i\omega t} + J_1(\beta) e^{i(\omega+\Omega)t} - J_1(\beta) e^{i(\omega-\Omega)t} \right] \ , \quad (3.19)$$

with β the modulation depth that is proportional to the applied voltage, and J_0 and J_1 the Bessel functions of the respective order (see Appendix B). The second equation is approximated by the Jacobi–Anger expansion [61]. From thereon, one can see that the phase modulation leads to two additional frequencies being present in the laser beam, the so-called sidebands. The original frequency is called the carrier. As the frequencies are in superpositions, they can be treated separately.
The detected E-field E_{out} can now be calculated by inserting Equation 3.19 into the initial E_{out} (Equation 3.16) of the Michelson interferometer. For the carrier $E_{out,c}$ and sidebands $E_{out,\pm}$ this results in

$$E_{out,c} = -iE_0 J_0(\beta) \sin\left(2\pi \frac{\Delta L}{\lambda}\right) e^{-i\omega t + ik(L_x+L_y)} \ , \text{ and} \quad (3.20)$$

$$E_{out,\pm} = \mp iE_0 J_1(\beta) \sin\left[2\pi \left(\frac{\Delta L}{\lambda} \pm \frac{\Delta L}{\lambda_\Omega}\right)\right] e^{-i(\omega\pm\Omega)t + ik_\pm(L_x+L_y)} \ , \quad (3.21)$$

with λ the wavelength of the laser and λ_Ω the wavelength of the phase modulation. At this point, the Schnupp asymmetry [62, 63] is introduced to the interferometer by setting an asymmetric initial arm length with $\Delta L = n\lambda$. This way, the carrier frequency is set on the dark fringe, while the sidebands are not. Without this trick, the resulting signal at the end of this calculation would still be proportional to the second order of h. For the output E-field, this yields

$$E_{out,c} = 0 \ , \text{ and} \quad (3.22)$$

$$E_{out,\pm} = \mp iE_0 J_1(\beta) \sin\left[2\pi \left(\frac{\Delta L}{\lambda_\Omega}\right)\right] e^{-i(\omega\pm\Omega)t + ik_\pm(L_x+L_y)} \quad (3.23)$$

without the presence of a gravitational wave. With the presence of a gravitational wave $\Delta L \to \Delta L + Lh$, the carrier E-field changes to

$$E_{out,c} = -iE_0 J_0(\beta) e^{-i\omega t + i2kL}\ 2\pi \frac{L}{\lambda} h\ , \tag{3.24}$$

using $\sin(x) \approx x$ as $2\pi \frac{L}{\lambda} h \ll 1$. For the E-field of the sidebands, ΔL is approximated by $\Delta L \to (1 + O(h))$ as the zeroth order gives the needed linear term, while the higher order terms are later anyway rejected by the analysis. Therefore, Equation 3.23 does not change. Now, the measured output power of the photodiode P_{out} can be calculated as

$$\begin{aligned} P_{out} &= |E_{out}|^2 = |E_{out,c} + E_{out,+} + E_{out,-}|^2 \qquad (3.25)\\ &= P_{in} J_0^2(\beta) 4\pi^2 \frac{L^2}{\lambda^2} + 2P_{in} J_1^2(\beta) \sin^2\left(2\pi \frac{\Delta L}{\lambda_\Omega}\right) \\ &\quad + 2P_{in} J_1^2(\beta) \sin^2\left(2\pi \frac{\Delta L}{\lambda_\Omega}\right) \cos\left(2\Omega t + 8\pi \frac{L}{\lambda_\Omega}\right) \\ &\quad + P_{in} J_0(\beta) J_1(\beta) 4\pi \frac{L}{\lambda} h \sin\left(2\pi \frac{\Delta L}{\lambda_\Omega}\right) \cos\left(\Omega t + 4\pi \frac{L}{\lambda_\Omega}\right)\ , \qquad (3.26) \end{aligned}$$

leading to four terms. Two DC terms and two oscillating terms, one oscillating at 2Ω and one at Ω, which is also linearly proportional to h, the variable of interest. This term can be singled out by demodulating the signal with a local reference oscillator of frequency Ω and then applying low-pass filtering. Assuming a linear photodiode with transimpedance gain G, the read-out voltage signal is

$$V_{signal} = \langle G P_{out} \cos(\Omega t) \rangle = G P_{in} J_0(\beta) J_1(\beta) 2\pi \frac{L}{\lambda} \sin\left(2\pi \frac{\Delta L}{\lambda_\Omega}\right) \cdot h \tag{3.27}$$

independent of any intensity fluctuations and linear in h. Signal strength can now be optimised by adjusting the laser power P_{in}, the arm length L or the Schnupp asymmetry ΔL, which has a natural optimum at $\Delta L = \frac{\lambda_\Omega}{4}$. How these parameters can be optimised is presented in the following Sections.

3.4. Fabry–Pérot Cavities

To effectively increase the arm length of the interferometer, the beam path can be folded by bouncing the light back and forth in the arms. An elegant solution are Fabry–Pérot cavities [23]. The simplest form of a Fabry–Pérot cavity is an optical resonator consisting of two planar partly transmissive mirrors. For the sake of understanding their role as an extension of the Michelson interferometer, it is

merely enough to cover the plane wave response. How Gaussian beams couple into such cavities and what additional problems arise with that is described in Section 3.8.
When a beam encounters such a cavity, most of the incident light beam is reflected by the input mirror as a promptly reflected beam. The leakage beam into the cavity starts circulating. If the cavity length matches a multiple of the wavelength, constructive interference leads to a standing wave in the cavity, building up the amplitude of the beam. The cavity is now at resonance, and the amplitude of the leakage beam out of the cavity can be comparable to that of the incident or promptly reflected beam. Small deviations of the resonance criteria $2L = \lambda n$, will lead to large changes in amplitude. Therefore, Fabry–Pérot cavities are very sensitive instruments for measuring length changes. Extending the Michelson interferometer with Fabry–Pérot cavities, one can determine the reflection coefficient r as the ratio between incident and reflected E-fields

$$r = \frac{-r_i + r_0 e^{i4\pi\frac{L}{\lambda}}}{1 - r_i r_o e^{i4\pi\frac{L}{\lambda}}} \ , \tag{3.28}$$

with r_i, r_o the reflection coefficients of the input and output mirrors (assuming lossless mirrors), L the length of the cavity, λ the wavelength of the beam.
The reflective coefficient depends on the length of the cavity for several pairs of $r_i = r_o$ and t_i, where $r_i = r_o$ can be seen in Figure 5. Instead of describing the curves by r_i, r_o, the Finesse $\mathcal{F}$

$$\mathcal{F} = \frac{\pi\sqrt{r_i r_o}}{1 - r_i r_o} \tag{3.29}$$

is calculated, which gives a measure for the sensitivity of the cavity for said resonance criteria, as it can also be expressed as

$$\mathcal{F} = \frac{2\Delta\lambda}{\lambda} \ , \tag{3.30}$$

with the ratio between the resonant peaks at $\frac{\lambda}{2}$ and $\Delta\lambda$ the Full Width at Half Maximum (FWHM) normalised to the amplitude in the cavity of it. Higher values in Finesse $\mathcal{F}$ lead to stricter resonance criteria with larger amplitudes.
By using $r_i \neq r_0$, the cavity can also be tuned to reflect or transmit more power through itself when resonant. For the implementation in the Michelson interferometer, the Fabry–Pérot cavity is overcoupled by choosing $r_i < r_0$ so that the most power is reflected back into the interferometer.

To model the influence of the Fabry–Pérot cavity as arms of the Michelson interferometer, the reflection coefficient of the Fabry–Pérot cavity r (Equation 3.28) is

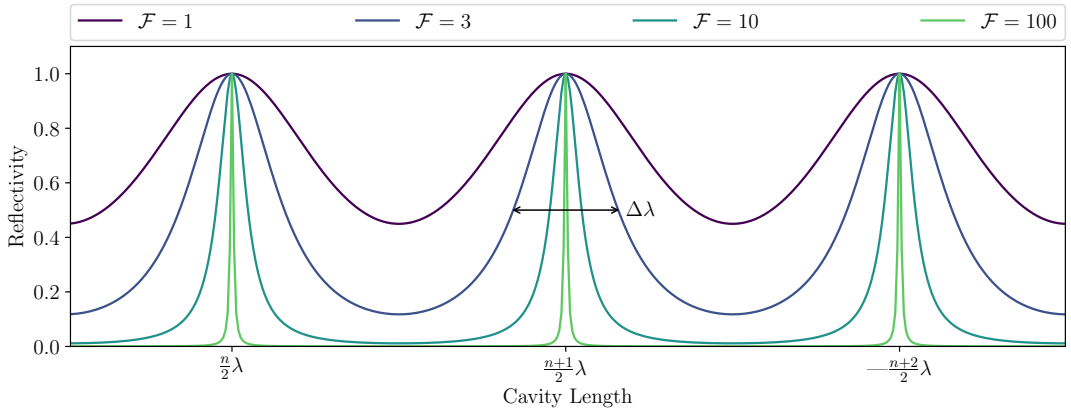

Figure 5: The reflectivity and, therefore, response of several Fabry–Pérot cavities with different Finesse. The larger the Finesse, the stricter the criteria for resonance.

inserted as the reflection coefficients r_x/r_y of E_{out} of the Michelson interferometer (Equation 3.16). The sidebands do not need to be in resonance with the Fabry–Pérot cavities. It is even favourable, as the Schnupp asymmetry only has to be applied from the beam splitter to the input mirrors, which is easier to implement. From there on, the calculations of Section 3.3 can be repeated. To have a more precise response, Equation 3.28 is replaced by

$$r = \left(1 - \frac{\mathcal{F}_{ac}\epsilon}{\pi}\right)\left(1 + i8\mathcal{F}_{ac}\frac{\delta L_{x,y}}{\lambda}\right) \tag{3.31}$$

the reflection coefficient of a near resonance, lossy, and over-coupled Fabry–Pérot cavity, with ϵ the fractional power loss in one round trip, $\delta L_{x,y}$ the length deviation from the optimum resonance length and $\mathcal{F}_{ac} \approx \frac{2\pi}{t_i^2}$ the Finesse of an over-coupled cavity. Altogether, this leads to the following response at the photodiode for a Michelson interferometer with Fabry–Pérot cavities as arms

$$V_{signal} = 4GP_{in}J_0(\beta)J_1(\beta)\mathcal{F}_{ac}\frac{L}{\lambda}\sin\left(2\pi\frac{\Delta L}{\lambda_\Omega}\right)\left(1 - \frac{\mathcal{F}_{ac}\epsilon}{\pi}\right)\cdot h\ , \tag{3.32}$$

which increased the signal linear in $\mathcal{F}_{ac}$.

3.5. Power Recycling

When operating a Michelson interferometer at dark fringe at the photodiode, all the power of the recombined beams from the arms have to be reflected back to the laser source due to energy conservation. Instead of wasting this power, a partially transmitting mirror, called a power recycling mirror, is installed between the laser

source and the beam splitter. Together with the arms of the interferometer, it again forms a Fabry–Pérot Cavity, the recycling cavity. On resonance, the amplitude of the created standing waves increases proportionally to the finesse of the cavity. The calculations follow those from Section 3.4, but in a more sophisticated manner, as the carrier and sidebands need to be resonant in the power recycling cavity and the complex transmission and reflection coefficients of the arm cavities have to be used to calculate those of the recycling cavity. As the principles are the same, the underlying calculation is skipped in this Section, and the result is presented as

$$V_{signal} = \frac{4}{\sqrt{\pi}} G P_{in} J_0(\beta) J_1(\beta) \mathcal{F}_{ac} \sqrt{\mathcal{F}_{rc}} \frac{L}{\lambda} \cdot h \ , \tag{3.33}$$

with $\mathcal{F}_{rc}$ the Finesse of the recycling cavity. The signal could only be increased by $\sqrt{\mathcal{F}_{rc}}$ as the sidebands are not resonant in the arm cavities.

3.6. Mode Cleaning Cavities

Up to this point, the interferometer can be described by planar waves. As in Section 3.1 introduced, this does not depict the reality of laser beams. Therefore, the cavities do not only have to be length-matched but also have the mirrors match the curvature of the Gaussian beam in the cavity, as the cavity resonant modes span their own set of Gaussian modes. This is called mode matching; the complex beam parameter q_{input} has to be matched to q_{cavity}. Through misalignment and various other processes, higher-order modes can be generated in the cavities and, therefore, in the interferometer. The detailed processes that lead to these HOMs are discussed in-depth in Section 3.8.
At the detector photodiode, HOMs lead to a lower contrast as they are not at dark fringe due their additional Gouy phase, lowering the SNR [26]. When entering the interferometer, HOMs reduce the power in the TEM_{00} of the laser beam as a consequence of energy conservation, again reducing the SNR of the detector. Therefore, mode cleaners are installed at the in- and output of the interferometer. With the suppression of the HOMs, the non-uniformities of the laser beam are decreased with better pointing stability [64]. Additionally, the cavity acts as a low-pass filter on intensity noise [65].
To use a Fabry–Pérot cavity as a mode cleaning cavity, it has to be of high Finesse, mode matched to the TEM_{00} mode of the input beam, and locked to the laser frequency. To achieve this, the length of the cavity is kept variable and controllable by a piezoelectric actuator. A feedback loop matches the cavity length to the laser frequency of the TEM_{00} mode. This locking technique, called PDH locking, is described in depth in the following Section. Due to the additional Gouy phase of the HOMs, they do not resonate in the mode cleaning cavities. They are not

transmitted but reflected at the input mirror as a consequence of the high Finesse of the cavity.

3.7. Pound–Drever–Hall Locking

The state of a Fabry–Pérot cavity can be monitored by measuring its reflected power. If the cavity is in resonance, the reflected power drops to zero as the leakage beam destructively interferes with the incident beam. When the cavity length or the laser frequency changes, the reflected power increases as the cavity goes out of resonance. But the increase in reflected power alone provides no information about the direction the cavity goes out of resonance. Therefore, a nulled lock-in detection based on the non-reflective sidebands is applied as introduced in Section 3.3.
The reflected power P_{ref} measured at the photodiode can then be calculated by multiplication of the sideband enhanced input E-field E_{in} (Equation 3.19) and the complex reflection parameter $r(\omega)$ of the Fabry–Pérot cavity (3.28). Then, taking the absolute square of it leads to

$$\begin{aligned} P_{\text{ref}} = P_c|r(\omega)|^2 + P_s\left(|r(\omega+\Omega)|^2 + |r(\omega-\Omega)|^2\right) \\ + 2\sqrt{P_c P_s}\left[\text{Re}\left(Err\right)\cos\Omega t + \text{Im}\left(Err\right)\sin\Omega t\right] + [2\Omega \text{ terms}] \ , \end{aligned} \tag{3.34}$$

with P_c and P_s the respective power in the carrier or sideband, and

$$Err = \left[r(\omega)r^*(\omega+\Omega) - r^*(\omega)r(\omega-\Omega)\right] \ , \tag{3.35}$$

the so-called error signal with ω the laser frequency and Ω the modulation frequency of the sidebands. By mixing the detected power with a reference frequency of Ω, the error signal can be retrieved. A comparison between the reflected power and the error signal of a cavity as a function of length can be seen in Figure 6.
This can now be used as an observable which highlights in which direction the cavity drifts out of resonance. Subsequently, this can be used to actively regulate the length of the cavities [66]. This technique was originally developed for the stabilisation of microwave oscillators [67] by R.V. Pound and adapted for optical frequencies by R. W. P. Drever et al. in [16].

3.8. Generation of Higher Order Modes

Constructing such an advanced instrument, all components can only be created and aligned to a certain precision. Imperfections in the mirror surface smoothness or the homogeneity of the refractive index will lead to deformation in the wavefront. Thermal expansion due to the local absorption of laser light or a change in refractive index in components will lead to similar results. Misalignment and deformations of

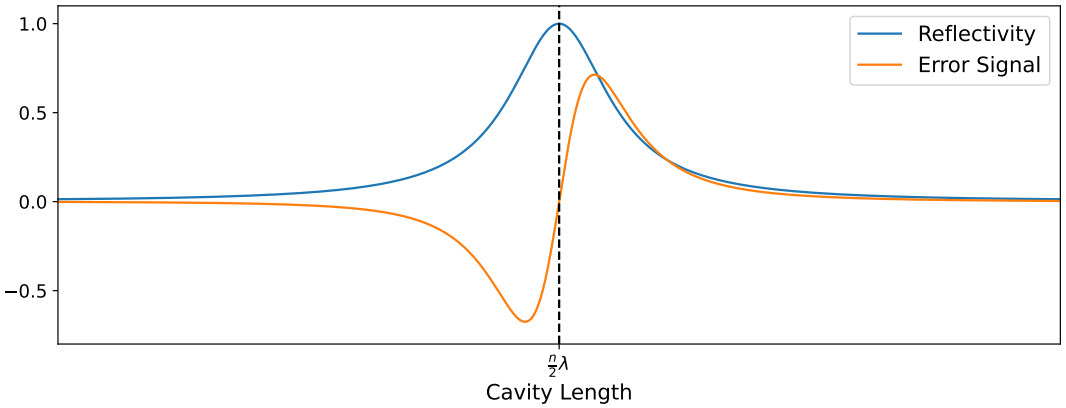

Figure 6: Comparison between the reflectivity of a cavity around resonance and the generated error signal produced by applying the PDH technique of nulled lock-in detection.

beams result in different responses of the Fabry–Pérot cavities. And the list goes on. All these effects contribute to the generation of HOMs [24, 68].
In this Section, the generation of HOMs due to a mode mismatch between the input beam and cavity normal modes shall be exemplarily discussed. Mode mismatches can be categorised into four cases, as illustrated in Figure 7.
A description of each case is laid out following the approach provided in [69][2], where the mismatched beam in fundamental mode is described in the bases of the normal modes of the cavity in first order. For simplicity, only HOMs up to the second order are considered, and the modes are only considered in two dimensions $HG_{nm}(x, y, z) \to HG_n(x, z)$ with $z = 0$ without loss of generality. Therefore, the fundamental and the first two orders reduce to

$$\mathrm{HG}_0(x) = \sqrt{\frac{2}{\pi}} e^{-\frac{-x^2}{w_0^2}} \quad , \quad \mathrm{HG}_1(x) = \frac{2\sqrt{2}}{\sqrt{\pi}} \frac{x}{w_0} e^{-\frac{-x^2}{w_0^2}} \quad , \tag{3.36}$$

$$\text{and} \quad \mathrm{HG}_2(x) = \frac{1}{\sqrt{\pi}} \left(\frac{4x^2}{w_0^2} - 1 \right) e^{-\frac{-x^2}{w_0^2}} \quad , \tag{3.37}$$

using Equation 3.14.

Tilt Mismatch
From the perspective of the normal modes of the cavity, a tilted beam at angle α can be described as

$$E(x) = E_0 \mathrm{HG}_0 e^{ik\alpha x} \quad , \tag{3.38}$$

[2]The source uses a different normalisation for the set of used Hermite-Gaussian modes.

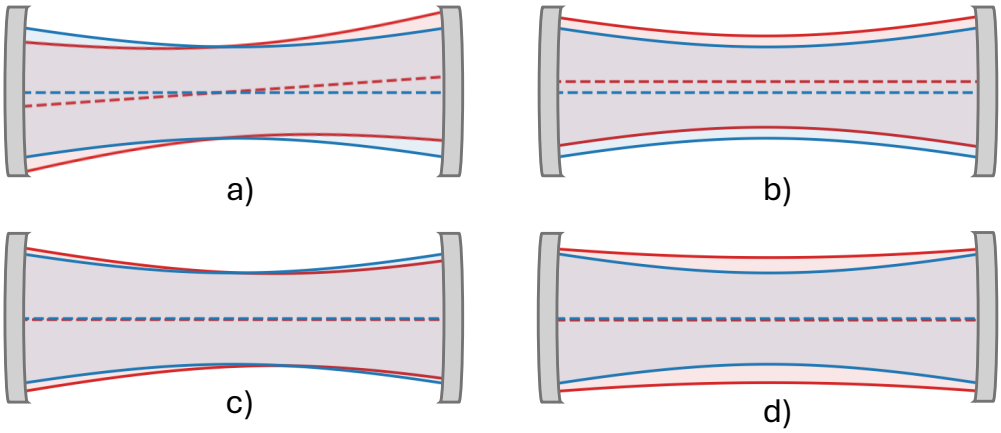

Figure 7: Illustration of the four ways of misaligning an input beam (red) to the normal mode of the cavity (blue). A tilt between the optical axes a), an offset between the optical axes b), a mismatch in waist position c), and a mismatch in waist size d).

as the wave propagates along a line described by $e^{-ik(z+\alpha x)}$. For small angles, this can be approximated by

$$E(x) \approx E_0 \mathrm{HG}_0 \left(1 + ik\alpha x\right) = E_0 \left(\mathrm{HG}_0(x) + \frac{ikw_0\alpha}{\sqrt{2\pi}} \mathrm{HG}_1(x)\right) \ , \tag{3.39}$$

using the Taylor expansion of $e^x \approx (1 + x)$ up to the firstorder. A tilted input beam therefore induces an additional $\frac{\pi}{2}$ out-of-phase first-order mode.

Optical Axis Offset

For an offset of a between the optical axis of the input beam and the normal modes of the cavity, the beam can be described as

$$E(x) = E_0 \mathrm{HG}_0(x - a) = E_0 \sqrt{\frac{2}{\pi}} e^{-\frac{-(x-a)^2}{w_0^2}} = E_0 \sqrt{\frac{2}{\pi}} e^{-\frac{-x^2}{w_0^2}} e^{-\frac{ax}{w_0^2}} e^{-\frac{-a^2}{w_0^2}} \ , \tag{3.40}$$

where $e^{-\frac{-a^2}{w_0^2}} \approx 0$. By using the Taylor expansion of $e^{-\frac{ax}{w_0^2}}$ up to first order, the beam can be approximated with

$$E(x) \approx E_0 \sqrt{\frac{2}{\pi}} e^{-\frac{-x^2}{w_0^2}} \left(1 + \frac{2ax}{w_0^2}\right) = E_0 \left(\mathrm{HG}_0 + \frac{a}{w_0} \mathrm{HG}_1\right) \ , \tag{3.41}$$

which results in an additional in-phase Hermite-Gaussian mode of first order.

Waist Position Mismatch
In the case of a waist position mismatch, $z_0 = b$ instead of $z_0 = 0$ for the input beam, the curvature of the beam becomes relevant again as $R(-b) \neq 0$ (see Equation 3.11). Therefore, the input beam can be described as

$$E(x) = E_0 \sqrt{\frac{2}{\pi}} e^{-\frac{-x^2}{w_0^2}} e^{-\frac{ikx^2}{2R(-b)}} \tag{3.42}$$

in the normal modes of the cavity. Taylor expanding $e^{-\frac{ikx^2}{2R(-b)}}$ to first order, leads to

$$E(x) \approx E_0 \sqrt{\frac{2}{\pi}} e^{-\frac{-x^2}{w_0^2}} \left(1 - \frac{ikx^2}{2R(-b)}\right) \tag{3.43}$$

$$= E_0 \left[\mathrm{HG}_0 - \frac{i\sqrt{2}kw_0^2}{8R(-b)} \left(\mathrm{HG}_2 + \frac{1}{\sqrt{2}}\mathrm{HG}_0\right)\right] \ , \tag{3.44}$$

a $\frac{\pi}{2}$ out-of-phase second order and fundamental term.

Waist Size Mismatch
For the waist size mismatch of Δw, the beam can be described in the normal modes of the cavity by $w_0 \to w_0 + \Delta w$:

$$E(x) = E_0 \sqrt{\frac{2}{\pi}} e^{-\frac{-x^2}{(w_0+\Delta w)^2}} \ . \tag{3.45}$$

Taylor expanding the whole exponential function around w_0 up to first order leads to

$$E(x) \approx E_0 \sqrt{\frac{2}{\pi}} e^{-\frac{-x^2}{w_0^2}} \left(1 + \frac{2x^2\Delta w}{w_0}\right) \tag{3.46}$$

$$= E_0 \left[\mathrm{HG}_0 + \frac{\sqrt{2}\Delta w}{2w_0} \left(\mathrm{HG}_2 + \frac{1}{\sqrt{2}}\mathrm{HG}_0\right)\right] \ , \tag{3.47}$$

an in-phase second order and fundamental term.
The rule of thumb for all cases can be expressed as asymmetric variations lead to odd Hermite-Gaussian HOMs while symmetric ones lead to even Hermite-Gaussian HOMs, which corresponds to their intensity cross-sections. The three dimensional case of $HG_{nm}(x, y, z)$ can be easily derived by [51]

$$HG_{nm}(x, y, z) = HG_n(x, z) HG_m(y, z) \ . \tag{3.48}$$

A standard way [64] to detect and then correct these misalignments is the Ward technique [69]. The already implemented sidebands, which stabilise the cavity

length via the PDH technique, are here detected with two quad photodiodes. One in the near-field and one in the far-field of the beam to disentangle the in-phase and $\frac{\pi}{2}$ terms of the generated HOMs. By subtracting mixed powers of different quadrants, an error function proportional to the asymmetric HOMs can be created.

3.9. The Einstein Telescope

The Einstein Telescope is planned as a next-generation laser interferometer instrument to detect gravitational waves, increasing the sensitivity by over a magnitude [14, 70, 71, 32]. The official site location is still up for debate. However, it will be chosen from the following locations, with operation planned to start in 2035: the Meuse-Rhine Euroregion (Belgium, Netherlands and Germany), Sardinia (Italy) [72], and the newest contender, Lusatia (Germany) [73].
Instead of deploying one broadband interferometer, the xylophone approach of one high-frequency and one low-frequency optimised interferometer is chosen. In order to understand the design choice, the fundamental noise sources have to be discussed. As an example, the sensitivity curve of the low-frequency interferometer of the Einstein Telescope is presented in Figure 8.

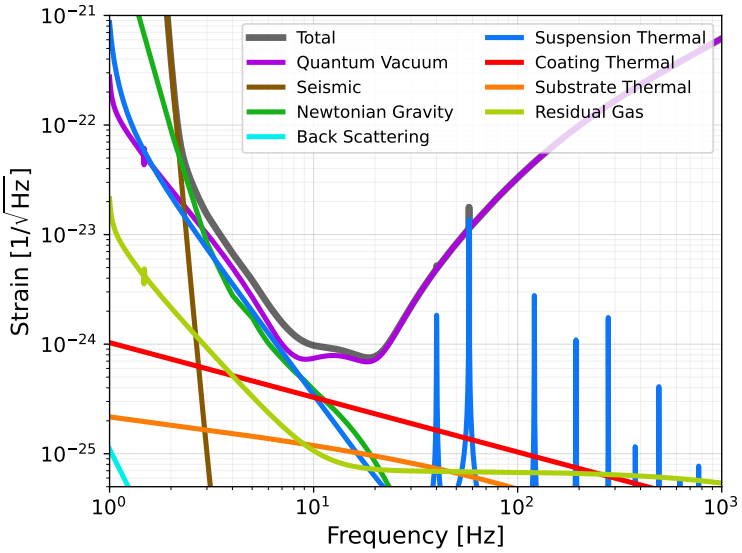

Figure 8: Sensitivity curve for the proposed low-frequency interferometer of the Einstein telescope with each noise contribution marked. Created with [74].

The main limiting factor of a laser interferometer is the quantum noise of the laser itself. It can be roughly divided into radiation pressure noise, which dominates for low frequencies ($< 50\,\mathrm{Hz}$), and shot noise, which dominates at higher

frequencies ($> 200\,\mathrm{Hz}$) [71]. The radiation pressure noise arises from the laser amplitude fluctuation, leading to variation in the momentum transfer between the emitted photons and the suspended mirrors, causing vibrations. This effect scales proportionally to the laser power in the interferometer. Shot noise, on the other hand, is due to the phase uncertainty of the light field itself and scales with the square of the power. Therefore, it is operated at a laser power in the Fabry–Pérot cavities of 18 kW to avoid unnecessary radiation pressure noise in the aspired frequency range, while the high frequency one is using a laser power of 3 MW to increase the SNR in comparison to the shot noise in the high frequency range[71].

Another major noise source are thermal effects, as in the suspension, the coating or the substrate of the optics itself. For the suspension, additional vibrations are generated, while for the coating and substrate, the thermal load leads to deformation, changes in refractive index or Brownian fluctuations. As these effects drop off with frequency, the low-frequency interferometer is more affected. Therefore, the low-frequency interferometer is equipped with cryogenic compliant suspension with silicon as mirror material and is cooled to 10 to 20 K. In contrast, the high-frequency interferometer pushes the techniques used in second generational detectors, such as Advanced LIGO [31] and Advanced Virgo [75], to the next level at room temperature.
Following the concept of the advanced Virgo detector, a 17 meter long superattenuator consisting of a six-stage pendulum system for horizontal seismic isolation is planned. Similarly, a cantilever spring system will be used for vertical seismic isolation. Both are hosted by a inverted pendulum, further attenuating in the horizontal. To reduce the influence of local gravitational forces generated by mass fluctuations in the environment, the detector will be built at a depth of 200 to 300 m.
As a detector layout, two versions are presented, one consisting of two L-shaped detectors at different locations and one equilateral triangle-shaped detector at one location with three xylophone interferometers interlocked. An artist's impression of the triangular-shaped version is given in Figure 9. For both arm cavity length between 10 km an 20 km are suggested [32]. The advantage of two L-shaped detectors is the better localisation of sources and the veto of false signals created by the environment, while the triangle-shaped detector is equally sensitive to each polarisation of gravitational waves and has a more cost-efficient infrastructure.

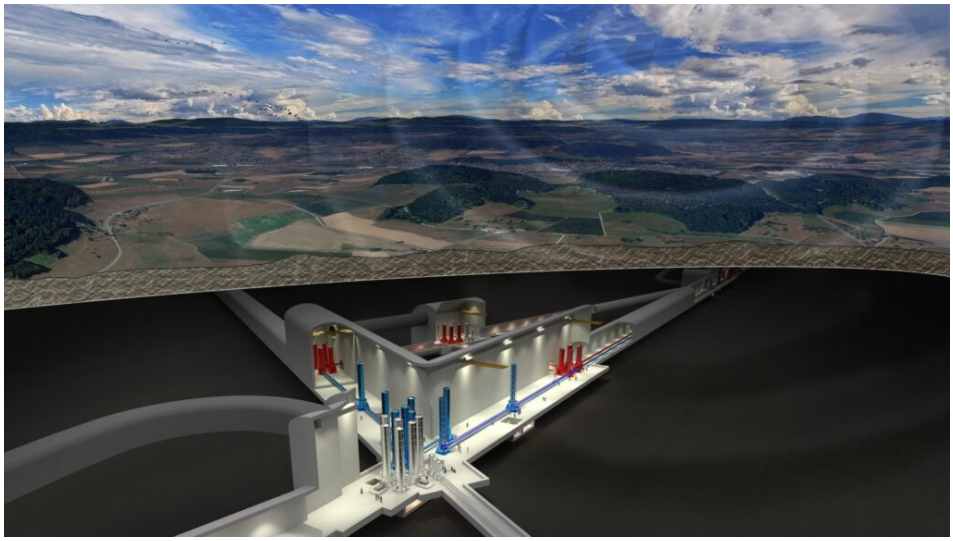

Figure 9: Artist's impression of the triangular-shaped detector layout of the Einstein Telescope. Image taken from [76].

4. Phase Camera Design

Wavefront deformations caused by thermal lensing, mirror surface roughness, and misalignment in the interferometer, for example, can create different mode content for each radio-frequency component. This mode content deteriorates the response of the instrument to gravitational waves. Therefore, a monitoring tool is needed to detect these wavefront aberrations across all radio-frequency components to trace down noise sources and eliminate them. Such a tool, for example, is a phase camera, which depicts the phase and amplitude of the wavefront by means of a reference beam, called heterodyne detection and analyses the signal similarly to the nulled lock-in detection in Section 3.3. There are of course different techniques to realise such wavefront sensors capable of imaging the phase and amplitude [18] like time of flight cameras [77], optical lock-in cameras [78] or scanning pinhole phase cameras [19], each with their own advantages and disadvantages.[3]
The significant advantage of a phase camera is that the spatial amplitude and phase of the wavefront can be measured simultaneously for all sidebands if digital demodulation is used. In Advanced LIGO, for example, five sideband frequencies result in eleven to monitor wavefronts including the carrier [79].
This comes at the cost of the need for high-speed digitisers at sample rates of $\geq 500\,\mathrm{MSa/\,s}$. An initial and well-established design of the phase camera is the scanning pinhole camera, where a piezo-driven mirror is used to scan the wavefront over the diode [19], keeping the cost of the digitiser low.

In this work, this concept is extended by introducing a static 1D/2D image sensor. A spatial image sensor has the advantage of a stable phase relation between pixels at higher frame rates. The development is driven by the availability of the low-cost, high-speed digitiser ASIC CTC, which was initially developed for the SST Camera of CTAO, allowing the equipping of large pixel number sensors. Although, for the proof of concept, the commercial Spectrum M4i.4451-x8 digitising cards [80] are used for prototyping of the signal chain. A suitable spatial image sensor is found as a multimode fibre array equipped with individual photodiodes.
In this Section, the general concept of phase cameras is introduced, followed by the introduction of the fibre-based camera, with the novel feature of a multimode fibre array as an imaging sensor. Then the fibre-based camera is described in depth, starting with the optical setup used in the laboratory. The influence of the multimode fibre array on the observed phase is discussed. A detailed description of the electrons developed for the signal chain is followed.

[3] This list is not exhaustive.

4.1. Concept of the Phase Camera

The concept of locked-in amplified detection is already introduced in Section 3.3. For the phase camera, this concept is extended by introducing heterodyne detection of the signal combined with I-Q demodulation of the signal, to recover the phase and amplitude of each radio-frequency component [20]. Heterodyne detection is the interference of the observable beam with a frequency-shifted reference beam. This has two reasons: First, as the carrier and the sidebands of the laser beam are the observables of the phase camera, the sidebands can no longer be used as a reference for the demodulation/mixing. Second, the frequency shift is needed as sidebands of the modulation frequency of Ω are indistinguishable from each other when demodulating again, as

$$
\begin{aligned}
P_{\text{homodyne}} &= |E_c(x,y,t) + E_+(x,y,t) + E_-(x,y,t)|^2 && (4.1)\\
&= |E_c(x,y)\exp\left[-i(\omega t + \phi_c)\right] && (4.2)\\
&\quad + E_+(x,y)\exp\left[-i((\omega+\Omega)t + \phi_+)\right]\\
&\quad + E_-(x,y)\exp\left[-i((\omega-\Omega)t + \phi_-))\right]|^2\\
&= P_c + P_+ + P_-\\
&\quad + 2|E_c||E_+|\cos\left[\Omega t + \phi_c - \phi_-\right]\\
&\quad + 2|E_c||E_+|\cos\left[-\Omega t + \phi_+ - \phi_c\right]\\
&\quad + 2|E_-||E_+|\cos\left[2\Omega t + \phi_+ - \phi_-\right] && (4.3)
\end{aligned}
$$

contains two cosine terms with the same frequency Ω. Adding the presence of a reference beam of frequency ω_{ref} to create the heterodyne detection, the detected power is extended by

$$
\begin{aligned}
P_{\text{heterodyne}} &= |E_c(x,y,t) + E_+(x,y,t) + E_-(x,y,t) + E_{ref}(x,y,t)|^2 && (4.4)\\
&= P_{\text{homodyne}} + P_{ref}\\
&\quad + 2|E_c||E_{ref}|\cos\left[\omega_{ref}t + \phi_{ref} - \phi_c\right]\\
&\quad + 2|E_c||E_{ref}|\cos\left[(\omega_{ref}+\Omega)t + \phi_{ref} - \phi_+\right]\\
&\quad + 2|E_c||E_{ref}|\cos\left[(\omega_{ref}-\Omega)t + \phi_{ref} - \phi_-\right]\ . && (4.5)
\end{aligned}
$$

The sidebands can now be individually acquired by mixing the detected signal with the modulation frequency relative to the reference frequency. Therefore, the frequency-shifted reference beam is strictly speaking part of the phase camera, as without it, the separation of sidebands by mixing the signal is not possible.
To extract the phase of an arbitrary radio-frequency component and, therefore, a term in Equation 4.5, the I-Q demodulation shall be exemplary derived. But first, the mixing process is extended by

$$
I = P\cos\left(\omega_m t\right)\ , \qquad Q = P\sin\left(\omega_m t\right)\ , \tag{4.6}
$$

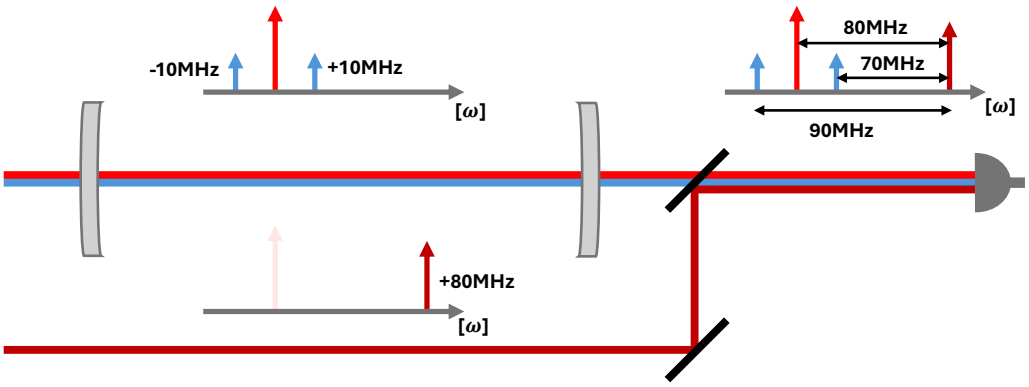

Figure 10: Schematic for the heterodyne detection of the sidebands and carrier signal for an arbitrary cavity. The sideband modulation frequency is set to 10 MHz, while the reference is 80 MHz detuned to the initial laser frequency. In relation to a shifted reference, the sidebands can individually be distinguished as they are seen as 70 MHz and 90 MHz modulations.

which are defined as in-phase (I) and quadrature (Q) terms of the signal, with P the detected power of the photodiode and ω_m the mixing frequency. Now I is calculated by using Equation 4.5 as input, but only considering the ω_{ref} term for simplicity.

$$I = 2|E_c||E_{ref}| \cos(\omega_{ref} t + \Delta\phi) \cos(\omega_m t) \tag{4.7}$$
$$= 2|E_c||E_{ref}| \cos[(\omega + \omega_m)t + \Delta\phi] \cos[(\omega - \omega_m)t + \Delta\phi] \ , \tag{4.8}$$

with $\Delta\phi = \phi_{ref} - \phi_c$. For $\omega = \omega_m$, which is the desired value, the equation simplifies to

$$I = 2|E_c||E_{ref}| [\cos(\Delta\phi) + \cos(2\omega t + \Delta\phi)] \ . \tag{4.9}$$

By applying a suitable low-pass filter, one can get rid of the second term dependent on 2ω. All that is left is a cosine term depending on the relative phase between the wanted observable and the reference beam. For a signal consisting of multiple frequencies, a lower cut-off frequency reduces the influences of unwanted frequencies and, therefore, increases the SNR. In this work, a low-pass filter is applied by summing over an integration time of the mixed signal. Calculating Q leads to a similar result, but replaces the cosines with sines. By applying

$$\Delta\phi = \arctan\left(\frac{Q}{I}\right) \ , \qquad A = \sqrt{I^2 + Q^2} \ , \tag{4.10}$$

the relative phase $\Delta\phi$ and the mixed amplitude A can be calculated. In other words, the I-Q demodulation represents a discrete Fourier transformation evaluated at one frequency. Increasing the integration time (a decrease of cut-off frequency) and, therefore, the number of samples, the frequency bins and, therefore, frequency resolution increases. As the phase of one of these frequency bins is evaluated, the SNR increases with the smaller frequency bins as less of the noise floor is present in the observable. A large enough integration time is also needed to separate the individual sidebands in the frequency spectrum.

From these calculations, it is evident that the phase camera is only able to measure the phase of wavefronts in relation to the reference beam. A change in signal or reference is indistinguishable. In Section 5.3, it will be evident that a non-stable reference is the limiting factor in phase resolution. Additionally, if $\omega \neq \omega_m$,

$$\Delta\phi = \arctan \frac{\sin\left[(\omega - \omega_m)t + \Delta\phi\right]}{\cos\left[(\omega - \omega_m)t + \Delta\phi\right]} = \Delta\omega t + \Delta\phi \tag{4.11}$$

phase ramps with the frequency $\Delta\omega = \omega - \omega_m$ are observed in the phase. Differences in frequency greater than the image rate of the camera are enough to make the phase time series uninterpretable. A synchronisation between the different frequency oscillators is therefore essential. Following from Equation 4.6, the noise for the phase and the amplitude can be calculated by error propagation, leading to

$$\sigma_{\mathrm{Ampl}} = \sigma_{\mathrm{Signal}} \text{ and } \sigma_\theta = \frac{\sigma_{\mathrm{Ampl}}}{\mathrm{Ampl}} \ . \tag{4.12}$$

The noise in amplitude therefore only depends on the noise floor of the signal chain, the integration time of the I-Q demodulation and the intensity noise of the laser itself. The phase noise, on the other hand, also depends on the detected amplitude of the demodulated signal.

4.2. Fibre-Based Camera Overview

The novel feature of the fibre-based phase camera is the 2D image sensor. The expertise of parallel fast digitisation of photo detectors was already present at the local institute. The challenge at hand is to find a suitable spatial 2D sensor sufficient for the needs of a phase camera. Two ideas were proposed, each with its own advantages and disadvantages. The first was using a 2D Avalanche PhotoDiode (APD) array. Tightly pitched and fast APDs could monitor the laser beam directly, similar to the established phase cameras. But the tightly laid out APDs on one substrate would lead to high cross-talk between the pixels for radio frequency signals as observed in quadphotodiodes [81]. Additionally, arrays larger than 8×8

or 1×128 are hard to manufacture. In principle, a prototype camera with a limited number of pixels would be possible, but not scalable.

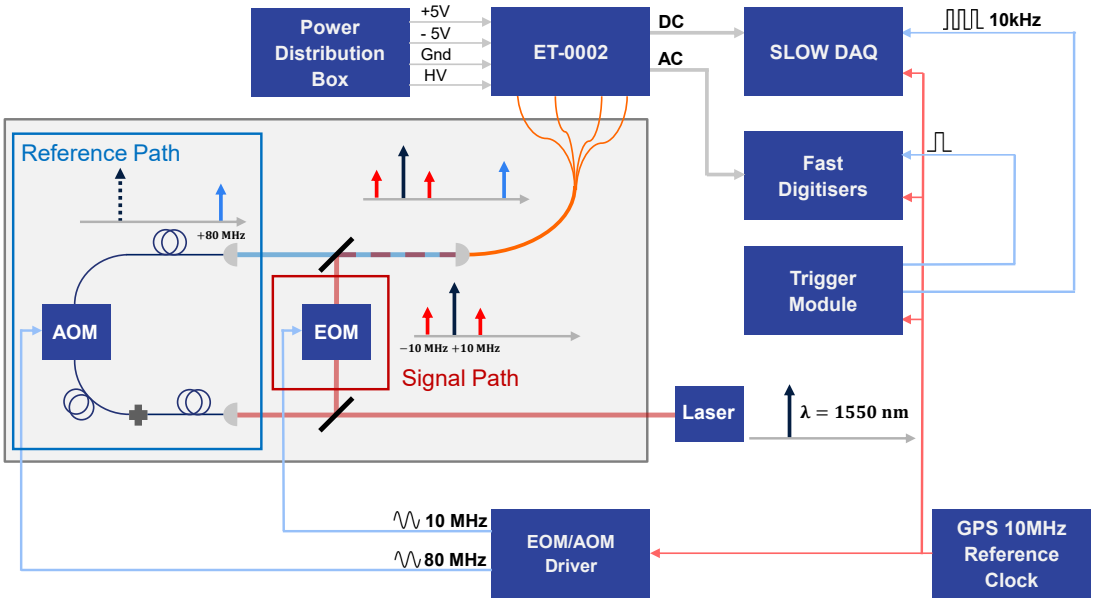

Figure 11: Schematic of the phase camera as it is set up in the laboratory. The EOM is not part of the phase camera, but creates the sidebands in order to test the phase camera.

Therefore, the second approach, a camera based on an optical fibre array was chosen. An arbitrary amount of optical fibre can be packaged and glued together, solving the scalability problem. By using individual Positive Intrinsic Negative (PIN) photodiodes at the end of each fibre as read-out, the radio frequency cross-talk in the substrate in can not emerge. This all comes at the cost of power loss at coupling into the individual fibres, resulting in the need for high input laser power and/or higher gain amplifiers. Additionally, the signal propagation in the optical fibre has to be understood.

A schematic overview of the fibre-based camera as it is tested in the laboratory is given in Figure 11. A 1550 nm laser is split into two paths via a beam splitter: A signal path with an EOM to generate the wanted sidebands to observe and a reference path including an Acousto-Optic Modulator (AOM) to shift the frequency for heterodyne detection. The AOM is fibre-coupled to simulate circumstances at a large infrastructure such as the Einstein Telescope. Both beams are recombined with a second beam splitter and observed with the fibre array, where each individual pixel intensity is measured with a photodiode and amplified by the ET-0002 amplifier board. The Alternating Current (AC) port is digitised by fast (> 500 MSa/ s)

digitisers to extract the phase and amplitude of each radio-frequency component, at the same time, the overall laser intensity is monitored via the Direct Current (DC) port digitised with the low spec SLOW DAQ digitisers. A trigger module sets the frame rate of the camera. For correct operation of the camera, all needed signal generators and DAQ electronics are synchronised by a shared 10 MHz clock. A detailed description of each component is given in the following Sections.

4.3. Optical Setup

During the course of this work, the optical setup was changed multiple times to adapt to new insights or beam configurations. A characterisation of the beam parameters is therefore left out, as it is also not needed to understand the operation principles of the phase camera and its characterisation in performance. For the analysis of wavefront phase images, this becomes relevant again and is provided in the dedicated Sections.
Nevertheless, the fundamentals to generate the heterodyne detection stayed the same. These can be grouped into the laser source, a signal path which generates sidebands, and the reference path, shifting the beam frequency to enable heterodyne detection. All of them are presented in the following Sections.

4.3.1. Laser Source

As a laser source in the laboratory, the CoSF-F-ER-B-LP from Connet Laser Technology [82] is used. It is a 1550 nm fibre-coupled laser with an adjustable power range from 10 mW to 200 mW. The phase noise over the relevant frequency spectrum up to 10 kHz is below 1 mrad, with a Relative Intensity Noise (RIN) that is below -145 dBc/Hz. In the later Sections, it will be evident that the phase noise of the laser is below the best measured phase resolutions of the fibre-based phase camera (Section 5.3) and the RIN is below the noise floor of the developed amplifier board (Section 5.1). Therefore, it is a suitable choice for testing the fibre-based phase camera.
To create a free-space laser beam, the THORLABS TC12APC is used as a collimator with a waist diameter of 2.27 mm at a distance of 10.20 mm in front of the laser.

4.3.2. Signal Path

For the generation of sidebands, the EOM QUBIG PM7-SWIR1_10 [83] is used. As the sidebands are only generated to test the phase camera, their exact frequency is arbitrary. Therefore, it is a resonant EOM of nominal centre frequency of 10 MHz that any function generator can drive. The modulation depth, depending on the input voltage and order n of the sideband, can be seen in Figure 12 and follows

$|J_n|^2$ with J_n being a Bessel function (see Appendix B). It is directly derived from Equation 3.19 and the voltage to modulation depth β response of the device. For use in the laboratory, the modulation depth β is varied depending on the measurement if more or less power is needed in the sidebands (Section 5.3) or if more frequencies in the frequency range are needed to be probed (Section 5.5.2). Instead of 10 MHz, 10.045 MHz is used as it is the measured centre frequency of the EOM.

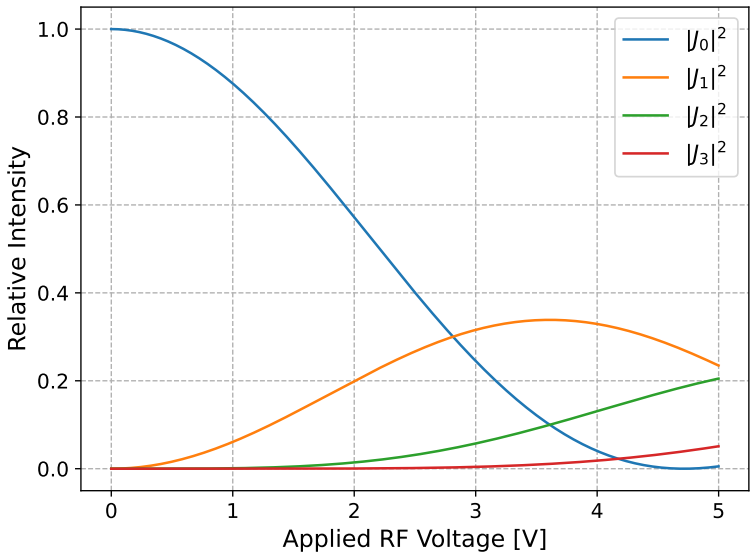

Figure 12: The calculated relative intensity for sidebands of nth order, depending on the applied Radio Frequency (RF) voltage at resonance frequency, is represented by the associated Bessel function $|J_n|^2$.

4.3.3. Reference Path

To enable heterodyning detection, one of the split optical arms needs to be shifted off the natural frequency of the laser. In the phase camera setup, this is the reference path, which is strictly speaking part of the phase camera itself. For frequency shifting, the fibre-coupled AOM AERODIODE 1550AOM-11 [84] with a nominal shifting frequency of 80 MHz is used. The fibre coupling is indispensable at a large facility like the Einstein Telescope, where free-space distribution of the laser is not an option, as it may be several hundred meters away.
In order to efficiently couple into the fibre, the input beam must be focused onto the fibre core at a certain incident angle depending on the fibre characteristics. For simplicity and stability of the setup, a collimator is used for this purpose.

Typically, these are applied to parallelise the divergent light of a fibre to a certain waist diameter, but can also be used vice versa. Matching the waist diameter and position of the to-be-focused beam to the specs of the collimator, it will focus the light into the fibre. For the used THORLABS TC12APC, the waist diameter is 2.27 mm at a distance of 10.20 mm in front of the collimator.
The AOM shifts the frequency of the input laser by applying an acoustic wave to an optical medium. The incident light is diffracted off the crystal by Bragg diffraction. The scattered light is then Doppler shifted up or down by the applied acoustic frequency and emitted at a certain angle due to the momentum transfer of the vibrating crystal to the light field [85, 86].
For phase camera measurements, the combination of function generator Aimtti TGF4082 and amplifier Mini-Circuits ZHL-6A-S+ is used to provide the 80 MHz signal in the needed power range of 15 to 35 dBm to drive the AOM.

In order to characterise the reference path, the throughput power depending on the RF driving power, laser input power and laser frequency is measured. For both, the Siglent SDG6052X is used to drive the AOM, as the Aimtti TGF 4082 has a maximum output frequency of 80 MHz. To measure the power of the beam, the light power meter THORLABS PM16-122 is used to measure the output power. For each set of parameters, 120 seconds worth of data is collected at a rate of roughly 1 Hz and then averaged.
For the dependency between the set RF driving amplitude and frequency shifted transmitted power, the RF driving signal is set to 80 MHz sine wave with V_{high} varied between 100 mV an 800 mV while V_{low} remains at 0 mV. This is repeated for different laser input powers. As the used light power meter can only handle powers up to 40 mW, the input powers above are extrapolated from the measurements within the limit. The results can be seen in Figure 13.
On the left, the percentage of transmitted frequency-shifted laser power to set RF driving amplitude is proportional to a square law and is independent of the input laser power. Therefore, the setup can be used at different optical powers without recalibration of the reference path. To extrapolate the results, a square fit is used with fit values $a = 2.11 \times 10^{-5} \pm 1.19 \times 10^{-12}$ and $x_0 = (-43.5 \pm 0.3)\,\text{mV}$.
For the frequency response of the AOM, the amplifier is driven with a sine wave of $V_{\text{low}} = 0\,\text{mV}$ and $V_{\text{high}} = 800\,\text{mV}$ over the frequency range of 60 MHz to 100 MHz in steps of 1 MHz. The deployed input power is $\approx 28\,\text{mV}$, measured in front of the fibre collimator.
The throughput power dependent on the frequency can be seen in Figure 13 on the right. To determine the resonance frequency of the AOM, a Gaussian function is fitted to the curve, which results in a resonance frequency of $(79.477 \pm 0.001)\,\text{MHz}$ with a FWHM of $(22.975 \pm 0.001)\,\text{MHz}$. Due to the width of the resonance, it is not

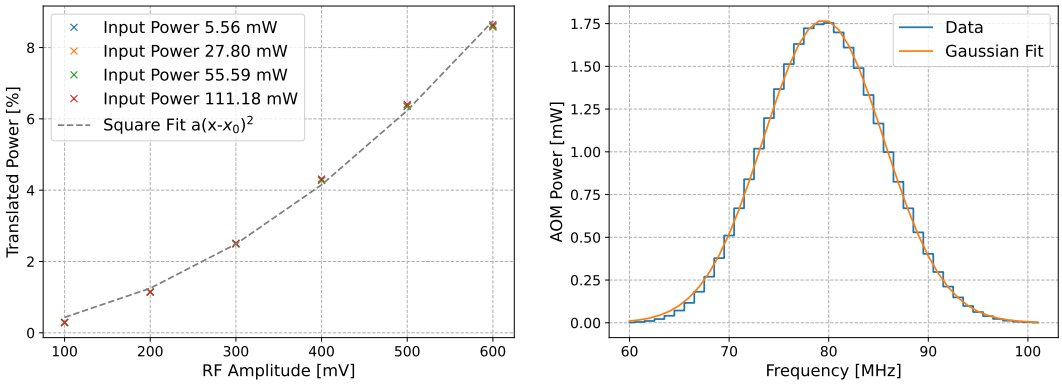

Figure 13: Left: Transmitted power of the AERODIODE 1550AOM-11 AOM in dependency of the driving RF amplitude. A dependency on the laser input power could not be found. Right: The transmitted power in dependency of the input RF frequency.

essential to precisely drive the AOM at it. In contrast, for certain measurements, it comes in handy to drive the AOM at different frequencies. For example, in Section 5.5.2 the AOM frequency is varied up to 15 MHz to probe the frequency space better. If not explicitly mentioned, the AOM is driven at 80 MHz.

4.4. Optical Fibre Array

For the fibre-based phase camera, two fibre arrays are used. A 2D 8 × 8 array from MEISU Optics and a 1D 1 × 64 array from SQS Vláknová optika. Both feature multimode fibre with a core diameter 105 µm, a cladding diameter of 125 µm are arranged in a pitch of 127 µm. The large core diameter was chosen in order to maximise the amount of light coupled into the fibres. The front of both fibre arrays detecting the laser light can be seen in Figure 14. On the other end, each fibre is terminated with a Ferrule Connector Physical Contact (FC/PC) connector for flexible connection of arbitrary read-out detectors.
To understand the signal propagation through the fibre array, the physical fundamentals of optical fibres are presented in Section 4.4 to 4.4.2 which follow [87, 88, 89, 53].

4.4.1. Description of Optical Fibre

An Optical fibre is a cylindrical waveguide made of a dielectric core material with a higher refractive index than the cladding material on the outside. This can either be a smooth gradient or a strict boundary called a step-index fibre. This boundary

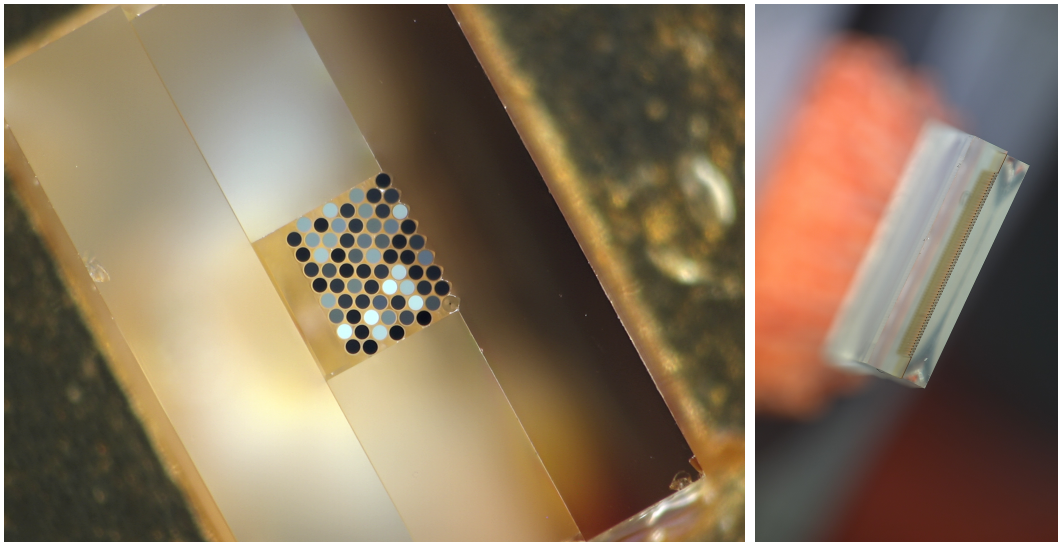

Figure 14: Left: 2D 8 × 8 fibre array fabricated by MEISU Optics with a nominal pitch of 127 µm between the individual fibres. The first layer is kept in place by V-grooves seen on the right. The other layers are loosely stacked and glued, resulting in pitch variations farther away from the grooves. Some fibres appear black as the other end is covered. Right: 1D 64 pixel fibre array produced by SQS Vláknová optika also with a pitch of 127 µm and a V-grooves keeping all fibres in place.

condition leads to total inner reflection for light at angles smaller than the critical angle

$$\sin \varphi_{\text{crit}} = \cos \theta_{\text{crit}} = \frac{n_2}{n_1} \ . \tag{4.13}$$

The light is therefore contained in the fibre by repeated total inner reflection and can be transmitted over large distances. For larger angles than the critical angle, only a fraction of the light power is reflected back into the core, and the rest is transmitted into the cladding and then out of the fibre until the propagating laser power is depleted. A depiction is given in Figure 15 using rays to illustrate the light path. From thereon, it becomes apparent that the maximum angle to couple into the fibre, the opening angle α_{open}, can be obtained by

$$n_0 \sin \alpha_{\text{open}} = n_1 \sin \theta_{\text{crit}} = \sqrt{n_1^2 - n_2^2} \ , \tag{4.14}$$

using the refraction law with the critical angle θ_{crit} as boundary and Equation 4.13. Instead of the opening angle, fibres are often specified with the

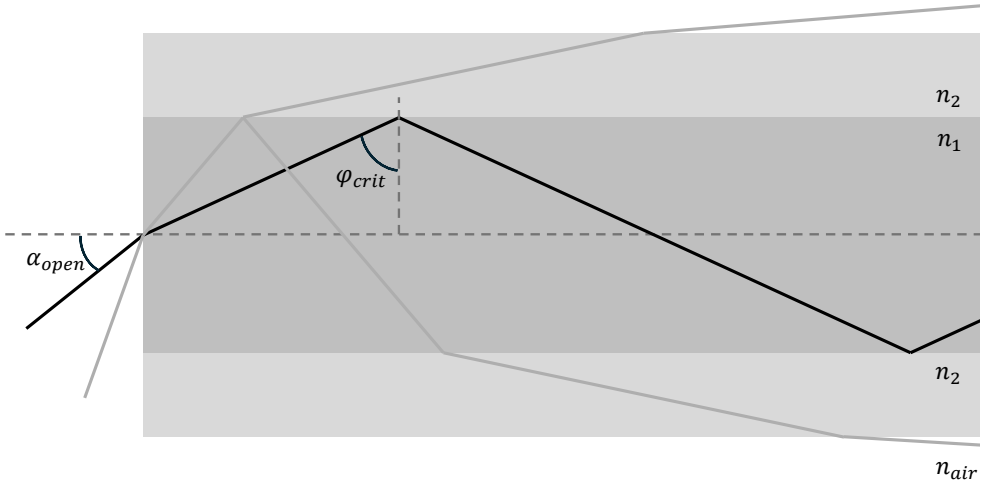

Figure 15: Propagation of rays in optical fibre. Rays entering at a smaller angle than α_{open} are totally reflected and can be propagated over long distances. Rays at a greater angle than α_{open} reflect and transmit normally until the propagating laser power is depleted.

Numeric Aperture (NA), which is defined as

$$\mathrm{NA} := n_0 \sin \alpha_{\mathrm{open}} = \sqrt{n_1^2 - n_2^2} \tag{4.15}$$

and directly relates to the opening angle.
From this simple description, one can see that the light inside the fibres can propagate through different paths or modes depending on the angle for sufficiently large core diameters. Therefore, each mode will have a different phase after propagation through the fibre. How this impacts the measured signal of the phase camera is described in Section 4.4.3. Nevertheless, the attributes of these modes must be characterised.

4.4.2. Modes of Step-Index Fibres

To describe the modes in step-index fibre, the Helmholtz equation (Equation 3.5) must be solved for the boundary conditions of the fibre:

$$n(r) = \begin{cases} n_1 & , r \leq a \\ n_2 > n_1 & , r > a \end{cases} . \tag{4.16}$$

Therefore, it is preferred to describe the Helmholtz equation in cylindrical coordinates

$$\partial_r^2 u + \frac{1}{r}\partial_r u + \frac{1}{r^2}\partial_\varphi^2 u + \partial_z^2 u + n^2 k^2 u = 0 \, . \tag{4.17}$$

Additionally, the free space wave number k has to be modified to account for the dielectric medium by using $c = \frac{\omega}{k} = c_{\text{medium}} n$. In order to solve this Equation with the boundary condition of Equation 4.16, a separation of variables $u \equiv u(r, \varphi, z)$ $= u(r)v(\varphi)w(z)$ is performed. As a wave propagating in z direction is envisioned, $w(z)$ must be of the form of $e^{-i\beta z}$, with propagation constant β. This leads to

$$\frac{r^2}{u}\left(\frac{d^2u}{dr^2} + \frac{1}{r}\frac{du}{dr}\right) + r^2\left(n^2k^2 - \beta^2\right) = \frac{1}{v}\frac{d^2v}{d\varphi^2} = const\ , \tag{4.18}$$

with both sides independent of each other.
As v must be continuous in 2π, it takes the form of $\cos l\varphi$ or $\sin l\varphi$ with *const* chosen to be l^2 for $l \in \mathbb{N}_0$. Therefore, the radial dependent Equation can be written as

$$r^2\frac{d^2u}{dr^2} + r\frac{du}{dr}\ + \left[\left(n^2k^2 - \beta^2\right)r^2 - l^2\right]u = 0\ . \tag{4.19}$$

Applying the boundary condition of Equation 4.16 yields

$$r^2\frac{d^2u}{dr^2} + r\frac{du}{dr}\ + \left(U^2\ \frac{r^2}{a^2} - l^2\right)u = 0 \quad , r \leq a \tag{4.20}$$

$$r^2\frac{d^2u}{dr^2} + r\frac{du}{dr}\ - \left(W^2\frac{r^2}{a^2} + l^2\right)u = 0 \quad , r > a\ , \tag{4.21}$$

with $U = a\sqrt{k^2n_1^2 - \beta^2}$ the core parameter and $W = a\sqrt{\beta^2 - k^2n_2^2}$ the cladding parameter. Equation 4.20 represents the Bessel Equation and Equation 4.21 the modified Bessel Equation. Both have two linear independent solutions, but only

$$J_l\left(\frac{Ur}{a}\right) \quad , r \leq a \tag{4.22}$$

$$K_l\left(\frac{WR}{a}\right)\ , r > a\ , \tag{4.23}$$

are physically relevant as the other solutions diverge. A detailed description is given in Appendix B with an illustration of said functions. Additionally, both functions have to be continuous at the boundary $\partial_r u\big|_{r=a}$, leading to the following wave transverse modal field

$$u(r,\varphi) = \begin{cases} \frac{J_l\left(\frac{Ur}{a}\right)}{J_l(U)}\begin{pmatrix}\cos l\varphi\\ \sin l\varphi\end{pmatrix} & , r \leq a \\ \frac{K_l\left(\frac{Wr}{a}\right)}{K_l(W)}\begin{pmatrix}\cos l\varphi\\ \sin l\varphi\end{pmatrix} & , r > a \end{cases}\ , \tag{4.24}$$

with

$$\frac{U\partial_r J_l(U)}{J_l(U)} = \frac{W\partial_r K_l(W)}{K_l(W)} \quad \text{or} \quad \frac{UJ_{l-1}(U)}{J_l(U)} = -\frac{WK_{l-1}(W)}{K_l(W)} \ . \tag{4.25}$$

In the latter part, the identities from Appendix B were used. Using these boundary conditions, a finite number of solutions for each l with the mth solution called Linear Polarised (LP_{lm}) modes can be found. As these were derived from the Helmholtz Equation 4.17, they span a complete set of modes that can describe an arbitrary field composition in an optical fibre. Each LP_{lm} has its own propagation constant β_{lm} derived from the definition of U and W. Additionally, each mode exists in x and y polarisation as the scalar wave approximation of the Helmholtz Equation does not take care of the vector nature of electromagnetic fields. An example of the phase of these transverse fields can be seen in Figure 16. A handy parameter to describe optical fibres is the normalised waveguide parameter

$$V^2 = U^2 + V^2 = (ak\mathrm{NA})^2 \ , \tag{4.26}$$

which gives a dimensionless quantity which is proportional to the number of contained modes of the fibre. For V below ≈ 2.405 only a single mode is transmitted. For high V values, the number of modes can be approximated by

$$M = 4\left(\frac{V}{\pi}\right)^2 \ . \tag{4.27}$$

For the fibre type used in the phase camera (Section 4.4), approximately 900 different modes propagate through the fibre for both polarisations. This will lead to a phase dispersion between the modes as each one propagates at its individual propagation constant β.

4.4.3. Phase Dispersion of Multimode Fibre

For the phase camera, a stable phase relation between the sidebands and the reference beam is key. To see if the phase dispersion in the optical fibre is a problem, the signal propagation through the fibre is simulated with the tools discussed in Section 4.4.2. For a more straightforward implementation, the Python package *ofiber* [90] is used to calculate the individual propagation constant β and the respective irradiance for each mode of the used multimode fibre at a certain wavelength. The acquired phase for each mode through the 1 m of multimode fibre is then weighted by the normalised irradiance distribution of the modes.
For a wavelength of 1550 nm, the spread in acquired phase between the modes is of magnitude 1×10^5 rad. Naively, one could think that this is the end of the fibre-based camera, but this is not the observable. For heterodyne detection, the

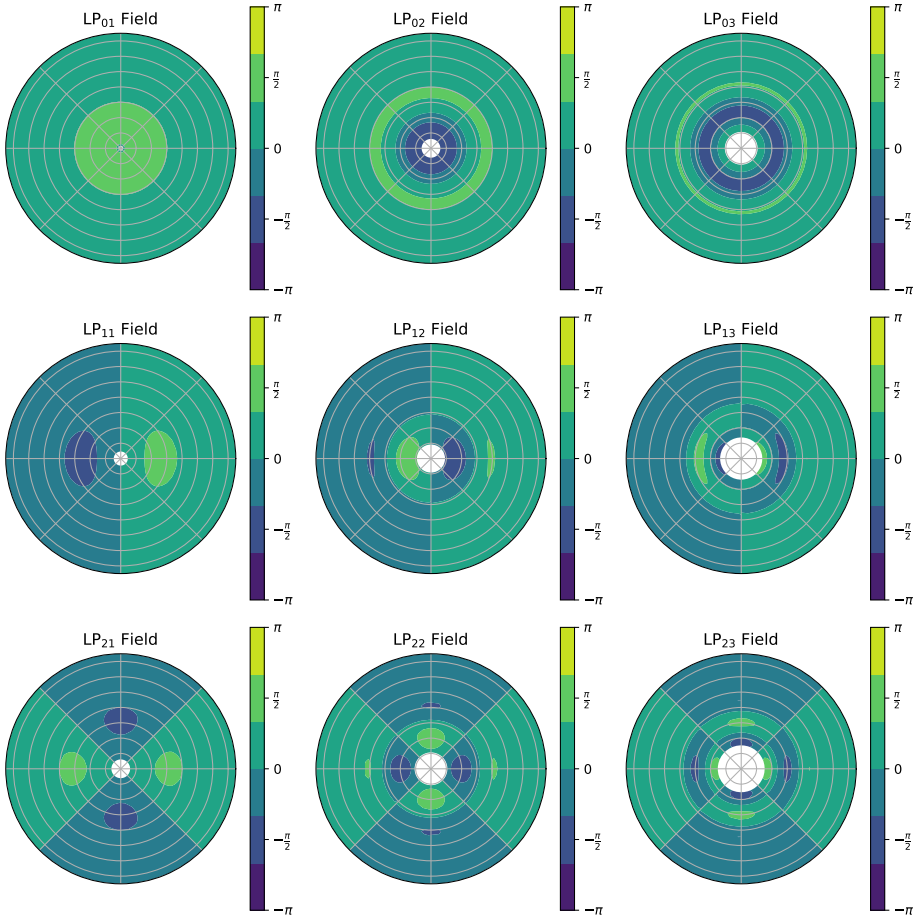

Figure 16: The spatial intensity profile of all linear polarised (LP_{lm}) modes up to the order $l = 2$ and $m = 3$ of the used multimode fibres. The higher the order, the less power is transferred in the core. Created with [90].

phase relation between the signal and the reference beam is measured. Therefore, two wavelengths have to be propagated through the fibre and then compared to each other. As the signal and reference wavelength are only separated on the MHz scale, they propagate in similar modes. The propagation constant β differs at the magnitude of $1\,\mathrm{m\,s^{-1}}$ with $\beta \approx 0.7c$. This leads to a small constant offset in the acquired phase for each mode. In the case of the phase camera, the mean of the phase dispersion is measured as a photodiode captures the whole output of the fibre. The interesting part is that this offset changes with the difference in wavelength between the signal and reference beam. For the used multimode fibre this corresponds to $\approx 30.5\,\frac{\mathrm{mrad\,m}}{\mathrm{MHz}}$. This is measured and confirmed in Section 5.5.2 as the signal chain must first be introduced to understand the measurement setup.

4.4.4. Optical Cross-Talk

From medical endoscopy, it is known that optical cross-talk between individual fibres in a bundle leads to a decrease in contrast due to the evanescent field of one fibre coupling into another [91]. In the case of a phase camera, observing a coherent light source, the spilt light will also interfere with the carried light. Therefore, it will not only change the observed intensity but also result in an additional phase shift, as seen in Figure 17, where the two waves are added in the complex plane. Depending on the intensity and phase relative to each other, the additional phase shift varies. The effect is maximal for a relative phase difference of $\pm 90°$ and scales with roughly one order of magnitude of additional phase shift per 10 dB of cross-talk.

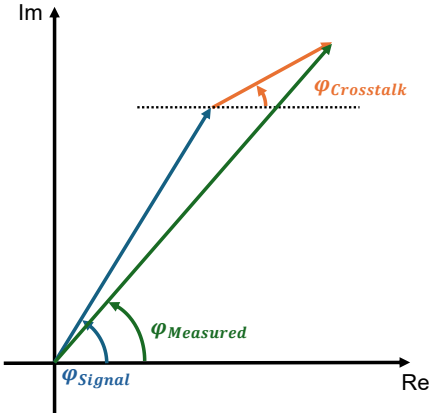

Figure 17: Illustration of how cross-talk influences the phase of the observed wave in the complex plane.

To estimate the optical cross-talk between parallel optical fibres, the calculations of N. Ortega-Quijano, F. Fanjul-Vélez, and J. Luis Arce-Diego [92] are used, which are based on coupled mode theory for guided-wave optics pioneered by A. W. Snyder and P. McIntyre [93, 94]. It uses the assumption of a focused beam, which is strictly speaking not the case for our phase camera. This results in a consideration of only LP_{0q} modes, neglecting most of the modes. We will later see if this leads to inaccuracies. First, let's do the approximation.
For a multimode fibre with fibre parameter $V \gg 1$ and n next neighbour fibre, the cross-talk P_{ct} to input power P_{in} can be described by

$$\frac{P_{ct}(z)}{P_{in}} \approx \frac{1}{2} G \left[1 - \operatorname{sinc} \left(\frac{2}{\pi} \sqrt{\frac{n}{G}} C_q z \right) \right] , \tag{4.28}$$

with z the length of parallel fibres, C_q the coupling constant. G given as

$$G = \frac{1}{1 + \left(\frac{\Delta\beta}{2C_q}\right)^2} \cdot \frac{1}{1 + \frac{1}{n}} \ , \tag{4.29}$$

with $\Delta\beta$ the difference in propagation constant between the neighbouring fibres, which can be approximated as

$$\Delta\beta \approx 2V\sqrt{2\delta}\frac{\Delta d_{core}}{d_{core}^2} \ \left(\frac{\sin\theta_q}{\sin\theta_c}\right)^2 \ , \tag{4.30}$$

with δ, the relative refractive index difference between core and cladding, Δd_{core} the diameter difference between fibres, θ_c, the opening angle and the corresponding opening angle in the fibre θ_q, if only core diameter inhomogeneities shall be studied. Using the assumption of a focused light source coupling into the fibre, the coupling strength for the $\mathrm{LP_{0q}}$ is proportional to e^{-d_s} with d_s the distance between the cores of the neighbour fibres.

The calculated cross-talk intensities for the used hexagonal arranged 2D array can be seen in Figure 18 for different estimates of core diameter differences Δd_{core}. For perfectly identical fibres, the cross-talk increases exponentially with the length of parallel propagation until it oscillates around the 50% mark. Adding a difference in core diameter between the fibres leads to a saturation of cross-talk at a certain distance, with a strong suppression of maximal cross-talk. One order in magnitude in core size differences leads to a suppression of $-20\,\mathrm{dB}$ of cross-talk. For the used fibre array, the maximum parallel propagation distance is about 30 cm. The core size difference is estimated to be 0.1 nm, which is still a generous estimation. In total, a negligible amount of $-110\,\mathrm{dB}$ cross-talk is expected.
This raises the question of how this translates to the case of a collimated beam coupling into the array. Different modes would have different coupling coefficients C_q, shifting the cross-talk curve up or down. However, calculating them is not necessarily beneficial, as approximation already showed some insights, which translate to the general case. The cross-talk will be low. Generally, only modes with nearly identical propagation constant $\Delta\beta \ll 1$ do couple [95] as seen in Equation 4.29. Therefore, fabrication tolerances in fibre core diameters are an excellent way to suppress the cross-talk as seen in Figure 18. Even if the coupling for the other modes is significantly higher, the variance in $\Delta\beta$ will suppress the cross-talk by several tens of decibels. It is sufficient to have cross-talk below $-30\,\mathrm{dB}$ to have an additional phase shift below 1 mrad, smaller than the resolution of the camera.

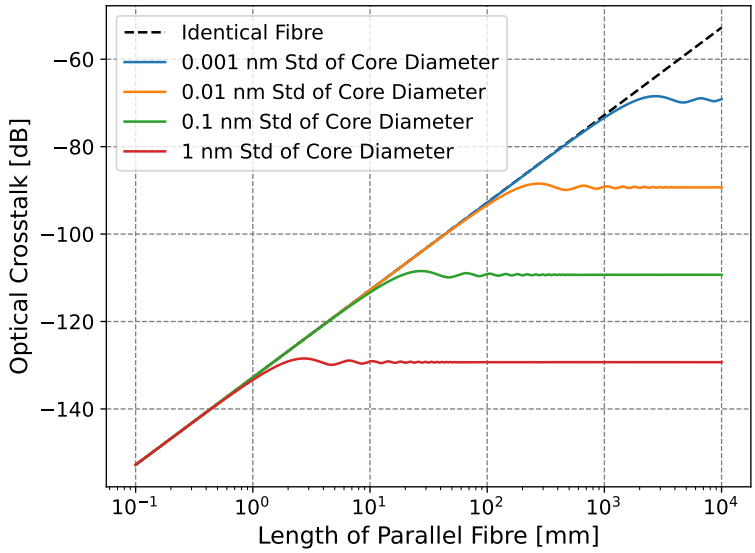

Figure 18: Estimated optical cross-talk between the used multimode in the fibre bundle for different variations in core diameter.

4.5. Requirements for Amplifier and Digitiser

To successfully design a signal chain that is suitable to measure the small intensities of individual pixels of the fibre array, requirements need to be derived. The following example can be used as a guideline to formulate these requirements: To not disturb the operation of the interferometer, the less power out-coupled from the system, the better. As an order of magnitude, 10 mW for the signal and reference beam can be assumed for the operation of the phase camera. Recalling Equation 4.5, the typical amplitudes for the carrier and sidebands in relation to the reference beam can be calculated, where the sidebands can be up to −60 dB weaker (Equation 3.19). The DC power has to be separated from the phase-sensitive AC powers due to their difference in magnitude. For the best spatial resolution of the fibre array, the beam size should be approximately of the same size as the fibre array. Using a box intensity profile for the beam of width $d_{beam} = 8\,\mathrm{mm}^2$, the size of the 1D array, the core diameter of the used multimode fibre $d_{core} = 105\,\mu\mathrm{m}^2$ as detector cross section of a pixel, and a gain of $G = 1\frac{\mathrm{A}}{\mathrm{W}}$ for the photodiode, the measured signal AC amplitude for the carrier is $\approx 3.4\,\mu\mathrm{A}$ and for the sideband $\approx 34\,\mathrm{nA}$ using −40 dB weaker sidebands. Therefore, an arbitrary digitiser of dynamic range 1 V would need an amplifier with a transimpedance gain $\approx 100\,\mathrm{dB}$ to not saturate the carrier signal, while remaining best SNR for the sideband signal. This also has to be done at 250 MHz in order to measure all available sidebands.

The systematic difference in amplitude in carrier and sidebands also leads to restrictions in the used digitiser resolution. For the extreme case of −60 dB weaker sidebands, at least a 12-bit resolution is needed to resolve the faint amplitudes.

4.5.1. Amplifier Board: ET-0001

The ET-0001 is the first prototype amplifier board designed for the fibre-based phase camera and is based on the LMH6629 [96]. An LMH6629 in transimpedance configuration converts the photocurrent of the photodiode by a gain of 60 dB V/A. With the photodiode capacity of 2 pF, a feedback capacity of 0.55 pF is needed to keep the amplifier stable. Together, this leads to a theoretical bandwidth of 285 MHz. Thereafter, the signal is split into the AC and DC path with a frequency crossover. For the AC path, a high pass filter with a crossover frequency of 1.5 kHz is chosen, while for the DC path, a low pass filter with a crossover frequency of 6 MHz. As the specifications for the digitiser in the DC path were unknown at the moment of designing the board, the rather optimistic crossover frequency was chosen to also allow high-speed digitisers.
In the DC path, a second inverted amplifier stage follows with a gain of 20 dB and bandwidth of 450 MHz. In the AC path, three inverting amplifier stages of the same design lead to an overall gain of 60 dB at slightly reduced bandwidth. The power supply of each amplifier is filtered by a tantalum capacity of 6.8 µF and a ceramic capacity of 100 nF as close as possible to the supply pin to reduce the influence of trace inductance. As amplifier stages on the same power supply are cascaded, the individual supplies are additionally isolated with 4.7 µH inductors by forming an LC low-pass filter with both filter capacities [97]. This prevents a power supply disturbance created by one amplifier from propagating to another to unsettle it. To increase the bandwidth of the photodiode, a negative voltage can be applied to the cathode.

Unfortunately, the board has some design flaws. The most critical of them is the transimpedance amplifier, which heavily oscillated due to parasitic capacities. A stable configuration with different feedback capacities to counter the parasitic input capacities could not be found, as this seems to be a fundamental layout problem [98]. The standard practice of cutting out the ground plate around the op-amp was not sufficient to prevent the buildup of parasitic capacities [99]. Instead of iterating the layout, the LMH6629 is replaced by a transimpedance amplifier as an integrated circuit in the follow-up board, which is way less susceptible to parasitic capacities. The second one is the missing potential decoupling the amplification stages by placing a small-valued resistor between them. As a result, multiple cascaded amplification stages oscillated. Also, the gain for these stages is too small and, therefore, the bandwidth is too big without any use, decreasing the potential

SNR. Last but not least, the gain of the AC path was way too high. A third voltage gain stage is not needed.
With these lessons learned, ET-0002 was designed.

4.5.2. Amplifier Board: ET-0002

ET-0002 was designed together with Dr. Adrian Zink, who also laid out the board. The LMH34400 [100] replaces the LMH6629 as the transimpedance amplifier. It has a fixed gain of 92 dBV/A at a bandwidth of 240 MHz. As the amplifier runs on single supply, the output is on a 1 V pedestal voltage. The signal is then split again into an AC and DC path. An illustration is given in Figure 19 with the individual components highlighted.
The frequency crossover is reworked to a crossover frequency of ≈ 11 kHz for both paths while containing a load of 100 Ω for the LMH34400. After the frequency crossover in the AC path, the signal gets amplified by two inverting amplifier stages based on the LMH6629 design of ET-0001. The first stage has a gain of 15 and the second one of 15.9. Both stages can be bypassed. For all future measurements, the second amplification stage is bypassed. The signal is then conditioned to 50 Ω for transmission. With signal termination at the digitiser, this leads to an overall gain of $\approx$ 110 dB. To avoid any aliasing, an anti aliasing filter in form of the MiniCircuits LFCN-160+ [101] is used, which cut-off frequency is at 230 MHz, just below the Nyquist frequency of the slowest Analogue-to-Digital-Converter (ADC) (250 MHz) used.
In the first version of the board, the DC path signal was directly digitised after the frequency crossover with the 1 V pedestal from the LMH34400 still applied with no additional amplification. As this decreases the dynamical range of the following ADC, it is changed in the first revision. The pedestal is now subtracted by a differential amplifier based on the OPA182 [102], subtracting the DC signal from a 1 V reference. This reference is created by a tunable shunt voltage reference drawing the voltage from the 2.5 V supply. Instead of tuning every board, the reference is slightly below 1 V to have a small positive offset, so an ADC can be used, which can only measure positive voltages. The small offset can then be digitally subtracted.
As the LMH6629 runs on a symmetric 2.5 V supply and the LMH3440 on a single supply of 3.3 V, the power supply got completely reworked and uses three low noise high Power-Supply Rejection Ratio (PSRR) Low-DropOut regulator (LDO regulator) of type TPS72325. The individual voltage supply of each amplifier is then filtered by the recommended bank of capacitors. Similar to ET-0001, the amplifiers run on the same power line, which is individually isolated by a 4.7 µH inductor. To stabilise the photodiode bias voltage, several filter capacities were added with an additional low-pass RC filter at a cut-off frequency of 160 Hz.

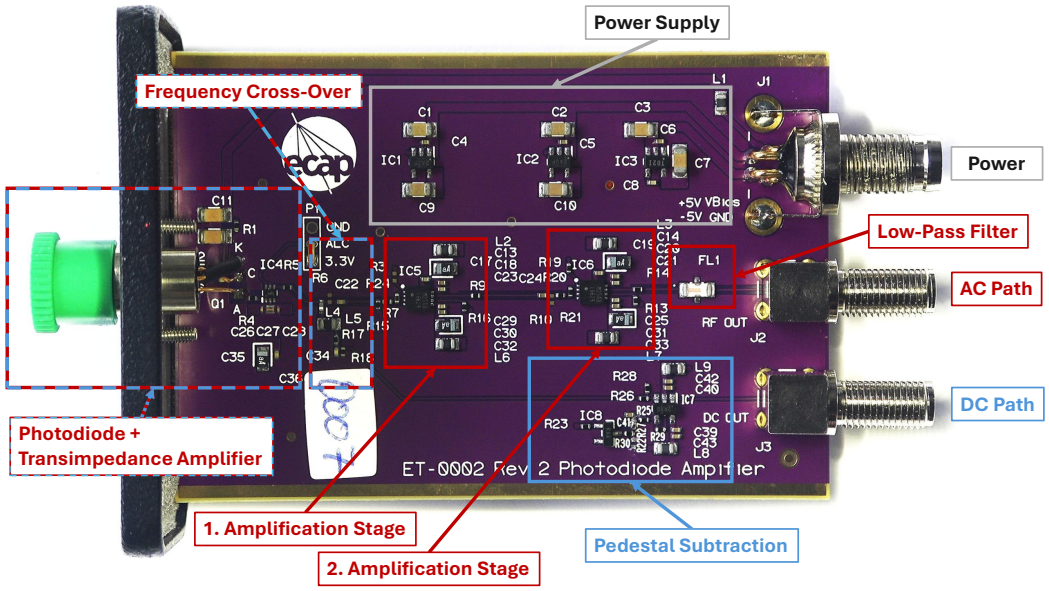

Figure 19: Amplifier board ET-0002 Rev 2 with the individual components marked. The AC Path is highlighted in red, the DC path in blue and the power supply in grey.

As this is a high-gain low-noise amplifier board, it is very susceptible to electromagnetic radiation in the radio band. Therefore, the board is placed in an EMI/RFI shielded box (Hammond 1457C802EBK).

4.5.3. Spectrum Instrumentation M4i.4451-x8

To enable the parallel detection of multiple sidebands across a 250 MHz spectrum, a suitable digitiser with a sampling rate of at least 500 MSa/ s is needed to fulfil the Nyquist Theorem [103]. Additionally, the digitiser has to be able to digitise bursts of several microseconds of samples at moderate rates of at least 100 Hz continuously. For prototyping, six specimens of the flexible plug-and-play digitiser card Spectrum M4i.4451-x8 [80] were used for easy prototyping of the camera electronics. For a complete camera of 4096 pixels, they shall be replaced by the CTC ASIC of the TeV Array Readout electronics with GSa/s sampling and Event Trigger (TARGET) family developed for the SST of CTAO, which are more cost-effective but less performant (see Section 6 or Chapter II of this thesis starting with Section 10).
The Spectrum M4i.4451-x8 is a 500 MSa/ s, 250 MHz, 14 bit resolution digitising card with four channel and a PCI Express x8 interface for communication and data transfer. Each channel has a SubMiniature version A (SMA) input connector and can be run in buffered or high frequency configuration with a pool of following

options: Six choosable voltage ranges, ranging from ±200 m V to ±10 V, with the option of AC or DC coupling, 50 Ω or 1 MΩ termination, an positive offset up to 100%, and a selectable 20 MHz bandwidth filter. Due to the lower bandwidth of 125 MHz and worse baseline noise over all voltage ranges, the buffered path is not used. If not stated otherwise, the following settings are used: A voltage range of ±1 V, AC coupling, 50 Ω, and no 20 MHz bandwidth filter.

The two data-taking modes relevant for this work are the First In First Out (FIFO) mode and the Multiple Recording mode, which will be referenced as burst mode. In FIFO mode, the cards sample and digitise continuously. For characterising the I-Q demodulation, for example, this mode allows maximum flexibility, as different integration times can be used and compared for the same data set. At four channels, this creates a data rate of 4 GB s^{-1}. With a writing speed of 3.4 GB to disk, this will saturate the onboard buffer of 4 GB after a maximum of 5 s of data taking. A continuous use of the phase camera is therefore not feasible with this mode.
In burst mode, the cards digitise a selectable number of samples after a trigger. This trigger can be applied externally via the trigger input or internally created by software. Each event is given a timestamp for timebase reconstruction. A continuous digitisation and calculation of phase points of up to 1 MHz is therefore possible in this mode with less flexibility.

To synchronise the sampling speed of the cards with the setup, an external 10 MHz reference clock is applied. For using multiple cards in parallel, the StarHub module is used for synchronising between all channels.
In order to set up the card and take data, a Python library with programming examples is included. This is taken as a basis to develop an easy-to-use software framework *ETscripts* to set up, take data, read out and reconstruct data. This software framework also features the calculation of phase signals and the creation of images. For more information, see Appendix C.

4.5.4. Electrical Cross-Talk

As described in Section 4.4.4, cross-talk can lead to additional phase shift. Printed Circuit Boards (PCBs) can be particularly prone to cross-talk as many signal traces can run in proximity due to the restricted space. Even with proper spacing and shielding, two parallel signal traces can form a capacity, leading to capacitive coupling, ergo cross-talk.
The cross-talk of the Spectrum M4i.4451-x8 card is specified in the data sheet at $\leq$ 96 dB for 1 MHz and at $\leq$ 82 dB for 20 MHz [80], negligible for any phase measurement. However, for the reconstruction of the phase of sidebands, signals over the whole bandwidth are monitored. Therefore, it is crucial to measure and

understand the cross-talk over the whole bandwidth.
To determine the cross-talk induced by one channel to another, a sine wave of 900 m V amplitude is feed individually onto each channel from 10 MHz to 500 MHz in steps of 10 MHz. As a signal source, the function generator SDG6052X is used and connected via 2 m of SMA cable. For each frequency 1 ms worth of data is recorded in the FIFO mode.
To evaluate the cross-talk, the measured Root Mean Square (RMS) of the cross-talked channels is divided by the measured RMS of the signal channel. The results for card zero on channel zero can be seen in Figure 20.

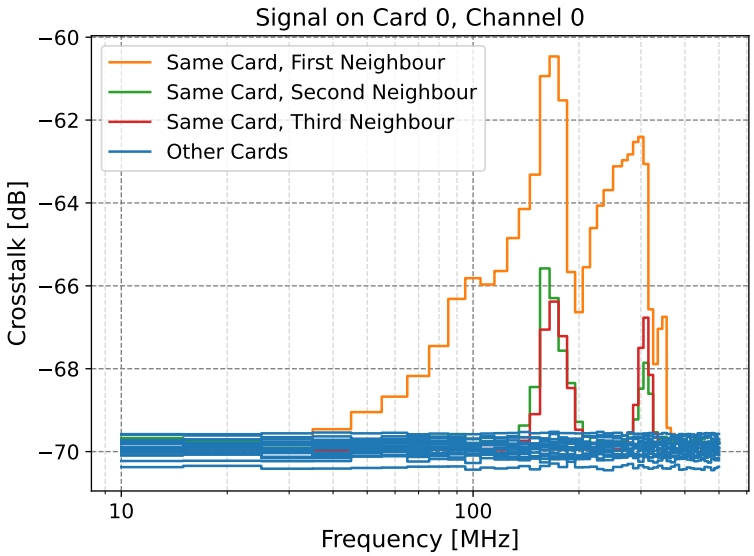

Figure 20: Recorded cross-talk for each of the 24 channels besides the signal channel 0 of card 24. The nearest neighbours are colour-coded.

The first thing stands out is the −70 dB cross-talk over the whole frequency spectrum for channels which are not on the card. This is purely artificial and due to the described method and not physical cross-talk. Here, the RMS of the baseline noise is weighted against the signal RMS. Given the 900 mV amplitude of the input sine wave, one can calculate the baseline noise to be 200 µV, which is below the specified $\leq 232\,\mu V$.
More interesting is the first neighbour channel with three resonances around $\approx$ 100 MHz, $\approx$ 180 MHz, and $\approx$ 300 MHz. The latter two resonances can also be seen on the second and third neighbours. Although clearly measurable, the maximum cross-talk is still below 60 dB and, therefore, negligible for any phase shifts as discussed in section 4.4.4.

4.5.5. SLOWDAQ

For monitoring the laser power with the DC path of ET-0002, the requirements for the digitiser are less constrained. The DC path of ET-0002 has a frequency cut-off at 11 kHz, leading to a required sampling frequency of 22 kSa/ s. The frequency cut-off was chosen in order to have some headroom in design, but not out of necessity.
The internal ADC of the Arduino Due [104] is chosen as a digitiser due to its availability and simplicity. It features twelve analogue inputs that are capable of sampling voltages between 0 V and 3.3 V at 10 bits at 1 MSa/ s. But only one channel at a time, leading to a maximum of 83.3 kHz sampling rate, ignoring switching times if all twelve channels are activated. An external reference clock is used as switching, and therefore, sampling frequency. The data can then be written to disk via a USB interface.
An external reference clock is used as switching, and therefore, sampling frequency Two of these Arduinos are placed in a RF tight box forming the so-called SLOWDAQ box. Each SLOWDAQ box features therefore 24 channel with one reference clock input and two USB outputs. Additionally, a low-pass filter with cut-off frequency of 1.6 kHz is interconnected between the SLOWDAQ inputs and the Arduino Due inputs to reduce the noise. In standard operation, a burst reference clock of 10 kHz is used to digitise n samples per channel at the burst frequency, where n is the number of reference clock cycles. Usually n equals 100 for frequencies below 100 Hz and decreases proportionally to the burst frequency. Only the mean per burst and channel is used. For parallel use with the phase demodulation data recorded with the fast digitisers, the burst reference clock is synchronised with the trigger signal.

4.6. Synchronisation

It is key for heterodyne interferometry to have a stable reference frequency. Take for example, the EOM and AOM frequency drivers running on different reference clocks, e.g. two different function generators. A slight difference in frequency of 1 Hz would already lead to a 2π phase shift after one second. Even worse, two reference frequency generators will never have the same temperature dependency, leading to temperature frequency shifts all over the place. The same behaviour is also true for digitisers, as earlier or later digitisation of the beating will result in a shifted phase. Therefore, a GPS-based 10 MHz reference clock is distributed to all signal-relevant instruments.

5. Characterisation of the Signal Chain

Starting an investigation of the expected noise, the noise floor is measured. From there on, the phase resolution of the phase camera is characterised. The limitation of the phase resolution is studied by the phase noise spectra, with the coupling of different noise sources to the phase discussed in depth, followed by the investigation of intrinsic frequency-dependent phase shifts of the fibre-based phase camera.

5.1. Expected Noise Floor

The expected noise floor of the system is dependent on the propagation of the noise through different amplification stages in the signal chain. Consequently, it is easier to discuss the contributions to the noise floor in reverse order [105].

Spectrum M4i
Starting with the digitiser. Ideally, digitisation should not contribute to the noise, as it should translate the voltage into discrete values as true to the source as possible. However, the quantisation of continuous values with limited resolution introduces quantisation noise. Assuming the quantisation noise is uniformly distributed, it can be expressed as $V_{\mathrm{RMS}} = \frac{\mathrm{LSB}}{\sqrt{12}}$, with LSB, the Least Significant Bit [106]. For the Spectrum cards with 14-bit resolution running at a voltage range of $\pm 1\,\mathrm{V}$, $\mathrm{LSB} \approx 122\,\mu\mathrm{V}$, this results in a quantisation noise of $V_{\mathrm{RMS}} \approx 35\,\mu\mathrm{V}$. Comparing that to the RMS noise level the manufacturer provides over the whole bandwidth of 250 MHz $\mathrm{N}_{\mathrm{digitisation}} < 1.9\,\mathrm{LSB}$ or $\mathrm{N}_{\mathrm{digitisation}} < 232\,\mu\mathrm{V}$ for the same voltage range, the quantisation noise is not the dominating factor but the electrical noise of the auxiliary electronics of the digitiser. This noise level is also confirmed by measurements. As it is insignificant compared to the rest of the signal chain, a decomposition of the individual sources is left to the manufacturer.

Low-Pass Filter
Moving to the ET-0002 amplifier board, the last stage the signal passes through is the MiniCircuits LFCN-160+ [101] low-pass filter with a cut-off frequency of 230 MHz, acting as an anti-aliasing filter. Therefore, any frequency spill-over of frequencies higher than the Nyquist frequency of 250 MHz is suppressed. The bandwidth of the noise calculation can therefore be fixed to 250 MHz. As there are no further amplification stages after the low-pass filter, its noise contribution is deemed negligible compared to prior stages

Second Amplification Stage
The second amplification stage uses a LMH6629 configuration with a gain of 15.9 at a bandwidth of 245 MHz. In the current configuration of the ET-0002 amplifier

board, it is bypassed, as it is only planned as a backup if there is not enough amplification to avoid lengthy redesign and lead times. As an implementation of this amplification stage is not planned, the noise calculation is skipped.

First Amplification Stage
The first stage also uses a LMH6629 configuration with a gain of 11.2 and a bandwidth of 360 MHz. For an inverting OP amp configuration, there are four independent noise contribution: the referred input current noise i_N, the referred input voltage noise e_N and the thermal noise of both resistors $N_{t,464\,\Omega}$ and $N_{t,41.3\,\Omega}$. Theoretically, the input current noise i_N has a contribution to both inputs of the op amp. In the inverting amplifier configuration, only the inverting input is affected, as the non-inverting input is shorted to ground. The resulting noise is calculated as:

$$N_{i_N} = i_N R_f = 4\,\frac{\mathrm{pA}}{\sqrt{\mathrm{Hz}}} \cdot 464\,\Omega = 1.8\,\frac{\mathrm{nV}}{\sqrt{\mathrm{Hz}}}\ , \tag{5.1}$$

with R_f being the feedback resistor. The input reference voltage noise e_N applies only to the non-inverting input due to its definition. For the noise calculations, the signal path is assumed to be grounded. Therefore, the noise sees a non-inverting amplifier configuration as the input resistor is grounded. It can be calculated as follows:

$$N_{e_N} = e_N \left(\frac{R_{\mathrm{input}} + R_{\mathrm{feedback}}}{R_{\mathrm{input}}} \right) = 0.7\,\frac{\mathrm{nV}}{\sqrt{\mathrm{Hz}}} \cdot \left(\frac{41.3\,\Omega + 464\,\Omega}{41.3\,\Omega} \right) = 8.6\,\frac{\mathrm{nV}}{\sqrt{\mathrm{Hz}}}\ . \tag{5.2}$$

The thermal noise or Johnson noise [107] can be calculated in general by

$$N_{\mathrm{thermal}} = \sqrt{4 k_B T R}\ , \tag{5.3}$$

where T is the temperature of the resistor and is assumed to be 300 K, k_B is the Boltzmann constant, and R is the respective resistor value. For the feedback resistor this results in $N_{t,464\,\Omega} = 2.8\,\mathrm{nV}/\sqrt{\mathrm{Hz}}$ while for the input resistor the gain of the amplifier has to be taken into account resulting in $N_{t,41.3\,\Omega} = 9.2\,\mathrm{nV}/\sqrt{\mathrm{Hz}}$. Overall, the complete amplifier section noise can be summarised by

$$N_{\mathrm{AMP}} = \sqrt{N_{i_N}^2 + N_{e_N}^2 + N_{t,464\,\Omega}^2 + N_{t,41.3\,\Omega}^2} = 13.0\,\frac{\mathrm{nV}}{\sqrt{\mathrm{Hz}}}\ . \tag{5.4}$$

Transimpedance Amplifier
The transimpedance amplifier for the ET-0002 is the integrated circuit LMH34400 with a gain of 92dB at a bandwidth of 240 MHz. The RMS of the referred input current noise is 50 nA. Nevertheless, as the phase extraction sort of applies a bandpass, it cis helpful to consider the frequency-dependent referred input current noise. As upper limit one can assume $i_N = 4\,pA/\sqrt{Hz}$ which then corresponds to

$$N_{TIA} = i_N \cdot G_{TIA} \cdot G_{AMP} = 1.8\,\frac{\mu V}{\sqrt{Hz}}\ . \tag{5.5}$$

Due to the high internal feedback resistor of 12.2 kΩ, the thermal noise is completely dominated by the transimpedance amplifier. It is

$$N_{thermal} = \sqrt{4k_B TR} \cdot G_{intern} \cdot G_{AMP} = 0.6\,\frac{\mu V}{\sqrt{Hz}}\ , \tag{5.6}$$

with k_B the Boltzmann's constant, T the temperature, which is assumed to be 300 K, and G_{intern} an internal an amplification factor with no detailed definition from the manufacturer. Therefore, it is evaluated as amplification factor and not as additional feedback resistance in the transimpedance amplifier to set an upper limit on the noise.

Frequency Cross-Over
Monitoring the DC intensity of the beam does not require high amplification at large bandwidth and small noise gains or 500 MSa/s digitisation. Therefore, a frequency cross-over with a cross-over frequency of 11 kHz is implemented, reducing the noise-relevant Bandwidth BW to $\Delta BW = 249.75$ MHz.

Photodiode
As the photodiode, the FCI-InGaAs-120 with FC/PC connector is used with an input capacity of C = 2 pF and reactance of $R_\lambda = 0.95$. The noise equivalent power is $P_{NEP} = 4.5 \times 10^{-15}\,W/\sqrt{Hz}$ resulting in a noise of

$$N_{NEP} = P_{NEP} R_\lambda G_{TIA} G_{AMP} = 1.9\,\frac{nV}{\sqrt{Hz}}\ . \tag{5.7}$$

Additionally, one must account for the shot noise, which depends on the power and, therefore, on the pixel position. It is described by

$$N_{shot}(\text{pixel}) = \sqrt{2eP_{pixel}R_\lambda} \cdot G_{TIA} G_{AMP}\ . \tag{5.8}$$

As an example: $N_{shot}(\text{pixel}) = 0.8\,\mu V/\sqrt{Hz}$ for a laser power of 10 µW coupling into the optical fibre.

Total Noise
In total, the total noise can be calculated as

$$\mathrm{N}_{\mathrm{total}}(f) = \sqrt{\mathrm{N}_{\mathrm{NEP}}^2 + \mathrm{N}_{\mathrm{shot}}^2(\mathrm{pixel}) + \mathrm{N}_{\mathrm{TIA}}^2 + \mathrm{N}_{\mathrm{AMP1}}^2 + \mathrm{N}_{\mathrm{thermal}}^2 + \mathrm{N}_{\mathrm{digitisation}}^2} \tag{5.9}$$

$$\approx 2.1 \, \frac{\mu\mathrm{V}}{\sqrt{\mathrm{Hz}}} \, . \tag{5.10}$$

As the signal is driven with a 50 Ω to the digitiser with a 50 Ω termination, the total noise power is $\mathrm{N}_{\mathrm{total}}(f) = 42.4\,\mathrm{fW\,Hz^{-1}} \approx -103\,\mathrm{dBm\,Hz^{-1}}$. To characterise and test the noise of the electrical signal chain, the shot noise is dismissed as it depends heavily on the laser power and spatial composition. The total noise without it is $1.9\,\mu\mathrm{V}/\sqrt{\mathrm{Hz}}$, which corresponds to $\mathrm{N}_{\mathrm{total}}(f) = 36.0\,\mathrm{fW\,Hz^{-1}} \approx -105\,\mathrm{dBm\,Hz^{-1}}$. To yield the total noise of the board, one can either take

$$\mathrm{N}_{\mathrm{total}} = 1.9 \, \frac{\mu\mathrm{V}}{\sqrt{\mathrm{Hz}}} \cdot \sqrt{BW} \tag{5.11}$$

or using the power of the logarithmic scale

$$\mathrm{N}_{\mathrm{total}} = -105 \, \frac{\mathrm{dBm}}{\mathrm{Hz}} - 10 \log_{10}(BW) \, , \tag{5.12}$$

which leads to a total noise of $\mathrm{N}_{\mathrm{total}} = -21\,\mathrm{dBm} = 20.0\,\mathrm{mV}$

5.2. Measurement of the Noise Floor

For the measurement of the noise floor, the AC port of ET-0002 is hooked up to a Tektronix MSO064B oscilloscope with 4 GHz bandwidth. The internal Fast Fourier Transformation (FFT) function of it is used to reveal the noise spectrum with frequency bins of 1 kHz width. A comparison between expected and measured noise can be seen in Figure 21 for the amplifier board ET-0002 with serial number SN0024. The average noise floor is calculated with a sliding window average over 100 frequency bins.
Over the whole measured frequency range of 625 MHz, the average noise floor performs better than the expected noise floor, with a clear cut-off starting at 250 MHz. The deviations from the mean appear more severe than they actually are. Over the relevant frequency range of 250 MHz, roughly one in a thousand frequency bins performs worse than the expected noise floor, which can be explained by statistical variance.
Starting at ≈ 60 MHz, the noise floor worsens by $4\,\mathrm{dB\,Hz^{-1}}$ due to the frequency-dependent gain of the amplifiers that peaks at around ≈ 150 MHz. Additionally, the LMH3440 shows a significant bump in the noise spectra [100] which is not taken into account in the noise calculation, as it was assumed to be flat for simplicity.

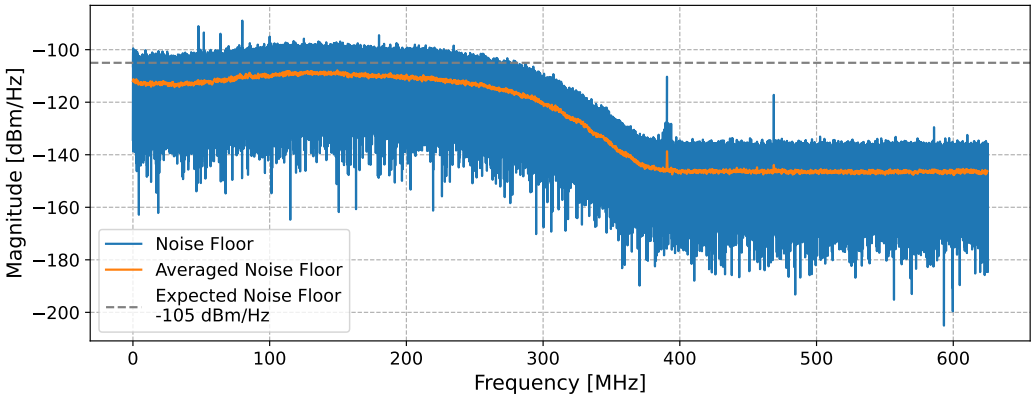

Figure 21: Noise floor measurement of the amplifier board ET-0002 with serial number SN0024.

The peaks above 300 MHz can be attributed to the oscilloscope, which is also visible in different measurements. Below 100 MHz, the peaks could be attributed to the laboratory environment, especially the one at 80 MHz, which corresponds to the driving frequency of the AOM.
For the first batch of ET-0002 amplifier boards (SN0004 - SN0022), the mean spectral power density is $-113.48\,\mathrm{dBm\,Hz^{-1}}$, which corresponds to a noise level of $-29.48\,\mathrm{dBm}$ over the whole bandwidth of 250 MHz.

5.3. Amplitude and Phase Resolution

The next step is to test the amplitude and phase resolution of the signal chain and, therefore, the camera. To this end, measurement runs of several seconds at a trigger rate of 1 kHz were conducted with the optical setup operating and 24 amplifier boards connected to the Spectrum Instrumenation digitiser cards. At each trigger, 32,758 samples are digitised with 2 ns bin width. Therefore, different integration times can be tested with the same data set by simply reducing the number of samples used, thereby isolating the influence of the integration time alone. As one is interested in the amplitude and phase resolution as a function of the detected power, the EOM is driven at 4.8 V to create three upper and lower sidebands at different power levels. The amplitude and phase of each sideband and carrier are extracted by the I-Q demodulation for each pixel. The standard deviation of the amplitude or phase gives the resolution. A demodulo algorithm is used for phase measurement to avoid artefacts from phase jumps due to the modulo 2π nature of the phase.
The amplitude resolution as a function of the power of the demodulated signal power for different integration times can be seen in Figure 22 as dots. In solid lines,

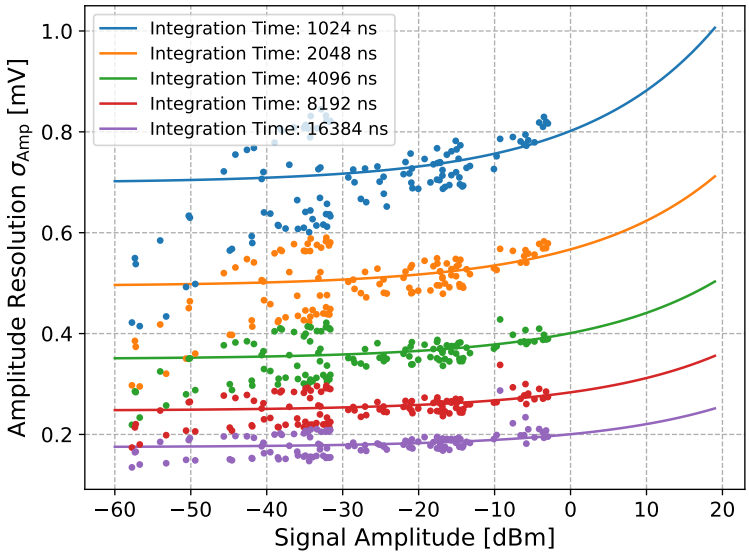

Figure 22: Amplitude resolution of the signal chain as a function of the measured signal power for different integration times. In solid lines, the expected amplitude resolution for a noise floor of −110 dBm that incorporates the shot noise picked up by the photodiode.

the expected amplitude noise that is calculated with Equation 4.12 with a noise floor of $-110\,\mathrm{dBm\,Hz^{-1}}$ that includes the signal amplitude-dependent shot noise introduced by the photodiode (see Section 5.1). The expected noise floor was set to $-110\,\mathrm{dBm\,dBm\,Hz^{-1}}$ to match the measured resolution better.
The first deviations from the expected signal are for low signal amplitudes below −40 dBm, where the amplitude resolution artificially performs better than expected. This is because the amplitude is a purely positive-valued observable. Therefore, the amplitude distribution is cut off at zero, limiting the possible error values.
The second one is the bimodal distribution of the amplitude resolution around the expected value which is most evident for signal amplitudes $< -30\,\mathrm{dBm}$. This is systematic because different sidebands are used to generate different signal powers. Here, the second-order upper sideband performs systematically better than the lower one. This is also true for the first-order sidebands visible in the signal amplitude range of −30 to −10 dBm, while the carrier, with most data points above −10 dBm, follows the expected amplitude resolution. As two different amplitude resolutions are possible for the same signal amplitude and are only dependent on the detected sideband order, it is concluded that it must be a systematic error introduced by the EOM. Apart from these minor variations, the amplitude resolution of the phase camera behaves as expected and is below 1 mV over the specified signal amplitude

range. Different amplitude resolutions, depending on the signal amplitude, can therefore be neglected for the observed signal amplitudes.

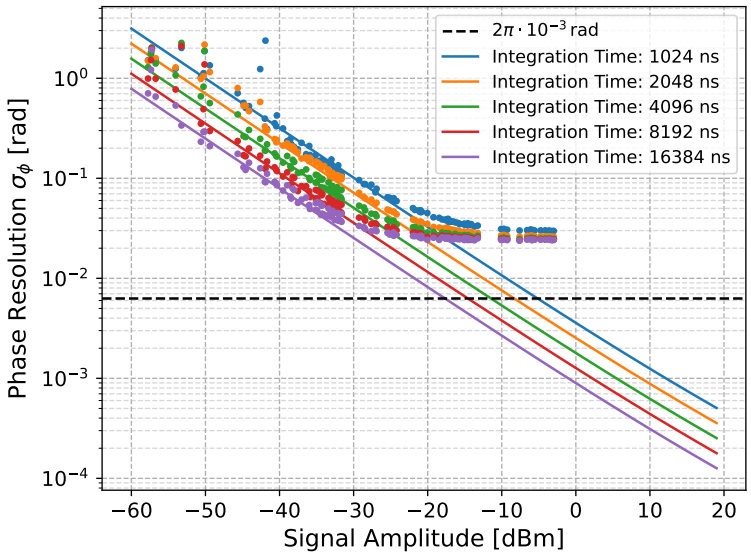

Figure 23: Phase resolution of the signal chain as a function of the measured power for different integration times. In solid lines, the expected phase resolution for a noise floor of −110 dBm that incorporates the shot noise picked up by the photodiode.

Complimentary in Figure 23, the phase resolution against the power for different integration times as dots and the expected phase resolution as solid lines. The same noise floor with shot noise dependency is chosen to calculate the expected phase noise as introduced in Equation 4.12. Apart from a few points at the top left, where the demodulo algorithm fails, the measurement points are in agreement with the measurement up to a power of −30 dBm. Here, the resolution saturates at 2 to 4 $\times$ 10^{-2} rad, depending on the integration time. Taking a look at the phase waveform itself reveals low-frequency oscillations which are not explainable by the signal chain. These are introduced into the optical setup by vibrations, acoustic injections, and thermal changes for long runs. A detailed description and breakdown of these effects is discussed in Section 5.4. Similar systematics as in the amplitude resolution can also be observed in the phase resolution.
To test if the signal chain is even capable of reaching the desired objective of a phase resolution of $\leq 2\pi \times 10^{-3}$ rad, these oscillations are subtracted by a 'true' phase signal. The attentive reader might have asked why 32,768 samples were taken per phase point when only a maximum of 8192 is used. With an integration time of 32,768 samples, a high-resolution 'true' phase signal is generated. The

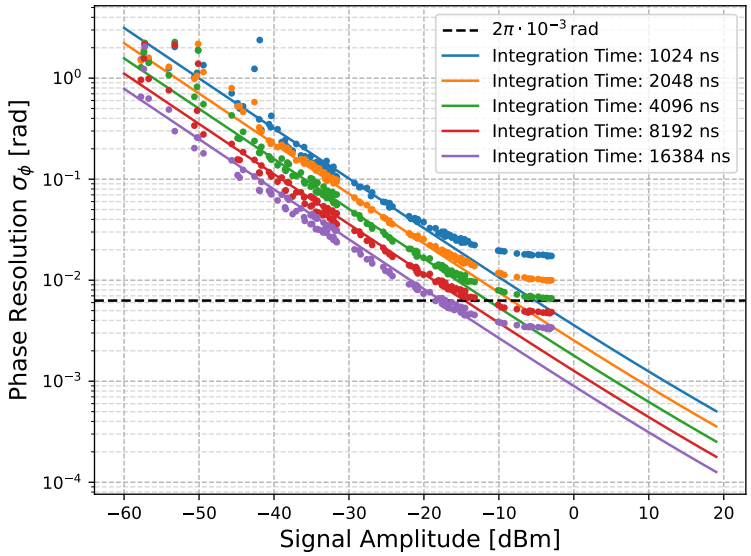

Figure 24: The phase noise resolution after subtracting the vibrations caused by the optical setup. In solid lines, the expected phase resolution for a noise floor of −110 dBm that incorporates the shot noise picked up by the photodiode.

results can be seen in Figure 24. The magic $2\pi \times 10^{-3}$ rad line is crossed for high enough integration times besides 1024 µs before the resolution saturates again. It is assumed that this is an artefact of the simple subtraction method.
Nevertheless, it can be concluded that the main limiting factor for the phase resolution is the optical setup of the phase camera itself.

5.3.1. Phase Resolution Across the Camera

The consequences of an amplitude-dependent phase resolution are that the reconstruction of the phase is not of the same quality over the whole wavefront phase image. An exemplary extreme case, where this can lead to trouble, is illustrated in Figure 25. Here, the amplitude of a wavefront and the associated phase resolution are depicted over the position of the camera. For simplicity, the reference beam is approximated as a flat intensity field, while the signal beam is modelled as a Gaussian beam. Both together feature a detected amplitude of 1 mV. The black dashed lines indicate the position/amplitude where the phase resolution drops below $\frac{\pi}{2}$ rad. Therefore, the outskirts of the Gaussian beam can not be reconstructed, as the phase can not be distinguished from noise. Such cases can be prevented by not using the phase camera at its absolute limit.

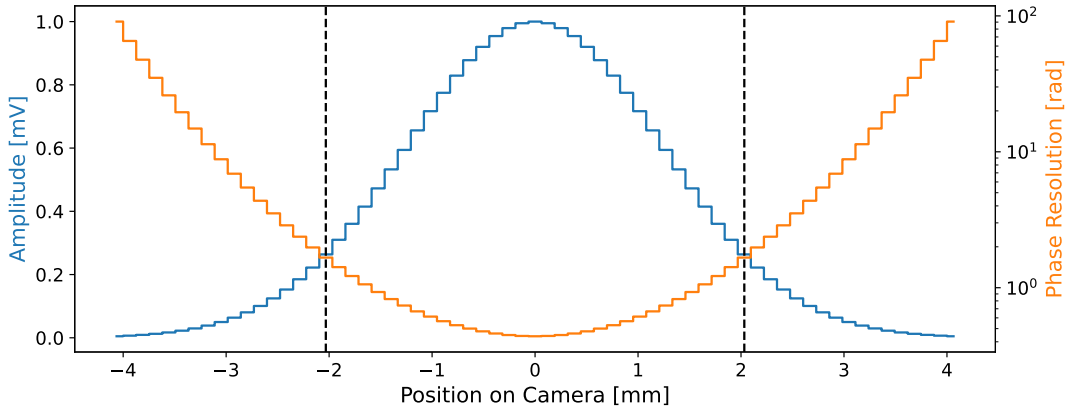

Figure 25: Expected phase resolution (blue) for a Gaussian amplitude distribution (orange) over the camera. The black dashed lines mark where the phase resolution drops below $\frac{\pi}{2}$ rad and the phase is indistinguishable from noise.

5.3.2. Phase Noise Spectra

To identify the noise sources of the optical setup of the camera and the auxiliary optics, the Power Spectral Density (PSD) of the phase time series is investigated. A trigger rate of $1 - 2$ kHz is applied for runs of length up to 5 s. For maximum SNR, an integration time of 65.536 ns per trigger is used. Three measurements of different optical setups are displayed in Figure 26: The old optical setup with different posts mounting the optics and no thermal stabilisation (blue), the new optical setup with heavier, more inert posts and thermal stabilisation (orange), and the new optical setup with thermal stabilisation but low signal amplitude (green). For the new setup, the mean PSD from 60 individual measurements is taken to further increase the SNR. To match the 1 kHz trigger rate and, therefore, the bin size of the previously recorded data of the old setup, a Gaussian filter with a standard deviation of 2 frequency bins is used on the new set of data taken at 2 kHz. New data for the old setup is unfortunately no longer possible, as it has been decommissioned.
Starting from the left, the most significant change between measurements is the slow thermal drift that dominates the PSD below 10 Hz that can be suppressed by three orders of magnitude by thermal stabilisation of the setup. The peak around 6 to 7 Hz is speculated to be the air conditioning of the laboratory.
Above 10 Hz the PSD is dominated by different frequency peaks that change with the optical setup. These suggest that the different resonance peaks originate from certain elements of the setup, such as the posts, mounts or clamps of optical elements, which were substituted moving from the old (blue) to the new setup (orange). Vibrations through seismic or acoustic origin can excite these resonances.

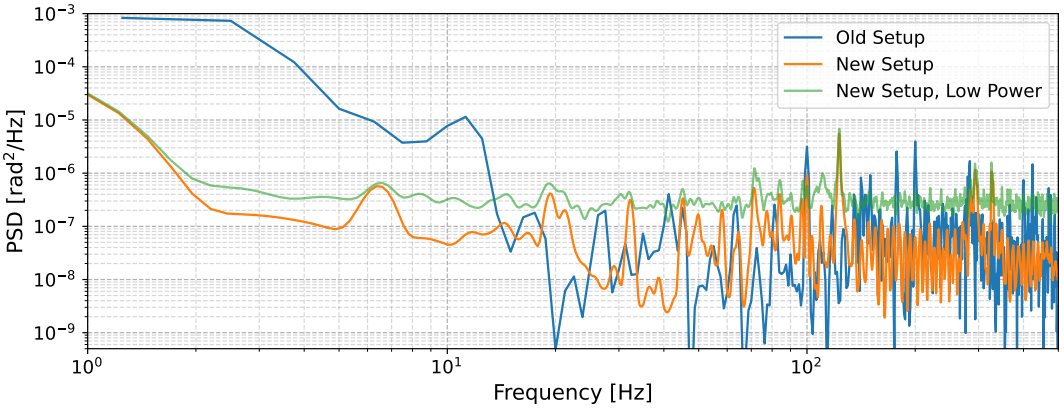

Figure 26: Power spectral density (PSD) of the phase for different optical setups. Individual noise sources appear as peaks, while thermal drifts in the phase introduce a 1/f noise. For low-power signal measurements, the general noise floor increases.

As PSD of the phase does not improve above a certain signal amplitude, the PSD should follow the shape of the compliance curve of the optical table. The optical table used in this work does not match the passive isolator legs. Therefore, no compliance curve from the manufacturer exists. A specific measurement is skipped as the limitations of the phase camera directly correspond to the seismic isolation of the setup. For lower powers and, therefore, worse SNR as in (green), the noise floor absorbs the individual peaks and characteristics of the optical table. Here, the limitation is the signal chain and not the auxiliary optics.
How thermal drifts and vibrations from seismic or acoustic sources couple into the phase measurement, which elements they affect and how to mitigate them are presented in the following Sections.

5.4. Phase Noise Coupling

To understand how noise couples into the phase, one has to look again at the demodulated observable $\Delta\varphi$ of the phase camera

$$\Delta\varphi = \Delta R - \Delta G + \Delta L \tag{5.13}$$

with ΔR the beam curvature difference between signal and reference beam, ΔG the difference in Gouy phase and ΔL the difference in optical path length between the two beams, as introduced in Equation 3.9. Noise can couple into the phase by any means of these three parameters. To determine the magnitude of influence of each of these parameters, the minimum phase resolution obtained in Section 5.3 -

observed as flattening in the power vs phase resolution curve - can be used as an upper limit.
The most direct impact has ΔL on the phase noise. The phase resolution limit of 4×10^{-2} rad directly translates to an oscillation with a standard deviation of ≈ 10 nm in the optical path length between the reference and signal path. With a stretch or compression of the optical axis of the beam, the Gouy phase changes and, therefore, ΔG. For a 10 nm length change, the Gouy phase changes by 2×10^{-10} rad, using Equation 3.11 and the Rayleigh length ≈ 2 m of the signal beam. A change in Gouy phase due to noise is therefore negligible.
Modelling noise coupling to ΔR is more complicated, as it depends on the change of curvature itself and the spatial coordinates perpendicular to the optical axis. Additionally, offsets from the optical axis result in different cross-sections of the curvatures. In theory, anti-correlated noise in pixels above and below the optical axis could be detected if the vibrations perpendicular to the optical axis between the two beams are sufficient large.
Using the beam parameters from Section 5.3, the signal beam used as a demonstrator has a waist of 80 cm in front of the camera and a beam radius of ≈ 2800 µm, leading to a curvature of ≈ 320 m at the camera. Taking the 10 nm as a benchmark again, the curvature changes by 4 µm. Projected onto the camera over the entire beam diameter, a maximum phase change of$\approx 3 \times 10^{-7}$ rad is expected.
For noise perpendicular to the optical axis, the offset must be in the order of 100 µm to have a measurable phase noise of 10 mrad. Consequently, the primary source of phase noise is caused by optical path length variations in the auxiliary optics, or more precisely, in the reference path.
After mixing the signal and reference path, the observable is the to be demodulated modulation frequency of several MHz. Length changes of the discussed types are less restrictive, as the wavelength of these beating frequencies is of the magnitude of several meters. Even strong noise, changing the combined optical path by a few mm, is therefore negligible.
An overview of the typical noise sources observed by the phase camera is provided in the following Sections.

5.4.1. Thermal Noise

Thermal effects change slowly compared to the frame rate of the camera and are perceived as a slow varying drift of the phase in the timescale of several seconds to hours. For the in Section 5.3 discussed phase resolution, thermal drifts are not a major concern as the measurement is on the timescale of a few seconds. However, for long monitor runs, the absolute phase can and will shift as seen in the PSD in Section 5.3.2. As a start, the optical breadboard the setup is mounted on is made out of solid aluminium. Aluminium has a thermal expansion coefficient of

23.1 µm m/K [108]. A temperature change of 1 mK is enough for a length change of 23.1 nm for one meter of Aluminium. Of course, the translation to the optical path difference depends on how the optical path is set up on top of the breadboard. But this is just a simple illustration of how susceptible the phase camera is to thermal drifts (as every other measurement on the nanometer scale).
To thermal stabilise the auxiliary optics, a black aluminium box is built on top of the breadboard, covering the auxiliary setup and the fibre array of the phase camera itself. With an additional gold foil on top, the mixing of air is prevented, while the gold foil reflects thermal radiation for further thermal isolation. A temperature stability of 5 mK over a time span of five minutes and 30 mK over one hour can be achieved. This drops the spectral power density of the phase noise by up to three orders of magnitude in the low frequency region below 10 Hz (see Figure 26).

More problematic is the thermal expansion of the optical fibre of the reference path. In the final version of the camera at a facility such as the Einstein Telescope, the reference laser input can be hundreds of meters away from the nominal camera. Such a long fibre is susceptible to various forms of noise, including thermal drifts. To estimate the additional phase per degree of temperature change, the description of optical fibre introduced in Section 4.4.1 is modified by the thermal dependency of refractive index in addition to the thermal expansion coefficient of borosilicate glass 3.3 µm m/K [109]. The thermal dependency of the refractive index is taken from [**fibre˙T˙dependencies**]. Positive and negative coefficients with magnitudes of 10 ppm/K can be found. As the paper is not very clear with the materials used, and the core and cladding could have different coefficients, all possible combinations are tried. The result is a thermal-induced phase change of magnitude 10 to 100 rad K^{-1}. Bad in any case.
But the more interesting question is, how does this slow thermal drift does affect the scientific goals of the phase camera. The wavefront curvature changes of all radio-frequency components in the laser frequency spectrum shall be monitored, and HOMs shall be spotted. This is done with the relative comparison of different frames. An absolute phase shift between frames does not restrict this kind of analysis, if slow enough or a stable relation between the pixels is given, such as in the fibre-based phase camera.

5.4.2. Vibrational Noise

A simple model, without loss of generality, to elaborate how vibrational noise can couple into the phase is a laser reflected off a mirror that vibrates along the optical axis at frequency ω_{vib}. The phase of the reflected beam $\varphi(t)$ can then be described as

$$\varphi(t) = \varphi_0 + \frac{4\pi}{\lambda} A \cos\left(\omega_{\text{vib}} t + \alpha\right) \,, \tag{5.14}$$

as the vibration periodically in- and decreases the optical path length, with φ_0 the initial phase of the laser, A the amplitude of the vibration, λ the wavelength of the laser and α the phase of the vibration [110, 111]. Mixing the reflected beam with a reference beam, as in the phase camera,modifies the frequency terms in Equation 4.5. This shall exemplarily be shown for the term of an arbitrary sideband with frequency $\omega_h = \omega \pm \Omega$:

$$P_{\omega_{\text{H}}} = 2|E_{\text{ref}}||E_{\text{signal}}| \left[\cos\left(\omega_h t + \varphi_0\right) \pm \frac{4\pi}{\lambda} A \cos\left(\left(\omega_h \pm \omega_{\text{vib}}\right) t \pm \varphi_0 + \alpha\right)\right] . \tag{5.15}$$

Phase modulation of the vibration generates sidebands around the heterodyne frequency ω_h. These vibration sidebands are not to be confused with the sidebands used for locked-in detection. If such sidebands are present in the phase camera, those sidebands will gain additional vibration sidebands. An illustration is given in Figure 27.

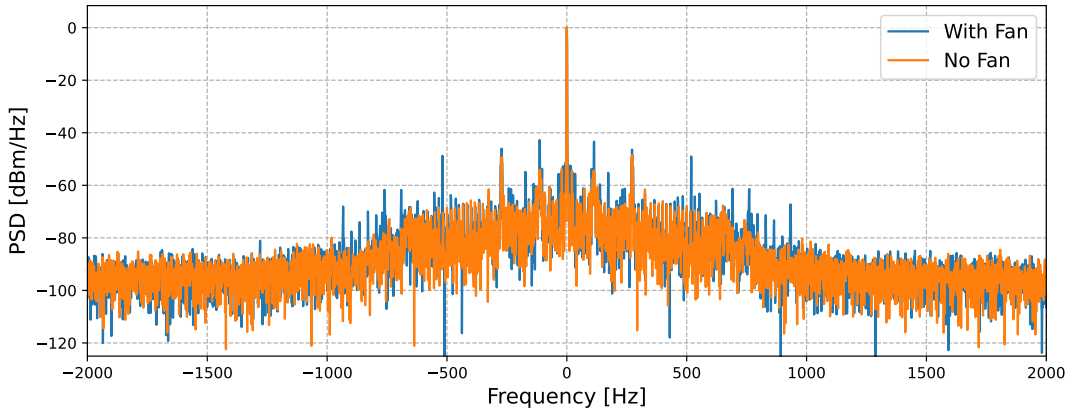

Figure 27: Power spectral density (PSD) of the digitised signal of an arbitrary pixel around the carrier frequency peak of 80 MHz before demodulation. The sidebands created by vibrations are symmetrical around it. One time with a fan mounted on the table for increased vibrations in blue and one time without it in orange.

It is a cut out of the FFT of the raw signal measured with one pixel of the phase camera around the carrier frequency of 80 MHz. In order to resolve vibration

sidebands in the Hz range, one second is continuously sampled in 2 ns steps. Carrier frequency is at 0 Hz at 0 dBm Hz^{-1} with its 20 dBm Hz^{-1} boosted noise floor ± 1 kHz around it. In the blue measurement, a 100 mm cooling fan is strapped to the optical table, rotating at ≈ 27 Hz. The seven-blade configuration generates many different vibration frequencies that are passed onto the auxiliary optics and appear as frequency peaks. Powering off the fan let them disappear.

When demodulating such a phase-modulated signal, the demodulation can not separate between the signal frequency and the vibration sidebands. For example, an even exorbitant high integration time of 100 µs at a sampling speed of 500 MHz leads to a frequency resolution of only 10 kHz. Therefore, the phase modulation by the vibrations is visible in the phase measurement itself as phase noise if the vibrations are lower in frequency than the frequency resolution of the demodulation itself.
In order to find out which optical elements are most susceptible to vibrations seen as resonant peaks in the PSD of the phase, a simple 'pling' test is conducted. Individual optical elements are gently struck with a pen, inducing vibrations at their resonant frequencies while a phase measurement is running. A FFT analysis of the vibrations reveals the resonance frequencies. Comparing that to the PSD of the phase, most peaks could be matched. A reason why there are so many different discrete peaks in the old optic setup is the use of a mixture of different posts, post mounts, and clamps. Different weights, heights and mounting rigidity lead to a variety of different resonance frequencies. In order to reduce the number of resonance frequencies and also to comply with the laser height of the ET Pathfinder (see Section 7), new standardised one inch thick posts and clamps were purchased. The increased width, from half to one inch, dampens the vibrations due to the higher mass. A comparison of the phase PSD between the old and new setup with the same noise floor can be seen in Figure 28. The number of resonance frequencies could be reduced, and the integrated power over the peaks could be decreased.

5.4.3. Acoustic Noise

Acoustic noise and, therefore, sound waves can couple to the phase measurement of the phase camera in two ways: Either by inducing vibrations in individual elements of the optical setup or by changing the optical path length through changes in the refractive index of air due to the pressure oscillations of sound waves. The coupling and, therefore, phase modulation is the same as explained in Section 5.4.2. To measure the acoustic spectrum of the laboratory, the Earthworks Audio M23R omnidirectional microphone [112] is used. It features a frequency range of 3 Hz to 23 kHz, a sensitivity of 36 mV Pa, and a gain flatness of ± 0.5 dB.
The recorded acoustic spectrum is then compared to the phase PSD. A match

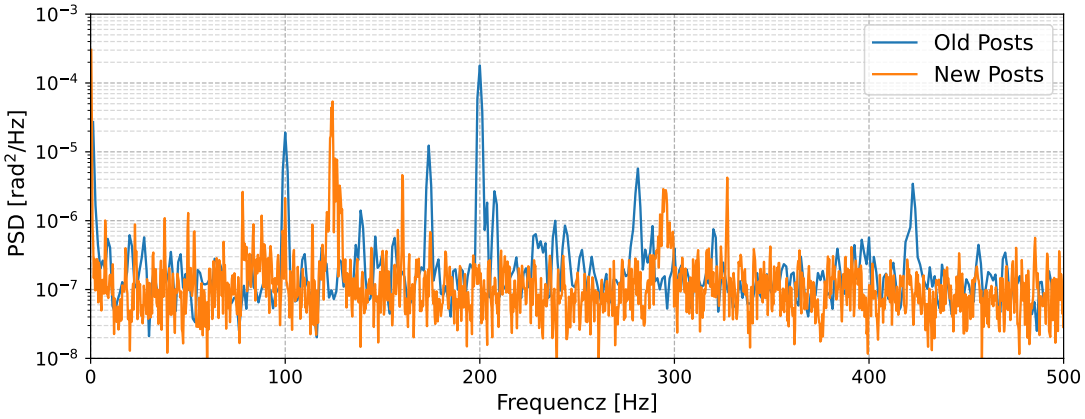

Figure 28: Power spectral density (PSD) of the phase for the old and new optical setup. The number of resonance peaks could be minimised.

with frequency peaks could be found for 320 Hz and 420 Hz. While the 320 Hz coincides with a resonance frequency of the posts, 420 Hz does not. As the noise source could not be traced down, 420 Hz is likely picked off by the optical fibre in the reference path. Besides that, the bump around 10 to 20 Hz in the phase PSD seems to correspond to frequency peaks in the acoustic spectrum at 15 Hz and 21 Hz. This low-frequency rumble is assumed to be the air conditioning, blowing fresh air into the laboratory. Unfortunately, it is not possible to turn it off, so it remains uncertain. In general, the contribution of acoustic noise to the PSD is minor in comparison to thermal and vibrational noise.

5.4.4. Noise Susceptibility of the Reference Beam

To test the extent of the noise susceptibility of the reference beam path, the demodulated phase of the symmetric upper and lower sidebands is subtracted. As both phases are measured relative to the reference beam, the noise contribution from the reference path cancels, and the relative phase between the sidebands remains with the noise contribution of the signal path. Additionally, the relative phase resolution between two sidebands decreases systematically by 3 dB as the subtraction of uncorrelated noise from the amplifier increases the overall noise by 3 dB. This has the same effect as halving the integration time for the phase resolution of a single sideband.
The phase resolution of the subtracted signal can be seen in Figure 29 with the expected phase resolution adjusted. It follows the expected phase resolution curve without the saturation observed in Figure 23. This concludes that the noise from the auxiliary optics is completely dominated by the one coupling into the reference

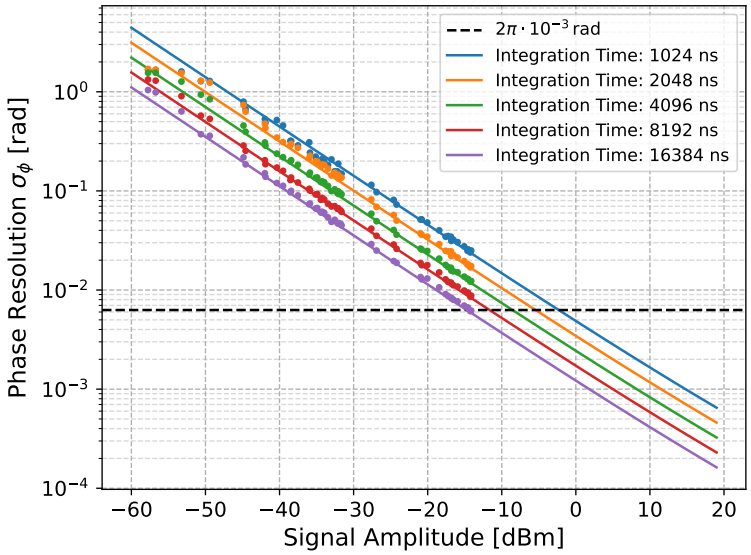

Figure 29: Phase resolution of the phase camera for relative phase images between different radio-frequency components. The noise from the optical setup is successfully subtracted from the image. The general resolution across different powers is reduced by $\sqrt{2}$ in comparison to absolute-phase images, as the statistical noise from two individual measurements is quadratically added.

path. For measurements at facilities as the Einstein Telescope, things will only get worse as the reference beam from the initial laser can be hundreds of meters away. The seismic noise pick of the optical fibre will increase again. Different strategies must be used to address with this problem.
Nevertheless, one is interested in the 2D phase images themselves and how the phase spatially relates to each other in the wavefront. With a static 1D or 2D fibre array as imaging sensor, this will always be given. Oscillations in the optical path will shift the phase of the wavefront constantly over all pixels without changing the features creates by the possible mode content. This then allows averaging over multiple phase images

5.5. Frequency Dependent Phase Shifts

Due to the design of the fibre/based phase camera, two intrinsic phase shifts between the sideband/carrier will occur depending on the frequency. One is due to the optical path length the signal beam has to travel from the observed cavity, or in the case of the laboratory setup, from the EOM to the fibre array. The other is due to the light propagation in the multimode fibre of the fibre array as described

in Section 4.4.3. The relative phase relations of a phase image of an arbitrary sideband are still correct, but the absolute phase is shifted. These shifts need to be accounted for as these are artefacts introduced by the camera. Both of these shifts could be successfully predicted and measured, as the following section presents.

5.5.1. Along Optical Path

The phase shift along the optical path is determined by the different wavelengths of the individual sidebands. As it propagates along the same optical path, the higher-frequency sideband will naturally acquire more phase. To calculate it, only the length of the path and the frequency difference between the two wanted sidebands are needed. For the first upper and lower sidebands in the laboratory setup, this would be 20.090 MHz or 14.92 m translated into the wavelength. Therefore, the phase of the upper sideband will be 2π ahead after 14.92 m. Expressed more formally, the phase shift due to the optical path length is calculated by

$$\Delta\varphi = 2\pi\frac{L}{\Delta\lambda} = 2\pi\frac{L\Delta\nu}{c} \tag{5.16}$$

with L the optical path length and $\Delta\lambda$ the difference in wavelength or by using the dispersion relation of light; $\Delta\nu$ the difference in frequency and c the speed of light.

5.5.2. Fibre Induced

The fibre induced phase shift is, in principle, similar to the one along the optical path. Different frequencies propagate over a certain distance. However, because of the different modes, the frequencies can propagate in the multimode fibre, the description is more sophisticated. A detailed description is given in Section 4.4.3 with a prediction of 30 $\frac{\text{mrad m}}{\text{MHz}}$ for the used multimode fibre in the phase camera.
To measure this shift, a reference without the fibre is necessary to evaluate the difference. Therefore, the heterodyne beam is split in front of the fibre array and monitored with a single photodiode in parallel. As the photodiode, the ET-0002 is directly mounted into the laser beam. A schematic of the setup can be seen in Figure 30.
To probe as many frequencies as possible, the EOM is run at 4.8 V to create three upper and lower sidebands with a 10.045 MHz spacing between each other. To further increase the probed frequency space, the AOM is operated at 80 MHz to 65 MHz in 3 MHz steps in different runs. This was done as the EOM is resonant and can only be operated at around $\approx$ 10 MHz. Therefore, the AOM gives way more leverage in the frequency space.
The phase of each sideband and run is then subtracted from the phase measured without the fibre as the mediator. The result for the 1 m fibre array can be seen in

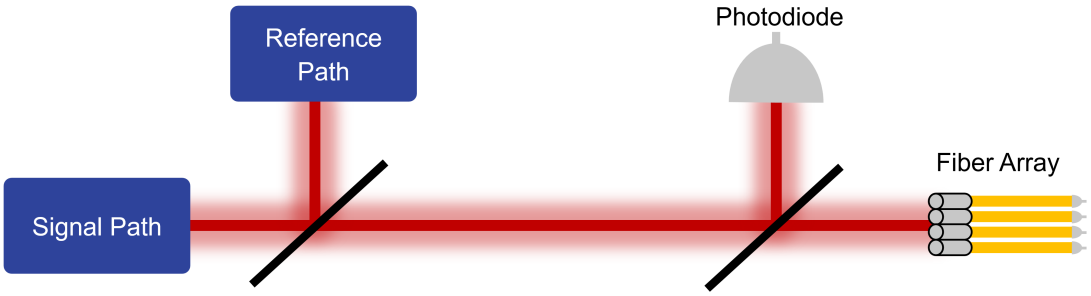

Figure 30: Schematic of the setup used to determine the fibre-induced phase shift. The photodiode and fibre array have different optical path lengths to the beam splitter.

Figure 31 in blue with a fitted slope of $(33.314 \pm 0.001)\,\frac{\text{mrad}}{\text{MHz}}$ in green. It is important to note is that the individual photodiode and the fibre array were at different positions along the optical axis. Therefore, a phase shift along the optical path is introduced that depends on the path length difference. To measure the optical path length difference, one fibre of the fibre array is extended by an extra 1 m patch cable fibre. The phase shift induced by the fibre is now doubled, while the phase shift due to the difference in optical path length stays the same. The results are again displayed in Figure 31 in orange with a fitted slope of $(64.497 \pm 0.001)\,\frac{\text{mrad}}{\text{MHz}}$ in red. Combining the two results with the measured length of the fibre $(1.020 \pm 0.001)\,\text{m}$ leads to an overall fibre induced phase shift of $(30.6 \pm 0.9)\,\frac{\text{mrad m}}{\text{MHz}}$ and a phase shift of $(2.0 \pm 0.9)\,\frac{\text{mrad m}}{\text{MHz}}$ due to the optical path length difference of $\approx 10\,\text{cm}$. Comparing that to the predicted value of $30.5\,\frac{\text{mrad m}}{\text{MHz}}$, the measurement is in good agreement. However, there are also some systematics in the measurements, which can be better spotted in the residuals at the bottom of Figure 31. Seven discrete offsets are on top of the predicted phase shift, independent of the frequency, but correspond to the seven radio-frequency components of each run. As they are symmetric and centred around the carrier frequency of the AOM of each run, an additional phase shift due to propagation differences can be ruled out. Therefore, it is assumed that this is an intrinsic systematic of the EOM as it shifts with different AOM frequencies.

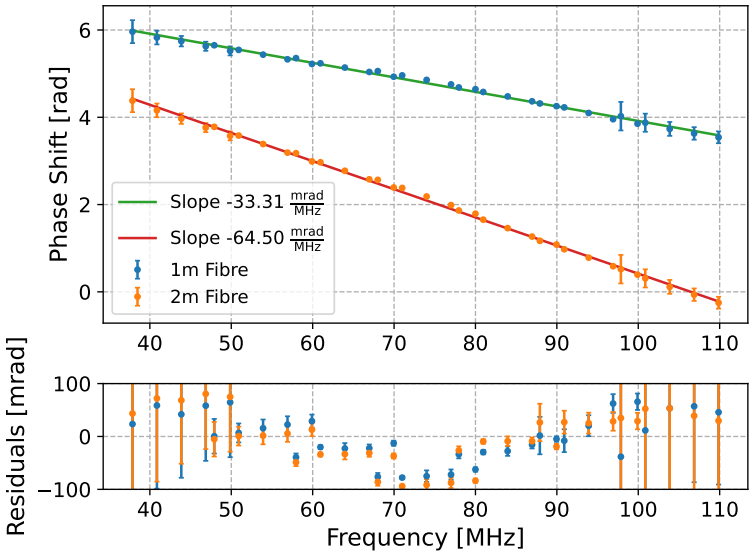

Figure 31: The fibre-induced phase shift for a 1 m and a 2 m fibre with the corresponding linear fit to determine the coefficient, and the associated residuals in the bottom panel.

6. Implementation of CTC

For the characterisation of the signal chain, the Spectrum Instrumentation digitiser cards were well-suited due to their specifications. However, for a full-scale camera, the Spectrum Instrumentation digitiser cards are just too costly. A different digitisation solution must be found for a 64-pixel camera, which is also scalable to higher pixel counts, such as 4096. As a high number of ADCs of 14-bit precision and 500 MSa/ s is relatively expensive, the choice was made to use the CTC ASIC of the TARGET ASIC family instead, which drops the cost per digitisation channel significantly by a few magnitudes and is in-house supported.
CTC is developed for the front-end electronics of the SST camera, a Cherenkov camera of the SST of CTAO, a ground-based gamma-ray observatory. It is a 16 channel digitiser at 1 GSa/ s with 12-bit precision, a continuos sampling buffer of 16 µs and a dynamic range of 2.2 V [21]. An in-depth description can be found in Section 10.8, with the needed calibration routines in Section 11, the performance analysis for Cherenkov cameras in Section 13 and the implementation into the said front-end electronics in Section 13.6. At this point, the ASIC is well understood, the operation parameters optimised, the calibration routine standardised and, therefore, the ASIC is ready for all kinds of different tasks. The necessary changes and developments for implementing CTC in the phase camera to meet its requirements are described in the following Section.

6.1. Hardware Setup

For the first mixed-digitised fibre-based phase camera, two of the TARGET evaluation boards used to characterise and test the TARGET ASICs were repurposed, resulting in a 56-pixel version. Therefore, it also features the companion ASIC Cherenkov-T5-Trigger Extension Asic (CT5TEA), whose main feature is a single-shot trigger logic to detect photo pulses, which is not used for the phase camera. But it also provides the necessary DC offset voltage, called pedestal voltage, to operate the CTCs ADCs at the correct operation point. To control the ASICs and to transfer data, the board hosts a piggy-board Field Programmable Gate Array (FPGA). A detailed description of the arrangement of the Printed Circuit Board (PCB) itself is given in Section 11.1.

As the performance of CTC is temperature dependent (see Section 11.5 or 11.6.1), a heat stabilisation setup is built on top of the ASIC to avoid recalibration due to drifts of the ambient temperature. It consists of a copper block on top of the ASIC to give the ASIC a higher thermal capacity. A temperature sensor in the form of a thermistor is mounted in a hole in the block. On top of the block sits a Peltier element that regulates the system to 25 °C by monitoring the thermistor.

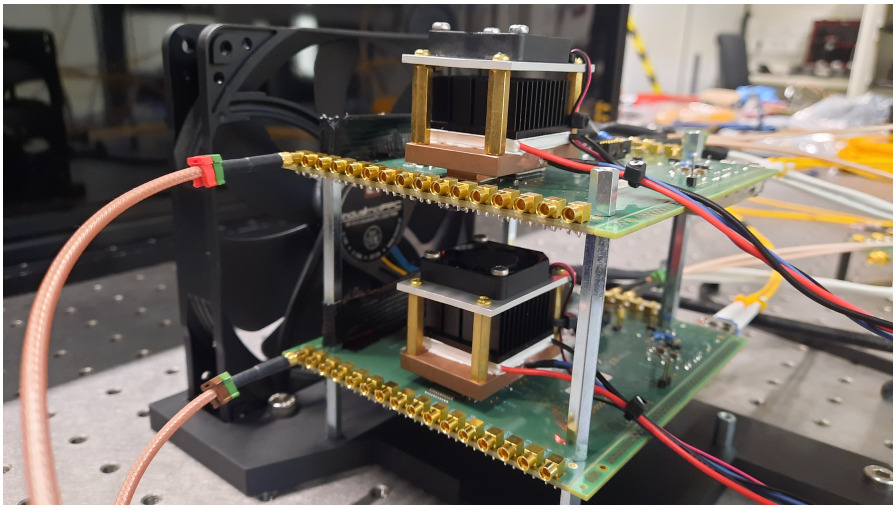

Figure 32: The two used TARGET evaluation boards SN0001 and SN0002 with the temperature stabilisation setup mounted on top of CTC. Small baffles prevent the fan from directly cooling the Peltier elements.

To dissipate heat, a heat sink is glued on top of the Peltier element, with a fan cooling it. An image of the complete hardware setup can be seen in Figure 32.

To successfully measure phase, the sampling of CTC needs to be synchronised with the rest of the setup, e.g., the EOM and AOM drivers, the trigger unit, and the Spectrum Instrumentation digitiser cards. The sampling clock of CTC is a fraction of the clock given by the FPGA. By synchronising the FPGA, CTC is automatically synchronised as well. Synchronising the FPGA with the standardised 10 MHz reference is possible, but it is not the best option. All clocks in the FPGA are created from a 125 MHz reference clock. As this is not a multiple of 10 MHz, multiple TARGET evaluation boards would run in arbitrary synchronisation phases. The data acquisitions introduced in the following Section 6.2 would not be possible, as the synchronisation state of the board is not deterministic. Hence, the 125 MHz clock is directly fed to the FPGA via an Input/Output (IO) Micro-Miniature CoaXial (MMCX) pin. An additional clocking board is used to convert the 10 MHz clock to the required 125 MHz clock. For this, the Si5350/51-20QFN-EVB clock distribution board based on the Si5350/51 clock generator is used [113], which supports up to eight high-quality clock outputs.

6.2. Data Acquisition

In contrast to the initial purpose of the ASIC of digitising photon pulses, AC coupled intensity oscillations of a photodiode shall now be digitised. With a

dynamic range of 2.2 V, the operational pedestal is set to 1.5 V instead of 750 mV to support the digitisation of negative amplitudes in the linear response regime of the ASIC (see Section 11.6.1).
Additionally, the waveform size, which is 128 ns in photon-pulse operation, has to be increased to achieve a reasonable phase resolution. For the best resolution, the whole storage of 16 µs could be digitised. However, this limits the trigger rate to < 50 Hz due to the digitisation time of ≈ 20 µs per 32 samples. Therefore, the middle ground of waveforms with a duration of 4032 ns is chosen, which allows for trigger rates up to 200 Hz.
In order to read out the 4032-sample waveform, the multi-trigger mode has to be used. Instead of reading a singular 4032-sample waveform, the full length is split into nine adjacent segments of 448 samples each. There, in turn, are digitised in sequence and later joined together in analysis. This, however, leads to two interesting problems.
First: The start of an event is not at the start of the joined together waveform, but can be at the end, depending on the internal set trigger look-back time. This is because of the cyclic nature of the storage sampling array operated in 4096 storage cell mode, which is implemented as it is more robust. The problem is illustrated in Figure 33. As the waveform is 4032 samples long, all storage samples are blocked for digitisation after each trigger, and new samples are not overwritten. If the trigger look-back time is too long, the digitisation starts behind the initial trigger. Therefore, the signal starts at the end of the waveform, as the storage array pointer has overtaken the trigger timestamp.

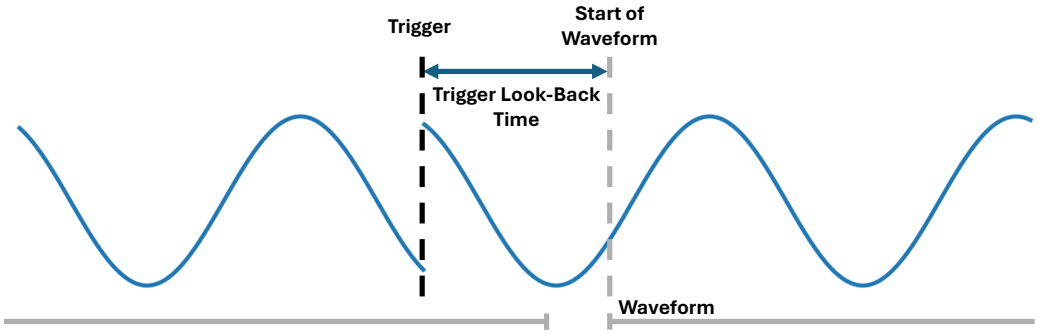

Figure 33: Depiction of the storage cell array digitising an arbitrary signal. It starts from left to right and is continuously overwritten from left to right. If the trigger lock-back time is not set correctly, the start of the waveform does not correspond to the trigger time stamp. As the waveform is nearly as long as the storage cell array, the event start is digitised at the end of the waveform.

There are multiple ways to prevent this. The most straightforward approach is to cut off the end portion and treat the start of the waveform as the actual start. For

the ASIC parameters used in this thesis, this corresponds to a cut at the 3845th sample. Although one loses information, it is a valuable option for proof-of-concept studies. All relevant measurements are done with this simple technique. A more elegant solution would be to digitise a 4480-sample waveform in ten sequential 448-sample waveforms. Then, cutting the repeating samples and glueing the start of the signal at the start of the waveform. This would also allow a full readout of the 4096-sample storage sampling array. With the 4032 sample long waveforms, this is unfortunately not possible, as there would be a 64-sample gap in the waveform. Another option is to tune the trigger look-back time to avoid such situations, but this would limit the waveform length to 4032 samples.

Second: With the extended data structure of the multi-trigger waveforms, the necessary calibration steps of pedestal subtraction and applying a DC transfer function (see Section 11.5 and 11.6.1) can not be performed with the TARGET libraries, the software to operate the TARGET ASICs. Instead of adjusting the outdated code, a different solution is found that also reduces the amount of calibration data needed, as the software can handle multi-trigger waveforms when they always start at the same storage cell number (first cell ID). This also has the advantage that storage and sampling array effects are avoided, as it is always read out the same way. In order to achieve this, several tweaks were needed.
The first one is that the trigger frequency must be a multiple of 4096 ns. Consequently, only one first cell ID is possible. But this first cell ID is entirely arbitrary, as it changes with each restart of the ASICs or a change in trigger settings of the trigger unit, as it switches at arbitrary times. Therefore, a setup routine is implemented.
As the first step, the firmware was modified by Dr. Adrian Zink, so the addressing of the storage sampling only starts when an initial trigger signal is detected, the syncing pulse. With trigger frequency as a multiple of the storage sample array (4096 ns), the same first cell ID is used for all waveforms after each restart. This also means that the trigger signal is engaged all the time, which can be a problem when using multiple TARGET evaluation boards or digitisers in general, as the data listener or trigger on/off settings can not be started in unison. Fortunately, the TARGET and Spectrum waveforms are timestamped and could be assigned to each other. However, to make it even simpler, an attenuator [114] is installed into the trigger line. Therefore, the trigger generator runs continuously in unison with the storage sampling array, guaranteeing the same first cell ID, but can be externally disconnected and reconnected as needed. For example, when every digitiser is ready for data.

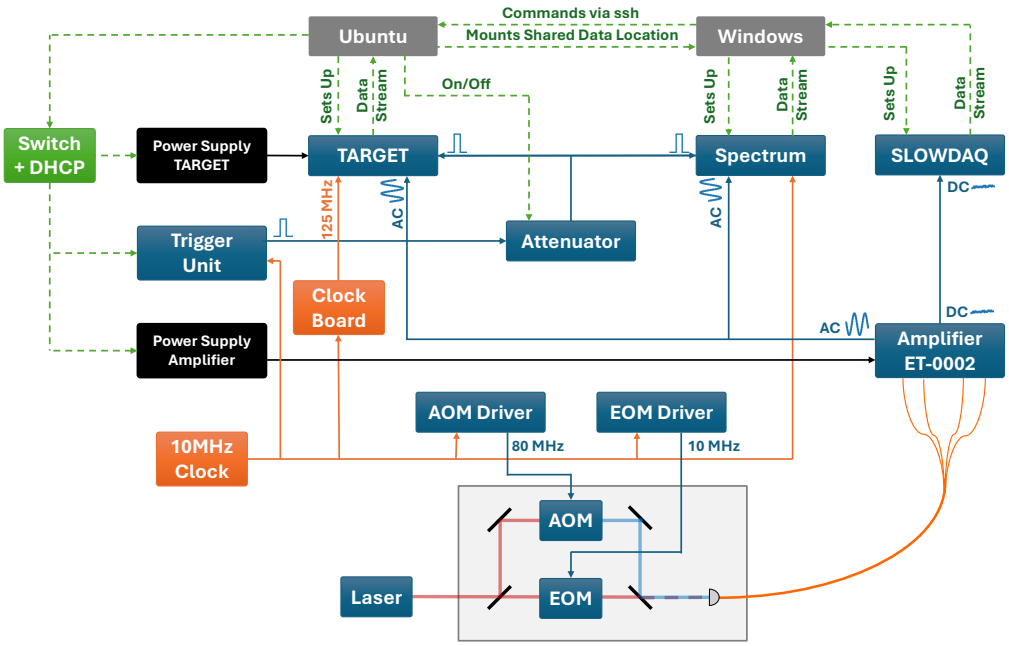

Figure 34: Illustration of the operation set-up to run the TARGET digitisers (CTC) in parallel to the Spectrum Instrumentation digitiser cards. The two workstations with different operating systems are colour-coded in grey, the communication lines as green dashed lines, analogue signals in blue, power supplies in black, and the 10 MHz clock for synchronising each device in orange.

6.3. TARGET x Spectrum Operation

The next hurdle to run TARGET and the Spectrum Instrumentation digitiser cards in parallel for one camera is that the TARGET software [115] (see Section 11.1) can only be operated on a Linux operating system, while the Spectrum Instrumentation digitiser cards run on Windows. In this work, Ubuntu is chosen as the Linux system used without any preference. An overview of the entire setup for running the phase camera with the two different digitisers in parallel, and which machine controls which devices, is given in Figure 34.

The following describes the routine for a standard measurement. Although two machines are used, the whole sequencing is controlled by the Windows machine. When starting a measurement, the Windows machine logs into the Ubuntu machine via *SSH* to initialise and set up the TARGET evaluation boards. Therefore, the Ubuntu machine deactivates the trigger line by activating the attenuator. The trigger frequency can now be set by communicating with the trigger unit. Then, the initialising routine for the TARGET evaluation boards starts by power-cycling them.

Freshly powered, the communication is established, and the necessary parameters are set. Then the trigger on the TARGET evaluation boards is activated and the attenuator switched off for a trigger pulse to synchronise the storage array addressing pointer to the trigger frequency to guarantee the same first cell ID in each waveform. With the attenuator switched on again and the trigger line deactivated, the Windows machine initialises the Spectrum Instrumentation digitiser cards.
Each Spectrum Instrumentation digitiser card is allocated its own processing thread, which opens a listener for it. Another thread is started that connects to the Ubuntu machine via *SSH* to start the TARGET listeners. All triggers of the digitisers are armed, and the trigger line is activated by deactivating the attenuator. Data is now taken for an arbitrary amount of time until the attenuator is switched back on, and the individual triggers are deactivated and the listeners closed.
The raw TARGET data is stored locally on the Ubuntu machine, one file per module. It is calibrated by a pedestal subtraction (Section 11.5) and a DC transfer function (Section 11.6.1) is applied. The waveforms are combined into a numpy file, the trigger timestamps into a separate one and then transferred to the Windows machine. Then, the TARGET and Spectrum data are demodulated individually, with their own timestamps and pixel mappings. Combined images can then be created in post-processing, the analysis of the data.

6.4. TARGET Performance

Before analysing the phase camera images, the TARGET performance as part of the phase camera is evaluated. Critical performance parameters, such as the baseline noise and cross-talk, are described in depth in Section 13.3 and 13.2. The impact on the phase resolution is discussed here.
For both used TARGET evaluation boards, the baseline noise is below 0.6 mV [21], two orders of magnitude smaller than the amplifier noise of the ET-0002 amplifier boards and is therefore negligible. The cross-talk in a frequency range up to 200 MHz is below −40 dB for the next-neighbour channel and even lower for the rest [21]. For the proof-of-concept camera, this is negligible. However, for the next iteration, one could equip only eight channels per ASIC to avoid unnecessary cross-talk, since the ASIC is not the primary driver of camera cost.
From the characterisation of the amplifier board ET-0002 in Section 5.1, it is already apparent that the bottleneck in phase resolution, excluding the auxiliary optics, is the amplifier board and the integration time. For CTC, it is limited to the finite storage sampling array of 16 µs or in this works case 4032 ns. In a more sophisticated next iteration of the phase camera based on CTC, one could try to slow down the sampling speed to 500 MSa/ s doubling the integration time as the bandwidth is already limited by the input Switched-Capacitor Array (SCA) to 220 MHz without loss in trigger frequency.

Nevertheless, the phase resolution is tested for the CTC ASIC in the same way as for the Spectrum Instrumentation digitiser cards as in Section 5.3. A comparison between both for the same integration time of 4032 ns can be seen in Figure 35,along with the expected phase resolution.

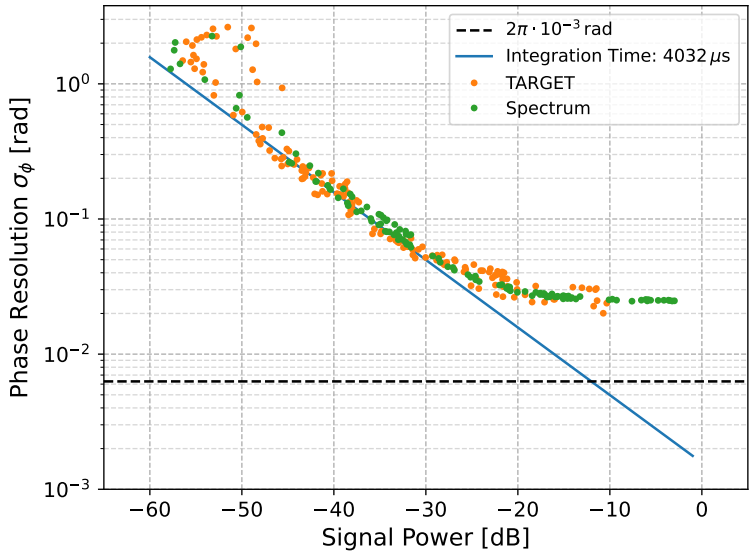

Figure 35: Comparison in phase resolution between the Spectrum Instrumentation digitiser cards and the TARGET CTC ASIC as digitiser for the fibre-based phase camera.

Both perform as expected with a higher deviation in the TARGET evaluation boards. For powers below ≈ -50 dB the phase resolution seems worse than it is as jumps due to the modulo 2π constraint can not be avoided, while for powers above ≈ -30 dB the phase resolution is limited by the noise introduced by the auxiliary optics (see Section 5.4). Therefore, the CTC ASIC is also a viable option as a digitiser for the presented phase camera.

6.5. Trigger Delays

From triggering to digitisation, delays accumulate internally in TARGET and via the individual trigger lines. These delays will shift the phase of the measurement depending on the frequency of the demodulated signal. Measuring with multiple modules will cause systematic phase shifts in the phase image depending on the digitiser of the pixel. Therefore, the individual shift of each digitiser has to be matched. To address the issue, one can adjust the trigger look-back time for each module to match the time discrepancy. For the mixed-digitiser phase camera with

TARGET evaluation boards and Spectrum Instrumentation digitiser cards, the TARGET evaluation boards are adjusted relative to the Spectrum Instrumentation digitiser cards in post-processing of the phase images. The trigger delays between the Spectrum Instrumentation digitiser cards and the two TARGET evaluation boards could be measured by digitising a pulse and comparing the pulse position in each waveform. Between evaluation board SN0001 and the Spectrum Instrumentation digitiser cards, a trigger delay of 65 ns is observed, while SN0002 to Spectrum has a delay of 61 ns. In Section 7.4, phase jumps between digitisers that depend on the frequency of the demodulated signal are indeed observed, but could not be corrected by applying the trigger delay corrections. More on that in the mentioned Section.

7. Measurement Campaign at the ET Pathfinder

With the signal chain characterised and a working 56-pixel proof-of-concept camera, the expressiveness and reliability of phase and amplitude images need to be studied. The long-term goal is to decompose a beam into its mode components to interpret anomalous behaviour in the interferometer or to stabilise cavities. But first, the image quality and correctness have to be ensured for depicting the phase and amplitude wavefronts of all kinds.

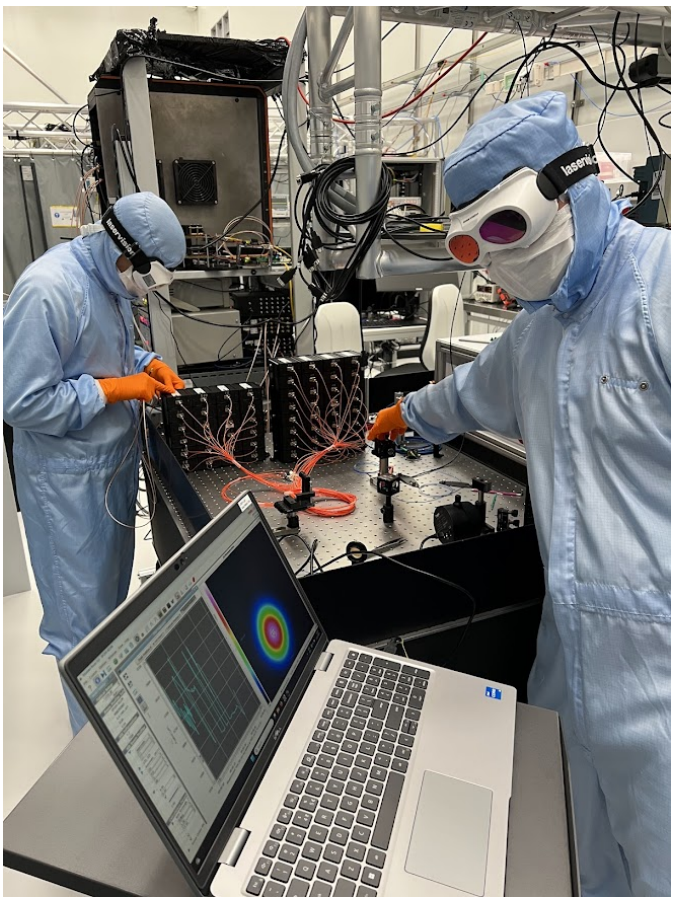

Figure 36: Fibre-based phase camera measurements at the ET Pathfinder. Image taken by Stefan Hild.

To do all that, a beam with different and well known-mode content is needed, and therefore, a stable but detunable cavity. As another thesis can be devoted to this task, a measurement campaign at the ET Pathfinder is conducted, where such a cavity in the form of an input mode cleaner is available. This also has the benefit of getting to know the state-of-the-art control systems for the Einstein Telescope,

the phase camera will interface with, gathering expertise on how to operate the phase camera at such a facility in a clean room environment. The campaign ran from 20.07.2025 to 01.08.2025. An impression of the measurement setup at the ET Pathfinder can be seen in Figure 36. With the required cleaning, setup and preparation taken into account, a total measurement time of roughly three days was possible. Therefore, the complete interpretation and analysis of the data is done in the aftermath.
With the required cleaning, setup and preparation taken into account, a total measurement time of roughly three days was possible.

Additionally, for this campaign, a scanning configuration for the 1D array is developed, enabling the creation of pseudo 2D images for a straightforward interpretation of HOMs.
This will also drive future hardware development for this project, as different camera setups yield different results in image quality. Static arrays benefit from stable phase relations between pixels in a single image, as they are imaged at the same time. In contrast, scanning configurations pick up different phase noise from the auxiliary optics per 1D image slice. However, economically speaking, the fewer pixels, the better. Therefore, the interpretability of static 1D slices shall be analysed. From thereon, one can determine the minimal configurations required to resolve the mode content.
First, the ET Pathfinder is introduced as a test bed for future technologies of the Einstein Telescope. Then, the to-be-monitored input mode cavity is presented with the different beam configurations of the phase camera to test different limits. The first measurements with the static 1D 56-pixel array are discussed with the emphasis on image interpretation and the impact of HOMs. A scanning setup is introduced to generate pseudo 2D images, which are then discussed in depth. The focus here also lies on interpretability, not on performance.
In general, the campaign serves as a proof-of-concept study of the novel fibre-based phase camera approach. Some points could have been handled differently in hindsight, but can not be changed afterwards. However, these lessons have to be learned to deploy a successful fibre-based phase camera.

7.1. ET Pathfinder

The ET Pathfinder is a dedicated test facility for research and development of the technologies required to build the Einstein Telescope [25, 22]. The focus is on technologies for the low-frequency interferometer of the Einstein Telescope, which requires cryogenic cooling and, therefore, new silica test masses and a new carrier laser wavelength, such as 1550 nm or 2090 nm. To this end, two fully functional interferometers with arm length of ≈ 10 m are built, which are shown in Figure 37.

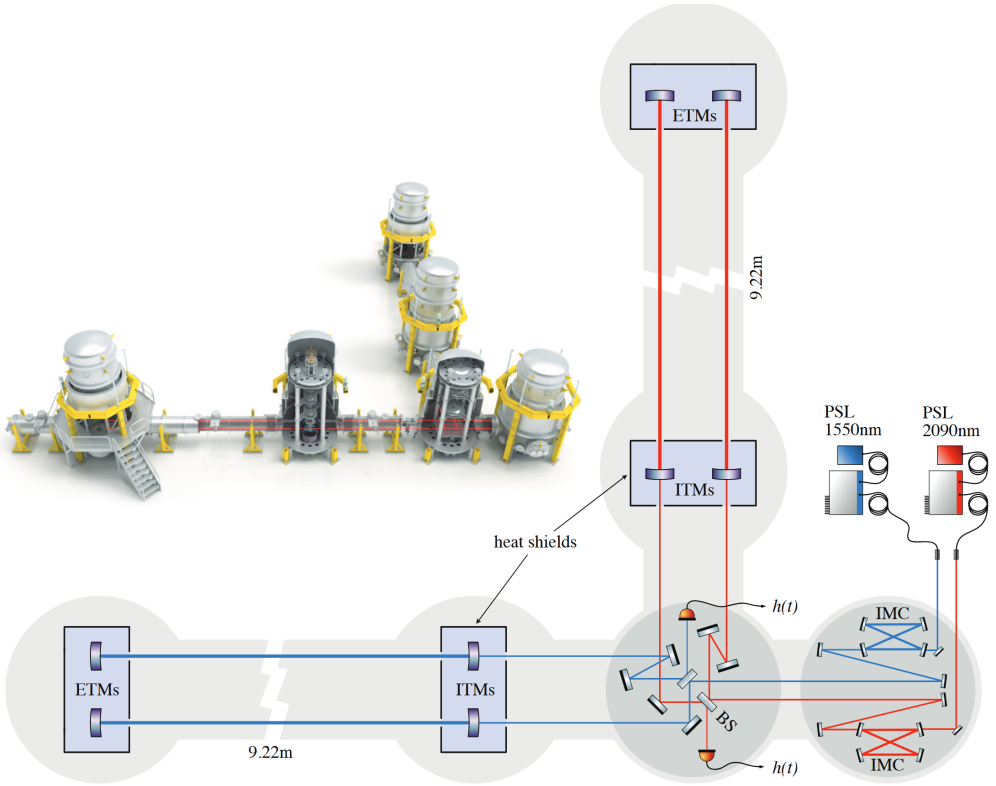

Figure 37: Illustration of the ET pathfinder with its vacuum tanks and two folded laser interferometers at 1550 nm and 2090 nm. Image taken from [25].

Six vacuum towers host the two interferometers of different wavelengths. A stabilised laser is passed into the beam injection tower, where an additional input mode cleaner is present. From thereon, the beam is split and mode matched to the Fabry-Perót cavities of the interferometer arms in the beam splitter tower. Four vacuum tanks house the test masses of the interferometer. As the 1550 nm runs on 18 K test mass temperature and the 2090 nm runs on 123 K, the interferometer is folded.
The sensitivity of the ET Pathfinder independent of the carrier wavelength goes down to $10 \times 10^{-19}\,\mathrm{m}/\sqrt{\mathrm{Hz}}$. This is beyond anything that is achievable in a simple laboratory setup and is necessary to develop the required technologies for the Einstein Telescope.

7.2. The Object of Interest: Input Mode Cleaner

For the measurement campaign, the reflection of the input mode cleaner is chosen. As the construction of the ET Pathfinder is still in progress, the laser injection tower

and beam splitter tower were not ready for the scheduled campaign. Therefore, a copy of the input mode cleaner is installed on the optical table, which also hosts the input stabilised laser [116] in the laser safety area of the clean room. The objective stays the same. It even allows for more extreme detuning of the cavity, as a loss of alignment can be readjust on the bench, whereas in vacuum this should not be risked.
An illustration of the entire optical setup surrounding the input mode cleaner can be seen in Figure 38. The prestabilised laser of output power of 70 mW is focused with lenses L1 and L2 to fit the aperture of the EOM, which modulates sidebands of 12.3 MHz onto the laser frequency. In front of the EOM, 10 % of the power is coupled out of the system to later create the frequency-shifted reference beam for the phase camera by coupling the beam into the fibre-coupled AOM. After the EOM, the beam is mode matched by lenses L3 and L4 to match the normal modes of the cavity. To control the cavity, photodiode PD1 monitors its reflection to generate the error signal for PDH locking. 90 % of that reflected power is then again coupled out and redirected to the phase camera as the signal beam. PD2 can be used to monitor the cavity transmission.

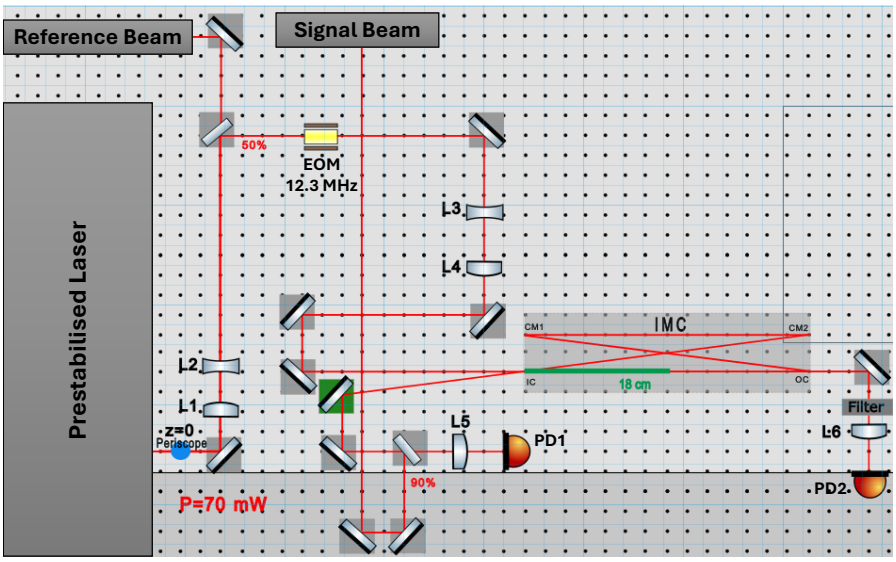

Figure 38: Optical Setup of the prestabilised laser, input mode cleaner and the auxiliary optics to operate it. Two additional beam splitters are used to create the signal and reference beam for the phase camera to analyse the reflection from the input mode cleaner. Adapted from [117].

The input mode cleaner is bow a tie cavity with an optical path length inside of $\approx 1.4\,\mathrm{m}$, with a flat input and output mirror of 99.40 % reflectivity, two curved mirror of 99.99 % reflectivity and a curvature radius of 3 m. This results in a finesse

of $\mathcal{F} = 395 \pm 65$ with a free spectral range of (201 ± 21) MHz and a FWHM of $\Delta\nu = (510 \pm 65)$ kHz [118]. It can be stabilised over several minutes by applying PDH locking with 12.3 MHz sidebands. Thermal drifts can de-lock the cavity as the dynamic range of the adjusting piezo attenuator saturates.
For measurements dominated by the TEM_{00} mode, the cavity is unlocked and fully reflects the power. To observe HOMs, it is locked and the input coupling is perturbed (Section 3.8). Therefore, the TEM_{00} is mainly transmitted through the cavity while the HOMs are reflected. Over the course of this campaign, the input coupling is intentionally worsened to increase the content of higher-order modes.

7.3. Beam Preparation

For measurements with the phase camera, the beams have to be prepared to meet its specifications for size and curvature. An illustration is given in Figure 39.

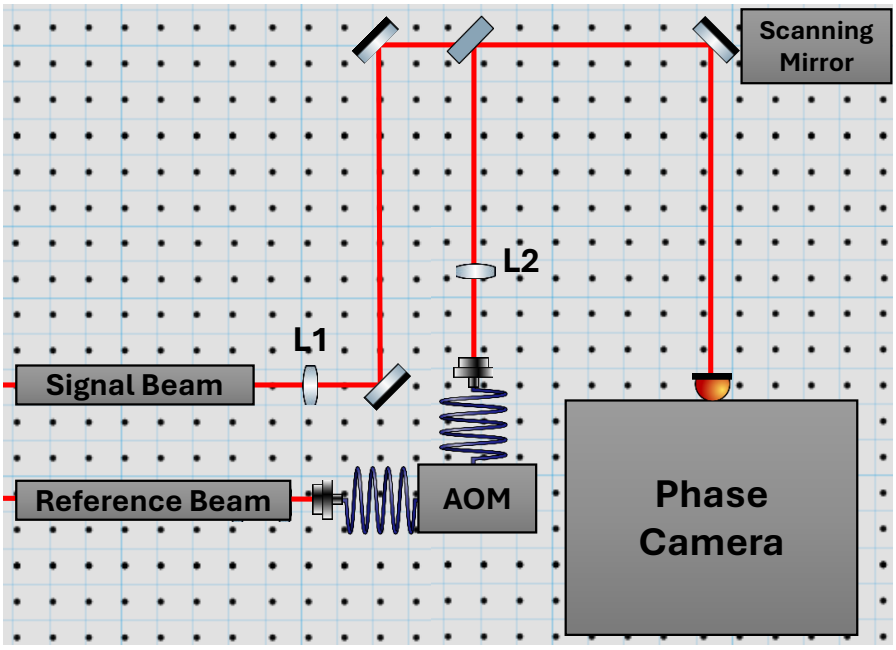

Figure 39: Optical Setup of the fibre-based phase camera itself. While lens L1 is permanent to adjust the oversized signal beam, L2 can be varied to test different limits of the phase camera. Created with [119] and [117].

The reference beam is coupled into the fibre-coupled AOM via a Thorlabs TC12APC-1550 collimator. This shifts the beam frequency by 80 MHz and then collimates it again by the same model. As the signal beam is too large in diameter, a convex lens (L1) of focal length of 750 mm is inserted 173 cm in front of the camera. Both are recombined at the beam splitter in front of the scanning mirror. A lens (L2)

can be implemented to adjust the reference beam. Depending on the conditions of the cavity, the signal path has a total power between 15 and 27 mW, while the reference beam after the AOM has 4.2 mW.
Two different reference-beam configurations are used to test the fibre-based phase camera. Configuration A, with L2 at 68.5 cm with a focal length of 50 mm, tries to minimise the impact of the reference beam on the depicted images by choosing a large waist size and curvature at the camera in comparison to the signal beam. The disadvantage is the low SNR of the images as the power density is very low. Configuration B, with no extra lens, tries to counteract this by running a reference beam with only slightly larger waist size at the camera. But the resulting difference in curvature yields very steep phase maps, which can be difficult to interpret when the phase difference between pixels exceeds π.
To determine whether the depicted waveform images match expectations, the signal and reference beam to the camera for both setups are characterised. The waist sizes of both beams are measured along the optical paths using the Thorlabs BP209IR beam profiler. At any measuring point, three independent measurements of the width are done to estimate the overall error. By fitting the waist size along the optical path, the curvature can be reconstructed.

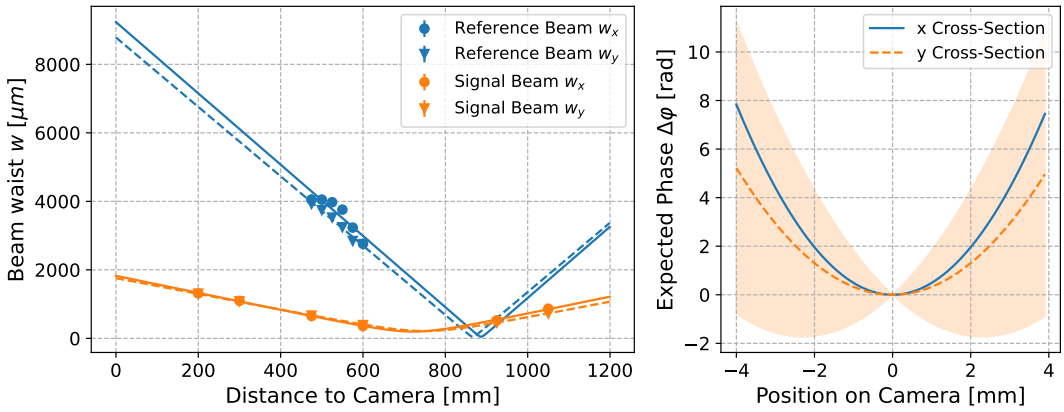

Figure 40: Left: Beam width in x and y direction for both the signal and reference beam in configuration A and the resulting fit. Right: The expected phase cross-section if measured at the phase camera as a result of the expected curvatures of both beams. For the cross-section in the y direction, the expected error is introduced as a semi-transparent area.

The results for configuration A can be seen in Figure 40 on the left. While the signal beam is probed evenly around the minimal waist size w_0, the reference beam could only be probed at certain positions due to restrictions of the optical layout. Because this waist distribution is generated by lens L2, the approximate position of

w_0 is known, which drastically improves the fit. The fit parameters for both beams in the phase camera relevant y dimension can be seen in Table 1. From there on, the expected width and phase measured with the phase camera for a Gaussian beam in TEM_{00} can be calculated. The results are in Figure 40 on the right.

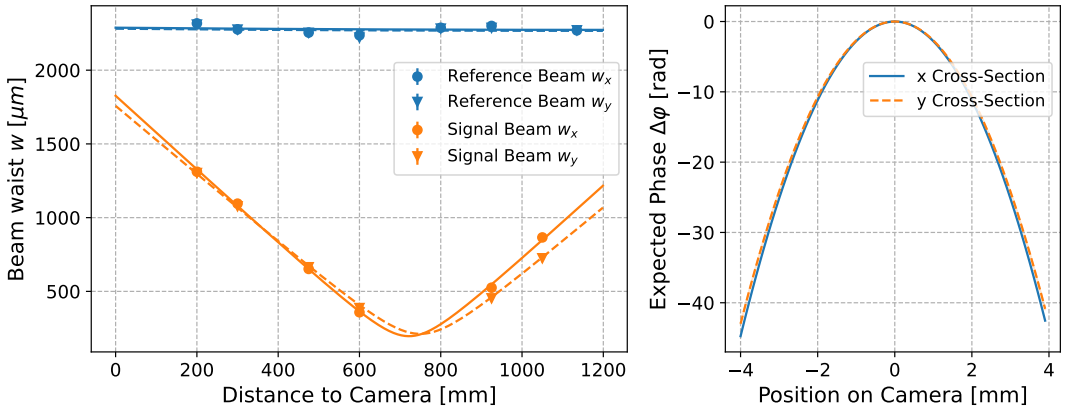

Figure 41: Left: Beam width in x and y direction for both the signal and reference beam in configuration B and the resulting fit. Right: The expected phase cross-section if measured at the phase camera as a result of the expected curvatures of both beams.

Table 1: Fit values waist position z_0 and waist size w_0 for the waist diameter fit of the Gaussian beams and the extrapolated waist size $w_0(z_{\mathrm{cam}})$ and curvature $R(z_{\mathrm{cam}})$ at the phase camera.

	Signal Beam	Reference Beam A	Reference Beam B
z_0 [mm]	750 ± 9	900± 600	1040 ± 20
w_0 [μm]	212 ± 3	49 ± 12	2330 ± 13
$w_0(z_{\mathrm{cam}})$ [μm]	1760 ± 20	9000 ± 6000	2340 ± 13
$R(z_{\mathrm{cam}})$ [mm]	761 ± 9	900 ± 600	106900 ± 20

The same is done for configuration B and can be seen in Figure 41 on the left. The fit parameters are again given in Table 1 for the y dimension. Only the reference beam changed in shape as lens L2 is removed from the optical setup. Again, the measurement points probing the reference beam are restricted as the waist of it is 12 mm in front of the collimator. Additionally, they are rather precise, leading to fit errors that are larger than the parameters. A comparison with the manufactured stated waist position and size showed no significant difference. Nevertheless, the phase camera measurements show a significant difference. More on that in Section

7.4.1. On the right of Figure 41, the expected phase at the phase camera can be seen. Much steeper than that of configuration A. The display of the expected error is waived.

7.4. Static 1D Measurements

Before analysing the phase and amplitude images taken by the fibre-based camera, the phase images must be corrected for phase shifts introduced by different trigger delays between the digitiser (see Section 6.5). An example can be seen in Figure 42, in blue, with the digitiser of each pixel mapped to a different marker. Taking only the Spectrum equipped pixel, the expected phase from Figure 40 can be seen. The same is true for the TARGET evaluation boards SN0001 and SN0002, but each is shifted differently in phase in relation to the Spectrum cards.

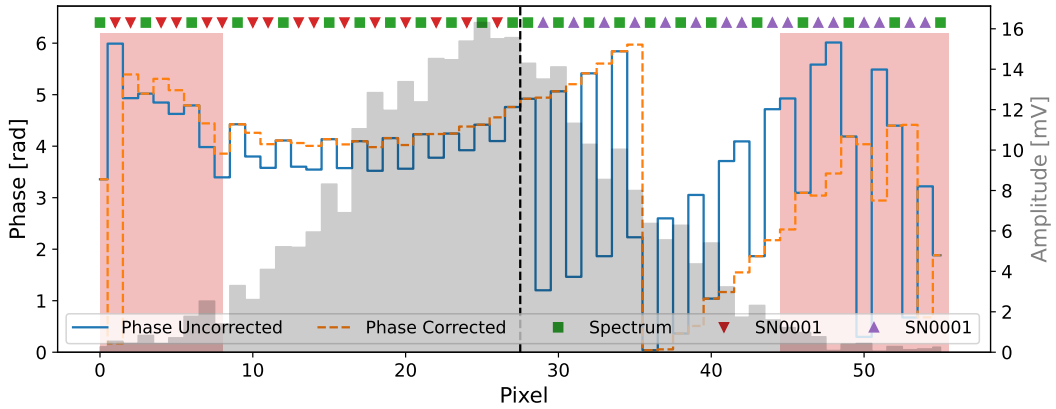

Figure 42: Illustration on how the different trigger delays between the digitisers lead to different phase offsets. In blue, the uncorrected phase image. The phase offset between pixels corresponds to the digitiser of the pixels, which is marked on the top. For the correct application of the algorithm, low-amplitude pixels are excluded, which can be seen from the superimposed grey amplitude distribution of the beam and the red-marked area, which indicates the excluded pixels.

As the trigger delays were unfortunately not measured at the ET Pathfinder, the phase shift is handled in software. For each measurement run and demodulation frequency, the phase shift is determined by adding a phase shift to only the TARGET specific pixel in a range of 2π. Because the phase resolution of pixels depends on the observed amplitude, low-amplitude pixels at the edges of the image sensor are excluded. The phase offset where the standard deviation of the difference between selected high SNR pixels is minimal is then the searched phase offset. This can be seen in Figure 42 with the amplitude across the image in grey and the

excluded pixel in the red area. The flatter the observed phase curvature and the higher the phase resolution, the better this algorithm performs. Manual tweaks were still necessary for some images. In future, the trigger delays of each TARGET CTC ASIC will be adjusted by firmware. To improve the interpretability of the images, jumps due to the modulo 2π nature are corrected.

7.4.1. TEM_{00} Measurements

For the measurement of dominantly TEM_{00}, the observed cavity is unlocked. Each displayed 1D measurement runs contains 10 s of data recorded at a trigger rate of 200 Hz. The TEM_{00} measurement of beam configuration A is displayed in Figure 43 for both sidebands and the carrier in phase and amplitude. For better visibility, only every 100th image is shown, and colour indicates the position in time, starting with blue and ending with yellow. In black, the expected phase and amplitude calculated in Section 7.3. As no amplitude calibration of the phase camera has been implemented and the accurate coupling factor of the fibre array is unknown, the expected amplitude is matched to the height of the measured amplitude for comparability. Nevertheless, one can compare the width of the measured amplitude distribution to the expected one.
The low power in the sidebands results in a general low SNR in both amplitude and phase. Taking the mean over multiple images, the phase is reconstructable with reasonable precision, where the amplitude can be distinguished from the baseline noise of the camera. Measurements close to the detection limit of the phase camera are therefore possible by integrating multiple images at the cost of a lower frame rate. For the carrier, detected at an order of magnitude higher amplitude, this is no longer required. It can also be concluded that the state of the observed beam does not significantly change in characteristics over the 10 s measurement period. A slight asymmetry in detected amplitude in the sidebands is detected, which can directly be introduced by the EOM. From visual analysis, the measured phases and amplitudes are in good agreement with the expected values. To quantify this statement, the measured mean phase $\Delta\phi$ and width of the amplitude Δw are fitted by

$$\Delta\varphi = \frac{2\pi}{\lambda}\left(\frac{(y-y_{0,sig})}{2R_{sig}} - \frac{(y-y_{0,ref})}{2R_{ref}}\right) \tag{7.1}$$

$$\Delta w = A\exp\left(-\frac{(y-y_{0,sig})}{w_{sig}}\right)\exp\left(-\frac{(y-y_{0,ref})}{w_{ref}}\right) + O \tag{7.2}$$

with λ the wavelength, y the position of the camera, $y_{0,sig}$ and $y_{0,sig}$ the mean position of the beams in the camera, R_{sig} and R_{ref} the respective curvatures, w_{sig} and w_{ref} the respective width, $A = |P_{sig}||P_{ref}|$ the mixed amplitude of both beams

and O to attribute the baseline noise. This is directly derived from Equation 3.9 and 4.5.

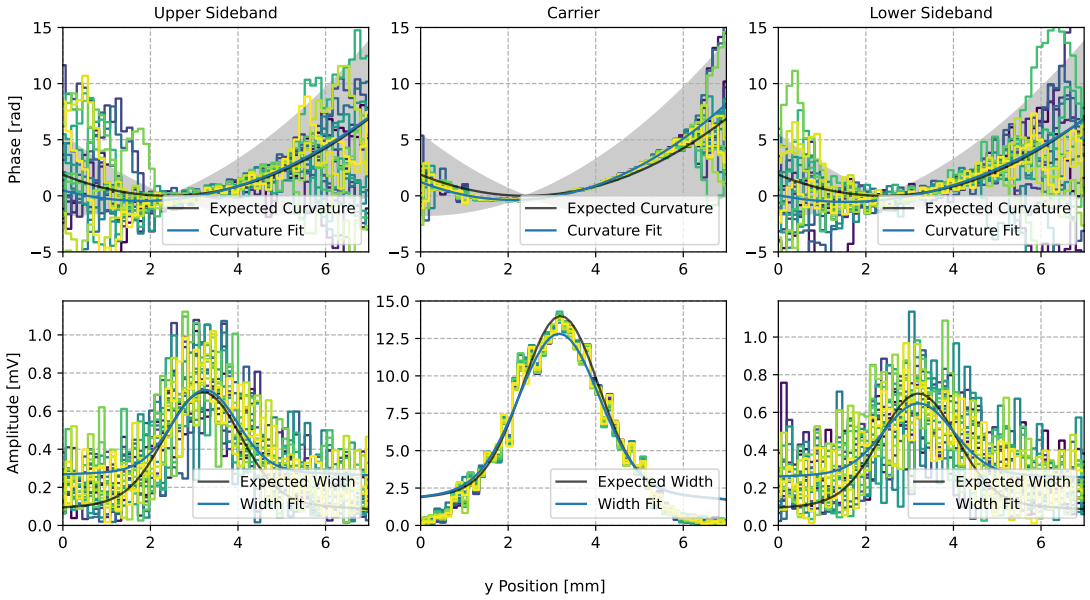

Figure 43: Phase and amplitude images of beam configuration A for both sidebands and the carrier. The expected curve shape in black with its standard deviation in grey is introduced in Section 7.3. The fit functions are provided in Equation 7.1 and 7.2 with the fit results displayed in Table 2.

Table 2: Fit values of Equation 7.1 and 7.2 for beam configuration A are displayed in Figure 43. For easier readability, the expected values from Table 1 are also displayed.

	Upper Sideband	Carrier	Lower Sideband	Expected
Curvature [mm]	800 ± 300	750 ± 40	800 ± 200	750 ± 9
Width [μm]	1888 ± 5	1949 ± 3	2340 ± 12	1760 ± 20

As different combinations of R_{sig} and R_{ref} lead to the same measured $\Delta\varphi$, the assumed R_{ref} has to be inserted as a parameter. The same is true for Δw with w_{sig} and w_{ref}. An overview of the fitted values is given in Table 2 with the expected values for comparison. For the reconstructed curvature of the signal beam, the fitted values are in good agreement with the expected values. Not so much for the amplitudes, where some systematics impair the results. Starting with the carrier, the most prominent feature of the expected and fitted curves is the shallow flanks on both sides that are not visible in the measured data. This suggests that the

assumed reference beam is larger than expected. The second feature that stands out is the systematic up-down structure of the measured amplitude itself, which can be traced to the different digitisers. A flat-field intensity to digitised amplitude calibration is advised to eliminate this systematic. Looking at the sidebands, the amplitude is barely distinguishable from the baseline noise. This skews the fit results due to the bad SNR.

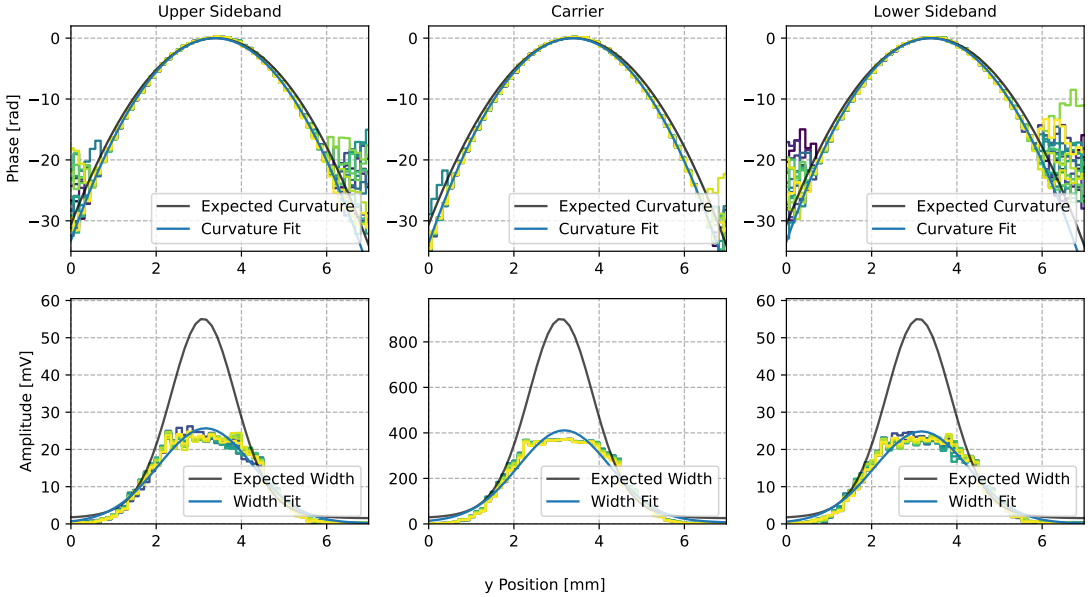

Figure 44: Phase and amplitude images of beam configuration B for both sidebands and the carrier. The expected curve shape in black with its standard deviation in grey is introduced in Section 7.3. The fit functions are provided in Equation 7.1 and 7.2 with the fit results displayed in Table 3.

Table 3: Fit values of Equation 7.1 and 7.2 for beam configuration B are displayed in Figure 44. For easier readability, the expected values from Table 1 are also displayed.

	Upper Sideband	Carrier	Lower Sideband	Expected
Curvature [mm]	700 ± 30	691 ± 25	700 ± 60	750 ± 9
Width [μm]	6500 ± 2000	5000 ± 600	6000 ± 1500	1760 ± 20

The same measurement and analysis is redone for beam configuration B and can be seen in Figure 44. The measured phase curvature is systematically smaller than expected across all radio-frequency components. Comparing the fit values in Table 3 comes to the same conclusion. As the reference is approximately a planar wave

of a collimated beam, its curvature is not sensitive to systematics. Hence, the observed phase curvature mirrors that of the signal beam. It is therefore concluded that the observed systematics are from the beam characterisation done in Section 7.3.
In the amplitude images, something interesting happens. The transimpedance amplifier of ET-0002 (see Section 4.5.2) saturates as there is too much DC laser power. Therefore, the amplitude distribution looks cut off. A correct reconstruction of the beam width via Equation 7.2 is therefore not possible, as seen in Table 3.
So far, both beam configurations have had problems in properly depicting the amplitude image, either by too much or too little signal. In the phase image, beam configuration B is more accurate, as the curvature of the collimated reference beam can be approximated as a planar wave. Therefore, the reference beam does not have to be precisely known, reducing the degrees of freedom of the fit. The observed systematics can be fully attributed to the beam characterisation with the beam profiler. Using this configuration in the future, one has to keep in mind that the observed phase difference between pixels must remain below π for interpretability and, of course, less power.

7.4.2. HOM Measurements

For the HOM measurements, the cavity is now locked and hence reflects less power. An analysis of beam configuration A is therefore skipped as the sidebands are barely observable. The evidence that the phase camera is capable of measuring HOMs can also be shown at the example of beam configuration B alone as seen in Figure 45. In the amplitude images, the carrier is clearly dominated by the presence of HOMs as the fundamental mode is resonant in the cavity and mainly transmitted. At the same time, the sidebands fully reflect and are therefore in the fundamental Gaussian mode. The asymmetry in sideband amplitude persists. A fit of HOMs and, therefore, mode decomposition of the carrier is provisionally skipped as the commissioning of the phase camera is prioritised in this work. But here the power of the phase camera shows, each radio-frequency component can be analysed individually in parallel. The HOMs of the carrier do not interfere with the imaging of the sidebands.

Table 4: Fit values of Equation 7.1 and 7.2 for beam configuration B displayed in Figure 45. For easier readability, the expected values from Table 1 are also displayed.

	Upper Sideband	Carrier	Lower Sideband	Expected
Curvature [mm]	700 ± 300	700 ± 100	700 ± 300	750 ± 9
Width [μm]	2287 ± 4	-	2011 ± 3	1760 ± 20

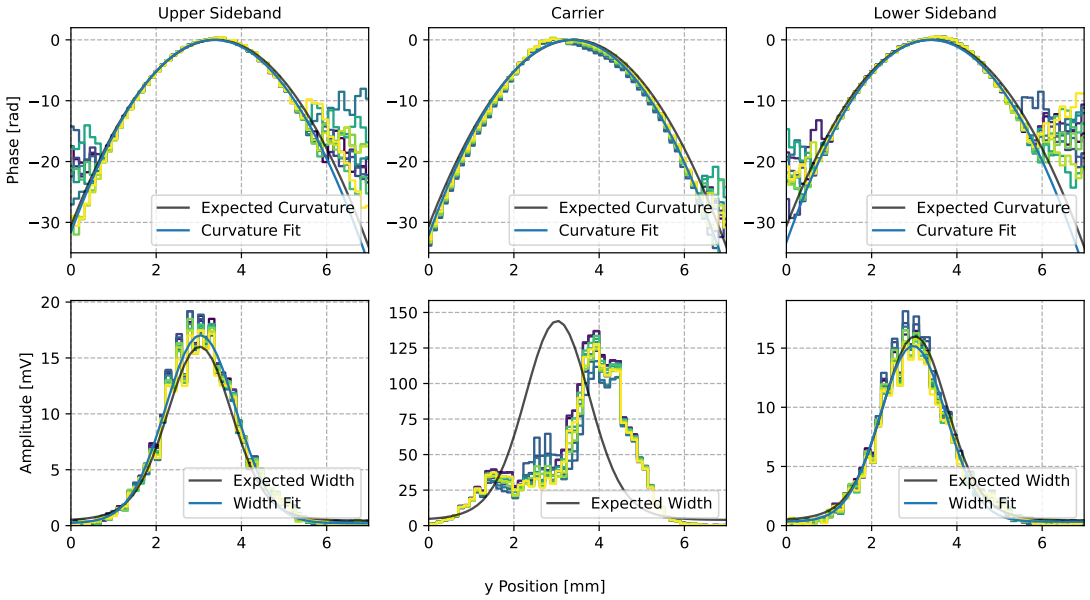

Figure 45: Phase and amplitude images of beam configuration B for both sidebands and the carrier. The expected curve shape in black with its standard deviation in grey is introduced in Section 7.3. The fit functions are provided in Equation 7.1 and 7.2 with the fit results displayed in Table 4.

In the phase images, the carrier shows clear deviations its expected phase as expected, since the expected phase is derived from a Gaussian beam in the fundamental mode. In the upper sideband, the phase behaves as expected, whereas in the lower sideband, similar deviations to those in the carrier are visible. At this point, it is uncertain to what extent these deformations are due to HOMs or different systematics. Nevertheless, these deformations are also reflected in the error of the fit values for the phase seen in Table 4. On top of that, there are the too-wide fitted amplitudes, which are more probable due to the systematics of the beam characterisation.

7.4.3. Cavity Locking

To showcase the use case of the fibre-based phase camera as a monitoring tool, the cavity locking is changed while the phase camera operates. The measurement run with every 200th image for clarity can be seen in Figure 46 for the carrier. As this was done with beam configuration A, the SNR in the sidebands is too low for an accurate interpretation. But this also highlights the advantages of a flatter phase curvature, as the phase deviations from the fundamental mode are more pronounced than in beam configuration B.

Two distinct amplitude distributions can be observed with some images of the transition itself. This can also be observed in the phase image, though it appears as three. Due to the mode composition and, therefore, the power being close to zero between peaks of the images in the earlier state (teal), the correction of the 2π modulo nature of the phase fails due to the low phase resolution. Therefore, the same phase configuration splits into two phase curvatures with 2π difference in phase at the minimum of the amplitude.

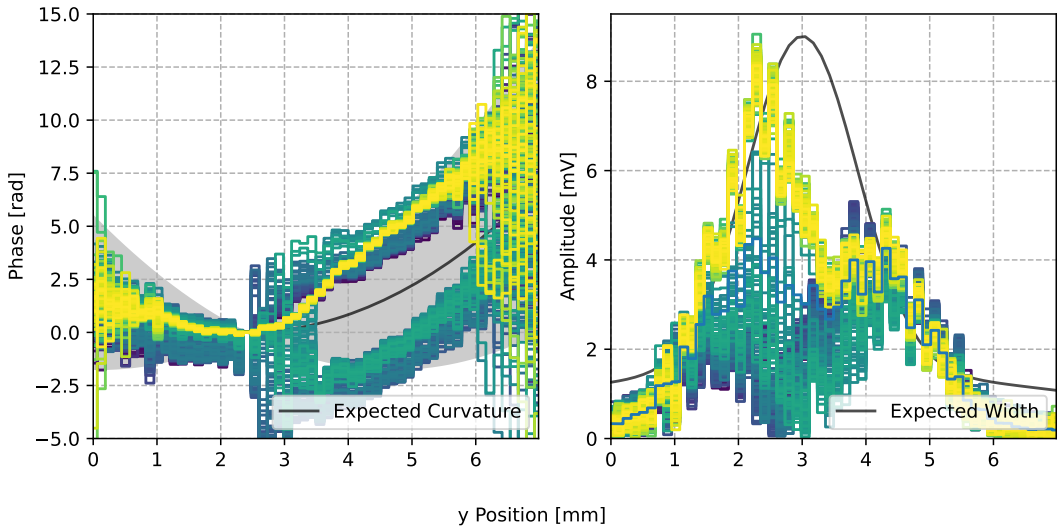

Figure 46: Phase and amplitude images of beam configuration A for both sidebands and the carrier. The position in time of an image is indicated by the colour, starting with blue and ending with yellow. The expected curve shape in black with its standard deviation in grey is introduced in Section 7.3.

7.5. 2D Images

To create 2D depictions of the wavefront, the recombined beam of the reflected cavity and the reference beam are scanned horizontally over the vertical 1D array. To facilitate this scanning, a step motor is used. On the moving axis of the motor, a custom-designed, 3D printed casing is mounted, which hosts a one-inch lens tube. A mirror is mounted in the lens tube using two screws.
With 32 pixel digitised by the TARGET evaluation boards, the trigger rate is limited to 200 Hz. Therefore, the scanning process has to be slow enough to ensure spatial resolution along the x-axis. Frame rates of order < 1 Hz are expected, enough to monitor HOMs and thermal drifts.

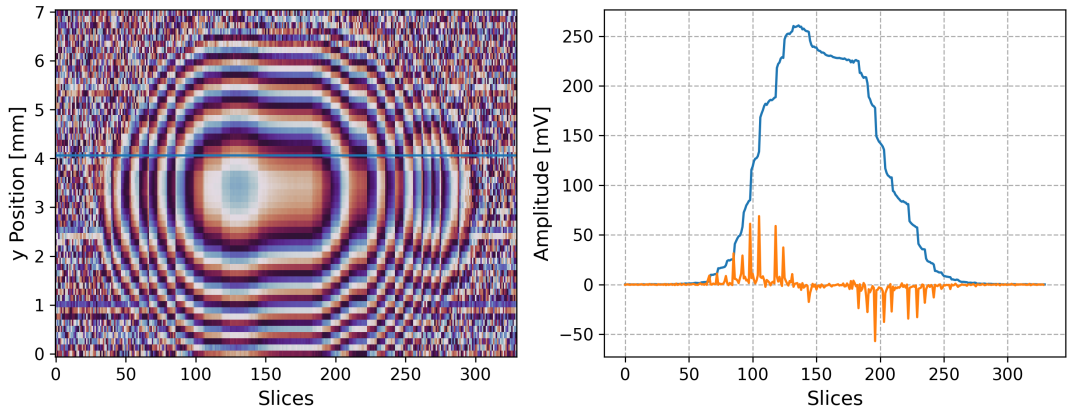

Figure 47: Left: A pseudo 2D phase image of a Gaussian in fundamental mode created by scanning the beams horizontally over the vertical 1D fibre array. The irregular movement of the step-motor-based scanner causes artefacts in the horizontal direction. Right: The associated horizontal amplitude cross-section of the amplitude of pixel 33 marked as a blue line on the left image. In orange, the associated derivation of the amplitude to determine the stepping of the scanner.

The scanning process is of low quality, because the stepping motor configuration was not optimal. Therefore, the rotation between steps is irregular. An example can be seen in Figure 47 on the left. The concentric circles one would expect from a Gaussian beam in fundamental mode are, at some point, elongated or cut. On the right, the associated horizontal amplitude cross-section of pixel 33 is shown, with its derivation in orange. Here, the individual steps of the stepping motor are visible in amplitude or as spikes in the derivation. Some steps take longer than others, some shorter, and all share that the amplitude drifts at each step, suggesting that the motor never truly stops.
To fix these artefacts in first order for the images taken during the campaign, the derivation of the pixel with the highest mean amplitude is used. If the distance between two spikes is greater than the normal/expected distance, the surplus is cut from the 2D images. This is, of course, a very simple correction, and by no means perfect, but sufficient for the here presented analysis. A reconstruction of the x-axis to mm is also left out to avoid unnecessary assumptions. If there will be a scanning 1D fibre-based phase camera, a better-suited motor has to be used, and the true position of the scanner has to be monitored.
For all the images presented here, beam configuration B is used.

7.5.1. TEM_{00} Measurements

An exemplary pseudo-2D image of all sidebands in phase and amplitude of a Gaussian beam in the fundamental TEM_{00} mode can be seen in Figure 48. Some artefacts in the horizontal are still visible in the phase images due to the basic correction technique. Additionally, the steep phase curvature in the phase images, together with the scanning steps of the step motor, results in a Moiré pattern to the left and right of the expected concentric circles of the phase wavefront. In amplitude, the different gains of the digitiser are clearly visible, as already observed in the 1D images.
To analyse the waveform deformations in the phase image, the different radio-frequency components phase images are subtracted from each other as seen in Figure 49. This method is introduced in 7.4 to originally negate the time-dependent phase noise due to fluctuations in the optical path length of the reference beam. However, this can also be used as a measure of how much the wavefronts in each radio-frequency component differ from one another. In the case discussed here, where the reflection of an input mode cleaner is measured, the sidebands should always remain in the fundamental mode as they are fully reflected. Therefore, they are a perfect measurement of the HOMs present in the carrier. For the TEM_{00} measurement, a flat response is expected and observed for all image combinations, as all three radio-frequency components are in the fundamental mode. The visible stripes are due to the phase shift corrections of the different digitisers, introduced in Section 49. Slight deviations can be observed in the middle of each subtracted image, suggesting a different coupling of the radio-frequency components into the cavity before they are fully reflected.

7.5.2. HOM Measurements

The phase and amplitude image for an exemplary HOM measurement can be seen in Figure 50. The most striking feature is that the amplitude image of the carrier is clearly dominated by HOMs, as it is, to first order, rotation symmetric, it is best described in the basis of Laguerre-Gaussian modes. The asymmetry was also observed using a detector card and is not a property of a poorly aligned reference beam. While both sidebands should not resonate in the input mode cleaner, the lower sideband also shows deviations from the fundamental Gauss mode in the amplitude image, suggesting a contribution from HOMs due to the cavity misalignment. Taking a look at the associated phase image reinforces the argument, as clear deviations of the concentric circles of a Gaussian mode in fundamental mode are visible. Although the correction of the scanning step motor is not of excellent quality, deformations in the vertical axis across the image give the HOMs influence away.

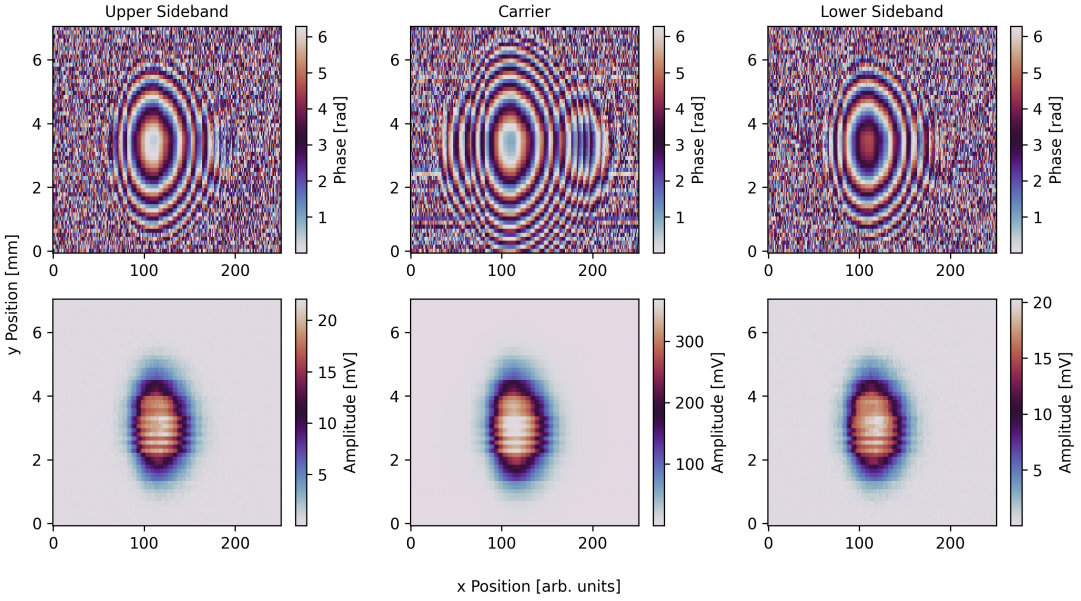

Figure 48: Pseudo 2D phase and amplitude images of beam configuration B for both sidebands and the carrier in the fundamental TEM_{00} mode. The additional concentric structures, left and right in phase, are a Moiré pattern due to the ratio between the phase curvature of the wavefront and the pixel width in the x-direction.

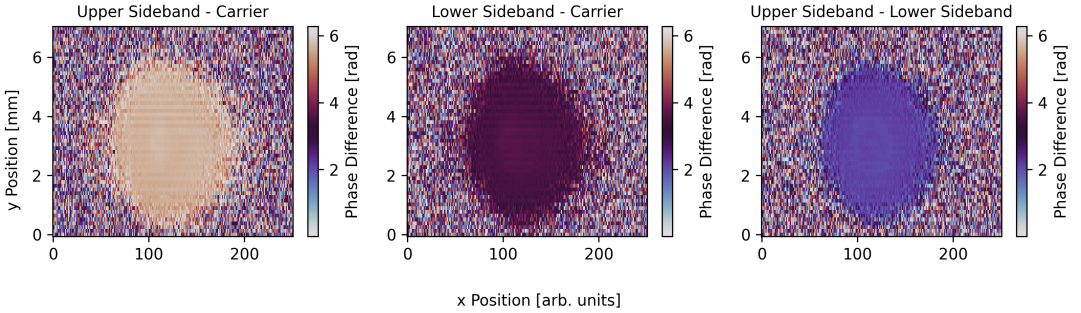

Figure 49: Subtracted phase images of the TEM_{00} measurement in Figure 48. The visible stripes are due to timing differences of the trigger between the three digitisers that are not fully corrected.

The wavefront deviations is measured by subtracting phase images and can be seen in Figure 51, for higher-oder mode measurements. A clear difference between the wavefronts of the sidebands to the carrier can be seen, as expected. The difference in the amplitude image of the sidebands is also visible in the phase when they are subtracted from each other. Again, the different frequencies of the beam couple differently to cavity. The phase camera can reveal and measure such asymmetries.

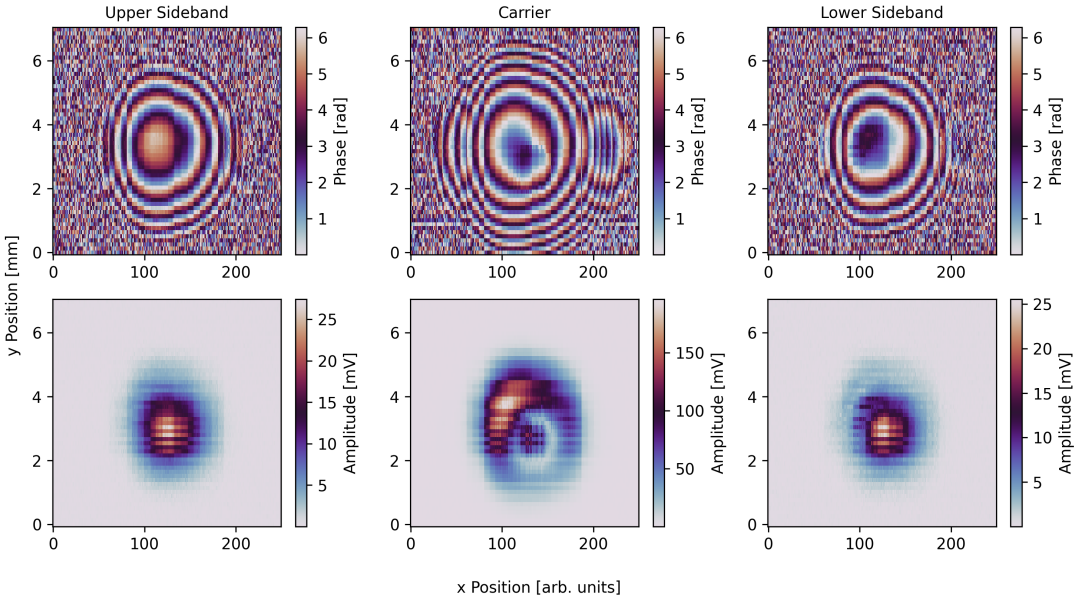

Figure 50: Pseudo 2D phase and amplitude images of beam configuration B for both sidebands and the carrier dominated by HOMs. The irregularities in the horizontal are due to the additional concentric structures left and right in phase, which is a Moiré pattern due to the ratio between the phase curvature of the wavefront and the pixel width in the x-direction.

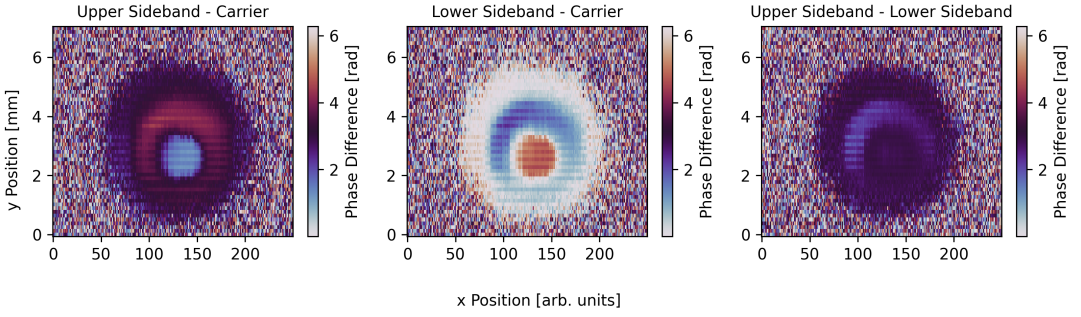

Figure 51: Subtracted phase images of the TEM_{00} measurement in Figure 50. The visible stripes are due to timing differences of the trigger between the three digitisers that are not fully corrected.

8. Summary and Outlook

For the direct detection of gravitational waves with an interferometer, different radio-frequency components in the laser beam are necessary for the signal generation, such as the length locking of certain cavities. Mode mismatches in cavities or wavefront aberrations in these radio-frequency components lead to the excitation of higher-order Gaussian modes, deteriorating the instrument response. A wavefront monitoring tool is needed to trace down the origins of these deviations. One of these wavefront-sensing tools is a phase camera that simultaneously observes the spatial amplitude and phase of the wavefronts of all radio-frequency components.

In this work, the concept of a phase camera was enhanced by the integration of the novel approach of using an optical multimode fibre array as a static 2D image sensor. For its development, an optical setup for testing and operating the camera was successfully implemented. The usability of the fibre array was evaluated and verified in terms of phase propagation and cross-talk in the context of the phase camera.
Due to the low coupling efficiency of the fibre array, a new high-gain, high-bandwidth, low-noise amplifier board with an integrated photodiode was developed. This resulted in a board capable of detecting optical beatings (the measurement signal of the phase camera) with an ample gain of $\approx 110\,\mathrm{dB}$, a bandwidth of $240\,\mathrm{MHz}$, and a noise floor of $-105\,\mathrm{dBm\,Hz^{-1}}$.
To evaluate the developed signal chain, the first 24-pixel version of the phase camera based on the commercially available Spectrum Instrumentation M4.4451-x8 digitising cards was constructed. The software framework *ETscripts* was established to operate and analyse data of the phase camera, managing the data flow from raw waveforms of individual pixels to complete 2D phase and amplitude images.
The amplitude resolution could be verified to match the expected values below $1\,\mathrm{mV}$ over all specified signal powers. For the phase resolution, it was shown that the limiting factor of it is not the signal chain itself, but length fluctuations between the signal and reference beam of the auxiliary optics. The phase noise spectrum was analysed, and noise sources, such as vibrations of the optical setup or thermal effects, could be successfully mitigated. A minimal phase resolution of $\leq 3 \times 10^{-2}\,\mathrm{rad}$ was achieved. Additionally, the method of relative-phase measurements between radio-frequency components was exemplified to further improve the phase resolution. Here, only the integration time and signal power limit the performance.
To study the viability of the large-scale variant of the phase camera, the TARGET ASIC CTC is successfully implemented as a cost-efficient digitiser in the form of a 56-pixel proof-of-concept phase camera. The waveform acquisition of the single-photon-detection-optimised ASIC was matched to the specifications of the phase camera. The ample phase resolution of $\leq 3 \times 10^{-2}\,\mathrm{rad}$ could also be achieved

with the ASIC. Frame rates up to 200 Hz could be verified with a theoretical ceiling of 270 Hz.
In a commissioning study at the ET Pathfinder, the capability of measuring the mode content of all available radio-frequency components simultaneously could be successfully proven. The correct depiction of the wavefronts in amplitude and absolute phase was shown in the context of the observed systematics. Absolute amplitude and relative phase measurements demonstrated the phase camera's ability to visualise the higher-order mode content.

With the successful commissioning of the proof-of-concept fibre-based phase camera, the full-scale 4096-pixel version can now be tackled. A new multimode fibre array of 4096 individual fibres will be procured. The plan is to use at least 64 pixels in the x and y axes, and a spiral going outward as a cost-efficient but performant interim solution that can be extended at any time to the full 4096-pixel version. The high pixel count will then also allow the separate use of the Spectrum Instrumentation digitiser cards to monitor time-dependent high-speed noise up to several MHz in parallel to the spatial mapping of the wavefront with CTC.
Furthermore, the demodulation of the raw signal to obtain phase and amplitude information will be implemented on FPGA basis to handle the increased data stream and to enable real-time sensing. With the now established signal chain consisting of the high-gain, high-bandwidth, low-noise amplifier circuit ET-0002 and CTC, dedicated hardware, including the FPGA, is possible for convenient use in the laboratory. The phase resolution could potentially be further improved by modifying ET-0002 by a notch filter to adjust the amplitude of the carrier to the sidebands. Therefore, the SNR of all radio-frequency components could be increased without the carrier saturating.

Overall, a fully functional fibre-based proof-of-concept phase camera has been established, further advancing the sensing tools required to achieve the sensitivities needed for gravitational wave detection.

Chapter II.
Characterising the Front-End-Electronics of the Small Sized Telescope of CTAO

9. Introduction

The idea of gamma-ray astronomy began around the 1950s, when radio and X-ray astronomy opened a new "window" to observe the universe [120, 121]. The gamma-ray window was seen as an opportunity to resolve the non-thermal sources of the isotropic cosmic-ray flux. With an opaque atmosphere for gamma rays, ground-based instrumentation seems off at first and indeed, the first breakthrough in gamma-ray astronomy was made in 1968 with the OSO-3 satellite mapping the gamma-ray sky. However, the limited size of satellites restricts the detector area to measuring the low flux of gamma rays above several hundred GeV. Using and understanding the atmosphere as part of the ground-based detector can negate this limitation. When it interacts with the atmosphere, the incident gamma-ray creates a cascading shower of particles that emit Cherenkov light, which can be detected on the ground. Therefore, the effective detector area is of the size of the diameter of the emitted light cone, which is about 250 m.

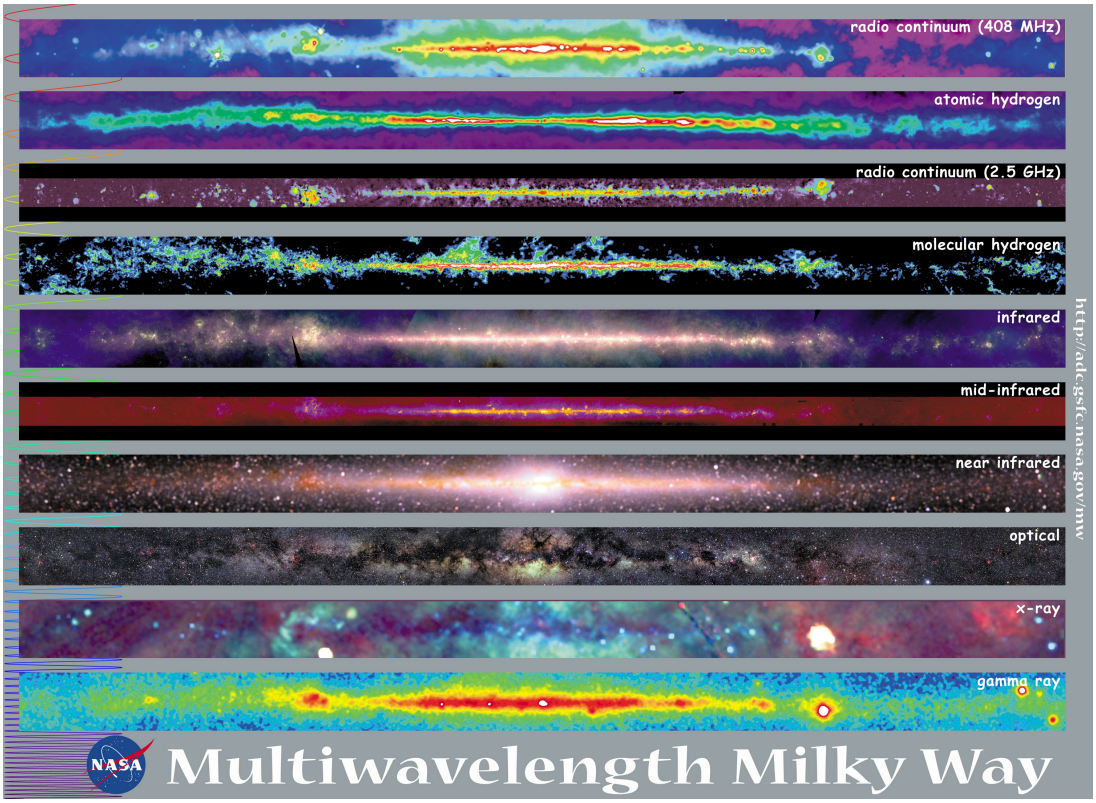

Figure 52: The Milky Way imaged across different wavelengths or "windows". Image taken from [122], image credit: NASA/CSFC.

The first pioneers of this technique were P.M.S Blackett, W Galbraith, and J.V. Jelley, measuring Cherenkov flashes with a 25 cm parabolic mirror, a 5 cm photomultiplier and a garbage can to shield stray light [120, 121]. Initially built as a proof-of-concept instrument to detect cosmic-ray-induced showers via Cherenkov light, they quickly realised the potential for gamma-ray detection.
In 1968, the first generation of Cherenkov telescope, the Whipple telescope on Mt. Hopkins in Arizona, with a dish size of 10 m and a photomultiplier with a diameter of 12.5 cm, began observing. The increased light-collecting area led to a 3σ detection of the first gamma-ray source, the Crab Nebula. But due to the high cosmic-ray background and systematics in the analysis, the result was controversial. Upgrading the single photomultiplier to a 37-pixel photomultiplier imaging camera enabled discrimination between gamma rays and cosmic rays based on their different detected shapes. This led up to the detection of the Crab Nebula at a significance of 3 to 5.6σ in 1989 [123]. Another major improvement was introduced by High-Energy-Gamma-Ray Astronomy (HEGRA) in 1992, the stereoscopic detection, imaging the shower with multiple telescopes, improving the shower reconstruction. Since then, the third generation of instruments e.g. High Energy Stereoscopic System (H.E.S.S.) [124], Very Energetic Radiation Imaging Telescope Array System (VERITAS) [125] and Major Atmospheric Gamma-Ray Imaging Cherenkov (MAGIC) [126] telescopes could increase catalogue of detected source above 50 GeV [127] to 300 objects. With the next-generational observatory CTAO already in the making, the boundaries of ground-based gamma-ray astronomy will be further pushed.

In this work, the author's contribution to the realisation of CTAO is presented in the form of the calibration and performance evaluation of the CTC and parts of the CT5TEA ASIC, the heart of the SST Camera. The challenges include accurately depicting of Cherenkov photon pulse amplitudes, which directly influence the energy reconstruction of the measured gamma rays. Critical performance parameters, such as the digitisation dynamic range and resolution, are improved by introducing new calibration techniques as well as advancing established ones. The major concern of the temperature-dependent performance of the camera is addressed by introducing in situ calibration routines for temperature-dependent performances. By testing different performance parameters, the suitability for Imaging Air Cherenkov Telescopes (IACTs) is evaluated and verified. Additional performance gains are made by the fine-tuning of the internal ADCs of the CTC ASIC.
Most results were already published in "CTC and CT5TEA: an advanced multichannel digitizer and trigger ASIC for imaging atmospheric Cherenkov telescopes" [21] and are here completed, enhanced and reordered for clarification of this thesis. The cited text passages are marked as follows "...".

The second part of this thesis is organised as follows. Starting with Section 10, the goals and principles of ground-based gamma-ray astronomy are introduced, beginning with the creation of extended air showers, their emission of Cherenkov radiation, and their detection with IACTs. This is accompanied by the introduction of the next-generation CTAO based on IACTs focusing on the camera design of the SST and its Front-End Electronics (FEE), the TARGET modules. The TARGET ASICs are introduced and described in the context of the camera.
Section 11 explains in detail the needed calibration steps to use the CTC ASIC to its fullest potential, based on the work on a specified evaluation board. This includes one-off calibrations in the laboratory as well as in-situ calibration techniques for readjustments during operation. New calibration routines are introduced, including Wilkinson ADC ramp tuning, block-dependent DC transfer functions, and the AC correction transfer functions, while established methods are reevaluated and improved. A temperature dependency analysis of calibration steps is included if necessary.
To maximise the potential, the fine-tuning of the Wilkinson comparator featured in CTC is explained in Section 12. In Section 13, the performance of CTC is evaluated, ranging from general criteria, such as power consumption, bandwidth, cross-talk, DC- and AC-noise, to IACT specific criteria. The suitability for IACTs is verified, followed by a summary in 14.

10. Ground-Based Gamma-Ray Astronomy

In this Section, the fundamentals of ground-based gamma ray astronomy with IACTs are introduced. The next-generation instrument CTAO is introduced along with an in-depth introduction to the SST and its camera electronics.

10.1. Key Science Topics of Gamma-Ray Astronomy

The science topics of gamma-ray astronomy are vast and diverse, ranging from the origin of cosmic rays to cosmological constrains and physics beyond the standard model. A small peek into the key topics shall be introduced. The selection follows the science goals of CTAO [128, 129], the next generation ground-based gamma-ray observatory. This section is by no means complete and is intended only as an overview to motivate why it is worth building such great instruments.

Understanding The Origin and Role of Relativistic Cosmic Particles

The origin of cosmic rays engages the science community since its detection in 1912 by Victor Hess [130]. Spanning over 12 orders of magnitude in energy, the cosmic ray spectrum consists primarily of hadrons. The flux is in first-order isotropic, as galactic and extra-galactic magnetic fields deflect charged particles, making the detection of sources by cosmic rays difficult. From the basic acceleration mechanisms of cosmic rays, it is known that gamma-rays are produced as by-products in both hadronic and leptonic scenarios. These gamma rays point straight to the acceleration region and are an important messenger for studying the origin of cosmic rays. In the hadronic scenario, neutral pions are generated by hadronic interactions, which promptly decay into two gamma-rays. In the leptonic scenario, gamma-rays are produced by the Bremsstrahlung, synchrotron radiation and inverse Compton scattering of accelerated electrons. Therefore, the cosmic ray population of the source can be probed by the spectral composition of gamma-rays. The excess of TeV gamma rays would pinpoint possible PeV accelerators and ultra-high-energetic cosmic-ray accelerators. By observing extended sources, the effects of cosmic-ray propagation on the interstellar medium can be studied, including their contribution to the generation of galactic magnetic fields, the growth of massive galaxies, and the chemical evolution of dense cloud cores.

Probing Extreme Environments

From the production of such high-energy particles, the existence of very extreme environments can be inferred. An additional example would be the environment of

neutron stars or black holes. Compared with UV and X-ray emission, gamma rays can escape such environments and are therefore the optimal candidates for study these objects.
Certainly not well understood are, for example, black-hole-powered jets of stellar massive black holes or supermassive black holes of active galactic nuclei. Time-resolved very high-energy gamma-ray spectral measurements could provide insight into the innermost jets and their short-term variability, which no other spectral range can provide. They are also considered sources of ultra-high-energy cosmic rays. Identifying this as hadronic acceleration could majorly boost our understanding of these complex objects.
The coincident detection of a compact binary merger candidate of Laser Interferometer Gravitational-Wave Observatory (LIGO) and a 1.7 s delayed Gamma Ray Burst (GRB) with Fermi Large Area Telescope (FermiLAT) in August 2017 marked the beginning of gravitational-wave multi-messenger astronomy [131]. The link between short GRBs and neutron star mergerd could be observed. Alerts from gravitational wave observatories could be used in the future for full-time observation of fast-paced events, such as GRBs. Strategies to follow up such merger events with future ground-based detectors, such as CTAO, are already well established [132].
Cosmological models can be constrained by a characterisation of the extragalactic background light in cosmic voids, which captures the integrated emission of galaxies over all cosmic ages. An analysis in optical light is difficult as the Milky Way outshines it. However, the radiation field itself leaves an imprint in gamma-ray spectra that can be used to determine its characteristics and the magnetic field of these cosmic voids.

Physics beyond the Standard Model

Detecting cosmic particles up to energies two magnitudes higher than those of the Large Hadron Collider (LHC) opens the door to studies beyond the standard model, such as Lorentz invariance violations that are not feasible with classical collider experiments. These could be observed as energy-dependent time delays in gamma rays or changes in their spectral composition. These time delays would also lead to a non-trivial refractive index of vacuum, indicating quantum gravity effects[133, 134]. Even a negative result is worthwhile for guiding the theory section.
From the rotation curves of galaxies [135] to the mass and emitted light distribution discrepancy of the bullet cluster [136] or the structure formation of galaxies [137] (and more), the existence of dark matter seems imminent. The oscillations of the Cosmic Microwave Background (CMB) predicted that 27 % of the available energy of the universe must be bound in dark matter. Although the gravitational effect is

observed, the nature of dark matter itself is unknown. One of the most regarded ideas are Weakly Interacting Massive Particles (WIMPs). The self-annihilation of such WIMPs is speculated to create gamma-rays. A detection of gamma rays from a dark matter halo accompanying galaxies, for example, could be groundbreaking.

10.2. Electromagnetic Showers

When a gamma ray enters the atmosphere, it interacts with it by pair-producing an electron-positron pair in the vicinity of a Coulomb field of an atomic nucleus. Due to the high energy of the primary gamma-ray, highly relativistic electrons and positrons radiate Bremsstrahlung in the atmosphere. This Bremsstrahlung can also produce electron-positron pairs, and the cascading cycle continues until the particles fall below the critical energy threshold at which ionisation starts to dominate the energy loss. The electromagnetic shower comes to a halt. The same considerations also apply to cosmic electrons and positrons, although showers start with Bremsstrahlung rather than pair production. From an electromagnetic shower alone, it is not easy to distinguish between an electron and a gamma ray as the incident particle.

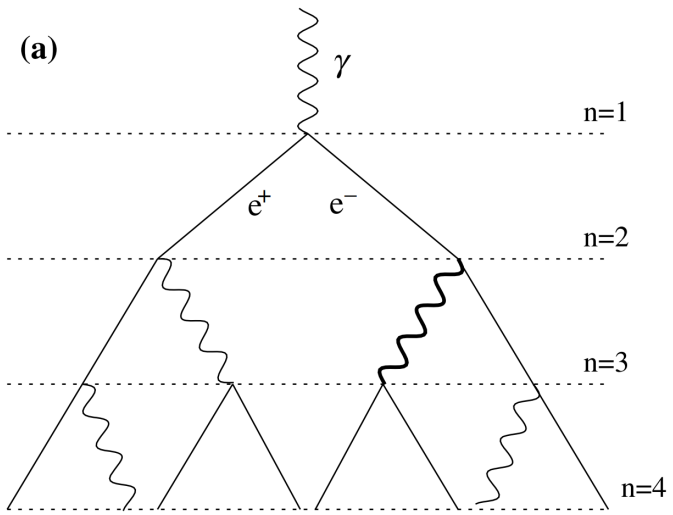

Figure 53: Illustration of the Heitler model with four steps, each separated by one radiation length. At each step, either Bremsstrahlung is emitted or a positron-electron pair is produced. Image taken and adapted from [138].

This simplified model can also be quantitatively described by the Heitler model [139] to calculate the expected number of particles as a function of the energy of the primary gamma-ray. As it assumes relativistic particles, the cross-section and, therefore, radiation length of Bremsstrahlung and pair production of electron-

positron pairs become identical [140]. Therefore, the cascade can now be quantified in n steps of radiation length X_{rad}, where the energy is evenly distributed over all particles in one step. An illustration is given in Figure 53.
After n-steps, the mean energy of an arbitrary particle is therefore given by $E = 2^{-n}E_\gamma$, where E_γ is the energy of the gamma-ray. The maximum number of particles N_{max} can then be derived by calculating the number of steps n_{max} until the energy of an arbitrary particle of a certain step equals the critical energy threshold $E_c \approx 85\,\text{MeV}$, where ionisation supersedes pair production in air [141]

$$n_{\text{max}} = \frac{1}{\ln 2} \ln\left(\frac{E_\gamma}{E_c}\right) , \tag{10.1}$$

which leads to $N_{\text{max}} = 2^{n_{\text{max}}}$ the maximum of amount of created particles. Translated into slant depth

$$X_{\text{max}} = X_{\text{rad}} \ln\left(\frac{E_\gamma}{E_c}\right) , \tag{10.2}$$

one can calculate the penetration depth of the shower into the atmosphere. For normal conditions, the radiation length is $X_{\text{rad}} = 37\,\text{g}\,\text{cm}^{-2}$ [141]. Using the barometric approximation for the atmosphere, the electromagnetic shower of a 1 TeV gamma ray, for example, reaches its maximum number of particles at $\approx 10\,\text{km}$ above sea level, assuming a zenith angle of 0°, and a first interaction altitude of $\approx 35\,\text{km}$ and has a maximum of approximately 12.000 particles.
The entire timescale of an electromagnetic shower is on the order of a few microseconds and occurs approximately along the trajectory of the incident particle. Coulomb scattering and the magnetic field of the Earth broaden the shower transversal. The confinement radius is about 80 m across the cascade and broadens with decreasing altitude and increasing energy [138, 142].

10.3. Hadronic Showers

The average point of first interaction happens on average at a much lower altitude for protons when compared to gamma-rays of similar energy due to
The most extensive background for the detection of gamma-ray induced electromagnetic showers are hadronic showers, as the cosmic ray flux is several magnitudes higher than the usual gamma-ray flux [121]. As the name suggests, a cosmic hadron - mainly protons - starts a cascading shower instead of a gamma-ray or electron/positron. The average point of first interaction happens on average at much lower altitude for protons when compared to gamma-rays of similar energy due to the higher radiation length of protons $X_{\text{rad}} \approx 120\,\text{g}\,\text{cm}^{-2}$ [143]. Additionally,

strong interactions are possible, leading to the production of mesons and light baryons via inelastic scattering. However, the most determining factor for shower development are pions, the lightest mesons. Simple models, such as [138] and [144], can successfully describe hadronic showers with pions as the only hadronic component, similar to the Heitler model introduced in Section 10.2.

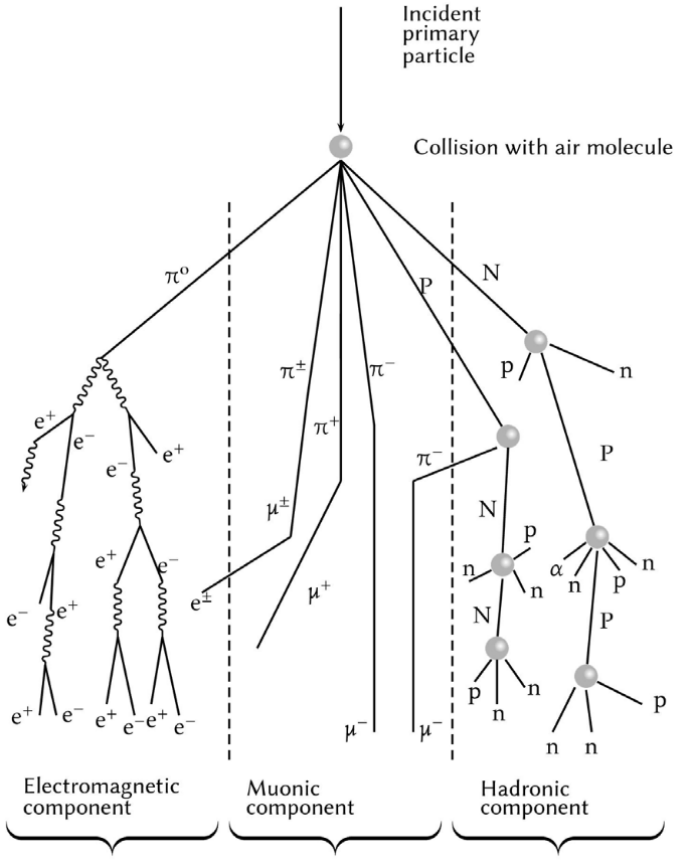

Figure 54: Schematic of a hadronic shower with each component marked and separated. Image taken and adapted from [145].

Due to the high transverse momentum transfer in inelastic scattering, the geometry of a hadronic shower is more irregular and broader than that of an electromagnetic one. Additionally, the decay of neutral pions

$$\pi^0 = \gamma + \gamma \tag{10.3}$$

$$\pi^\pm = \mu^\pm + \overset{(-)}{\nu}_\mu \tag{10.4}$$

creates electromagnetic subshowers, while the decay of charged pions leads to a muonic component. These muons can then either propagate down to the ground

if energetic enough or decay into electrons, which then again contribute to the electromagnetic component of the shower. An overview is given in Figure 54. Dominant electromagnetic subshowers pose a challenge for the separation of gamma rays from hadron-induced showers in ground-based gamma-ray astronomy, as their geometry is a key discriminator.

10.4. Cherenkov Radiation

Another effect which accompanies extensive air showers is Cherenkov radiation. A charged particle propagating in a dielectric medium polarises the surrounding molecules by inducing dipole moments. The polarisation relaxes once the charged particle has passed via the emission of electromagnetic radiation. For charged particles below the local speed of light in the medium, the dipole distribution is symmetrical, and the emitted electromagnetic waves cancel each other by destructive interference. For charged particles above the local speed of light, the distribution is no longer symmetric and a photonic shock front is created by the relaxing medium [146]. This can be illustrated by the Huygens principle as seen in Figure 55 on the left. The opening angle θ of the shock front can be calculated by

$$\cos\theta = \frac{1}{\beta n} \tag{10.5}$$

with $\beta = \frac{v}{c}$, the charged particle velocity v in units of the speed of light c, and n, the refractive index of the dielectric medium. In air, the opening angle of the Cherenkov cone is approximately 1.3° at sea level and decreases slightly with increasing altitude as the atmosphere gets thinner and the refractive index decreases.
From Equation 10.5, one can also derive the threshold energy needed to produce Cherenkov radiation by looking at the threshold $\theta = 0°$. With $\beta = \frac{1}{n}$, the threshold energy can be calculated from the relativistic kinetic energy of the particle. For an electron, this is approximately 21 MeV.
The energy loss of the charged particle by inducing Cherenkov light is in the magnitude of a few keV and, therefore, negligible in contrast to ionisation or other interactions not contributing to the development of the shower [148]. The number of photons N emitted along a certain path length x and in dependency of the wavelength λ can be calculated by [149]

$$\frac{d^2N}{dxd\lambda} = \frac{2\pi\alpha}{\lambda} Z^2 \left(1 - \frac{1}{\beta^2 n^2}\right) \ , \tag{10.6}$$

with α the fine structure constant and Z the charge of the particle inducing the Cherenkov light. Photons of shorter wavelengths dominate the spectrum because

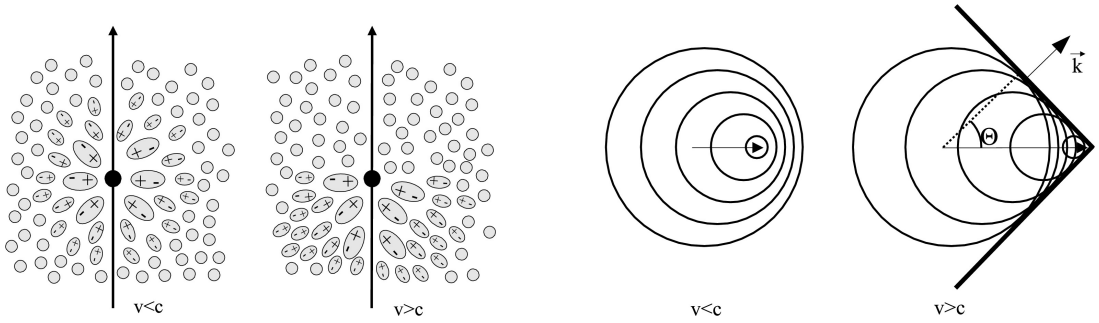

Figure 55: Illustration of Cherenkov Radiation. Left: The polarisation of the surrounding dielectric medium for particle velocities lower and higher than the local speed of light. Right: The emission of said dielectric medium in the wave picture for both cases. For particle velocities higher than the local speed of light, a cone-shaped shock front is formed by constructive interference. Image taken from [147].

the wavelength is inversely proportional to the photon number. With the cross-section of Rayleigh scattering increasing with decreasing wavelength, the Cherenkov spectrum in the atmosphere has a maximum between 300 nm and 450 nm [148], giving it a blue appearance. As the number of photons scales linearly with the propagation path length of the inducing particle and the propagation path length is proportional to kinetic energy, it is possible to reconstruct the energy of the particle by counting the number of emitted photons.
For extensive air showers, a light cone of Cherenkov radiation is formed, with a cross-section of 250 m radius [151] for electromagnetic showers, while for hadronic showers, the different subshower can be spotted over a larger area. An example of both can be seen in Figure 56 with the showers themselves at the top and the Cherenkov light pool on the ground at the bottom. The differences in the morphology of the detected Cherenkov light are the main feature used to discriminate between electromagnetic and hadronic showers.
The differences in the morphology of the detected Cherenkov light are the main feature used to discriminate between electromagnetic and hadronic showers.

10.5. IACTs: Imaging Air Cherenkov Telescopes

One way to capture the Cherenkov radiation produced by electromagnetic showers are IACTs. The purpose of these telescopes is to collect as many Cherenkov photons as possible during the time window in which the shower develops and to focus them onto a suitable camera. In contrast to optical telescopes, the field of view of an IACT is of the order of a few degrees as the Cherenkov shower image is about $\approx 1^\circ$

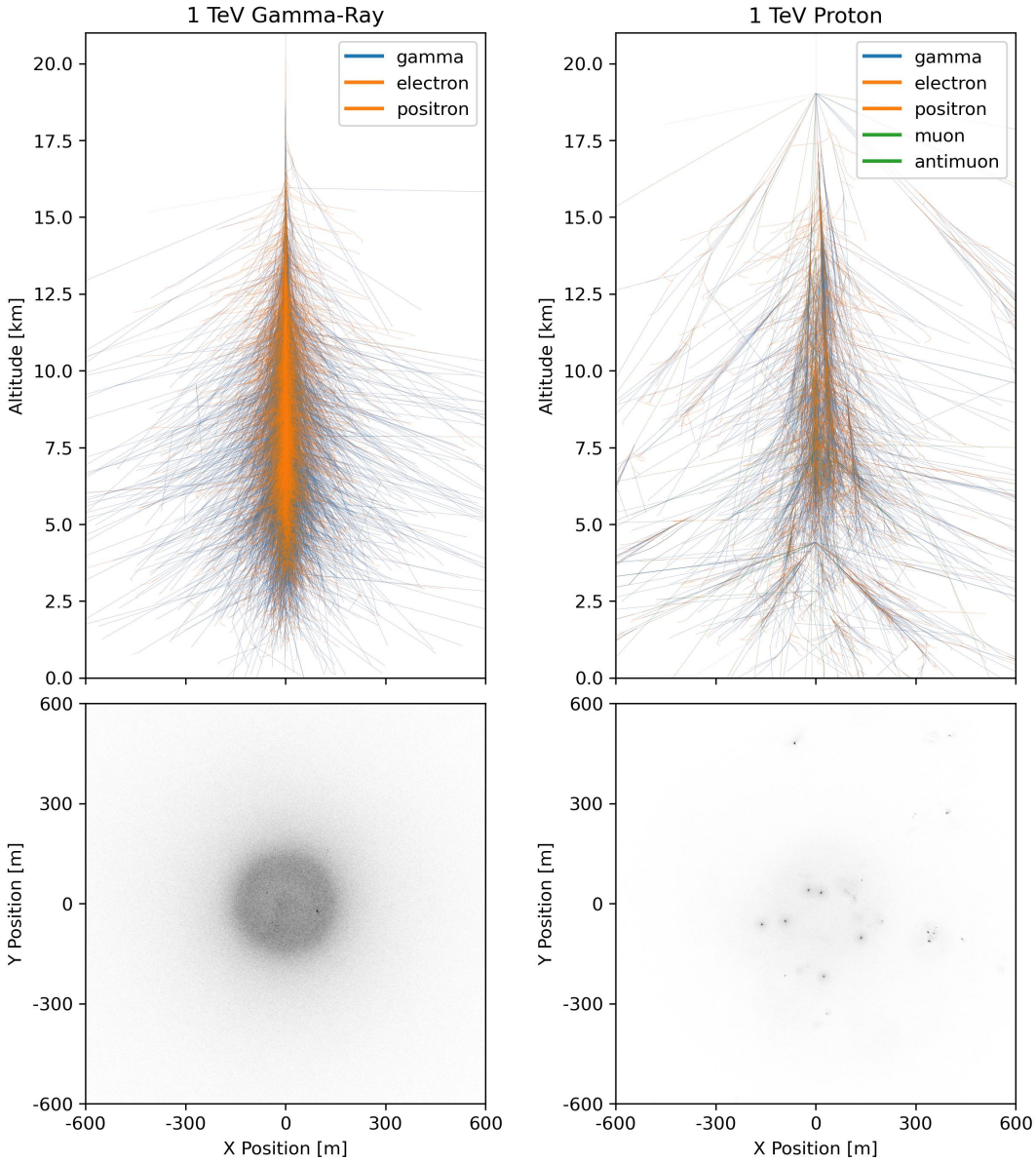

Figure 56: Top: Shower development in dependency of the altitude for both electromagnetic shower and hadronic shower, exemplary illustrated for a 1 TeV electron and proton. Bottom: The corresponding light pool at sea level created by the Cherenkov radiation. Image created with Showerpy [150].

extended and certain gamma-ray sources are expected to be extended up to a few degrees [151]. Additionally, the mirror quality and precision do not need to be of the same quality, as the angular resolution of IACT is intrinsically determined by

the size of the detected shower, which is of a few degrees.
The dominating background for IACTs is the Night Sky Background (NSB) or light pollution in general. IACTs have therefore a low duty cycle of 10 % as for example the full moon makes observations impossible. With nominal NSB conditions, a background photon rate of several MHz is expected [152]. An integration imaging camera is therefore not favourable, as the SNR drops below usefulness on the order of nanoseconds. However, due to the Cherenkov radiation and shower particles both travelling approximately at the speed of light, all Cherenkov photons (at the edge) of a shower arrive in a time frame of about 2 ns [151]. A camera with a sampling rate at the scale of nanoseconds can therefore discriminate the Cherenkov photon burst from continuously incoming NSB photons. As a consequence, individual pixels of Cherenkov cameras are equipped with PhotoMultiplier tubes (PMT)s or in newer generations of IACTs First G-APD Cherenkov Telescope (FACT)[153], Schwarzschild-Couder Telescope (SCT) and SST (see Section 10.7) with Silicon Photomultiplier (SiPM)s and digitisers at sampling rates of $\approx 1\,\mathrm{GSa/\,s}$

The images follow the characteristics of the incident showers, so in first-order elliptical distributions for electromagnetic showers and irregular shapes for hadronic ones. Depending on the impact point of the shower relative to the telescope and its inclination angle, the major axis of the ellipse changes. From the orientation of the major axis, the direction of the primary particle can be reconstructed. The integrated intensity over all pixels in the ellipse is proportional to the incident energy of the primary particle and, therefore, used to reconstruct it. Further parameters can be extracted to separate gamma-ray-induced showers from hadronic showers. This analysis was pioneered by M. A. Hillas in 1985 [155] and is still widely used for gamma-hadron separation. More sophisticated methods, such as *imPACT* [156] using likelihood fitting of pixel amplitudes, have also been established since then.
To further improve directional reconstruction and to increase the sensitivity across the whole energy range, the stereoscopic approach has been introduced [151]. Multiple IACTs in an array are used to detect the same shower. An illustration is given in Figure 57. Transferring the individual images of each telescope into a common camera frame and intersecting the major axes of each shower image greatly improves the directional reconstruction. The additional statistics in photon numbers improve the energy reconstruction. Moreover, coincidence triggers between multiple telescopes can now be used. This lowers the energy threshold of the telescopes as the individual trigger threshold can be decreased. Accidental trigger by NSB can then be vetoed. The same is true for single atmospheric muons, which can reassemble lower energetic gamma-ray showers when hitting an individual telescope.

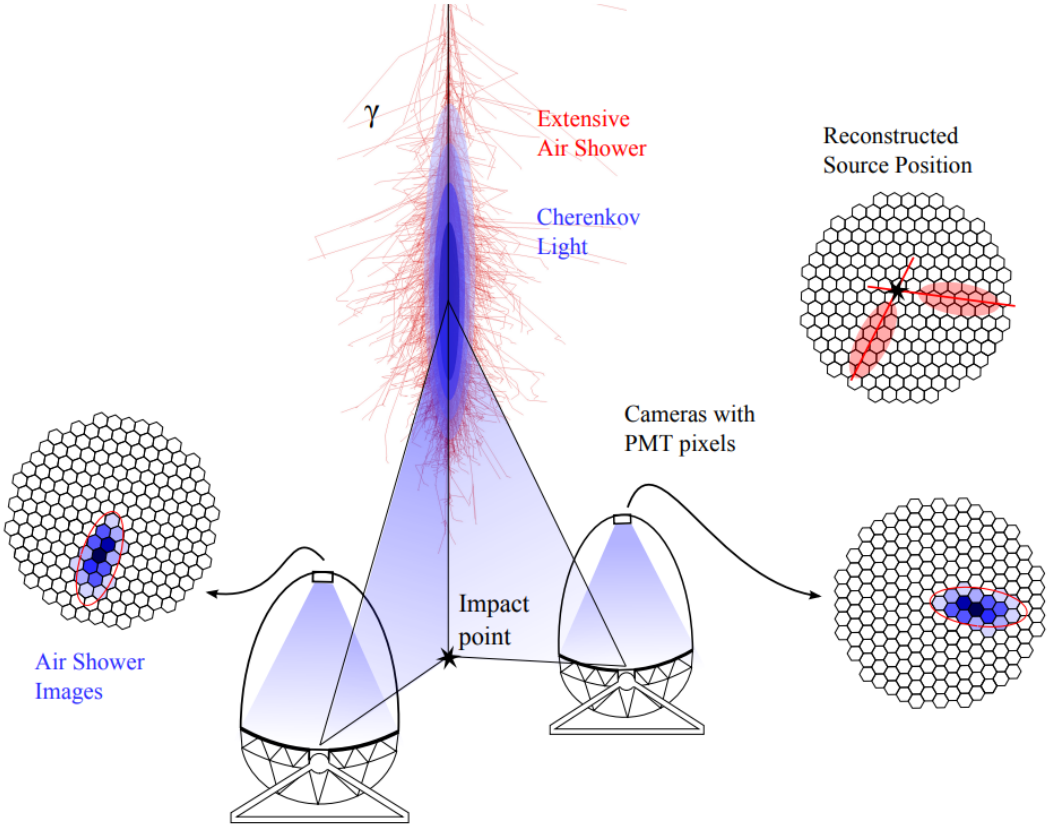

Figure 57: Illustration of the work principles of an IACT array. The Cherenkov radiation of an electromagnetic shower is imaged by separate IACT and follows the shape of an ellipse. By converting the separate images into a common frame, the impact point of the shower can be reconstructed. Together with the elongation of the ellipses, the shower direction can be reconstructed. Image taken from [154].

10.6. CTAO: Cherenkov Telescope Array Observatory

The next generation of ground-based gamma-ray detection with IACTs will be CTAO. It hosts an observatory site on both hemispheres for full sky coverage. One in the Atacama desert in Chile, close to Paranal Observatory, aiming at the centre of our own galaxy, and one at the Roque de los Muchachos Observatory on La Palma, the remotest island of the Canaries [157]. Utilising over 60 telescopes of three different size classes, CTAO will be able to detect gamma-rays in an energy range of 20 GeV to 300 TeV, pushing the sensitivity for ground-based gamma-ray detection another magnitude up while also expanding the energy range. The three telescope classes can be seen in Figure 58. A comparison to current gamma-ray detectors can be seen in Figure 59. In the low-energy regime, it closes the gap

between ground-based detectors and space-based detectors as FermiLAT [158]. For very high energies (5 TeV), it pushes the sensitivity for IACTs into areas dominated by Water Cherenkov Detectors as Wide-field Gamma-ray Observatory (SWGO) [159] and Large High Altitude Air Shower Observatory (LHAASO) [160] while achieving superior angular reconstruction.

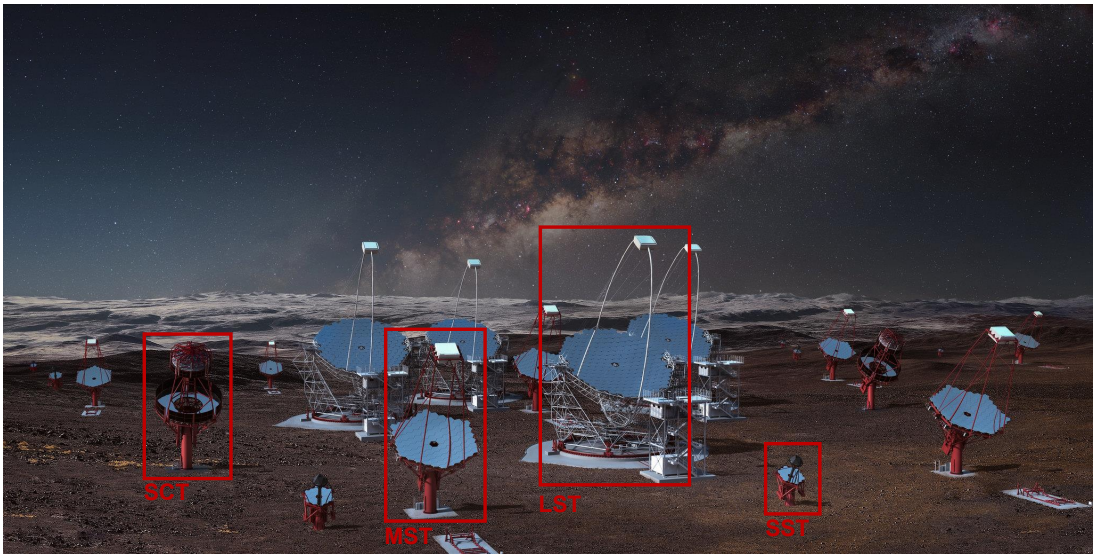

Figure 58: 3D rendering of a proposed array layout on the southern site featuring all for CTAO developed telescope classes. Image from CTAO [157] and edited.

The lowest energies are covered by the Large-Sized Telescope (LST), the largest telescope with a photon collection area of 400 m^2. With a field of view of 4.3° and a repositioning time of 20 s, it is perfectly suited for studying transient phenomena, gamma-ray bursts, and high-redshift active galaxy nuclei. In total, CTAO will feature four of these telescopes on the north site, with LST-1 already operating [161, 162].
The workhorse of the telescope array will be the Medium-Sized Telescope (MST), also in Davies-Cotton design, but with a photon-collecting area of 88 m^2. The smaller design makes it more cost-efficient than the LST, so more telescopes can be built to capture the decreasing flux in higher-energy gamma rays. The most sensitive energy range spans from 150 GeV to 5 TeV. Fourteen will be built on the north side and nine on the south side. An additional feature is that the north side will host the NectarCAM [163], and the south side will host the FlashCam [164]. While the NectarCam achieves a field of view of 7.7°, the FlashCam achieves on of 7.5°.
For the very high energy range of 5 TeV to 300 TeV, the SST is used, a Cherenkov telescope in Schwarzschild-Couder design [165, 166, 167, 168]. The dual mirror

configuration with higher order polynomial shape allows for better angular resolution in comparison with the Davies-Cotton design for equal mirror sizes, minimisation of coma aberrations and minimisation of the photon time of arrival at the premise of a small, compact and light camera, which additionally reduces the cost of the overall telescope [169]. The primary mirror of the SST is segmented into 16 aspherical mirrors, which combined span 4.3 m wide, while the secondary mirror is a monolithic 1.8 m wide one [170]. Together, the telescope has an effective photon-collection area of $\approx 5\,\mathrm{m}^2$ [157] with a possible field of view 10.5° [166]. 37 of these SSTs are planned to be built on the south site at a spacing of $\approx 250\,\mathrm{m}$ over an area of $\approx 3\,\mathrm{km}^2$ to account for the steeply decreasing flux of gamma-rays in this energy regime.

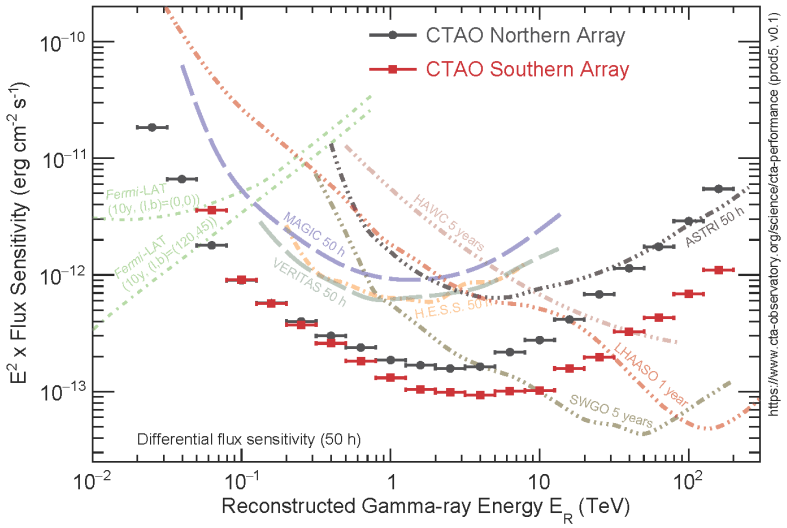

Figure 59: The differential sensitivity for both array sites in comparison to operating and future gamma-ray observatories. Image from CTAO [157].

Additionally, there is the SCT, a mid-sized telescope in the same vein as the SST with a photon collection area of $50\,\mathrm{m}^2$. A proof of concept version is already in place at the Fred Lawrence Whipple Observatory in Arizona and successfully detected the Crab Nebula [171]. It uses the Schwarzschild-Couder design [165] and the same digitisation ASIC in their camera as the SST explained in Section 10.8. At least ten SCTs shall be included in the southern array in the future [171].

10.7. The SST Camera

The highly pixelated compact camera to be placed in the SST is the SST Camera [172, 173, 174]. It faces 2048 pixels of 0.16° size and a combined field of view of ≈ 9°

in a 570 mm × 570 mm × 500 mm housing at 90 kg. A CAD drawing of the camera and its components can be seen in Figure 60. As photodetector, uncoated SiPMs from Hamamatsu Photonics (S14521-1720) are used due to their compactness, robustness against high illumination levels, high quantum efficiency, low cross-talk and low cost. Each SiPM tile features 256 individual pixels of 3 × 3 mm, which are joined into 64 pixels of size 6 × 6 mm.

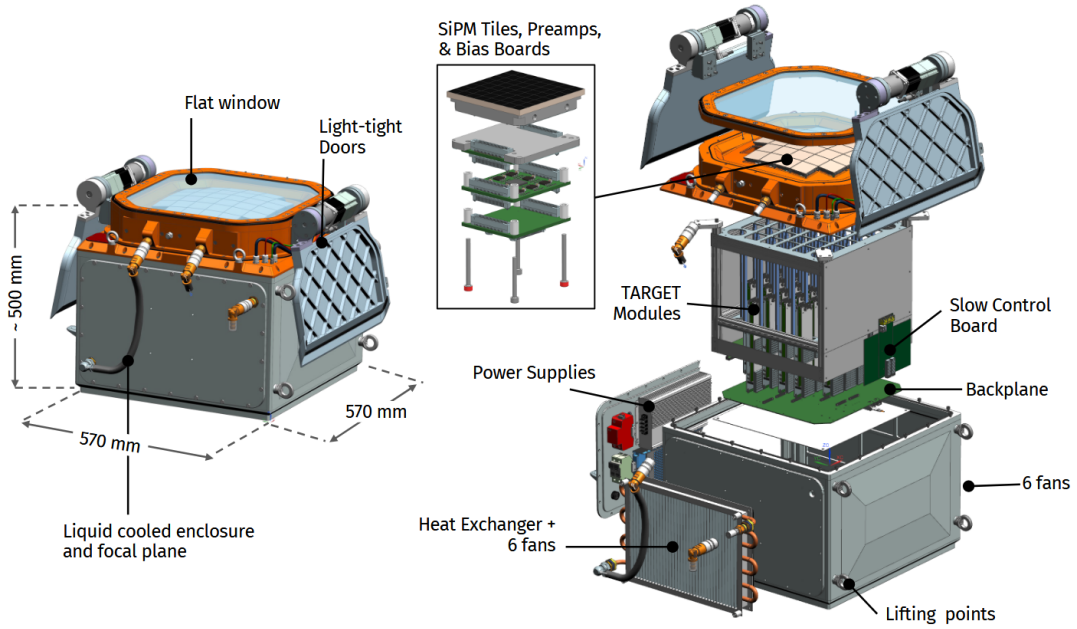

Figure 60: Explosion CAD view of the SST Camera with every major element highlighted and marked. Image taken from [174].

32 of these SiPM tiles are used in the camera and are aligned on a sphere to follow the focal plane given by the telescope. They are also thermally coupled to the front plate, which is water-cooled to keep them at a constant temperature and, therefore, the operation window. To protect the tiles, a flat coated window is installed on top that only transmits light between 290 nm and 550 nm to cut off unnecessary NSB photons and to maximise the yield of Cherenkov photons in comparison. Additional protection is provided by the light-tight aluminium doors, which can be closed if necessary.
The SiPM tile itself is connected to the bias board, which controls the individual bias voltage of each pixel to match the gain, and to the preamp board, which preamplifies and preshapes the signal. The preshaping is done by a pole-zero cancellation shaper, which also benefits from the thermal stability of the front plate.

The bias voltage, data acquisition, power supply and first-level triggering are provided by the TARGET module, based on the TARGET ASICs (see Section 10.8). A detailed description follows in Section 10.9. Each of the 32 TARGET modules is connected to the backplane, synchronising the modules, handling the camera-level trigger, and transferring the digitised data to the camera server via 10 Gbps Ethernet. If two adjacent TARGET modules trigger, the backplane will cause a camera trigger, instructing all TARGET modules to read out. Additionally, the back plane communicates with the slow control board, monitoring, for example, the temperature in the camera, the NSB intensity and, the flashers. The flashers are LED-driven scintillating fibres at the corners of the focal plane to gain match the individual pixels when the doors are closed. An external heat exchanger keeps the camera in thermal equilibrium. Together, the SiPM, the bias board, and the TARGET module form the FEE module.

10.8. The Cherenkov TARGET C Architecture

Before introducing the TARGET module, it makes sense first to introduce the namesake of the module, the TARGET ASICs. "The functional blocks of the ASICs are trigger (CT5TEA), analog sampling with a 16,348 deep storage buffer and analog-to-digital converters (ADCs) for signal digitization (CTC) and digital-to-analog converters (DACs) for internal operation settings. The trigger and sampling paths are split into two separate ASICs, reducing cross-talk between the sampling and trigger paths, providing a lower trigger threshold and larger dynamic range [175, 176]. Figure 61 presents an overview of both signal paths.
Each ASIC processes 16 individual channels in parallel. An adjustable DC baseline per channel, the operational pedestal voltage, is set by DACs in CT5TEA. By summing the analog signals of four adjacent channels, four trigger groups are formed per CT5TEA. If the sum in one trigger group exceeds an adjustable threshold, a trigger signal is output as Low-Voltage Differential Signaling (LVDS). An FPGA can then collect these outputs for further processing as for example giving out readout instructions to CTC.

For the sampling in CTC, a small Switched-Capacitor Array (SCA) of 32 + 32 cells is used to keep the capacitive load at a minimum. The cells are following the signal until disconnected sequentially with a 1 ns delay, retaining a proportional charge. The 1 ns delay between the sampling cells result in a nominal sampling speed of 1 GSa/s. The 64 1 ns delays are generated by a temperature-stabilized internal time base. A delay-locked loop keeps the transition from last to first sampling cell in phase with an external 15.625 MHz clock (SST clock). The SCA is arranged in two blocks of 32 cells, allowing it to store one block while the other block samples the applied signal to avoid any dead time (ping-pong mode). The

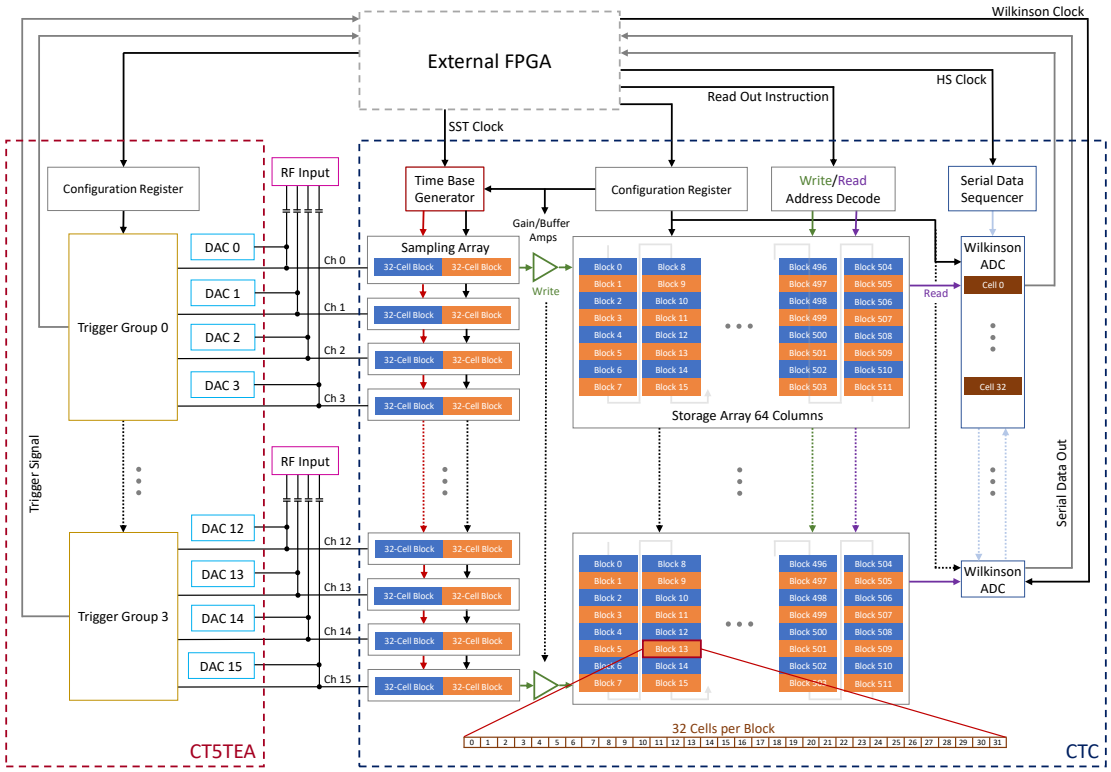

Figure 61: "Operational schematic of the CT5TEA and CTC ASICs. The analog signal of each channel is fed in parallel into both ASICs. Digital-to-Analogue-Converter (DAC)s of the CT5TEA create a DC baseline voltage for each channel, the operational pedestal voltage, to set the working point of the CMOS based SCA of CTC. Four channels form a trigger group in CT5TEA, sending a trigger signal to an accompanying external FPGA if the analog sum of these four channels exceeds the trigger threshold. The sampling arrays in CTC sample continuously in ping-pong mode, namely, while one block is sampling, the other transfers the sampled voltages to the storage cell array. The storage blocks can be arbitrarily read out on demand, tapping the cell voltages to the Wilkinson ADCs. The digitized values are transferred to the FPGA via a serial data interface per channel, timed by the HS clock at 93.75 MHz." [21].

readout signal is transferred to the 16,348 sample-deep ring buffer storage array arranged in 512 blocks of 32 cells, buffering 16 μs at 1 GSa/s. The samples are continuously overwritten until a waveform is to be read out. Then, the blocks where the trigger occurred will no longer be overwritten while the sampling continues for the rest of the storage buffer. Blocks of 32 are random-accessible for digitization. In the case of a readout/digitization instruction, each cell of the 32-cell blocks is

digitized in parallel by Wilkinson ADCs. Here, the storage cell voltage is compared with a reference voltage ramp produced by charging an external capacitor with a constant current, which defines the slope of the ramp. At the start of the digitization, a 12-bit Gray code counter is reset and counts up with the speed of the externally applied Wilkinson clock. When the ramp voltage gets larger than the cell voltage, the counter's value is written to a register as the digitized value. With the currently used Wilkinson Clock of 208 MHz, it takes about 20 μs to digitize a full block [177]."

10.9. The TARGET Module

The TARGET is the heart of the SST Camera. It provides the TARGET ASICs and the SiPMs with the necessary infrastructure to operate. One could also say the camera was developed for these ASICs. A fully equipped module with connected SiPM tiles and preamp- and bias-board can be seen in Figure 62, called FEE. The TARGET module itself is the three stacked PCBs on the right. On top of the power board, providing the necessary power for the bias voltage (≈ 38 V [174]), the preamps, the shaper, and slow ADCs.
At the bottom, the primary board hosts two CTC and CT5TEA for digitisation and low-level trigger generation, the necessary FPGA to operate the ASICs and data transfer, and the shaping circuit. Together with the pole-zero-cancellation circuit in the preamp board, the shaping circuit transforms the exponentially decreasing flank of a photo pulse to a 10 ns width pulse. The primary board also serves as the interface to the backplane.
Function-wise, the auxiliary board in the middle is identical to the primary board, except for the FPGA and the interface to the backplane.

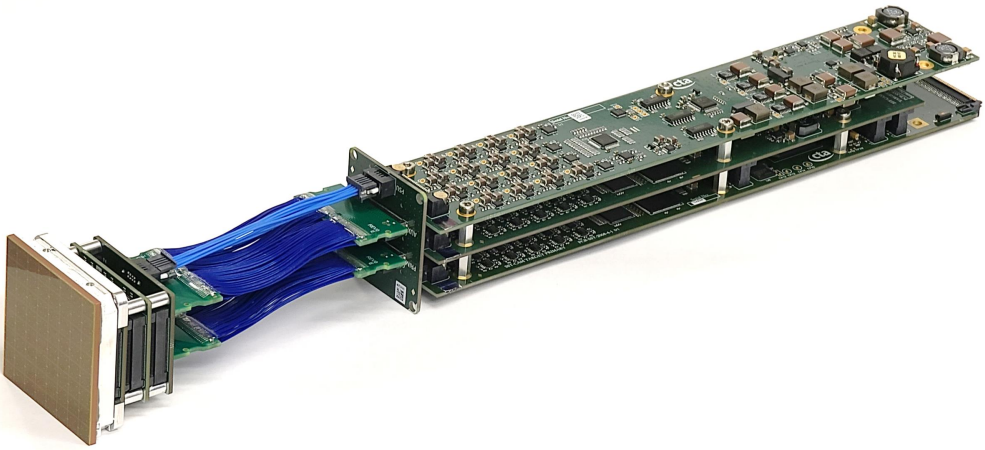

Figure 62: Image of the FEE consisting of the SiPM on the left, the preamp and bias board stacked behind, and the TARGET module on the right. Image by Jon Lapington.

11. CTC Calibration Chain

To successfully use the TARGET ASIC, several calibration steps have to be performed first. The following sections describe each in detail, what the reasoning behind it is and how it is applied. The emphasis on the calibration of the CTC ASIC is to increase the performance in intensity resolution as well as a distortion-free digitisation of signals. Nevertheless, some CTC calibration methods use functions of the CT5TEA ASIC. These calibration steps are therefore included as well. The calibration of the trigger logic in CT5TEA is omitted as it is not part of this work. An overview is given in Figure 63.

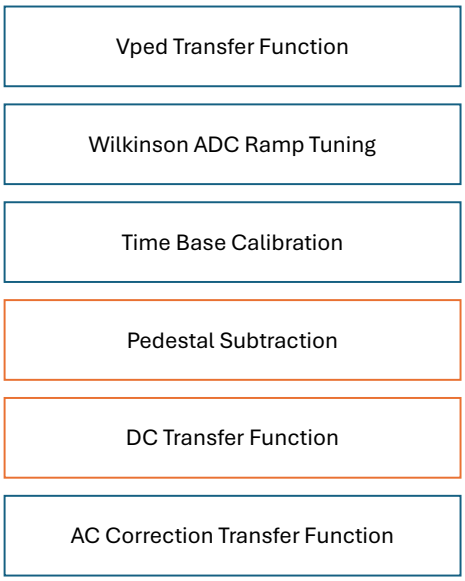

Figure 63: The proposed calibration chain of the CTC, including the `Vped` transfer function of CT5TEA, to enable in situ DC transfer functions. The orange calibration steps can be entirely performed without external equipment and can therefore be redone in situ at any given time.

The calibration chain starts with measuring the `Vped` transfer function to record the response of the DACs in CT5TEA that set the baseline (or pedestal) voltage to operate the CTC. This will later also be used to record the DC transfer function in situ without any external devices on the TARGET module. Second is the Wilkinson ADC ramp tuning, ensuring that the Wilkinson ADCs all have the same minimum dynamical range of 2.2 V. To establish that the two sampling array blocks are in phase, the timebase is adjusted by either inflating or deflating the length of each sample bin during timebase calibration. Next come the two in situ calibration steps, pedestal subtraction and the DC transfer function, which can be redone at

any time to respond to changing conditions, such as different temperatures. Both characterise the individual response of each storage cell in combination with the Wilkinson ADC. The pedestal subtraction defines the virtual null of the ADC by subtracting the response of a baseline measurement, while the DC transfer function maps the response of all voltages of the ADC. And finally, to reduce the AC noise in pulse mode operation, an AC correction transfer function is taken, where the response of the ASIC to the observable of a pulse, e.g. amplitude or integral, is measured.

"An example waveform of input amplitude 227.2 mV is shown in Figure 64 with different calibration steps applied. In the raw waveform, the pulse is visible with digitization artifacts. The structure of the 31st cell, seen as negative spikes, dominates the picture. After operational pedestal subtraction, the ASIC cell-to-cell variations in the baseline are largely removed, leading to a visibly cleaner waveform and improved signal-to-noise. However, the scaling in ADC is still non-linear, and the 31st cell of each block shows significantly worse behavior than the others. The block-dependent DC transfer function fixes both but leaves a bias of 27.0 mV. Applying the AC correction to the amplitude corrects it to 226.4 mV, matching the input amplitude to 0.3 %."

11.1. Evaluation Board and Software

"An evaluation board has been developed for the performance evaluation of CTC and CT5TEA, which customizes all elements needed to operate the ASICs. This board is shown in Figure 65. The control of the ASICs is handled by an FPGA piggyback board (Trenz TE0714-03- 35-2I) featuring an Xilinx Artix 7. A gigabit Ethernet link is used for slow control and data transmission to a computer. There is an MMCX connector for each input into the 16 channels of TARGET, terminated with a 50 Ω resistor and AC coupled via a 1 nF capacitor. A low-noise, 2.5 V output low-dropout (LDO) regulator (Analog Devices LT3045) is placed in close proximity to power the ASICs. The board can be triggered by an external signal, fed from an MMCX connector or created by the FPGA, based on signals from the CT5TEA or the FPGA itself. Additionally, there are four MMCX connectors where signals and functions of the ASICs and FPGA can be monitored. In this work, two evaluation boards were used, designated SN0001 and SN0002.

Figure 66 shows a schematic representation of all measurement setup configurations. Each signal can be individually plugged into one of the inputs of the evaluation board or distributed by a custom splitter board based on operational amplifiers (Texas Instruments OPA692). As signal sources, several function generators were used: a Keysight 33622A function generator for Gaussian-shaped pulses and square trigger pulses, an Active Technologies PG-1074 for square pulses with a rise time of 70 ps, an Active Technologies AWG-4022 for sine wave pulses, and a MAX9601EVKIT for

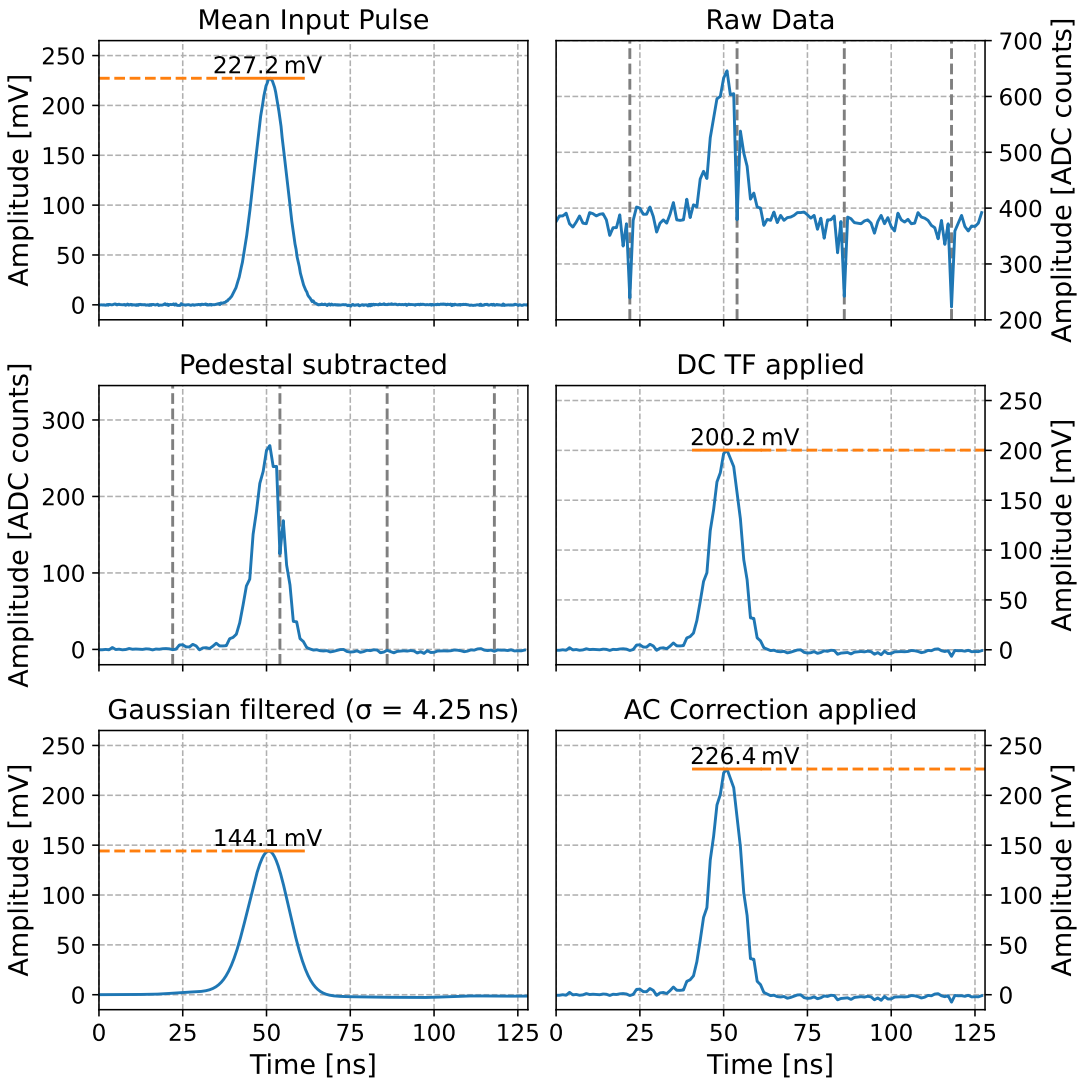

Figure 64: "Subsequent calibration steps applied to a waveform of a Gaussian-shaped pulse on SN0001. Top left, the mean input pulse is shown, digitized with a Tektronix MSO064b Oscilloscope. The raw digitized waveform is shown on the top right. Baseline subtraction is shown on the center left. Center right shows the waveform after the DC transfer function is applied. On the bottom left, a Gaussian filter with 1.5 ns width is applied. The input pulse amplitude was 227.2 mV and the amplitude of 200.2 mV is corrected to 226.4 mV by the AC correction as seen on the panel bottom right." [21].

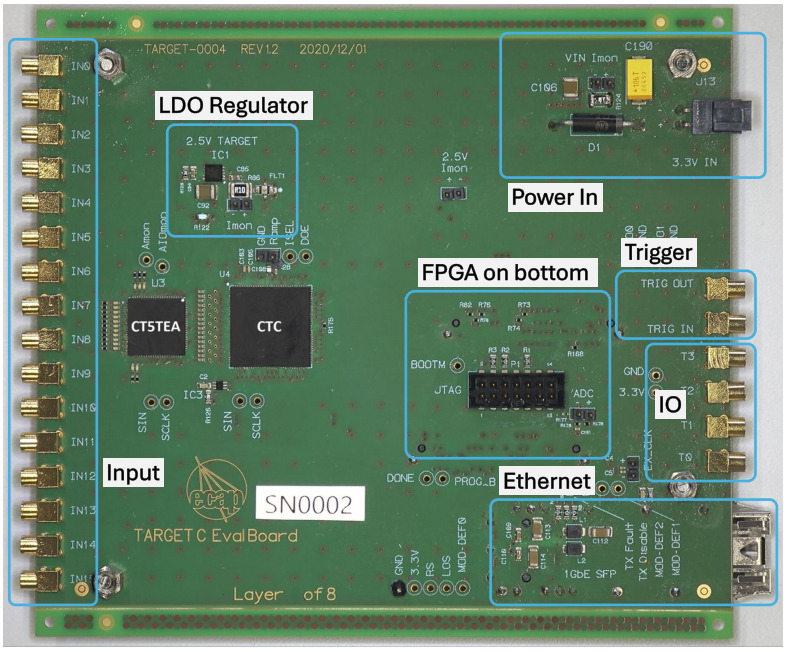

Figure 65: "One of the two evaluation boards used to operate CTC and CT5TEA with the FPGA and ethernet connector (SFP port) on the back side, 16 MMCX input connectors on the left, four user-configurable IO ports and Trigger input and output on the right. The board is supplied with a single 3.3V supply (Molex Nano-Fit connector top right)." [21].

translating such sine wave pulses to square waves. A digital multimeter (Keithley DMM6500) probes the DC offset at the ASIC inputs after the AC coupling. A detailed usage of each instrument is given in the specific section in which it is used. The TARGET libraries [115], a C++-based software, is used for communication with the FPGA and waveform data processing. It contains three packages for data readout and event building, as well as calibration of waveforms. *TargetDriver* provides functions to configure the FPGA and TARGET ASICs by simple register operations (read/write) and higher-level functions, for example, initializing an evaluation board with default settings. Routines for a camera state machine, as well as the event builder, are also provided. *TargetIO* handles the reading and writing of data. *TargetCalib* contains the calibration routines for TARGET data. Basic functions are also available in Python wrappers using SWIG, enabling the use of simple Python scripts."

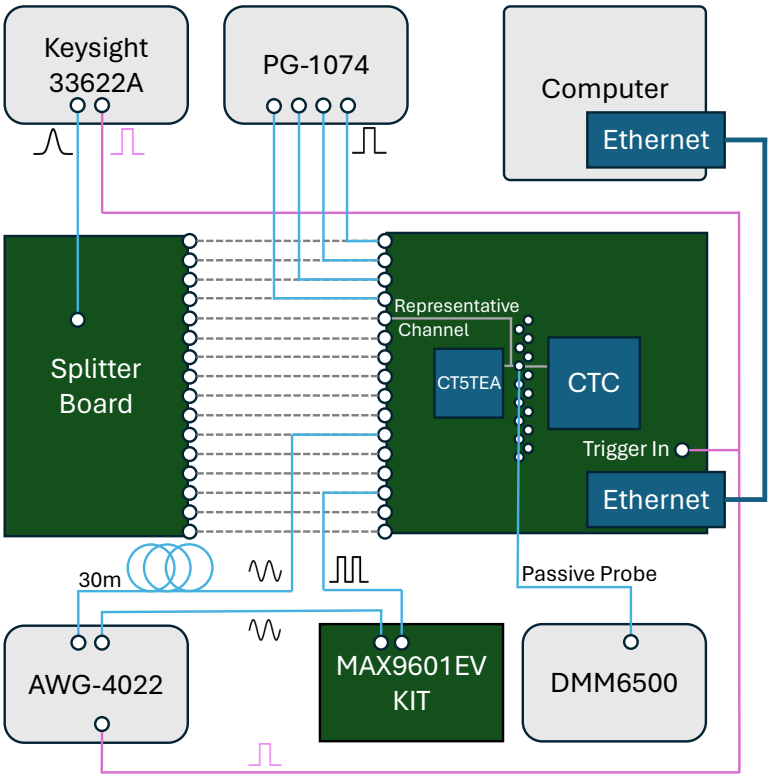

Figure 66: "Schematic representation of all measurement setup configurations. Each function generation can be individually plugged into the inputs of the evaluation boards or connected to the splitter board to inject the signal in parallel to all 16 channels. However, only the sketched setups were used." [21].

11.2. Vped Transfer Function

"To operate and set up the ASICs, different bias voltages are needed across the whole functionality of the ASICs. These DC voltages are created by 12-bit R-2R resistor ladder networks. The resistors are tuned so that no voltage gaps occur in the DAC output voltage as a function of DAC input value (see Figure 67). Most prominent of them are the CT5TEA ones that set up the necessary pedestal voltage per channel on the signal path, called `Vped`. These DAC output voltages were probed at the test point in front of CTC and measured with the Keithley DMM6500 multimeter with a mean standard error of $< 0.03\,\mathrm{mV}$ over 512 different DAC settings. A measurement is taken before and after four bits flip simultaneously to intercept significant voltage drops in the transfer function due to inaccuracies of the R-2R resistor ladder network. The range and linearity of the DAC output voltage can be tuned by the `VpedBias` parameter regulating the bias current of the output amplifier of the DAC. A higher bias leads to an earlier saturation of

the transfer function, reducing the dynamic range with no observable effect on the standard deviation. With current settings, an output voltage range of $> 2.2\,\mathrm{V}$ is achieved. The DAC performance is representative of all DACs in the TARGET ASICs.

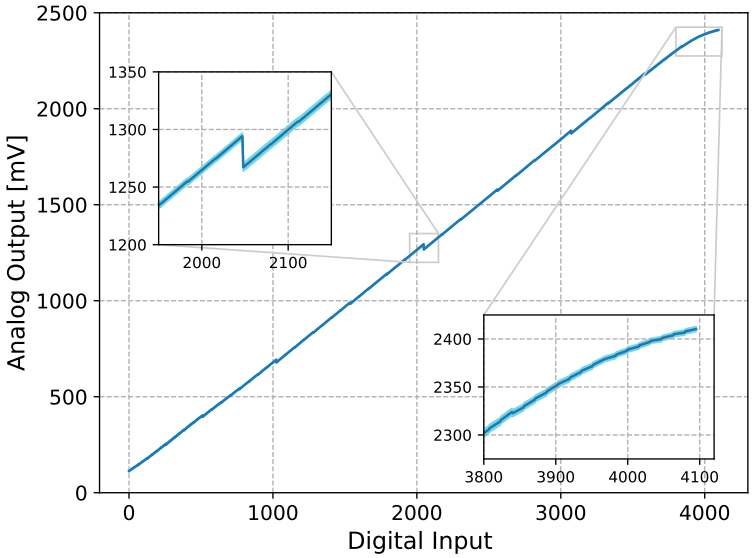

Figure 67: "The mean transfer function of the CT5TEA DACs of SN0001 and SN0002 controlling the pedestal voltage of the signal path with the standard deviation over all channels as semi-transparent area." [21].

For SN0002, an analysis of the temperature dependence of the DACs was performed, as temperature in the SST camera will not be constant. The output voltage difference due to a change in temperature for a given DAC setting is presented in Figure 68. The steps arise from bit flips in the R-2R resistor ladder network, introducing different numbers of resistors with different temperature dependence to the circuit. Around the operational pedestal voltage of 750 mV (gray dashed line), the temperature-induced offset scales with about $0.08\,\frac{\mathrm{mV}}{\mathrm{K}}$ assuming a linear response. For the saturation regime, the temperature dependence increases; however, as a fraction of the input signal (which reaches 2.4 V at a DAC value of 4096), the effect is negligible. The same is true for DAC values below 800, as voltages below 600 mV are not suitable for the CMOS SCA. For the use of an internal DC calibration (see Section 11.6.1), the DACs are deemed sufficiently temperature stable."

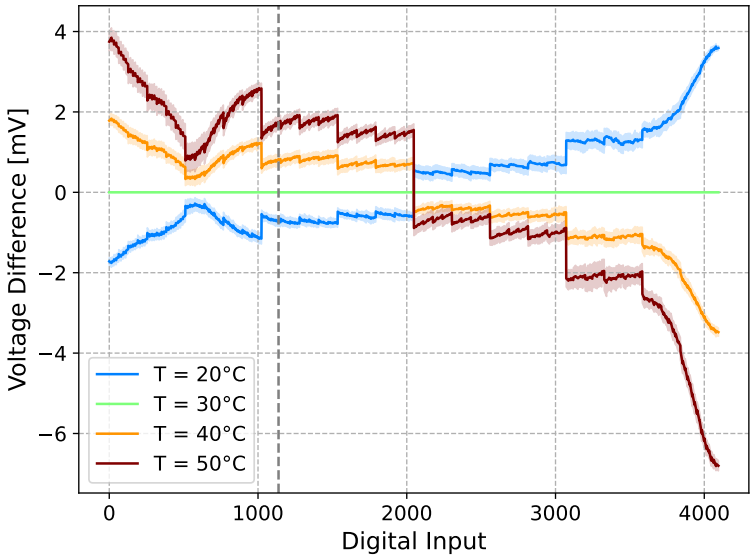

Figure 68: "Temperature-induced voltage difference of the CT5TEA DAC transfer function per DAC setting of SN0002. Standard deviation between the 16 channels marked as semi-transparent area and the operational pedestal voltage marked as gray dashed line." [21].

11.3. Wilkinson ADC Ramp Tuning

To ensure that every ASIC has the same digitisation range of 0.2 m V to 2.4 V and resolution, the parameters of the Wilkinson ADC must be calibrated. This can be done either by changing the switching behaviour of the Wilkinson comparator or by adjusting the slope of the Wilkinson ramp. Evaluating the effects of different comparator parameters is tedious, as baseline noise, dynamic range, and even pulse digitisation must be monitored. Not a task for calibrating thousands of modules. Therefore, the parameters of the comparator are tuned for one reference ASIC (SN0001) and given to the rest. A detailed description of this tuning can be found in Section 12. With the comparator fixed in performance, a fitting Wilkinson ramp must be accompanied.
The Wilkinson ramp is created by charging an external capacity with a constant current controlled by the parameter `Isel`. Therefore, `Isel` changes the slope of the ramp. Additionally, the minimum discharge level of the capacitor is set by `Vdischarge`, the baseline voltage level of the ramp. As the digitised value is created by running a 12-bit Gray-code counter until the ramp voltage matches the to-be-digitised value, the slope of the ramp controls the dynamic range and resolution of the digitiser. A too steep slope ensures the 2.4 V dynamic range, but has poor resolution, wheres as a too shallow one has potentially great resolution,

but can not digitise in the required range. Therefore, a sweet spot has to be found where full dynamic range is achieved at the best resolution, with a margin for ASIC-to-ASIC and temperature variations. Again, a matching ramp is found for the reference ASIC, to satisfy the requirements. The task now is to determine the individual settings for each ASIC to match the slope and discharge level of the reference ASIC as there is a large spread in capacity between modules. This Wilkinson ADC ramp tuning is therefore necessary before any other calibrations of the CTC.
The best-suited for the task is an oscilloscope to measure the ramp monitor test point per ASIC. In this work, the Tektronix M064B is used with the input set to 1 MΩ, as the test point views a copy of the ramp, and the amplifier can not drive a 50 Ω load. Additionally, the ASIC has to be in a temperature-stabilised environment at the same temperature as the reference, as the ramp is temperature-sensitive and the reason why certain calibration procedures are temperature-dependent.

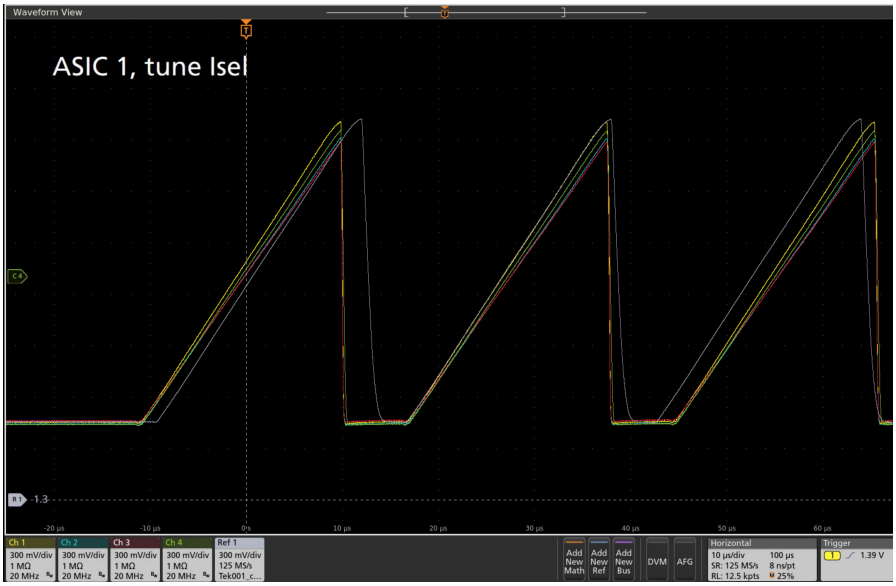

Figure 69: Snapshot of the ramp tuning for an arbitrary TARGET module hosting four ASIC, currently adjusting `Isel` of ASIC 1. In grey, the reference ramps with only the second ramp used for tuning. The slope and baseline of the ramp of ASIC 0 are already tuned. The different waiting time between ramps for the reference and the TARGET module is irrelevant. All channels have an additional 20 MHz filter to increase the SNR.

A best guess for `Isel` and `Vdischarge` is set as the initial condition. The oscilloscope digitises the slope and sends the waveform to a computer. A Python script cuts out the 20 % to 80 % range of the slope by observing the derivative of the ramp.

Then, the slope is determined by a linear fit and is compared to the reference slope. Depending on, whether the slope is steeper or shallower, `Isel` is increased or decreased. This continues until the slopes are in agreement. Then, the baseline voltage is adjusted in a similar way as the slope. A derivative spots the baseline area, and the mean voltage is compared to the reference. `Vdischarge` is then adjusted according to the voltage level.
Unfortunately, a different `Vdischarge` changes the slope, and a different `Isel` changes the minimum discharge level set by `Vdischarge`. Therefore, the process continues until there is good a agreement for both.
For fine-tuning, an additional scan around the determined `Isel` and `Vdischarge` values ±2 ADC-counts is conducted, as the parameter values are not increased or decreased in steps of one to save time. This also accounts for the voltage steps of the parameters DAC as non-linearities in the to-be-optimised parameter can lead to oscillations in the optimisation process. In that case, the loop is interrupted and the scan is performed.

11.4. Sampling and Time Base Calibration

"Based on the earlier work on the TARGET 5 ASIC [177], the sampling frequency is set to the default value of 1 GSa/s and is kept unchanged for all tests. While the beginning of every sampling cycle is synchronized with the FPGA clock, the length of the individual sampling cell has to be fine-tuned, such that the transition from the last cell of the second block to the first cell of the first block is in sync with the FPGA clock. The total length of the sampling array can be tuned with two settings. Via `SSToutFB_Delay` one can tune the length of the sampling array with 1 ns (at 1 GSa/s) granularity over a large range. By changing the `VtrimT` parameter, the length is controllable on the sub-ns level to fine-tune the total length to 64 ns.
A `VtrimT` scan is performed for each board at a constant `SSToutFB_Delay`. Here, a 50 MHz sine wave is applied to a channel for different `VtrimT` values. The digitized waveform of 128 ns length is then separated into two parts, split at the transition of sampling cell 63 to 0. Both parts are then individually fitted with a sine wave. The resulting phases of both fits are subtracted from each other. With a correctly set `VtrimT`, a phase difference below 20 ps is achieved, which is more than sufficient for operation." An example is given in Figure 70 for a suboptimal `VtrimT` = 840 DAC-counts resulting in a phase difference of 2.1 ns.
"To study the width of each sampling cell, square waves are used. The normalized distribution of edge transitions in the cells divided by the sampling frequency yields the width of each cell. This method was used instead of measuring zero-crossings of a sine wave [178], as sharp edges of square waves yield more precise results that are less sensitive to amplitude miss-calibration. To generate a square-wave signal with a rise time (10 - 90%) of 200 ps and an amplitude of about 200 mV, a sine wave

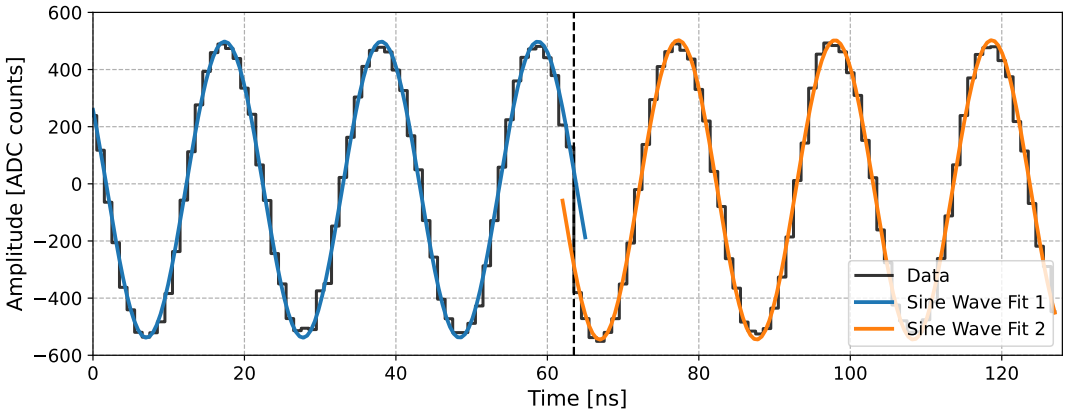

Figure 70: Measurement of the phase difference between the last sampling cell and the first for a `VtrimT` of 840 ns. A sine wave is fit to each complete transition of the sampling array. The phase difference between the two sine waves corresponds to 2.1 ns.

generated by the AWG-4022 function generator is fed into the MAX9601EVKIT board, an ultra-fast comparator. The edge of the comparator output pulse is then assigned to the sampling cell if the previous sample is under a certain threshold and the sample itself and the following one are above it. This threshold is arbitrary for sufficiently fast rise times and was set to 100 mV. An external trigger was used to cover all sampling cells equally, and 100,000 waveforms were recorded.
The time base for channel 0 of SN0001 after `VtrimT` tuning is shown in Figure 71. The spread around 1 ns is about 60 ps in standard deviation, excluding the 28th to 32nd cells of each block which further deviate up to 300 ps. It will later be seen that these cells show a different behavior in a range of other aspects. It is assumed that this behavior is due to the physical layout of the ASIC substrate, but a clear single indicator of why these cells are different was not found.
No shift of the time base between the channels is observed, which is a fair assumption as the time base signal propagates from channel 0 to channel 15. For the rest of this work, the time base is treated as 1 ns bin. Pulse shape distortion caused by the uneven sampling time base is handled by different calibration techniques and ultimately increases the effective AC noise (see Section 13.4).” Therefore, only the `VtrimT` scan has to be performed for a suitable sampling time base.

11.5. Pedestal Subtraction

The most basic form of waveform calibration is the pedestal subtraction. Here, a null measurement of the operational baseline is done to set the virtual zero. In

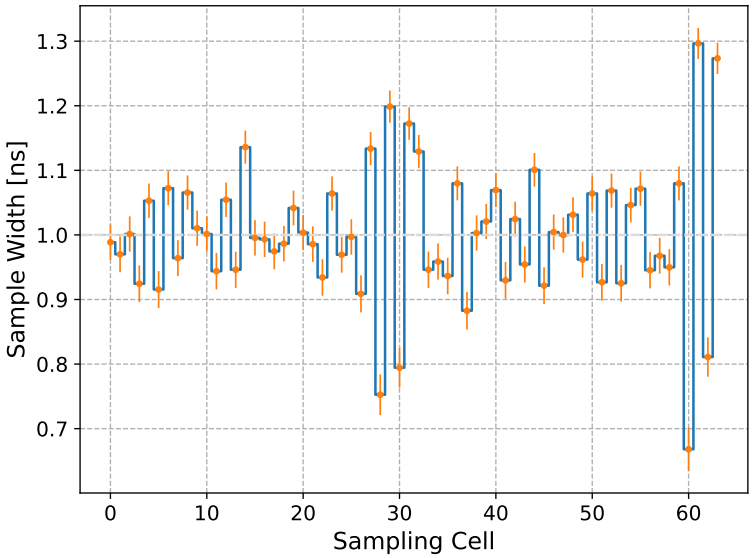

Figure 71: "Individual sampling cell width of the sampling array of channel 0 of SN0001 with the corresponding standard error." [21].

principle, the pedestal subtraction is part of the DC transfer function, which maps a voltage to the individual response of each storage cell in different digitisation blocks. But instead of looking at the complete dynamic range, only the baseline is calibrated. This is done to rapidly respond to baseline drift occurring in the ASIC as it takes only a fraction of the time of a full DC transfer function. A detailed explanation on how the calibration is generated and applied can therefore be found in Section 11.6.1 about the DC transfer function.
A reason for baseline drifts is the temperature dependency of CTC. In Figure 72, the difference in mean ADC value for an operational pedestal of 750 mV is given for different temperatures subtracted from the reference temperature of 30 °C. The 29th and 31st cells of each storage block are analysed independently, as they have different behaviours in the DC transfer function and therefore in their digitisation. More to that in Section 11.6.1. For the temperature dependency only the 31st cell deviates significantly as the ADC value grows by 0.5 $\frac{\text{ADC}}{\text{K}}$ instead of 0.2 $\frac{\text{ADC}}{\text{K}}$ as for the other cells. Therefore, let temperature differences not only slowly drift the baseline, but they also make it spikier. A new pedestal subtraction is therefore recommended between observation runs.

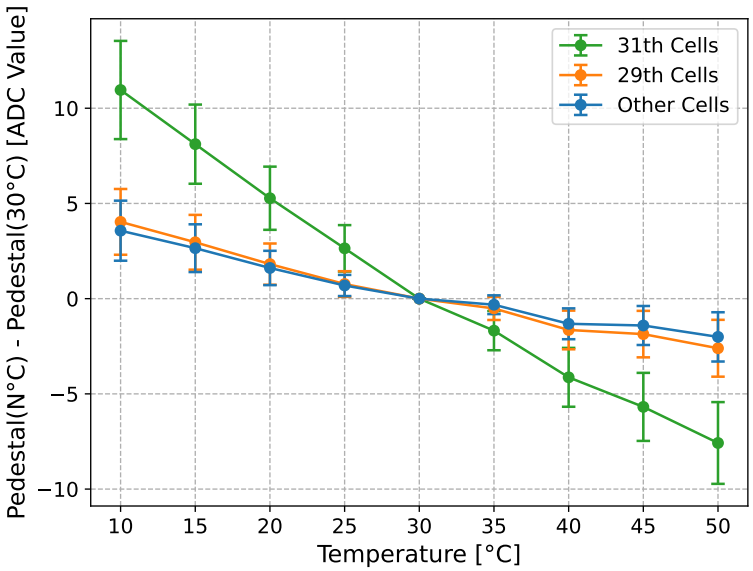

Figure 72: The ADC count difference of pedestal subtraction values at different temperatures. The colour code indicates the positions in the storage array blocks, as the 31st and the 29th cells behave differently in various aspects. The error bars indicate the standard deviation.

11.6. Transfer Functions

For the linearisation of the digitising ASIC CTC, a transfer function of input-output values has to be measured. This approach was split into two separate transfer functions. One in situ redoable DC transfer function to correct temperature-dependent changes in the digitisation response, and a AC transfer function to correct AC dependent sampling effects that are temperature-stable. Both are described in detail in the following Sections.

11.6.1. DC Transfer Function

"Individual storage cells have slightly different capacitor sizes that are read by non-linear Wilkinson ADCs. Thus, each storage cell needs to be calibrated against different input voltages to characterize the relation between voltages and ADC values (transfer function). This is done internally on the board with the DACs of CT5TEA creating the pedestal voltages as reference. Therefore, it is possible to re-calibrate the DC transfer function of the ASICs in situ. For on-the-bench calibration, an external trigger is used to cover all storage cells equally. For this purpose, the Keysight 33622A function generator is used, creating a 3.3 V square pulse of 25 ns width at 600 Hz, connected to the board's trigger input. The clocks

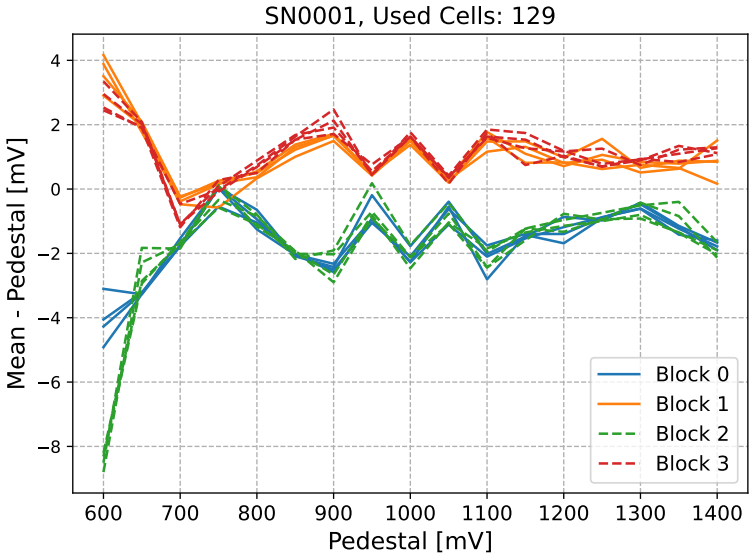

Figure 73: The mean response of storage cell 129 is subtracted by its individual response, depending on the digitisation block and the different pedestal voltages. A colour code indicates which digitisation block the storage cell is located in. For visualisation, only every eighth position is plotted. Therefore, block four is skipped.

of the function generator and the evaluation board are not synchronized to ensure an equal event distribution over all storage cells." This is also valid for the pedestal subtraction. "For one DC transfer function, the full voltage range of the DACs of CT5TEA is used in steps of 50 mV, resulting in a maximum voltage range of about 2.2 V."

"For each DC transfer function, 20,000 waveforms per DC voltage are recorded. It has been found that the digitization phase[4] of a storage cell influences the digitized value. Depending on whether the number of the digitization block is even or odd, the digitized value of the storage cell can change by up to ± 2 mV from the mean over all digitization blocks." For some pedestal voltages, it even performed worse. An example of this behaviour is given in Figure 73. The block dependency vanished at the operational pedestal of 750 mV as the standard implementation of the pedestal subtraction already takes the block dependency into account.

"Therefore, for the standard operation of 128-sample waveforms, an individual transfer function is constructed for each storage cell and its five possible digitization phases. It should be noted that switching noise associated with the addressing of the storage array means that a given set of DC transfer functions are only valid for a set trigger delay, i.e. look-back time between receiving an trigger and location in

[4]Position of the block in which the sample is located during the digitization process

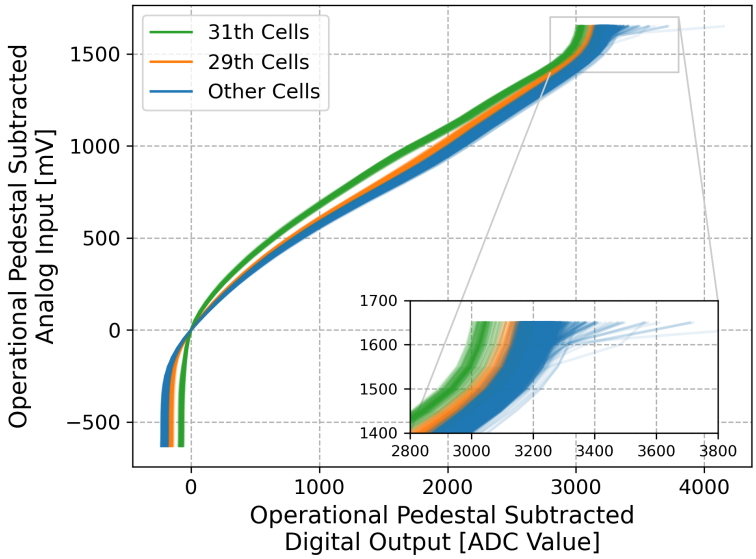

Figure 74: "All 4096 individual DC transfer functions of channel 0 for one digitization block phase of SN0001 with the operational pedestal already subtracted. The different behavior of each cell is color-coded, corresponding to its position in the storage block. A standard error or standard deviation of each individual transfer function is not given due to visibility reasons." [21].

the storage array."

"Example DC transfer functions of SN0001 of channel 0 in the first digitization phase can be seen in Figure 74. It is apparent that the operating pedestal voltage is already subtracted and that there are three distinct cell behaviors. This is a known feature since TARGET 5.

For large ADC counts, the slope/resolution of the transfer function increases/decreases again for most cells, with the exception of certain cells. These can be observed in the zoom panel of Figure 74. Due to tolerances in the fabrication process of the ASICs, some storage cells saturate earlier. Consequently, the stored voltage rises slower than the applied analog input, leading to higher ADC count values for the same analog input."

For the application of the DC transfer function, the calibration algorithm applying it must be performant enough to sustain online calibrations at a rate of 600 Hz [179]. A 2D lookup table for the DC transfer function to interpolate from is not sufficient as the algorithm has to search, scan, and interpolate it at a rate of 76.8 kHz for waveforms of 128 ns. Therefore, the transfer functions are pre-interpolated and then saved in discrete steps of n ADC value steps, so the location of the relevant part of the transfer function is just a division instead of a search algorithm. A

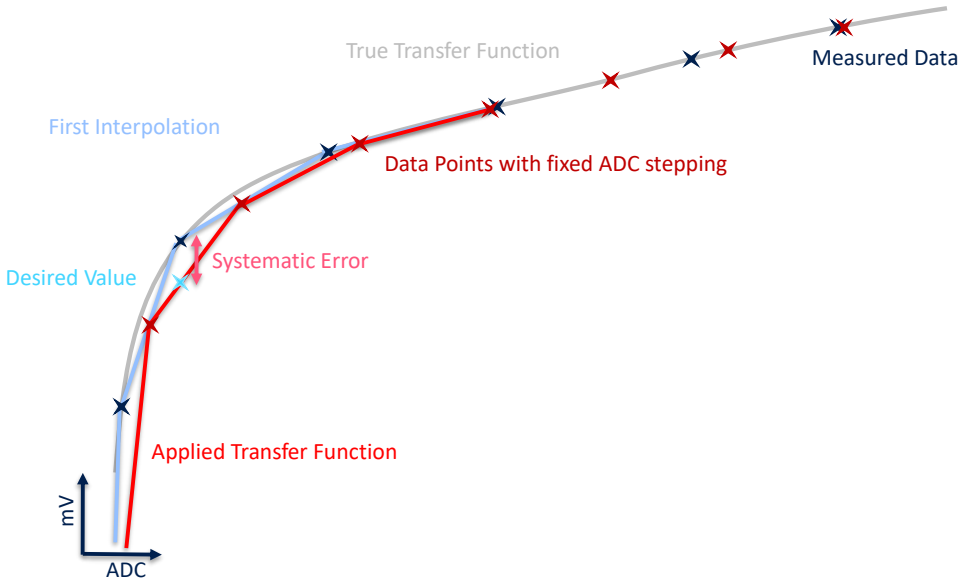

Figure 75: Illustration of the difference between the true transfer function of the storage cell, the stored and pre-interpolated transfer function, and the applied transfer function and how it creates a systematic error.

linear fit between the points of interest then calculates the value. However, this can lead to systematic error in applying the transfer function, as it is illustrated in Figure 75.
When measuring the transfer function, certain parts of the true transfer functions are probed. Pre-interpolation and the drawing with fixed ADC value steps already lead to deviations in regions of increased curvature. By applying the calibration algorithm now, the closest ADC value smaller than the required value is determined via an integer division and the points of interest are calculated by linear interpolation between the points. Therefore, the transfer function is now twice interpolated, which will lead to systematically errors as ADC values in regions with negative curvature of the transfer function will systematically be smaller and vice versa.
To test this systematic error, a "true" DC transfer function is generated by measuring 512 voltage values corresponding to all directly measured `Vped` settings, so roughly $\approx 5\,\mathrm{m\,V}$ difference per setting. Then transfer functions are generated using only 256, 128, 64 and 32 of these measurement points (evenly distributed), with an ADC stepping of 4, 8, 16, 32, 64 and 128, once linearly pre-interpolated and once quadratically. The voltage values of the "true" transfer functions are then reconstructed with these transfer functions to measure the systematic differences.

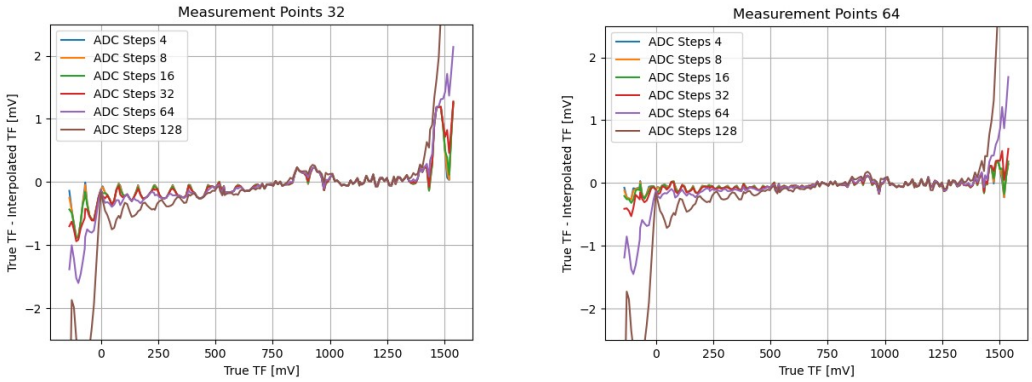

Figure 76: Estimated systematic error of DC transfer functions in dependency of the ADC steps used for the linear pre-interpolation and the amount of voltage measurements. Left: 32 voltage steps. Right: 64 voltage steps.

The results for the interpolated transfer function with 32 ($\approx 80\,\mathrm{mV}$ steps) and 64 ($\approx 40\,\mathrm{mV}$ steps) measurement points can be seen in Figure 76.
Independent of the measurement points, ADC steps, and interpolation type, the systematic error follows the shape of the transfer function exactly as expected. Even the small change in curvature around 900 mV can be spotted. The systematics are drastically increased below 0 V, negligible for pulse mode operation, and above 1.4 V, where the transfer function slowly enters the saturation regime. Here, the systematic is also negligible, as the SNR in pulse mode operation is very high. For the relevant area, does an increase in measurement points (smaller voltage steps) reduce the interpolation artefacts, while a decrease in ADC steps decreases the overall systematics, both as expected. From Figure 76 it becomes apparent that an ADC stepping of 32 ADC-counts with 64 ($\approx 40\,\mathrm{mV}$ steps) measurement points is sufficient for systematics below $\pm 0.4\,\mathrm{mV}$ over the whole dynamic range with a mean systematic of $\pm 0.1\,\mathrm{mV}$.
"The temperature within the SST camera is unlikely to remain uniform and constant over all operational conditions, and therefore a temperature analysis of the DC transfer functions has been performed. For each temperature, a DC transfer function with baseline subtraction is recorded. The baseline changes by up to $0.2\,\frac{\mathrm{ADC}}{\mathrm{K}}$ and even $0.5\,\frac{\mathrm{ADC}}{\mathrm{K}}$ for the 31st cell. But just like the DC transfer function, the baseline subtraction can be redone at any time, correcting the baseline shift independent from slope shifts.
An example of the temperature variations in the DC transfer function is presented in Figure 77 for SN0001, where each transfer function over all channels, storage cells, and block phases at a certain temperature is subtracted from the corresponding transfer function at the reference temperature of 30 °C and then averaged, standard

deviation as a semi-transparent band. From 0 mV up until 500 mV, the temperature dependence is nearly negligible with a change of about $< 0.1 \frac{\text{ADC}}{\text{K}}$. Above 500 mV and below 0 mV, the difference for one temperature grows approximately linearly with the pedestal voltage until the slope of the transfer function increases. With a temperature dependence of $1.75 \frac{\text{ADC}}{\text{K}}$, re-calibration of the DC transfer function is favorable for different temperatures."

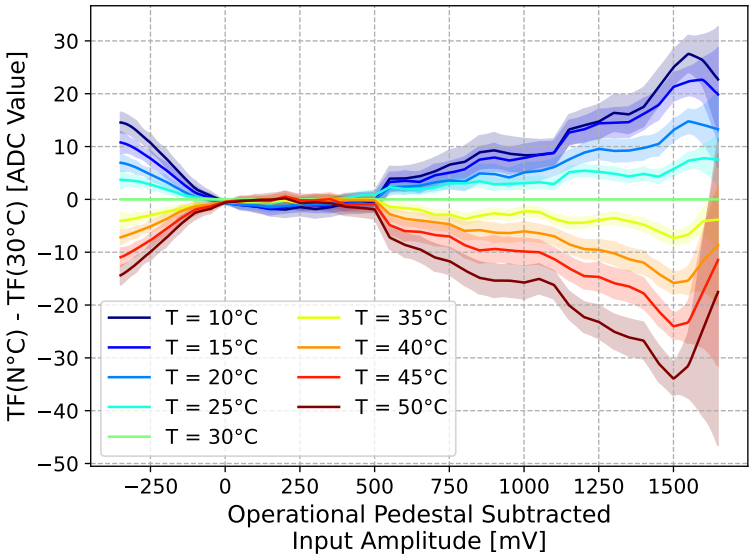

Figure 77: "Temperature dependence of a DC transfer function as voltage difference between the transfer functions at different temperatures of SN0001. Standard deviation over all channel and storage cells given as semi-transparent band." [21].

11.6.2. AC Correction Transfer Functions

"One way to improve the AC noise for pulse-shaped data that emerge in SiPM measurements is an AC Correction transfer function. The objective here is to directly correct the observable, such as the amplitude or the integral of the pulse. The advantage is that it reduces the noise and is sensitive to possible bias and gain mismatches from internal and external components. An external AC correction is essential as the absolute accuracy is not measurable with an internal DC calibration if for example a shaping circuit is used in front of the ASICs.
As a function generator, the Keysight 33622A is used, generating Gaussian-shaped pulses of 10 ns width similar to the expected output of the shaped photo multiplier pulses. With the signal splitter board, the pulses are injected parallel to the 16

channels of the evaluation board. The external trigger is used to cover all storage cells equally in all of their digitization phases.
To extract the pulses digitized by CTC, the pulses are upsampled by a factor of ten to allow a finer adjustment of the applied matched filter (Gaussian). The maximum amplitude of the filtered signal is assigned to the storage cell in which it occurred. The positive dynamic range of 1.65 V appears smaller because the matched filter artificially shrinks the amplitude. Around 100,000 waveforms are required (corresponding to around 25 maxima per storage cell), to obtain a mean standard error of 0.2 mV in a range of 0 - 1.3 V. In the saturation regime, the error increases up to 0.8 mV until the hard cap saturation due to the limited positive dynamic range of 1.65 V of the Wilkinson ADC reduces it again.
An example AC correction transfer function of SN0001 of channel 0 and all storage cells is shown in Figure 78. While linear from 50 mV to 2 V, it saturates smoothly due to the Gaussian filter. The AC correction transfer function is only valid if the pulses are extracted in the same manner. To not dictate the charge extraction method, it is possible to scale the entire waveform by the AC correction to address any possible bias without worsening the signal-to-noise ratio.

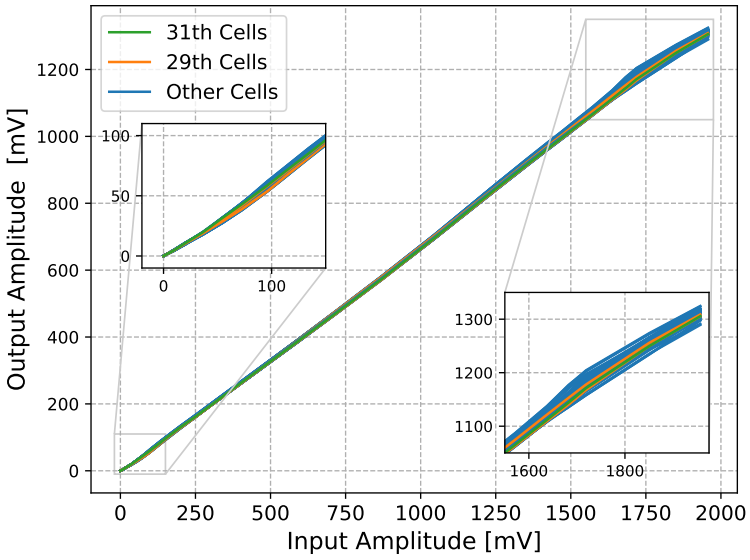

Figure 78: "Example of AC correction transfer functions of SN0001 with both non-linear regimes highlighted. A difference in 29th and 31st cell behavior is not observed." [21].

As the AC correction relies on external pulses, re-calibration while operated in a camera is not possible. Therefore the AC correction must be temperature stable or recorded at different temperatures in the lab prior to installation in the camera. The

temperature analysis results are presented in Figure 79. The transfer function is sufficiently stable with a temperature-induced spread below ±1 mV for amplitudes below 500 mV and a relative error below 0.5 % over four decades of degrees Celsius. The spike in the saturation regime of the transfer function at 1650 mV emerges from the lack of measured amplitudes where the slope changes. The evaluation of the performance under different temperatures is presented in Section 13.5."

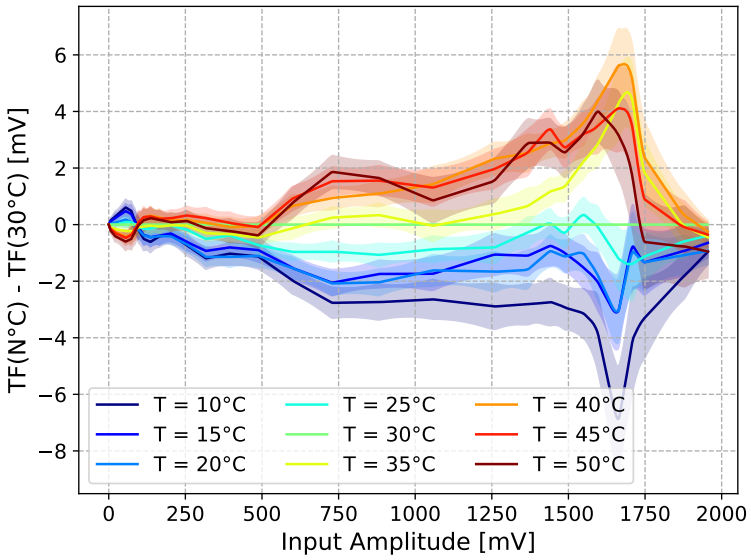

Figure 79: "The temperature dependence of the AC correction transfer function is given as the voltage difference between the transfer functions at different temperatures of SN0002. The standard deviation of all channels is given as a semi-transparent band." [21].

11.6.3. AC Correction in TARGET Modules

For characterisation and isolated use of the CTC, the main benefits of the AC correction transfer function are the linearisation of the input-output curve at small amplitudes and the correct scaling. In the context of the TARGET modules, this could become obsolete. With the addition of the SiPM and shaping circuit, additional calibration efforts must be implemented as the input-output curve of this signal chain has to be understood, similar to the intention of the AC correction transfer function. This would also cover the AC correction as it is part of the whole signal chain. Instead, the AC correction transfer function could serve an additional purpose.
The shaping circuit of the TARGET modules is designed in unison with the chosen SiPMs of the SST camera, so that a gain of 3.37 $\frac{\text{mV}}{\text{p.e.}}$ is generated. As it is fully

analogue, there are performance differences due to the part-to-part deviations. For the modules, an AC correction transfer function can nevertheless be used with the shaping circuit included. Therefore, the AC correction transfer function enables correction of the non-linearities of the ASIC as initially proposed and also addresses variations in the shaping circuit, to enforce equal conversion factors for each channel.

12. Wilkinson ADC Tuning

Several in-depth adjustments to the Wilkinson ADC are conducted to enhance its performance. To get a grasp of these adjustments, the Wilkinson ADC must be described in its full complexity beyond the initial description of "A clock counts up until a ramping voltage equals the to be digitised value". The necessary bits to understand the calibration are described in the respective section.

12.1. Wilkinson Comparator Tuning

The Wilkinson comparator is the component that compares the voltage value of the to-be-digitised storage cell to a voltage ramp. A minimalistic design based on three Metal–Oxide–Semiconductor Field-Effect Transistor (MOSFET) transistors and three auxiliary MOSFET to set the switching behaviour is chosen to save space on the silicone substrate. The schematic can be seen in Figure 80.

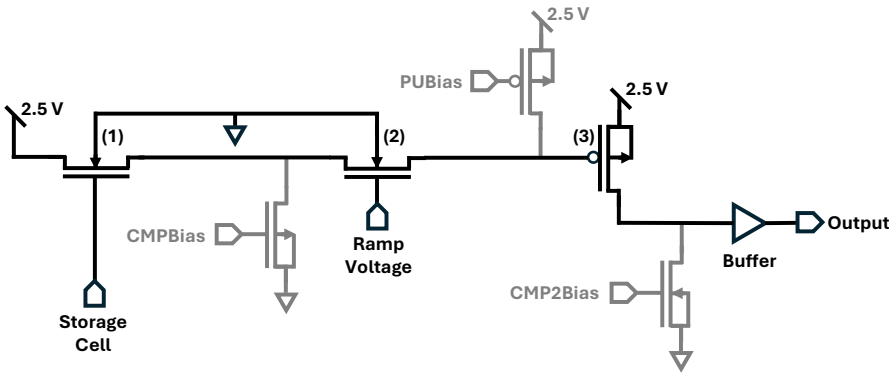

Figure 80: Schematic of the Wilkinson ADC comparing the storage cell voltage to the ramp voltage in order to generate the stop signal for the Wilkinson clock. In black the bare Wilkinson ADC with the individual MOSFETs marked and in grey the auxiliary MOSFETs to tune the switching behaviour of it.

For the digitisation process, the voltage of the to be digitised storage cell is applied to the gate of a n-typed Metal-Oxide-Semiconductor (nMOS) (1), which controls the current flow between the drain and source of it. The drain is supplied by the 2.5 V supply rail. Therefore, the current at the source of the nMOS is proportional to cell voltage. This current is then applied to the drain of another nMOS (2), whose gate is served by the Wilkinson ramp. Consequently, the nMOS is getting closed by the increasing voltage applied by the Wilkinson ramp at the gate. Depending on the current set by the initial nMOS (1), and, therefore, cell voltage, the current after the source is cut off at different times for the same voltage ramp. The source

current is then applied to a p-typed Metal-Oxide-Semiconductor (pMOS) (3) gate, which again controls the current of the 2.5 V supply rail. When the current cuts off of the two nMOS (1 + 2) construct, the pMOS (3) opens and a high level is created. This is then applied to a flip-flop to save the state, so that in no circumstance can the signal be generated multiple times for one digitisation process. The output is then transferred to the shift register, buffering the 12-bit Gray-code counter value, and stops it. For a new digitisation process, the flip-flop is reset.

In order to fine-tune the comparator and adjust its switching behaviour, three auxiliary MOSFETs are installed after the source of the primary ones. All of the auxiliary MOSFETs control the potential of the source by opening or closing their gates, adding or lowering the potential as their own source or drain is connected to ground or 2.5 V. Therefore, the voltage between the drain and source of the primary MOSFETs is changed, and so is their working point.
The three gates of the MOSFETs are controlled by separate DACs, called `CMPBias`, `PUBias` and `CMP2Bias`. While `CMPBias` and `PUBias` shift the switching point of the comparator up or down the voltage ramp for the same storage cell voltage, `CMPB2ias` changes the amplitude of the signal feeding the flip-flop, changing the register and stopping the Wilkinson clock. Therefore, the Wilkinson clock stops earlier or later depending on the setting. On a macroscopic scale, the baseline noise of the waveform and the dynamical range of the ADC do change with different settings. But unexpected phenomena, such as the spikiness of small pulses or a prepulse offset in digitisation blocks, are also observed.
The spikiness of small pulses was already found in [180] and could be suppressed by adjusting the `CMP2Bias` from 746 DAC-counts to 1200 DAC-counts. It is suspected that a lower value causes the comparator to switch too fast, leading to possible cross-talk from the switching process and introducing high-frequency switching noise to the voltage of an adjacent storage cell [181]. Different levels of prepulse offset were observed across different parameter settings, but a pattern was not found. Therefore, the Wilkinson comparator is optimised in terms of the dynamic range and baseline noise of waveforms.

The tuning process unfolded over multiple years, as several tweaks were made at different times, driven by new insights. It started with a coarse scan over the three parameters, conducted by Dr. Adrian Zink, to investigate the prepulse offset, the spikiness of small pulses, and the overall baseline noise. The three parameters with sufficient performance in all tested criteria and starting point for this work's tuning were `CMPBias` = 1600 ADC-counts, `PUBias` = 3200 ADC-counts and `CMP2Bias` = 1200 ADC-counts.
While investigating the performance of DC transfer functions, it was observed that

not all storage cells met the criteria of the dynamic range up to 2.4 V, as they saturate early. As there are < 4096 ADC-counts used in the transfer function, it can be concluded that the slope of the Wilkinson ramp together with the counting speed of the 12-bit Gray counter ratio is near the optimum and should be able to digitise higher voltages. Therefore, the switching behaviour of the Wilkinson ADC must be tuned.
The suitable parameters for this task are `PUBias` and `CMP2Bias`, as only they can alter the switching behaviour of the comparator depending on the input voltage from the storage cell. As the `PUBias` with 3200 DAC-counts is already near the limit of 4096 DAC-counts and the DACs start to get non-linear (see Section 11.2), only `CMPBias` is increased from 1600 DAC-counts to 1800 DAC-counts. This solved the dynamic range problem across all storage cells for the tested evaluation boards SN0001 and SN0002, and maintained the baseline noise at ≈ 0.90 ADC-counts. The performance published in [21] is a product of this tuning.
Evaluating the first batch of TARGET modules and, therefore, having a larger statistics for ASIC to ASIC variations, it became apparent that the adjustment from 1600 DAC-counts to 1800 DAC-counts is not enough for most ASICs. 1 % of all storage cells over all tested CTCs failed to reach the full dynamic range. The optimum is close but not yet found.

In preparation for the first measurements with a quarter of the SST camera on the telescope, all three Wilkinson comparator parameters were rescanned ± 200 ADC-counts around their respective value instead of blindly cranking up the `CMPBias` value. For each set, a baseline waveform is recorded at 750 m V to test the baseline noise, and one at 2.4 V is recorded to check whether the dynamic range is met. The best conclusion was nevertheless to increase the `CMPBias` by 200 ADC-counts from 1800 ADC-counts to 2000 ADC-counts as intuitively thought. All storage cells for all tested CTCs now reach the full dynamic range, with a small safety margin to accommodate more ASIC to ASIC variations. Therefore, the baseline noise increased from ≈ 0.90 ADC-counts to ≈ 1.00 ADC-counts, a valuable sacrifice as the baseline noise of a TARGET module in the camera will be dominated by the SiPM.
As the parameters grew historically, a brute force scan over all comparator parameters and for multiple ASICs parameters was conducted by Matthias Able [182] to testify if these parameters are truly ideal or just a local maximum in the phase space or statistically not representable for a large batch of CTC ASICs. All issues, including the baseline noise in waveforms, the dynamical range of the ADC, the spikiness of small pulses, and the prepulse offset, were quantified and tested for each parameter pairing. The short answer is: The historically grown parameters are ideal and statistically representable.

12.2. VBias Tuning

Strictly speaking, the `VBias` tuning is not part of the Wilkinson ADC tuning as the `VBias` controls the driving strength of the buffer between the sampling and storage cell array. But by changing the `VBias`, the dynamical range of the ADC can be adjusted, similar to the Wilkinson comparator tuning and is therefore an alternative worth mentioning. By increasing the driving strength of the buffer, higher voltages will be compressed, as the buffer has only a limited amount of headroom. Therefore, the voltage stored in the storage cells is smaller. With overall smaller voltages to cover for the Wilkinson ADC, the tuning must not be at the optimum. More dynamic range for the ADC is generated by decreasing the voltage range covered by the ADC. However, this also comes at the cost of not using the Wilkinson ramp and clock to its full potential, reducing the overall resolution of the ADC. A schematic of this process can be seen in Figure 81.

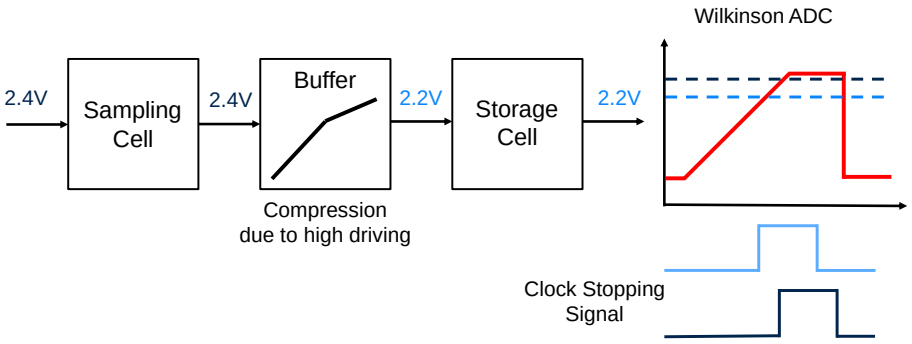

Figure 81: The signal chain from the sampling cell to the digitised value, illustrated as schematic blocks. Driving the buffer between sampling and storage cells compresses the storage cell voltage and, therefore, results in a lower digitised value for the same input voltage.

The compression also introduces a non-linearity into the response of the storage cells. But since each storage cell is calibrated by its own DC transfer function, this is acceptable, as it will be corrected anyway. Another disadvantage of this method is the significantly increased power consumption of the ASIC. An increase of 1200 ADC-counts to 1200 ADC-counts already leads to nearly twice the power consumption. Therefore, this is not a viable option for the SST camera. However, it might be an interesting option for different experiments.

12.3. Wilkinson Clock Adjustments

The 12-bit Gray code counter in the Wilkinson ADC is clocked by the Wilkinson clock. For this generation of TARGET ASICs, a clock frequency of 208.3 MHz was chosen. Initially, 250 MHz were planned to reduce the readout time per sample. But the frequency was too high for the receivers, so it was reduced to 208.3 MHz, twice the historic 104.167 MHz. This leads to inconsistent timing in the start of the 12-bit Gray-code code counter, resulting in 1 ADC-counts variations between digitised blocks. The issue only surfaced due to the better performance of the ASIC by better parameter settings, as the historical clock value of 104.167 MHz also leads to the same problem.
The start of the voltage ramp and the 12-bit Gray-code counter is clocked by the Ramp Sync clock, whose period is matched to the 12-bit state machine that transfers the digitised values. Therefore, the Ramp Sync clock period is twelve times that of the HS clock, clocking the 12-bit state machine. For the TARGET evaluation boards the HS clock period is 10.66 ns. Therefore, a digitisation process can be started every 128 ns. With the Wilkinson clock initially synchronised, running at a period of 4.8 ns (208.3 MHz), the Wilkinson clock period is not a whole multiple of 128 ns. It takes three Ramp Sync clock cycles until the phase of the Wilkinson clock and the Ramp Sync clock match again. The 12-bit Gray-code counter can therefore miscount as the inherited phase creates an imbalance between one and zero states, and the counter only responds to the one states. This is illustrated in Figure 82, where all three Wilkinson phases are displayed in correspondence to the ramp start and stop signal. For phases 1 and 2, the counter receives three clock instructions, while for phase 3, four clock instructions are introduced.

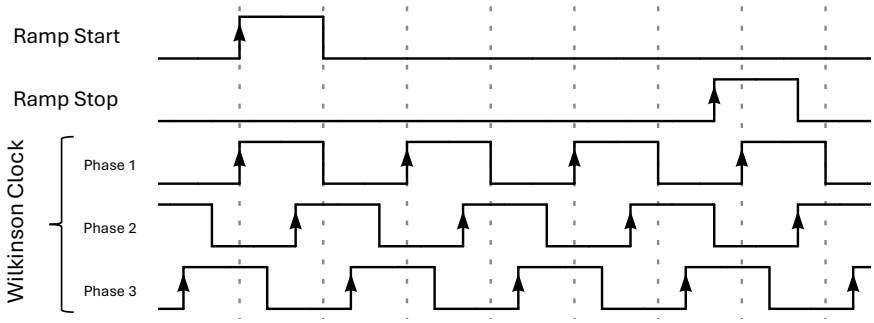

Figure 82: Illustration on how the different phases of the Wilkinson clock with respect to the ramp sync clock lead to 1 ADC-counts variations in the digitised value. Created with [183].

12.4. Wilkinson Ramp Start Synchronisation

While testing the first batch of TARGET modules for the Quarter CAMera (QCAM), the baseline noise of a pedestal (and DC transfer function) calibrated module behaved unexpectedly. Sometimes it was around 0.8 ADC-counts, even below the expected noise level measured with the evaluation boards, and sometimes it was twice or even three times that. This behaviour could be traced to the state of the TARGET module, whether it was power-cycled, freshly initialised, or only reconnected.

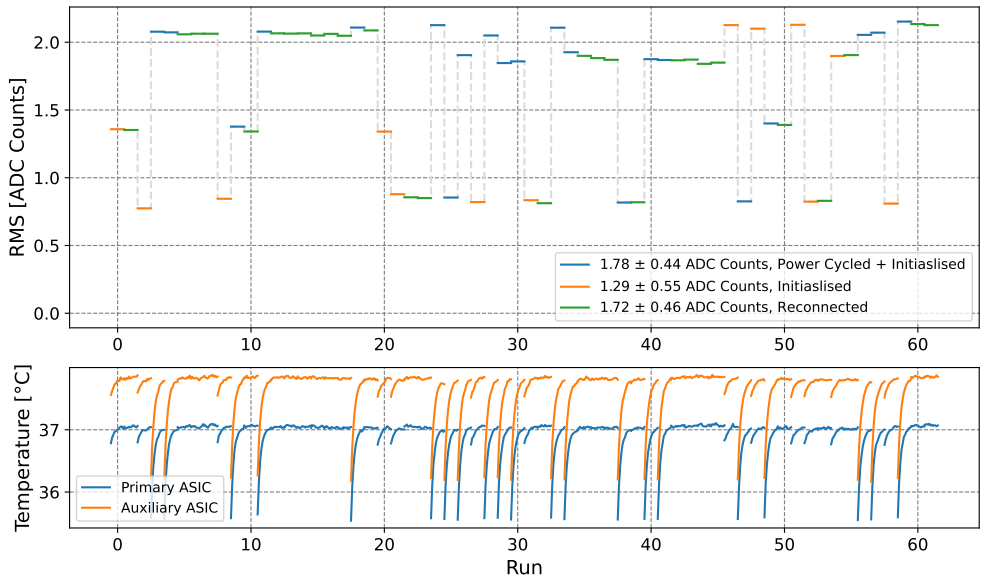

Figure 83: Top: RMS of the baseline noise depending on the initialisation process of the module. Bottom: Associated temperature per measurement run to exclude temperature effects.

To investigate this pattern, multiple pedestal runs are performed in which a random decision counter decides by chance whether the module is power-cycled, freshly initialised, or the computer only reconnects to the module. Between each run, there are 60 seconds of waiting time as the ASIC can fall out of thermal equilibrium after, for example, being power cycled. The temperature is monitored on both modules via the implemented PT100 between CTC and CT5TEA to exclude any temperature effects. From the first run, a pedestal calibration file is generated, and each subsequent run is calibrated with this reference pedestal. The mean baseline noise for each calibrated run can be seen in Figure 83 at the top, with the colour of the run indicating whether the module was power-cycled, initialised, or only reconnected. At the bottom, the monitored temperature of each respective board

is used to rule out any change in baseline noise due to temperature changes.
From here on, it becomes apparent that the initialising process[5] sets the module in a possibly different state, resulting in a change in baseline noise if a different state is set.
Comparing the setting of the ASICs on the evaluation board with the ones from the first batch of TARGET modules, only the HS clock, clocking the digitised value to the FPGA, has changed from initially 93.75 MHz to 62.5 MHz. This is done because the transceiver on the CTC, which clocks the serial data to the FPGA, has a lower bandwidth on the TARGET module than on the evaluation board. With lower bandwidth, the rising and falling times of edges slow down. Sequences as 010, for example, could be misinterpreted as 000, as the rising edge does not have enough time to cross the threshold to be interpreted as 1 before the next 0 is clocked in. An example can be seen in Figure 84.

Figure 84: Comparison between the serial data transmitted by CTC in yellow and the by the FPGA received and interpreted serial data in green, with the HS clock in purple. In this example, the FPGA correctly interprets the serial data, but the low bandwidth of the CTC transceivers is evident. Image by Adrian Zink.

As this is not always the case, but only for some events, it must be a more subtle change that influences the bandwidth of the transceivers. The suspected reason is the different PCB of the TARGET modules, where the data transmission lines are impedance-matched, as opposed to the evaluation board, where this is not the case. Therefore, the signal would over- and undershoot on the evaluation boards, thereby crossing the necessary thresholds. This is the assumption and is not measured, as the clock has to be changed anyway.

[5]Power cycling also has an initialising process to follow.

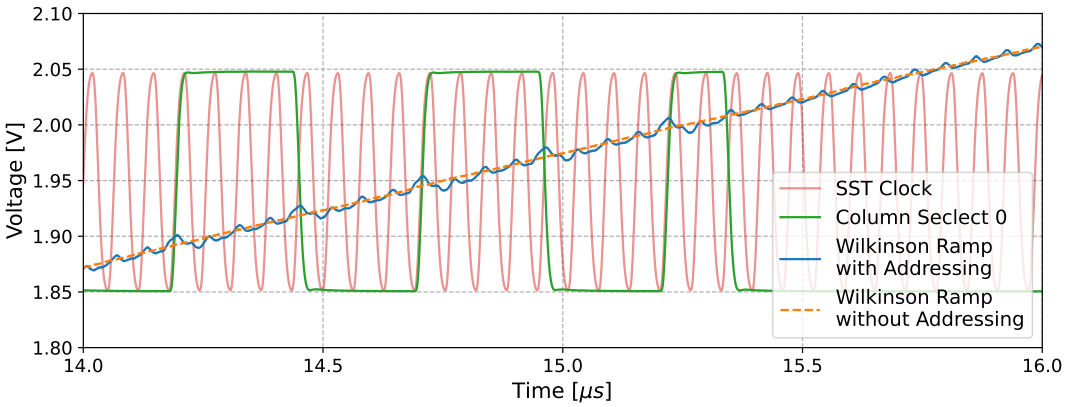

Figure 85: Comparison between the Wilkinson ramp with addressing and sampling while digitising (blue) and without (orange). The spikes on the ramp are introduced by different digital signals, such as the SST clock for sampling (red) or the Column Select 0, which is part of the 8-bit parallel bus addresses.

With the HS clock changed to 62.5 MHz, the data transmission issues are solved, but the new baseline noise dependency on the initialising states is introduced. A very similar issue is discussed in Section 12.3, where the ramp start period is not a whole multiple of another cycling observable, the Wilkinson clock. This time, it is the storage cell array of 4096 ns, which is not a multiple of 192 ns, the new Ramp Sync clock period, which is based on twelve cycles of the HS clock. When the Wilkinson ADC digitises a certain block in the storage cell, the 8-bit parallel bus continues to address the data transfer between the sampling and storage cells. Therefore, as this is a digital signal with sharp edges, systematic noise will be introduced to the Wilkinson ramp as seen in Figure 85.
For the old HS clock, which is a whole multiple of the storage cell array, this cross-talk, seen as bumps in the voltage ramp, is always at the same position. A pedestal (and DC transfer function) will cancel this effect. But with the new HS clock at 62.5 MHz, the bumps depend on the phase between ramp start and storage cell addressing. In principle, this is okay, as the pedestal is digitisation block-dependent and can handle it (and so can the block-dependent DC transfer function). But the phase between the ramp start and the storage cell addressing depends on the initialisation process, during which all clocks are synchronised. Consequently, three phases are created, observed in Figure 83. The pedestal file can have the same initialisation phase as the record one or not. Depending on the match, the baseline noise is as expected or worse.
To fix this issue, the HS clock is reduced again to 46.88 MHz, so the Ramp Sync clock period equals 256 ns, which is a whole multiple of 4096. To ensure that the

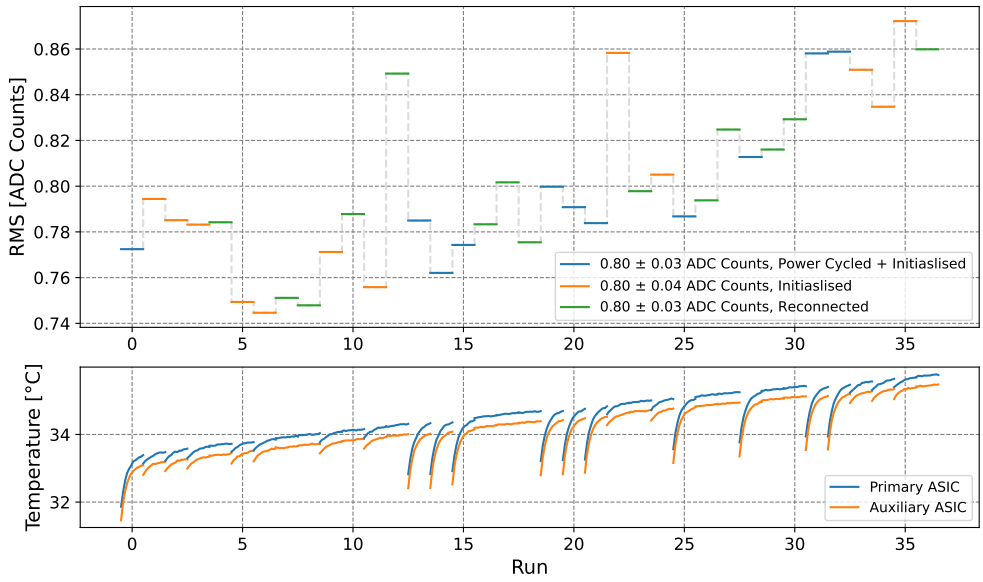

Figure 86: Top: RMS of the baseline noise depending on the initialisation process of the module, after firmware adjustments. A dependency of the initialising process is not given anymore. Bottom: Associated temperature per measurement run to exclude temperature effects. Over the measurement runs, the temperature increases by 2 °C, explaining the worsening baseline noise per run.

fix works, the initial test with multiple pedestal runs with random power cycling, initialising or reconnection in between runs, is conducted again. The results can be seen in Figure 86, with the top panel using the same colour coding as previously seen in Figure 83 and the temperature monitoring at the bottom.
The RMS of each run is 0.80 ADC-counts independent of the initialising process. Although the overall RMS gets worse as time (or runs) progresses. However, this is simply due to the overall increase in temperature across all runs, as can be seen at the bottom. The pedestal file used to calibrate all other runs is not at the same temperature as the later ones. From Section 11.5, it is already demonstrated that the pedestal is temperature dependent.

13. Performance Characterisation

To keep the performance characterisation of the ASICs as general as possible, the AC correction transfer function is only applied in pulse mode. For the evaluation of bandwidth, cross-talk, DC- and AC noise, it is therefore excluded.

13.1. Power Consumption

"The power consumption can be monitored by measuring the voltage drop over an external 0.1 Ω series resistor after the LDO linear regulator. Initialized and operating at a voltage offset of 750 mV (see Section 11.6.1), the operational pedestal voltage, the pair of ASICs consume on average (942.7 ± 0.1) mW, resulting in a moderate power consumption of (58.9 ± 0.1) mW per channel. This value strongly depends on the selected operational pedestal voltage." This can be seen in Figure 87, where the default operating pedestal voltage of 750 mV is marked with the grey dashed line. "The minimum is at the lowest settable pedestal voltage. As a common reference, the total consumption is (641.7 ± 0.1) mW at 150 mV. The highest total consumption is at an operational pedestal voltage of 1360 mV and is (1051.6 ± 0.1) mW. A correlation of the power consumption with the trigger rate or the amplitude of input pulses is not observed."

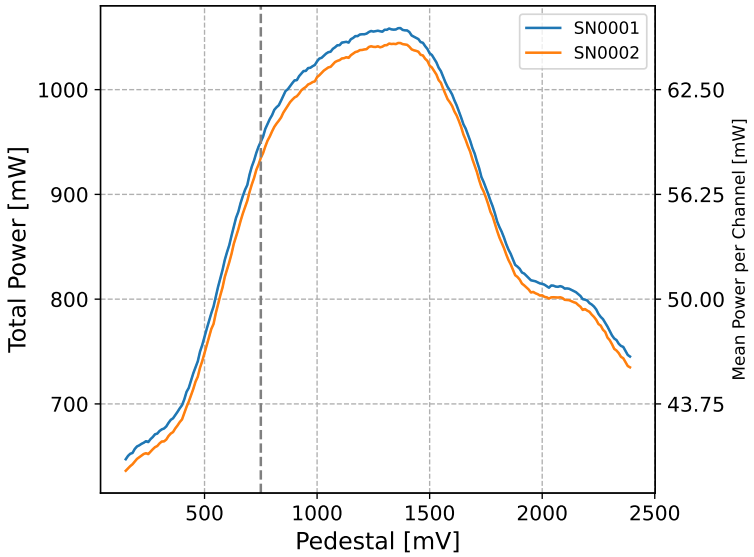

Figure 87: The total and per-channel power consumption of both ASICs of both evaluation boards as a function of the settable operational pedestal voltages.

13.2. Bandwidth and Cross-Talk

"For the bandwidth and cross-talk measurements, one data set is used for each evaluation board. This set is created by applying a sine wave pulse of 400 ns length, from 10 MHz up to 600 MHz at an amplitude of 500 mV to each input channel individually with the Active Technologies AWG-4022 function generator over a 40 m long coaxial cable. The short pulse and the long cable ensure that the amplitude of the sine wave signal is not distorted by reflections of mismatched input impedance of the evaluation board or ASIC. Additionally, the short pulse avoids memory effects in the storage cell array due to a possible charge-up of the individual capacities from a continuous sine wave. The operational pedestal voltage is set to 1.5 V instead of 750 mV to measure the negative amplitudes at a reasonable resolution. All data is calibrated with a DC transfer function with the 1.5 V pedestal voltage offset. The amplitude is extracted through a sine wave fit. Although frequencies above 500 MHz are not extractable for a 1GSa/s sampling, knowing the input frequency, the amplitude can still be extracted by a fit.

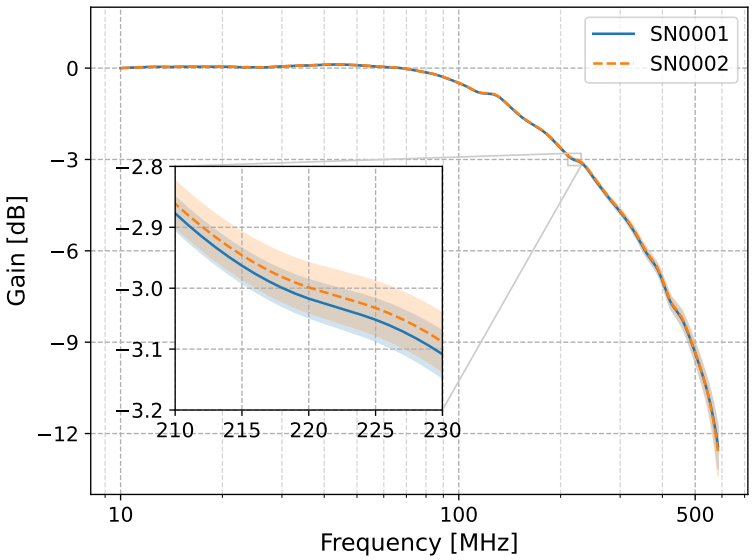

Figure 88: "The mean bandwidth of both ASICs with a 15 MHz sliding average, - 3 dB point highlighted. The standard deviation of the channel-to-channel spread as semi-transparent band." [21].

The bandwidth of both boards can be seen in Figure 88 smoothed with a 15 MHz sliding average to suppress ripples generated by the 64 ns sampling cell array. The channel-to-channel standard deviation is given as a semi-transparent band. The -3 dB point is around 220 MHz, with a gain flatness of 0.2 dB up to 80 MHz.

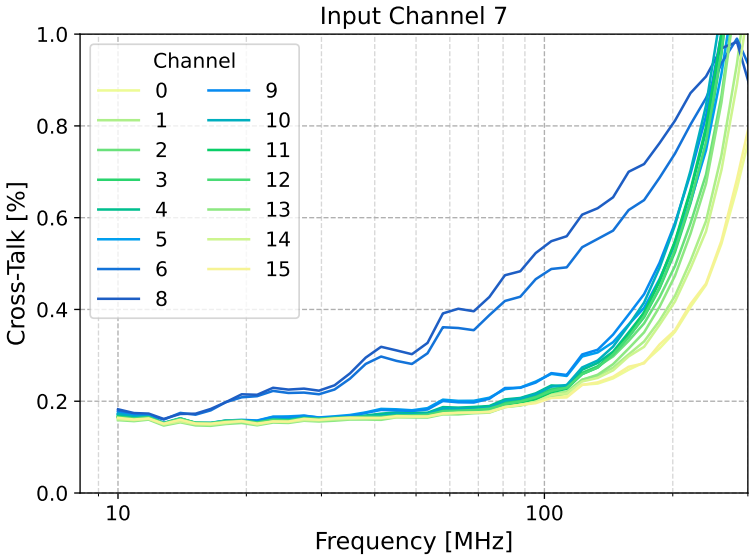

Figure 89: "Frequency dependent cross-talk with channel 7 as input channel. It should be noted that standard errors are included, but are not visible. The baseline noise of each channel creates an artificial cross-talk of about 0.2 %." [21].

Taking the $5\,\sigma$ width of a Gaussian-shaped pulse in the frequency spectrum, the ASIC is suited for pulses down to 3.6 ns over the whole - 3 dB bandwidth and digitizes pulses with widths up to 10 ns undistorted. This is matched to the pulses in the SST camera, where the exponential decay of a SiPM is shaped into a pulse of 10 ns width.
For the evaluation of the frequency-dependent cross-talk, the RMS of every measured channel divided by the RMS of the input channel is used. The results for channel 7 of SN0001 can be seen in Figure 89 with a mean standard error $<$0.01 mV. The color gradient gives the distance to the input channel on the board. Only the next neighbor channels receive a measurable cross-talk, while the other channels simply weigh the baseline noise against the amplitude, resulting in an artificial cross-talk of 0.2 %. Therefore, the cross-talk grows strongly over 100 MHz as the bandwidth of the ASIC drops, while the noise floor remains unaffected. Over the whole - 3 dB bandwidth of the ASIC, the overall cross-talk does not exceed 1 % for both modules.
For a more realistic approach that mimics cross-talk as in the SST camera, Gaussian-shaped pulses of 10 ns width are fed into the input channel. To quantify the level of cross-talk, the integrated pulse of the selected channel is divided against the integrated pulse of the input channel. The advantage of this method is that the integral minimizes the contribution of the noise floor, allowing a better signal-to-

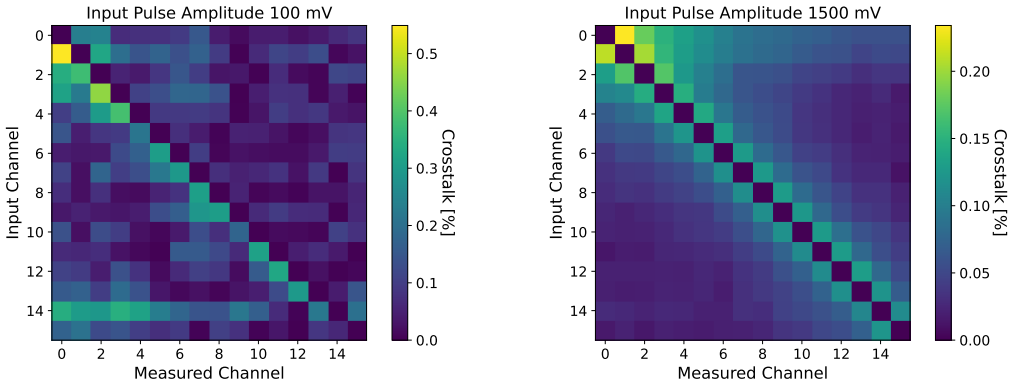

Figure 90: "Cross-talk matrices for pulse amplitudes of 100 mV ... [left] and 1.5 V ... [right] of SN0001. The integral of the selected channel is divided by the integral of the input channel." [21].

noise ratio and, therefore, less distorted cross-talk, as it is the favored method of charge extraction. In Figure 90, the corresponding cross-talk matrices for two different amplitudes can be seen. With the ground plane as close as possible to the signal track and a signal track distribution over two layers of the PCB, the cross-talk is successfully minimized to levels below 0.5 % for small amplitudes and 0.25 % for large amplitudes. The clustering of channel 0 to 3, and 15 and 16, suggests that most of the cross-talk is due to the traces of the evaluation board and not the ASIC itself, as these groups connect separately on top and bottom of the CT5TEA as opposed to the rest. This behavior is also visible in the frequency-dependent cross-talk."

13.3. DC Noise

"To evaluate the DC noise of CTC ASIC, the standard deviation of the calibrated DC voltages to generate the DC transfer function is used. It can be seen in Figure 91 and the noise correlates to the shape of the DC transfer function seen in Figure 74. Towards the increasing slopes of the DC transfer function, the DC noise increases drastically as the mV-to-ADC ratio drops significantly. The operational pedestal voltage of 750 mV is therefore chosen as a compromise between the lowest possible baseline noise while retaining a high dynamical range of positive voltages."

13.4. Effective AC Noise

"Most experiments using the TARGET ASICs receive pulsed or general AC data. Therefore, it is crucial to determine the effective AC noise of CTC. To measure the

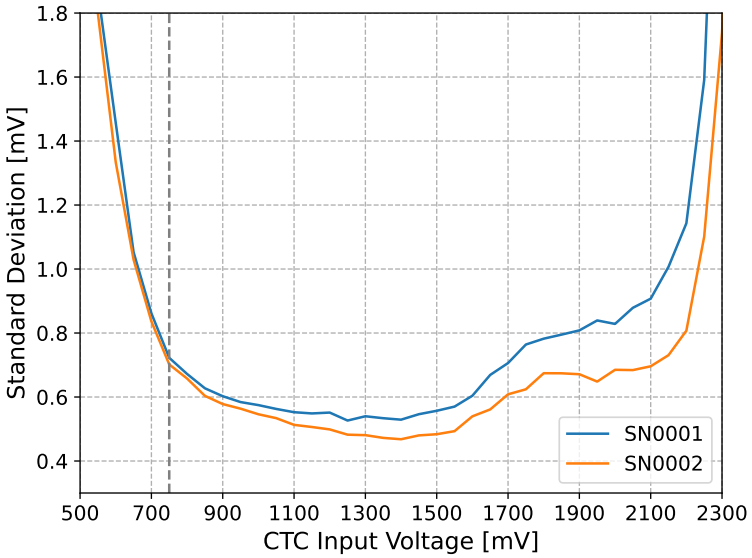

Figure 91: "DC noise level of each ASIC for the relevant voltages. The steep increase in noise to the edges results from the low mV to ADC ratio." [21].

effective AC noise of the ASIC, the splitter board, introduced in Section 11.1, injects sine wave pulses of different frequencies with amplitudes between 1 mV and 1000 mV into each channel. For that purpose, the Keysight 33622A is used, also generating the trigger at 600 Hz to cover all storage cells. 12,000 waveforms were recorded for each amplitude and each waveform is calibrated with a block-dependent DC transfer function. The data is fitted with a sine wave, and the standard deviation of the residuals yields a quantitative measurement of the effective AC noise.
The results for SN0001 are shown in Figure 92, with the standard deviation between the different channels as a semi-transparent band. As a comparison, a linear approximation of the effective AC noise at 10 MHz of TARGET 5 [177] is also shown. The effective AC noise is significantly reduced compared to TARGET 5 over the whole amplitude range.
As discussed in Section 11.4, most effective AC noise is due to the assumed sampling cell bin width of 1 ns. The residuals' non-linear behavior suggests an additional noise component, which was not observable in TARGET 5, possibly due to the larger noise level." The chosen way to improve the AC noise is presented in Section 11.6.2 in the form of the AC correction transfer function.

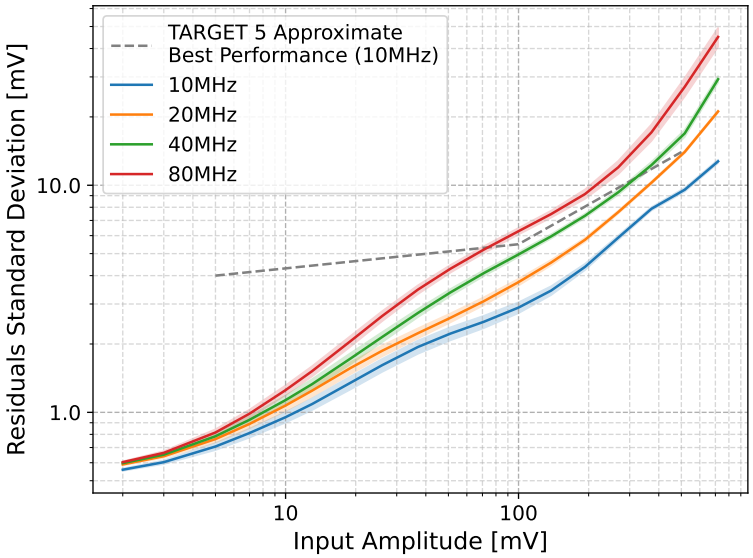

Figure 92: "AC noise of SN0001, with the standard deviation over each channel seen as a semi-transparent area. An approximated reference of the AC noise of TARGET 5 is given as the gray dashed function." [21].

13.5. Performance in Pulse Mode Operation

"To evaluate the performance of the CTC under realistic settings, it is tested in pulse mode operation with Gaussian-shaped pulses of 10 ns (FWHM) width. For this, data sets at different temperatures were recorded with amplitudes explicitly different from the ones used in the AC correction, probing the worst possible outcome."

"The resolution as a function of amplitude for fully calibrated ASICs can be seen in Figure 93 for both evaluation boards and two temperatures, with the temperature-induced difference in the bottom panel. For the 40 °C runs, an AC correction transfer function taken at 30 °C is used to test the temperature stability of the proposed calibration technique.

SN0001 shows a near constant resolution of $\leq$ 1 mV from 5 mV to 1000 mV for both temperatures. Only for amplitudes above 1 V, where the slope of the DC transfer functions increases, the resolution worsens linearly up to 1.6 mV towards the end of the input voltage range. Saturated amplitudes could in principle be extracted, but this goes beyond the scope of this paper.

For SN0002, the resolution looks similar to that of SN0001 for the 30 °C data set. However, at 40 °C, the resolutions worsen up to 1.2 mV between 10 mV and 100 mV. This is to be expected, as the tuning of the ASIC parameters was done on SN0001 and applied to SN0002. Manufacturing tolerances, in general, and slightly

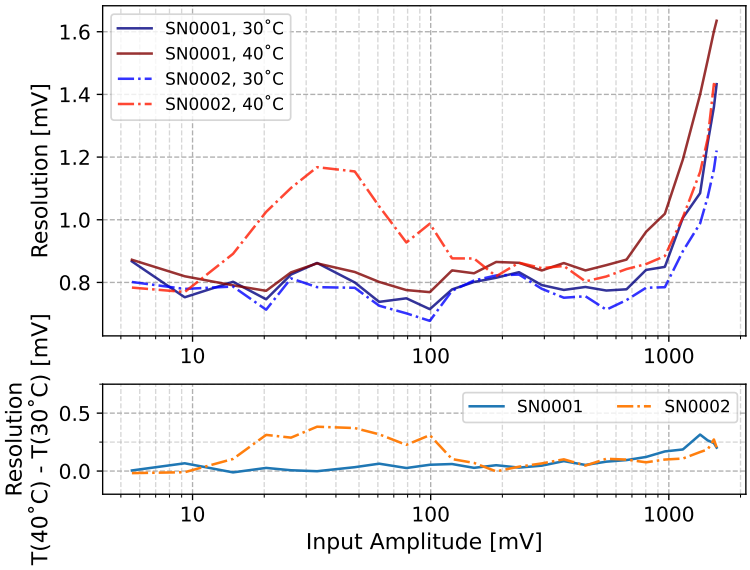

Figure 93: "Fractional resolution for both fully calibrated modules at two different temperatures (with the exception of the AC correction, which is fixed at 30 °C)." [21].

mismatched parameters, lead to a less robust calibration. Further modules must be tested to characterize these ASIC to ASIC variations, but SN0002 is a precedent for all the ASICs to follow.

Figure 94 shows the reconstruction quality achieved with the calibrated module. The bias is defined here as the absolute difference between the measured amplitude and the true amplitude. Similar to the resolution of the SN0001, the bias stays below 1 mV for nearly two magnitudes of input amplitudes for both temperatures, with slightly higher values below 10 mV. Above 600 mV the bias grows again up to 4 mV at 1.6 V input amplitude. The temperature induces difference in reconstruction quality swings between 3 mV for the whole voltage range of SN0001.

SN0002 performs even better at 30 °C, where the data matches the calibration data, and reconstructs with an accuracy of $\leq$ 1 mV over the whole input voltage range. However, it lacks temperature stability, as the bias increases linearly from 1 mV at 100 mV input amplitude to 12 mV towards the end of the input voltage range. The absolute numbers look more daunting than they actually are, as the relative bias never crosses the % mark above 100 mV input amplitude. Again, more ASIC-to-ASIC statistics are needed to better understand the SN0002 behavior at 40 °C.

The measured amplitude as a function of the input amplitude of SN0002 after full calibration is presented in Figure 95 for two different temperatures. The integrated

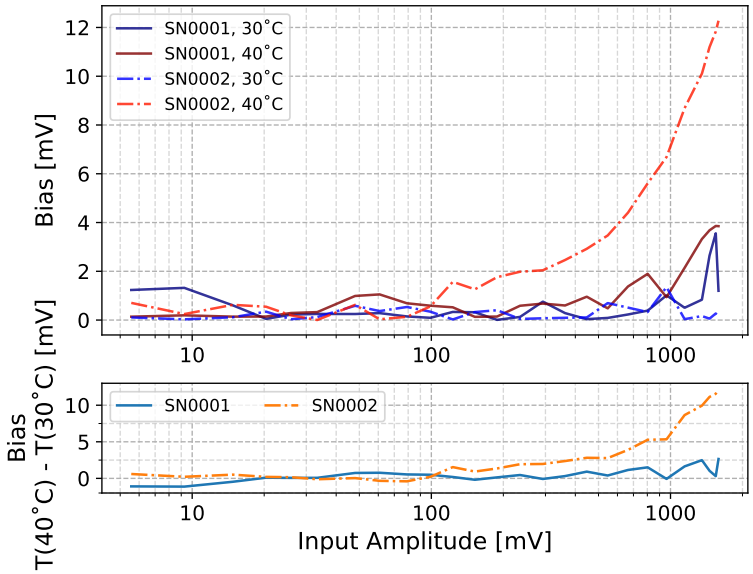

Figure 94: "Bias for both fully calibrated modules at two different temperatures (with the exception of the AC correction, which is fixed at 30 °C). The bias is defined as the absolute difference between the measured amplitude and the true amplitude." [21].

non-linearity is measured by subtracting each measurement point from a linear function connected by the first and last point. It is shown in the bottom panel of Figure 95 with the standard deviation of the channel-to-channel spread shown as error bars. Although the response of the ASIC changes, the linearity is given for the effective dynamic range and both temperatures. It only exceeds the 1 mV mark at around 1 V and shows a mild deviation for a temperature mismatch of 10 °C in the AC correction transfer function.
All in all, the calibration procedure is deemed temperature stable and the obtained performance results indicate that a single AC correction transfer function at a moderate temperature is satisfactory. The response is linear independent of the measured temperatures. The temperature-induced change in resolution at ten degree difference is 0.1 mV averaged over all input amplitudes and approximately worsens with rising amplitude. Only the bump in SN0002 shows an anomaly of 0.4 mV between 10 mV and 100 mV. The reconstruction quality worsens around 1.5 mV on average between both temperatures, with again SN0002 as an outlier. Above 100 mV, it grows up to 12 mV additional bias, although it never exceeds the 1 % mark in relative numbers."

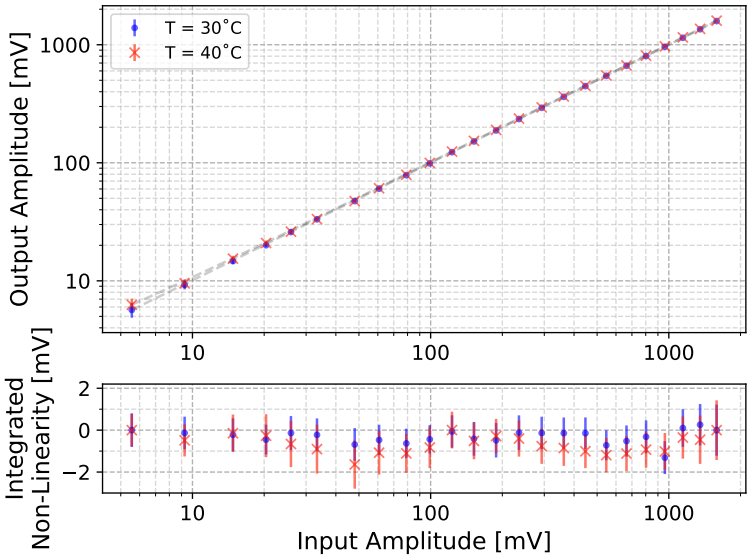

Figure 95: "Response of the fully calibrated SN0001 to different input amplitudes of 10 ns Gaussian-shaped pulses. The integrated non-linearity is given at the bottom with the channel-to-channel spread as error bars." [21].

13.6. Suitability for IACT Cameras

"To evaluate the performance in the context of an IACT camera the intensity resolution for the SST camera defined by the CTAO requirement [184] is used as a comparison. It is defined as the following

$$\frac{\sigma_{\mathrm{I}}}{\mathrm{I_T}} = \frac{1}{\mathrm{I_T}} \sqrt{\frac{\sum_{i=0}^{\mathrm{N}} (\mathrm{I_{M_i}} - \mathrm{I_T})^2}{N}},$$

where $\frac{\sigma_{\mathrm{I}}}{\mathrm{I_T}}$ is the fractional intensity resolution, $\mathrm{I_T}$ is the true intensity - the true number of photons impacting the camera per event, $\mathrm{I_{M_i}}$ the measured intensity of the event and N the number of measured events. As only the digitizer in the form of CTC is characterized here, a quantum efficiency of 40 % for the Silicon photomultipliers combined with the window transmission and a scaling of 3.37 mV per photo electron is assumed, representing the target values for the SST camera. Therefore, this process translates an intensity of one photon to an amplitude of roughly 1.35 mV. In addition to the intensity resolution of CTC, the Poisson error must be quadratic. The data set from Section 13.5 is used for comparison.
The results for SN0001 and SN0002 are shown in Figure 96. The minimal intensity resolution is defined by the Poisson error; intensity resolutions in the gray area are

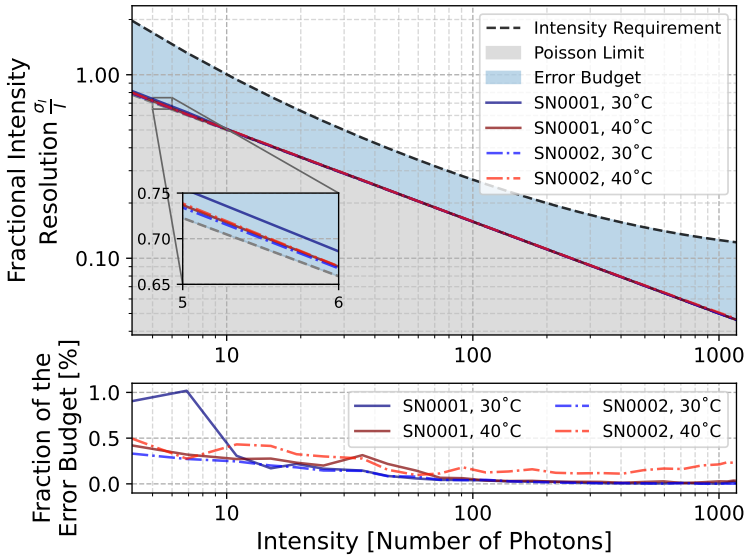

Figure 96: "Intensity resolution of fully calibrated modules with the SST requirement in black. The Poisson Limit is marked as the gray area. The performance of the whole SST camera must be in the blue area, defined as error budget as multiple components contribute to it. A quantum efficiency of 40 % for the photomultipliers is assumed with a 3.37 mV pulse per photo electron conversion." [21].

therefore not possible. On top as a black dashed line is the SST requirement. The blue area between them is the error budget, which can be calculated by quadratically subtracting the Poisson limit from the requirement, as the contributions are independent of each other. Both modules are nearly indistinguishable from the Poisson limit.
For better depiction, the fraction of used error budget (UEB) is given in the bottom panel as

$$\mathrm{UEB} = 1 - \sqrt{1 - \frac{\sigma_\mathrm{I}^2}{\sigma_\mathrm{Requirement}^2 - \sigma_\mathrm{Poisson}^2}}.$$

This is derived by dividing the quadratic difference between the requirement and the fractional intensity resolution by the error budget. The contribution of CTC is below 0.5 % over the whole span of given photon numbers for both modules and temperature data sets, except for SN0001 at 30 °C under ten photons. The temperature mismatch worsens the performance, but not to a significant level as the contribution from CTC itself is not significant, although the in Section 13.5 discussed performance losses due to temperature mismatch in SN0002 can clearly be seen. Between ten and 100 photons, the decline in resolution is the leading

factor for the worse performance, while for photon numbers above 100 it is the additional bias. Nevertheless, the TARGET ASICs are the least contributing noise factor in the signal chain of the SST. Additional contributions to the error budget will be the night sky background (NSB), photodetector noise, front-end electronics uncertainties, optical cross-talk and unaccounted temperature dependencies of different components."

14. Summary and Outlook

To extend the sensitivity of IACTs in the high-energy spectrum above 10 TeV, CTAO deploys 37 SST capable of detecting the faint gamma-ray flux. Therefore, a suitable Camera for the SST, the SST Camera, is needed to meet the performance requirements set by CTAO. One of these important requirements focuses on the performance of the front-end electronics, specifically the sampling and digitisation of the detected Cherenkov photon pulses. An incorrect readout of these pulses directly affects the energy reconstruction of the incident gamma rays. Therefore, a standardised and robust calibration chain for the front-end electronics needs to be developed and evaluated.
In this thesis, a standardised calibration chain for the front-end electronics using the digitisation ASIC CTC was introduced, and its performance was verified against different criteria such as linearity and amplitude resolution. A special emphasis has been placed on the temperature stability of different performance criteria, with the ability to in situ redo the associated measurements on the finished telescope. By introducing the tuning of the Wilkinson voltage ramp, the requirement of a minimal dynamical range of CTC above 2.2 V is met. Continuously sampling without time glitches of the sampling SCA was assured by a `VtrimT` tuning. The response of individual storage cells, combined with the non-linearities of the Wilkinson ADC, was handled through pedestal subtraction and the DC and AC transfer functions. It was shown that the DC transfer function and pedestal are temperature-dependent with a scaling of up to $1.75\,\frac{\mathrm{ADC}}{\mathrm{K}}$. Therefore, in situ versions were implemented using the DACs of the onboard companion ASIC CT5TEA to mitigate performance loss due to temperature drift successfully. The response of the ADC, the `Vped` transfer function, was deemed temperature stable with a rate of change of $0.08\,\frac{\mathrm{mV}}{\mathrm{K}}$. Also, a digitisation block dependency of the DC transfer function was found and incorporated to further improve the precision of the digitisation.
Further improvements were made by the in-depth tuning of the Wilkinson Comparator parameters, to guarantee the 2.2 V dynamical range at the best possible resolution over a large statistic of ASICs. Additionally, several investigations showed that the ASIC exhibits different digitisation behaviours depending on its initialising state. This could be traced to different clocks running in different phases relative to each other, depending on the starting conditions, and was successfully addressed.

Tuned and fully calibrated, the performance of CTC was evaluated over a wide range of criteria. The −3 dB bandwidth is determined to be 220 MHz, which is sufficient for photon pulses of widths as small as 3.6 ns. More than satisfactory for the planned 10 ns. The frequency dependent cross-talk is below 1 % over the whole −3 dB bandwidth and drops to 0.2 % for large amplitude pulses. Negligible

in contrast to the cross-talk observed in SiPMs. The DC noise corresponds to 0.7 mV at operational pedestal, below a quarter of an observed photon electron. The resolution of photon pulses is ≤ 1 mV over the majority of the dynamical range with potential bias of ≤ 1 mV and an integrated non-linearity ≤ 1 mV. All three were deemed temperature stable. For the suitability of IACT, the CTAO requirement of the intensity resolution was measured and tested in temperature stability. Overall, the TARGET CTC ASIC contributes only up to 0.5 % of the given error budget of the SST camera, independent of the temperature.

The validation and verification results demonstrate that the CTC is suitable for IACTs and meets the CTAO's performance requirements and is therefore ready for deployment in the SST Camera. This was further demonstrated by a successful on-sky campaign of a quarter of the SST Camera on the telescope in the summer of 2025, during which the new front-end electronics and calibration chain were first used to detect Cherenkov photon pulses. One of the many steps taken to the successful deployment and operation of the SST on the south side of CTAO. The future of high-energy gamma-ray astronomy looks bright.

Acronyms

AC Alternating Current. 31, 43, 45, 46, 53, 70, 103, 122, 123, 124, 130, 132, 137, 138, 139, 140, 150, 153, 154, 155, 156, 157, 161

ADC Analogue-to-Digital-Converter. 45, 49, 69, 102, 103, 117, 118, 119, 121, 122, 127, 128, 131, 132, 134, 135, 136, 138, 141, 142, 143, 144, 145, 148, 154, 161, 172

AOM Acousto-Optic Modulator. 31, 33, 34, 35, 49, 54, 66, 67, 70, 80, 81, 82

APD Avalanche PhotoDiode. 30

ASIC Application Specific Integrated Circuit. 2, 27, 46, 69, 70, 71, 72, 74, 75, 85, 96, 97, 102, 103, 115, 117, 118, 119, 121, 122, 124, 125, 126, 127, 128, 129, 130, 131, 132, 134, 137, 140, 143, 144, 145, 146, 147, 150, 151, 152, 153, 154, 155, 156, 157, 160, 161, 162, 172

CMB Cosmic Microwave Background. 105

CT5TEA Cherenkov-T5-Trigger Extension Asic. 69, 102, 117, 118, 119, 121, 122, 124, 125, 126, 127, 132, 133, 146, 153, 161

CTAO Cherenkov Telescope Array Observatory. 2, 27, 46, 69, 102, 103, 104, 105, 113, 114, 115, 158, 161, 162

CTC Cherenkov-TARGET-C. 2, 27, 46, 69, 70, 73, 74, 75, 85, 96, 97, 102, 103, 117, 118, 119, 121, 122, 124, 125, 128, 131, 132, 138, 139, 143, 146, 147, 153, 155, 158, 159, 161, 162, 172

DAC Digital-to-Analogue-Converter. 117, 118, 121, 125, 126, 127, 129, 132, 133, 142, 143, 161

DC Direct Current. 32, 43, 46, 49, 52, 69, 72, 74, 88, 103, 118, 121, 122, 123, 124, 125, 126, 131, 132, 133, 134, 135, 136, 137, 142, 144, 146, 148, 150, 153, 155, 161, 162

EOM Electro-Optic Modulator. 15, 31, 32, 33, 49, 54, 55, 65, 66, 67, 70, 80, 85

ET Einstein Telescope. 2, 77, 78, 79, 97

FACT First G-APD Cherenkov Telescope. 112

FC/PC Ferrule Connector Physical Contact. 35

FEE Front-End Electronics. 103, 117, 119, 120

FermiLAT Fermi Large Area Telescope. 105, 114

FFT Fast Fourier Transformation. 53, 62, 63, 172

FIFO First In First Out. 47, 48

FPGA Field Programmable Gate Array. 69, 70, 97, 117, 118, 119, 122, 124, 129, 147

FWHM Full Width at Half Maximum. 17, 34, 81, 155

GRB Gamma Ray Burst. 105

H.E.S.S. High Energy Stereoscopic System. 102

HEGRA High-Energy-Gamma-Ray Astronomy. 102

HOMs Higher Order Modes. 11, 12, 19, 21, 23, 24, 61, 78, 81, 88, 89, 90, 92, 95

IACT Imaging Air Cherenkov Telescope. 102, 103, 104, 110, 111, 112, 113, 114, 158, 161, 162

IO Input/Output. 70

LDO regulator Low-DropOut regulator. 45

LHAASO Large High Altitude Air Shower Observatory. 114

LHC Large Hadron Collider. 105

LIGO Laser Interferometer Gravitational-Wave Observatory. 105

LP$_{lm}$ Linear Polarised. 39, 40

LST Large-Sized Telescope. 114

MAGIC Major Atmospheric Gamma-Ray Imaging Cherenkov. 102

MMCX Micro-Miniature CoaXial. 70, 122, 124

MOSFET Metal–Oxide–Semiconductor Field-Effect Transistor. 141, 142

MST Medium-Sized Telescope. 114

NA Numeric Aperture. 37

nMOS n-typed Metal-Oxide-Semiconductor. 141, 142

NSB Night Sky Background. 112, 116, 117, 160

PCB Printed Circuit Board. 69, 119, 147, 153

PCBs Printed Circuit Boards. 47

PDH Pound–Drever–Hall. 1, 19, 21, 24, 80, 81

PIN Positive Intrinsic Negative. 31

pMOS p-typed Metal-Oxide-Semiconductor. 142

PMT PhotoMultiplier tubes. 112

PSD Power Spectral Density. 58, 59, 60, 62, 63, 64, 172

PSRR Power-Supply Rejection Ratio. 45

QCAM Quarter CAMera. 146

RF Radio Frequency. 33, 34, 35, 49

RIN Relative Intensity Noise. 32

RMS Root Mean Square. 48, 50, 52, 146, 149, 152

SCA Switched-Capacitor Array. 74, 117, 118, 126, 161

SCT Schwarzschild-Couder Telescope. 112, 115

SiPM Silicon Photomultiplier. 112, 116, 117, 119, 120, 137, 139, 143, 152, 162

SMA SubMiniature version A. 46, 48

SNR Signal-to-Noise Ratio. 8, 9, 14, 19, 25, 29, 30, 43, 45, 58, 59, 82, 84, 85, 87, 89, 97, 112, 128, 136

SST Small-Sized Telescope. 2, 27, 46, 69, 102, 103, 104, 112, 114, 115, 116, 119, 126, 136, 139, 143, 144, 152, 158, 159, 160, 161, 162

SWGO Wide-field Gamma-ray Observatory. 114

TARGET TeV Array Readout electronics with GSa/s sampling and Event Trigger. 46, 69, 70, 72, 73, 74, 75, 76, 84, 85, 90, 96, 103, 117, 119, 120, 121, 122, 124, 126, 128, 129, 134, 139, 143, 145, 146, 147, 154, 155, 162

TT gauge Transverse-Traceless gauge. 4

VERITAS Very Energetic Radiation Imaging Telescope Array System. 102

WIMPs Weakly Interacting Massive Particles. 106

A. General Relativity Supplement

This is by no means a complete introduction to tensor calculus or concepts of differential geometry, but it shall be a small refresher for people already familiar with it. For an in-depth introduction, see [27, 30, 28]. The Sections themselves use them as sources.

A.1. Tensor calculus

In general relativity, space and time can not be treated separately any more and are expressed in the 4-vector notation

$$x^\mu = (x^0, x^i) = (ct, \vec{x}) \ , \tag{A.1}$$

with c the speed of light. Greek indices like μ take values of 0, 1, 2, 4, while Latin indices take values of 1, 2, 3. Parallel to this vector space, there is a dual vector space, the cotangent space. Its elements are marked with lower indices as in

$$x_\mu = (x_0, x_i) = (x_0, x_1, x_2, x_3) \ . \tag{A.2}$$

The generalisation of these vectors and dual vectors is a tensor of rank (k,l), which is a multilinear map from the vector and dual vector space to $\mathbb{R}$. A vector is a tensor of rank (1,0), a dual vector of rank (0,1) and a scalar of rank (0,0). A vector space element can be transformed into a dual vector space element and vice versa, via the metric tensor $g_{\mu\nu}$ of rank (0,2). It gives a measure of the distance between points in space-time

$$x_\mu = g_{\mu\nu} x^\nu \quad \text{with} \quad g_{\mu\nu} g^{\nu\rho} = \delta^\rho_\mu \ = \begin{cases} 1, & \text{if } \mu = \rho, \\ 0, & \text{if } \mu \neq \rho. \end{cases} \ . \tag{A.3}$$

Here, the Einstein summation convention is used, which states that repeated indices are summed over. A special case is the Minkowski metric for flat space-time $\eta = \text{diag}(-1, +1, +1, +1)$. Therefore, indices can be raised and lowered as one likes in flat space-time. To change the coordinate frame of tensor T of rank (k,l), the following transformation has to be applied:

$$T^{\mu_1 \dots \mu_k}{}_{\nu_1 \dots \nu_l} = \frac{\partial x^{\mu_1}}{\partial x^{\rho_1}} \dots \frac{\partial x^{\mu_1}}{\partial x^{\rho_k}} \frac{\partial x^{\nu_1}}{\partial x^{\sigma_1}} \dots \frac{\partial x^{\nu_1}}{\partial x^{\sigma_k}} T^{\rho_1 \dots \rho_k}{}_{\sigma_1 \dots \sigma_l} \ . \tag{A.4}$$

For example, transforming the metric tensor $g_{\mu\nu}$ from coordinate frame x to x' is calculated as

$$g'_{\mu\nu} = \frac{\partial x^\rho}{\partial x'^\mu} \frac{\partial x^\sigma}{\partial x'^\nu} g_{\rho\sigma}(x) \ . \tag{A.5}$$

In general, the notation of partial derivates is often shorten to

$$\partial_\mu \equiv \frac{\partial}{\partial x^\mu} \tag{A.6}$$

for readability.

A.2. Curvature

The curvature of, for example, space-time depends on the metric. In order to describe it using the Riemann tensor, concepts tat depend on the coordinate frame, such as partial derivation, parallel transport, or geodesics, have to be generalised. This is done via connections, which relate vectors to the tangent space of nearby points. A set of unique connections is the Christoffel symbol, which can be constructed from the metric itself

$$\Gamma^\rho{}_{\mu\nu} = \frac{1}{2} g^{\rho\sigma} (\partial_\mu g_{\sigma\nu} + \partial_\nu g_{\sigma\mu} - \partial_\sigma g_{\mu\nu}) \ . \tag{A.7}$$

The partial derivative can then be generalised by introducing the covariant derivative ∇_μ, which acts on a vector field V^ν as

$$\nabla_\mu V^\nu = \partial_\mu V^\nu + \Gamma^\nu{}_{\mu\sigma} V^\sigma \ . \tag{A.8}$$

For a flat metric, such as the Minkowski metric, the Euclidean partial derivative is returned. Similarly can the concept of straight lines in curved space-time be generalised if a parametrised curve $x^\mu(\lambda)$ obeys the geodesic equation

$$\frac{\mathrm{d}^2 x^\mu}{\mathrm{d}\lambda^2} + \Gamma^\mu{}_{\rho\sigma} \frac{\mathrm{d}x^\rho}{\mathrm{d}\lambda} \frac{\mathrm{d}x^\sigma}{\mathrm{d}\lambda} = 0 \ . \tag{A.9}$$

Returning to a flat metric yields a straight line. Before applying the changes in parallel transport, the concept is first introduced. Parallel transport is the movement of a vector along a path. In Euclidean space, this is trivial as the vector is unchanged along the path. However, in curved space-time, the orientation of the vector depends on the path taken. This is illustrated in Figure 97 and mathematically by

$$\frac{\mathrm{d}}{\mathrm{d}\lambda} V^\mu + \Gamma^\mu{}_{\sigma\rho} V^\rho = 0 \ . \tag{A.10}$$

The concept of parallel transport can then be used to derive the Riemann tensor in a vivid way. Imagine a closed loop spanned by two vectors where V^μ is parallel transported around. The covariant derivation of the path describes the change of

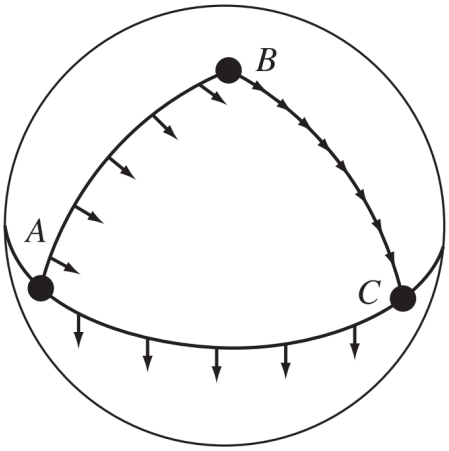

Figure 97: Parallel transport along the curved surface of a sphere. Starting at point A, the alignment of the vector changes due to the path on the curved space. Retreating to the start point A can not restore the initial alignment without backtracking. Image taken from [28].

the vector. Therefore, the commutator of both covariant derivations describes the difference in change of vector V^μ between the paths

$$[\nabla_\mu, \nabla_\nu] V^\rho = R^\rho{}_{\sigma\mu\nu} V^\rho - T^\lambda{}_{\mu\nu} \nabla_\lambda V^\rho, \tag{A.11}$$

with $R^\rho{}_{\sigma\mu\nu}$ the Riemann tensor describing the curvature

$$R^\rho{}_{\sigma\mu\nu} = \left(\partial_\mu \Gamma^\rho{}_{\nu\sigma} - \partial_\nu \Gamma^\rho{}_{\mu\sigma} + \Gamma^\sigma{}_{\mu\lambda} \Gamma^\lambda{}_{\nu\sigma} - \Gamma^\rho{}_{\nu\lambda} \Gamma^\lambda{}_{\mu\sigma}\right) \tag{A.12}$$

and $T^\lambda{}_{\mu\nu}$ the Torsion tensor

$$T^\lambda{}_{\mu\nu} = 2(\Gamma^\lambda{}_{\mu\nu} - \Gamma^\lambda{}_{\nu\mu}) \tag{A.13}$$

describing the torsion. By contracting the Riemann tensor, the Ricci tensor can be determined as

$$R_{\mu\nu} = R^\rho{}_{\mu\rho\nu} \tag{A.14}$$

describing the change of the volume element across the curvature. To calculate the mean curvature, the Ricci scalar is yielded by

$$R = R^\mu{}_\mu = g^{\mu\nu} R_{\mu\nu}. \tag{A.15}$$

B. Bessel Functions

Bessel functions are solutions to the Bessel differential equation

$$x^2\frac{\mathrm{d}^2y}{\mathrm{d}x^2}+x\frac{\mathrm{d}y}{\mathrm{d}x}+(x^2-\alpha^2)=0\ , \tag{B.1}$$

a linear ordinary differential equation of second order with $\alpha\in\mathbb{C}$ determining the order of the Bessel function [61]. They are common in physics as they solve the radial dependency of the Laplace equation $\Delta\Phi=0$ for circular or cylindrical symmetries [185]. Two solutions can be determined, the Bessel function of first kind

$$J_\alpha(z)=\sum_{m=0}^{\infty}\frac{(-1)^m}{m!\Gamma(m+\alpha+1)}\left(\frac{z}{2}\right)^{2z+\alpha}\ , \tag{B.2}$$

with Γ the gamma-function and of second kind

$$Y_\alpha(z)=\frac{J_\alpha(z)\cos(\alpha\pi)-J_{-\alpha}(z)}{\sin(\alpha\pi)}\ , \tag{B.3}$$

both of order α. For purely imaginary arguments z, the modified Bessel functions of first kind

$$I_\alpha(z)=i^{-\alpha}J_\alpha(iz) \tag{B.4}$$

and of second kind

$$K_\alpha(z)=\frac{\pi}{2}\frac{I_{-\alpha}(z)-I_\alpha(z)}{\sin(\alpha z)} \tag{B.5}$$

can be determined. The for in this work used Bessel functions α is reduced to $l\in\mathbb{N}_0$ where l corresponds to the lth order of the Bessel function. Therefore, $\Gamma(n)$ reduces to $(n-1)!$ in $J_n(z)$ while for $Y_n(z)$ and K_α, the limit $\alpha\to n$ has to be calculated. The mathematical display is skipped because it this is cumbersome and yields no real insight. Nevertheless, all the introduced Bessel functions for different orders of l can be seen in Figure 98.
In addition, following identities [89]

$$\pm U\partial_r J_l(U)=lJ_l(U)-UJ_{l\pm1}(U) \tag{B.6}$$

$$\pm W\partial_r K_l(W)=lK_l(W)\pm WK_{l\pm1}(W) \tag{B.7}$$

$$J_{l+1}(U)=\frac{2l}{U}J_l(U)-J_{l-1}(U) \tag{B.8}$$

$$K_{l+1}(W)=\frac{2l}{W}K_l(U)+K_{l-1}(W) \tag{B.9}$$

are used in Section 4.4.2 to prove

$$\frac{U\partial_r J_l(U)}{J_l(U)}=\frac{W\partial_r K_l(W)}{K_l(W)}\quad\text{or}\quad\frac{UJ_{l-1}(U)}{J_l(U)}=-\frac{WK_{l-1}(W)}{K_l(W)}\ . \tag{B.10}$$

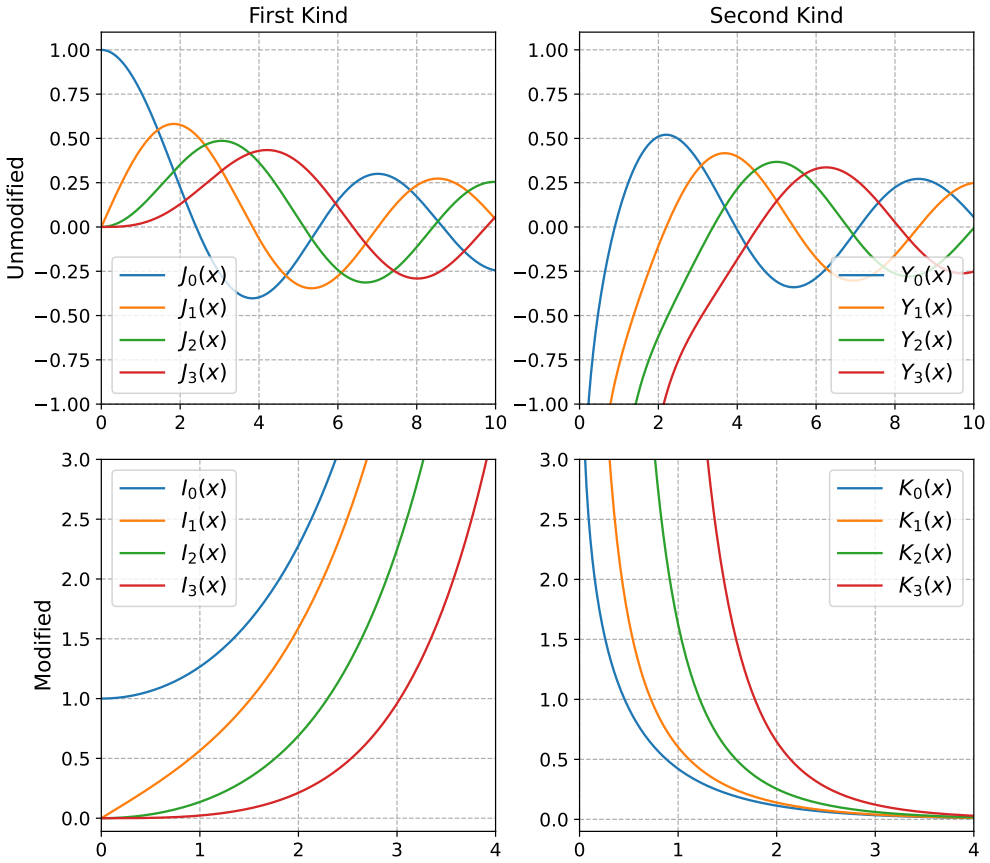

Figure 98: All four introduced Bessel functions used or mentioned in this work for different order of l.

C. Phase Camera Software: ETscripts

To streamline and standardise the analysis of phase camera images, the Python-based software framework *ETscripts* was created. It stands on four pillars: Digitiser-specific classes handling the read and write operations for the used digitiser, a mapping class documenting the setup from fibre pixel to digitiser channel, *ETtools*, the analysis tool, and a camera class defining the geometry of the camera and creating phase images. The repository can be found on the institute's internal git [186].

Depending on the digitiser, different digitisation classes are used. For the Spectrum Instrumentation M4i.4451-x8 digitising cards, three separate classes are used that are based on the programming examples of Spectrum [80].
The *card_class* is responsible for operating the digitiser. That includes setting specific registers for operation and digitising data. For digitisation, two different

modes can be used. Continuous digitisation, or digitisation of a fixed number of samples after each trigger is called burst mode. The digitised values are stored in a binary file per digitising card, with an additional .txt file containing the trigger timestamps in burst mode.
To document the set parameters and correctly interpret the data after recording, the *extract_parameter_class* is created. It checks the individual register for each setting independently of the *card_class* and writes them into a human-readable .txt file for quick checks and a machine-readable .csv file for further processing. To read in the data, the *read_data_class* is used. It takes the recorded binary files and creates an easier-to-understand Numpy array with shape (card number, channel). By reading the .csv file containing the individual settings for each card and channel, the ADC of each sample is translated to a millivolt value, and the timebase in nanoseconds is generated. In burst mode, the additional timestamp .txt file is also read in to generate the timebase.
When the CTC ASICs are used as digitiser, the *TARGET Libraries* [115] are responsible for communication, data taking, and calibration and are not part of *ETscripts*. Therefore, the data formatting has to be adjusted to be compatible with *ETscripts*, which is done using a translation script. As the digitisation parameters of CTC are fixed, there is no need for an extra *extract_parameter_class*.

Not only are the digitiser settings important to understand the data, but also the individual signal chain from pixel to digitiser. For this purpose, the *card_mapping* class is created. It documents the fibre-array pixel, the serial number of the amplifier box, the serial number of the used digitiser and its channel for both the high-speed digitisers and the SLOWDAQ boxes, in a standardised table. For the Spectrum Instrumentation M4i.4451-x8, the physical positions of the cards in the working station and the number of used threads are also noted for easier handling in the laboratory. This information can then be used to assign pixels to data arrays or to apply amplifier-specific frequency or phase responses.

As a pool for standardised analysis methods, *ETtools* is used. The functions range from simple conversion functions, such as millivolt to dBm, to FFT and PSD functions, and more. However, the primary function is to demodulate the raw signal for each pixel and calculate the phase and power of each sideband. For this, it takes the read-in data and the corresponding timebase, the camera mapping, the frequencies of the wanted sidebands to analyse, the integration time in terms of the number of samples, and the sampling speed of the used digitiser. The output is a data package consisting of: A metadata file where the pixel, used amplifier, etc., are noted, an array of the frequencies of the analysed sidebands, a timebase for the phase and intensity points and a time series of the phase and intensity of

each sideband. For efficiency, this process can be run in multithreading mode.
To build complete images out of these data packages, the *camera* class is used. It defines the geometry of the camera by assigning a pixel to the x and y coordinates. Using the metadata of the data package creates a phase and intensity array for an arbitrary point in the time series, ordered by pixel number. This array can then be used to create basic images or predefined imaging functions.

Bibliography

[1] A. Einstein. „Näherungsweise Integration der Feldgleichungen der Gravitation“. In: *K. Preuss. Akad. Wiss. 1* (1916), p. 688.

[2] A. Einstein. „Über Gravitationswellen“. In: *K. Preuss. Akad. Wiss. 1* (1918), p. 154.

[3] B. P. Abbott, R. Abbott, T. D. Abbott, M. R. Abernathy, et al. „Observation of Gravitational Waves from a Binary Black Hole Merger“. In: *Phys. Rev. Lett.* 116 (6 2016), p. 061102. URL: https://link.aps.org/doi/10.1103/PhysRevLett.116.061102.

[4] B. P. Abbott, R. Abbott, T. D. Abbott, F. Acernese, et al. „Multi-messenger Observations of a Binary Neutron Star Merger*“. In: *The Astrophysical Journal Letters* 848.2 (Oct. 2017), p. L12. ISSN: 2041-8213. URL: http://dx.doi.org/10.3847/2041-8213/aa91c9.

[5] A. Neronov. „Introduction to multi-messenger astronomy“. In: *Journal of Physics: Conference Series* 1263.1 (June 2019), p. 012001. ISSN: 1742-6596. URL: http://dx.doi.org/10.1088/1742-6596/1263/1/012001.

[6] P. Mészáros, D. B. Fox, C. Hanna, and K. Murase. „Multi-messenger astrophysics“. In: *Nature Reviews Physics* 1.10 (Oct. 2019), 585–599. ISSN: 2522-5820. URL: http://dx.doi.org/10.1038/s42254-019-0101-z.

[7] N. V. Krishnendu and F. Ohme. „Testing General Relativity with Gravitational Waves: An Overview“. In: *Universe* 7.12 (Dec. 2021), p. 497. ISSN: 2218-1997. URL: http://dx.doi.org/10.3390/universe7120497.

[8] A. K. Mehta, A. Buonanno, R. Cotesta, A. Ghosh, et al. „Tests of general relativity with gravitational-wave observations using a flexible theory-independent method“. In: *Physical Review D* 107.4 (Feb. 2023). ISSN: 2470-0029. URL: http://dx.doi.org/10.1103/PhysRevD.107.044020.

[9] G. Calcagni. „Quantum Gravity and Gravitational-Wave Astronomy“. In: *Handbook of Gravitational Wave Astronomy*. Springer Singapore, 2021, 1–27. ISBN: 9789811547027. URL: http://dx.doi.org/10.1007/978-981-15-4702-7_30-1.

[10] K. E. S. Ford and B. McKernan. *Using gravitational waves and multi-messenger Astronomy to reverse-engineer the properties of galactic nuclei.* 2025. arXiv: 2506.08801 [astro-ph.HE]. URL: https://arxiv.org/abs/2506.08801.

[11] B. Haskell and M. Bejger. „Astrophysics with continuous gravitational waves“. In: *Nature Astronomy* 7.10 (Oct. 2023), pp. 1160–1170. ISSN: 2397-3366. URL: https://doi.org/10.1038/s41550-023-02059-w.

[12] S. Mastrogiovanni, C. Karathanasis, J. Gair, G. Ashton, et al. „Cosmology with Gravitational Waves: A Review“. In: *Annalen der Physik* 536.2 (2024), p. 2200180. eprint: https://onlinelibrary.wiley.com/doi/pdf/10.1002/andp.202200180. URL: https://onlinelibrary.wiley.com/doi/abs/10.1002/andp.202200180.

[13] I. Tews, J. Margueron, and S. Reddy. „Confronting gravitational-wave observations with modern nuclear physics constraints“. In: *The European Physical Journal A* 55.6 (June 2019). ISSN: 1434-601X. URL: http://dx.doi.org/10.1140/epja/i2019-12774-6.

[14] M. Punturo, M. Abernathy, F. Acernese, B. Allen, et al. „The Einstein Telescope: a third-generation gravitational wave observatory“. In: *Classical and Quantum Gravity* 27.19 (2010), p. 194002. URL: https://dx.doi.org/10.1088/0264-9381/27/19/194002.

[15] A. Abac, R. Abramo, S. Albanesi, A. Albertini, et al. *The Science of the Einstein Telescope*. 2025. arXiv: 2503.12263 [gr-qc]. URL: https://arxiv.org/abs/2503.12263.

[16] R. W. P. Drever, J. L. Hall, F. V. Kowalski, J. Hough, et al. „Laser phase and frequency stabilization using an optical resonator“. en. In: *Applied Physics B* 31.2 (June 1983), pp. 97–105. ISSN: 1432-0649. URL: https://doi.org/10.1007/BF00702605 (visited on 08/25/2025).

[17] K. Kokeyama, K. Izumi, W. Z. Korth, N. Smith-Lefebvre, et al. „Residual amplitude modulation in interferometric gravitational wave detectors“. In: *Journal of the Optical Society of America A* 31.1 (Dec. 2013), p. 81. ISSN: 1520-8532. URL: http://dx.doi.org/10.1364/JOSAA.31.000081.

[18] A. W. Goodwin-Jones, R. Cabrita, M. Korobko, M. V. Beuzekom, et al. „Transverse mode control in quantum enhanced interferometers: a review and recommendations for a new generation“. EN. In: *Optica* 11.2 (Feb. 2024). Publisher: Optica Publishing Group, pp. 273–290. ISSN: 2334-2536. URL: https://opg.optica.org/optica/abstract.cfm?uri=optica-11-2-273 (visited on 07/11/2024).

[19] K. Agatsuma, L. Van Der Schaaf, M. Van Beuzekom, D. Rabeling, and J. Van Den Brand. „High-performance phase camera as a frequency selective laser wavefront sensor for gravitational wave detectors“. en. In: *Optics Express*

27.13 (June 2019), p. 18533. ISSN: 1094-4087. URL: https://opg.optica.org/abstract.cfm?URI=oe-27-13-18533 (visited on 09/04/2025).

[20] Z. Instruments. *Principles of lock-in detection and the state of the art*. Tech. rep. Zurich Instruments, Apr. 2010.

[21] B. Schwab, A. Zink, G. Varner, D. Depaoli, et al. „CTC and CT5TEA: An advanced multi-channel digitizer and trigger ASIC for imaging atmospheric Cherenkov telescopes". In: *Nuclear Instruments and Methods in Physics Research Section A: Accelerators, Spectrometers, Detectors and Associated Equipment* 1069 (Dec. 2024), p. 169841. ISSN: 0168-9002. URL: http://dx.doi.org/10.1016/j.nima.2024.169841.

[22] T. E. Team. *ETpathfinder DESIGN REPORT*. Sept. 18, 2025. URL: https://www.etpathfinder.eu/research/.

[23] N. Ismail, C. C. Kores, D. Geskus, and M. Pollnau. „Fabry-Pérot resonator: spectral line shapes, generic and related Airy distributions, linewidths, finesses, and performance at low or frequency-dependent reflectivity". In: *Opt. Express* 24.15 (2016), pp. 16366–16389. URL: https://opg.optica.org/oe/abstract.cfm?URI=oe-24-15-16366.

[24] W. Winkler, R. Schilling, K. Danzmann, J. Mizuno, et al. „Light scattering described in the mode picture". In: *Appl. Opt.* 33.31 (1994), pp. 7547–7550. URL: https://opg.optica.org/ao/abstract.cfm?URI=ao-33-31-7547.

[25] A. Utina, A. Amato, J. Arends, C. Arina, et al. „ETpathfinder: a cryogenic testbed for interferometric gravitational-wave detectors". In: *Classical and Quantum Gravity* 39.21 (Sept. 2022), p. 215008. ISSN: 1361-6382. URL: http://dx.doi.org/10.1088/1361-6382/ac8fdb.

[26] M. Maggiore. *Gravitational Waves. Vol. 1: Theory and Experiments*. Oxford University Press, 2007. ISBN: 978-0-19-171766-6, 978-0-19-852074-0. DOI: 10.1093/acprof:oso/9780198570745.001.0001.

[27] S. M. Carroll. *Spacetime and Geometry: An Introduction to General Relativity*. Cambridge University Press, 2019.

[28] B. Schutz. *A First Course in General Relativity*. 3rd ed. Cambridge University Press, 2022.

[29] N. T. Bishop and L. Rezzolla. „Extraction of gravitational waves in numerical relativity". In: *Living Reviews in Relativity* 19.1 (Oct. 2016), p. 2. ISSN: 1433-8351. URL: https://doi.org/10.1007/s41114-016-0001-9.

[30] R. M. Wald. *General Relativity*. Chicago, USA: Chicago Univ. Pr., 1984. DOI: 10.7208/chicago/9780226870373.001.0001.

[31] J. Aasi, B. P. Abbott, R. Abbott, T. Abbott, et al. „Advanced LIGO“. In: *Classical and Quantum Gravity* 32.7 (Mar. 2015), p. 074001. ISSN: 1361-6382. URL: http://dx.doi.org/10.1088/0264-9381/32/7/074001.

[32] M. Branchesi, M. Maggiore, D. Alonso, C. Badger, et al. „Science with the Einstein Telescope: a comparison of different designs“. en. In: *Journal of Cosmology and Astroparticle Physics* 2023.07 (July 2023), p. 068. ISSN: 1475-7516. URL: https://iopscience.iop.org/article/10.1088/1475-7516/2023/07/068 (visited on 03/12/2024).

[33] M. Maggiore, C. v. d. Broeck, N. Bartolo, E. Belgacem, et al. „Science Case for the Einstein Telescope“. en. In: *Journal of Cosmology and Astroparticle Physics* 2020.03 (Mar. 2020). arXiv:1912.02622 [astro-ph, physics:gr-qc], pp. 050–050. ISSN: 1475-7516. URL: http://arxiv.org/abs/1912.02622 (visited on 09/20/2023).

[34] A. Addazi, J. Alvarez-Muniz, R. Alves Batista, G. Amelino-Camelia, et al. „Quantum gravity phenomenology at the dawn of the multi-messenger era—A review“. In: *Progress in Particle and Nuclear Physics* 125 (2022), p. 103948. ISSN: 0146-6410. URL: https://www.sciencedirect.com/science/article/pii/S0146641022000096.

[35] E. Barausse. *Testing the strong equivalence principle with gravitational-wave observations of binary black holes*. 2017. arXiv: 1703.05699 [gr-qc]. URL: https://arxiv.org/abs/1703.05699.

[36] Y.-F. Wang, S. M. Brown, L. Shao, and W. Zhao. „Tests of gravitational-wave birefringence with the open gravitational-wave catalog“. In: *Phys. Rev. D* 106 (8 2022), p. 084005. URL: https://link.aps.org/doi/10.1103/PhysRevD.106.084005.

[37] B. P. Abbott, R. Abbott, T. D. Abbott, F. Acernese, et al. „A gravitational-wave standard siren measurement of the Hubble constant“. In: *Nature* 551.7678 (Nov. 2017), pp. 85–88. ISSN: 1476-4687. URL: https://doi.org/10.1038/nature24471.

[38] S. M. Vermeulen, P. Relton, H. Grote, V. Raymond, et al. „Direct limits for scalar field dark matter from a gravitational-wave detector“. In: *Nature* 600.7889 (Dec. 2021), 424–428. ISSN: 1476-4687. URL: http://dx.doi.org/10.1038/s41586-021-04031-y.

[39] K. Kadota, J. H. Kim, P. Ko, and X.-Y. Yang. „Gravitational wave probes on self-interacting dark matter surrounding an intermediate mass black hole“. In: *Physical Review D* 109.1 (Jan. 2024). ISSN: 2470-0029. URL: http://dx.doi.org/10.1103/PhysRevD.109.015022.

[40] S. Mukherjee. „A new gravitational wave probe to the nature of dark energy from the ageing of the Universe“. In: *Monthly Notices of the Royal Astronomical Society* 542.1 (July 2025), pp. 391–396. ISSN: 0035-8711. URL: https://doi.org/10.1093/mnras/staf1246.

[41] G. Cusin, I. Dvorkin, C. Pitrou, and J.-P. Uzan. „Stochastic gravitational wave background anisotropies in the mHz band: astrophysical dependencies“. In: *Monthly Notices of the Royal Astronomical Society: Letters* 493.1 (Dec. 2019), L1–L5. ISSN: 1745-3933. URL: http://dx.doi.org/10.1093/mnrasl/slz182.

[42] F. Muia, F. Quevedo, A. Schachner, and G. Villa. „Testing BSM physics with gravitational waves“. In: *Journal of Cosmology and Astroparticle Physics* 2023.09 (Sept. 2023), p. 006. ISSN: 1475-7516. URL: http://dx.doi.org/10.1088/1475-7516/2023/09/006.

[43] J. McGinn, A. Mukherjee, J. Irwin, C. Messenger, et al. *Rapid neutron star equation of state inference with Normalising Flows*. 2024. arXiv: 2403.17462 [gr-qc]. URL: https://arxiv.org/abs/2403.17462.

[44] B. Haskell and D. Jones. „Glitching pulsars as gravitational wave sources“. In: *Astroparticle Physics* 157 (2024), p. 102921. ISSN: 0927-6505. URL: https://www.sciencedirect.com/science/article/pii/S092765052300107X.

[45] D. Kasen, B. Metzger, J. Barnes, E. Quataert, and E. Ramirez-Ruiz. „Origin of the heavy elements in binary neutron-star mergers from a gravitational-wave event“. In: *Nature* 551.7678 (Oct. 2017), 80–84. ISSN: 1476-4687. URL: http://dx.doi.org/10.1038/nature24453.

[46] E. Bagui, S. Clesse, V. D. Luca, J. M. Ezquiaga, et al. *Primordial black holes and their gravitational-wave signatures*. 2023. arXiv: 2310.19857 [astro-ph.CO]. URL: https://arxiv.org/abs/2310.19857.

[47] S. C. Rose, S. Naoz, R. Sari, and I. Linial. „The Formation of Intermediate-mass Black Holes in Galactic Nuclei“. In: *The Astrophysical Journal Letters* 929.2 (Apr. 2022), p. L22. ISSN: 2041-8213. URL: http://dx.doi.org/10.3847/2041-8213/ac6426.

[48] A. Addazi, J. Alvarez-Muniz, R. Alves Batista, G. Amelino-Camelia, et al. „Quantum gravity phenomenology at the dawn of the multi-messenger

era—A review“. In: *Progress in Particle and Nuclear Physics* 125 (July 2022), p. 103948. ISSN: 0146-6410. URL: http://dx.doi.org/10.1016/j.ppnp.2022.103948.

[49] A. W. Goodwin-Jones, R. Cabrita, M. Korobko, M. V. Beuzekom, et al. „Supplementary document for Transverse Mode Control in Quantum Enhanced Interferometers: A Review and Recommendations for a New Generation“. In: *Optica* 11 (2024). URL: https://opg.optica.org/optica/abstract.cfm?URI=optica-11-2-273.

[50] R. Schnabel, N. Mavalvala, D. E. McClelland, and P. K. Lam. „Quantum metrology for gravitational wave astronomy“. en. In: *Nature Communications* 1.1 (Nov. 2010). Publisher: Nature Publishing Group, p. 121. ISSN: 2041-1723. URL: https://www.nature.com/articles/ncomms1122 (visited on 10/11/2025).

[51] A. Freise and K. Strain. „Interferometer Techniques for Gravi-tational-Wave Detection“. In: *Living Reviews in Relativity* 13.1 (Feb. 2010). ISSN: 1433-8351. URL: http://dx.doi.org/10.12942/lrr-2010-1.

[52] P. R. Saulson. *Fundamentals of interferometric gravitational wave detectors*. en. Second edition. Hackensack, NJ: World Scientific, 2017. ISBN: 978-981-314-307-4.

[53] D. Meschede. *Optics, light and lasers: The practical approach to modern aspects of photonics and laser physics; 3rd rev. and enl. ed.* Weinheim: Wiley-VCH, 2017, 528 pages. ISBN: 9783527413317. URL: https://bib-pubdb1.desy.de/record/399478.

[54] M. W. S. F. K. Kneubühl. *Laser*. Teubner Studienbücher Physik. Vieweg+Teubner Verlag Wiesbaden, 1999. ISBN: 978-3-322-93875-6. URL: https://books.google.de/books?id=4P67BAAAQBAJ.

[55] A. Siegman. *Lasers*. G - Reference,Information and Interdisciplinary Subjects Series. University Science Books, 1986. ISBN: 978-0-935702-11-8. URL: https://books.google.de/books?id=1BZVwUZLTkAC.

[56] E. D. Black and R. N. Gutenkunst. „An introduction to signal extraction in interferometric gravitational wave detectors“. In: *American Journal of Physics* 71.4 (Apr. 2003), pp. 365–378. ISSN: 0002-9505. URL: https://doi.org/10.1119/1.1531578.

[57] H. Kogelnik and T. Li. „Laser Beams and Resonators“. In: *Appl. Opt.* 5.10 (1966), pp. 1550–1567. URL: https://opg.optica.org/ao/abstract.cfm?URI=ao-5-10-1550.

[58] R. W. Boyd. „Intuitive explanation of the phase anomaly of focused light beams“. In: *J. Opt. Soc. Am.* 70.7 (1980), pp. 877–880. URL: https://opg.optica.org/abstract.cfm?URI=josa-70-7-877.

[59] P. A. Bélanger. „Beam propagation and the ABCD ray matrices“. In: *Opt. Lett.* 16.4 (1991), pp. 196–198. URL: https://opg.optica.org/ol/abstract.cfm?URI=ol-16-4-196.

[60] F. Pockels. *Ueber den Einfluss des elektrostatischen Feldes auf das optische Verhalten piëzoelektrischer Krystalle*. Abhandlungen der Königlichen Gesellschaft der Wissenschaften zu Göttingen. Dieterichsche Verlags- Buchhandlung, 1894. URL: https://books.google.de/books?id=yURAAQAAMAAJ.

[61] M. Abramowitz and I. Stegun. *Handbook of Mathematical Functions: With Formulas, Graphs, and Mathematical Tables*. Applied mathematics series. Dover Publications, 1965. ISBN: 9780486612720. URL: https://books.google.de/books?id=MtU8uP7XMvoC.

[62] L. Schnupp. *Presentation at European Collaboration Meeting on Interferometric Detection of Gravitational Waves*. Sorrent. 1988.

[63] R. Takahashi, J. Mizuno, S. Miyoki, and N. Kawashima. „Control of a 10 m delay-line laser interferometer using the pre-modulation method“. In: *Physics Letters A* 187.2 (1994), pp. 157–162. ISSN: 0375-9601. URL: https://www.sciencedirect.com/science/article/pii/037596019490054X.

[64] C. L. Mueller, M. A. Arain, G. Ciani, R. T. DeRosa, et al. „The advanced LIGO input optics“. In: *Review of Scientific Instruments* 87.1 (Jan. 2016), p. 014502. ISSN: 0034-6748. URL: https://doi.org/10.1063/1.4936974.

[65] B. Willke, N. Uehara, E. K. Gustafson, R. L. Byer, et al. „Spatial and temporal filtering of a 10-W Nd:YAG laser with a Fabry–Perot ring-cavity premode cleaner“. In: *Opt. Lett.* 23.21 (1998), pp. 1704–1706. URL: https://opg.optica.org/ol/abstract.cfm?URI=ol-23-21-1704.

[66] E. D. Black. „An introduction to Pound–Drever–Hall laser frequency stabilization“. en. In: *American Journal of Physics* 69.1 (Jan. 2001), pp. 79–87. ISSN: 0002-9505, 1943-2909. URL: https://pubs.aip.org/ajp/article/69/1/79/1055569/An-introduction-to-Pound-Drever-Hall-laser (visited on 09/20/2023).

[67] R. V. Pound. „Electronic Frequency Stabilization of Microwave Oscillators“. In: *Review of Scientific Instruments* 17.11 (Nov. 1946), pp. 490–505. ISSN: 0034-6748. URL: https://doi.org/10.1063/1.1770414.

[68] K. Strain, K. Danzmann, J. Mizuno, P. Nelson, et al. „Thermal lensing in recycling interferometric gravitational wave detectors“. In: *Physics Letters A* 194.1 (1994), pp. 124–132. ISSN: 0375-9601. URL: https://www.sciencedirect.com/science/article/pii/0375960194007174.

[69] E. Morrison, B. J. Meers, D. I. Robertson, and H. Ward. „Automatic alignment of optical interferometers“. In: *Appl. Opt.* 33.22 (1994), pp. 5041–5049. URL: https://opg.optica.org/ao/abstract.cfm?URI=ao-33-22-5041.

[70] D. McClelland, H. Lueck, R. Adhikari, M. Ando, et al. *3G R&D: R&D for the Next Generation of Ground-based Gravitational-wave Detectors*. arXiv:2111.06991 [gr-qc]. Nov. 2021. URL: http://arxiv.org/abs/2111.06991 (visited on 03/06/2025).

[71] E. S. C. E. Team. *Einstein Telescope Design Report Update 2020*. The website is not public. Sept. 3, 2025. URL: https://apps.et-gw.eu/tds/?r=18715.

[72] F. Amann, F. Bonsignorio, T. Bulik, H. J. Bulten, et al. „Site-selection criteria for the Einstein Telescope“. In: *Review of Scientific Instruments* 91.9 (Sept. 2020). ISSN: 1089-7623. URL: http://dx.doi.org/10.1063/5.0018414.

[73] Einstein Telescope EMR. *Saxony also wants to build the Einstein Telescope*. https://www.einsteintelescope-emr.eu/en/2024/12/06/saxony-also-wants-to-build-the-einstein-telescope/. Accessed: 2025.09.12. Dec. 4, 2024.

[74] ET. *ET-NoiseBudget*. The website is not public. Sept. 3, 2025. URL: https://gitlab.et-gw.eu/et/isb/interferometer/ET-NoiseBudget.

[75] F Acernese, M Agathos, K Agatsuma, D Aisa, et al. „Advanced Virgo: a second-generation interferometric gravitational wave detector“. In: *Classical and Quantum Gravity* 32.2 (Dec. 2014), p. 024001. ISSN: 1361-6382. URL: http://dx.doi.org/10.1088/0264-9381/32/2/024001.

[76] E. T. EMR. *Einstein Telescope in brief*. Accessed: 2025.09.12. URL: https://www.einsteintelescope-emr.eu/en/einstein-telescope-in-brief/.

[77] E. Muñiz, V. Srivastava, S. Vidyant, and S. W. Ballmer. „High frame-rate phase camera for high-resolution wavefront sensing in gravitational-wave detectors“. en. In: *Physical Review D* 104.4 (Aug. 2021), p. 042002. ISSN: 2470-0010, 2470-0029. URL: https://link.aps.org/doi/10.1103/PhysRevD.104.042002 (visited on 09/20/2023).

[78] H. T. Cao, D. D. Brown, P. J. Veitch, and D. J. Ottaway. „Optical lock-in camera for gravitational wave detectors“. In: *Opt. Express* 28.10 (2020), pp. 14405–14413. URL: https://opg.optica.org/oe/abstract.cfm?URI=oe-28-10-14405.

[79] L. Van Der Schaaf, K. Agatsuma, M. Van Beuzekom, M. Gebyehu, and J. Van Den Brand. „Advanced Virgo phase cameras“. en. In: *Journal of Physics: Conference Series* 718 (May 2016), p. 072008. ISSN: 1742-6588, 1742-6596. URL: https://iopscience.iop.org/article/10.1088/1742-6596/718/7/072008 (visited on 09/20/2023).

[80] *M4i.44xx-x8 - 14/16 bit Digitizer up to 500 MS/s*. Spectrum Instrumentation. Ahrensfelder Weg 13-17, 22927 Grosshansdorf, Germany, Dec. 2024.

[81] S. Datta, A. Joshi, and J. Rue. „Crosstalk analysis in large-area low-capacitance InGaAs quad photodiodes“. In: *Infrared Technology and Applications XXXIX*. Ed. by B. F. Andresen, G. F. Fulop, C. M. Hanson, P. R. Norton, and P. Robert. Vol. 8704. International Society for Optics and Photonics. SPIE, 2013, p. 870408. URL: https://doi.org/10.1117/12.2015609.

[82] *CoSF-D-ER-B-LP Narrow Linewidth Single Frequency Fiber Laser*. Connet Laser Technology. Building 9 Liando U Valley, No. 410 Jinggu Road Minhang, Shanghai 200240, China, 2023.

[83] *M7-SWIR1_10 Resonant electro-optic phase modulator with - wedged facet*. QUBIG. Grillparzerstr. 6, 81675 Munich Bavaria, Germany.

[84] *Fiber coupled AOM Standard version – 1550 nm*. AeroDIODE. Bâtiment COGNITIK 11, rue Ferdinand Buisson 33130 Bègles, France, 2022.

[85] J. Lekavicho. „Basics of acousto-optic devices“. EN. In: *Laser Applications* (1986).

[86] R. Paschotta. *Acousto-optic Modulators*. Sept. 10, 2025. URL: https://www.rp-photonics.com/acousto_optic_modulators.html.

[87] J. Jahns. *Photonik*. Berlin, Boston: Oldenbourg Wissenschaftsverlag, 2000. ISBN: 9783486593846. URL: https://doi.org/10.1515/9783486593846.

[88] J. D. L. Allan W. Snyder. *Optical Waveguide Theory*. Springer New York, NY, 1983. ISBN: 0-412-09950-0. URL: https://doi.org/10.1007/978-1-4613-2813-1.

[89] A. Ghatak and K. Thyagarajan. *An Introduction to Fiber Optics*. Cambridge University Press, 1998. ISBN: 0521577853. DOI: https://doi.org/10.1017/CBO9781139174770.

[90] S. Prahl. *ofiber: a python module for light propagation in optical fibers.* Version 0.8.1. May 2024. URL: https://doi.org/10.5281/zenodo.11117101.

[91] H. E. Parker, A. Perperidis, J. M. Stone, K. Dhaliwal, and M. G. Tanner. „Core crosstalk in ordered imaging fiber bundles". In: *Opt. Lett.* 45.23 (2020), pp. 6490–6493. URL: https://opg.optica.org/ol/abstract.cfm?URI=ol-45-23-6490.

[92] N. Ortega-Quijano, F. Fanjul-Vélez, and J. L. Arce-Diego. „Optical crosstalk influence in fiber imaging endoscopes design". In: *Optics Communications* 283.4 (2010), pp. 633–638. ISSN: 0030-4018. URL: https://www.sciencedirect.com/science/article/pii/S0030401809010670.

[93] A. W. Snyder and P. McIntyre. „Crosstalk between light pipes". In: *J. Opt. Soc. Am.* 66.9 (1976), pp. 877–882. URL: https://opg.optica.org/abstract.cfm?URI=josa-66-9-877.

[94] A. W. Snyder. „Coupled-Mode Theory for Optical Fibers". In: *J. Opt. Soc. Am.* 62.11 (1972), pp. 1267–1277. URL: https://opg.optica.org/abstract.cfm?URI=josa-62-11-1267.

[95] W. Louisell. *Coupled Mode and Parametric Electronics*. Wiley, 1960.

[96] *LMH6629 Ultra-Low Noise, High-Speed Operational Amplifier with Shutdown.* SNOSB18I. Revised December 2014. Texas Instruments. Apr. 2010.

[97] *Considerations for High-Gain Multistage Designs.* SBOA135. Texas Instruments. May 2013.

[98] P. Horowitz and W. Hill. *The Art of Electronics: The x Chapters*. Cambridge University Press, 2020. ISBN: 9781108499941.

[99] *OA-15 Frequent Faux Pas in Applying Wideband Current Feedback Amplifiers.* SLVA043B. Revised April 2013. Texas Instruments. Aug. 1990.

[100] *LMH34400 240-MHz, Single-Ended, Transimpedance Amplifier with Integrated Clamp.* SBOSA56B. Revised March 2023. Texas Instruments. Mar. 2022.

[101] *Low Pass Filter LFCN-160+*. Mini Circuits.

[102] *OPAx182 36-V, 5-MHz, Low-Noise, Zero-Drift, MUX-Friendly, Precision Op Amps.* SBOS936E. Revised August 2022. Texas Instruments. Nov. 2019.

[103] C. Shannon. „Communication in the Presence of Noise". In: *Proceedings of the IRE* 37.1 (1949), pp. 10–21. DOI: 10.1109/JRPROC.1949.232969.

[104] *Arduino® Due Product Reference Manual*. SKU: A000062. Modied January 2025. Texas Instruments.

[105] *Noise Analysis in Operational Amplifier Circuits*. SLVA043B. Texas Instruments. 2007.

[106] J. G. Proakis and M. Salehi. *Communication systems engineering*. en. 2nd ed. Upper Saddle River, NJ: Pearson, Aug. 2001.

[107] J. B. Johnson. „Thermal Agitation of Electricity in Conductors“. In: *Phys. Rev.* 32 (1 1928), pp. 97–109. URL: https://link.aps.org/doi/10.1103/PhysRev.32.97.

[108] W. Haynes. *CRC Handbook of Chemistry and Physics, 92nd Edition*. Taylor & Francis, 2011. ISBN: 9781439855119.

[109] A. Varshneya. *Fundamentals of Inorganic Glasses*. Academic Press, 1993. ISBN: 978-0127149707.

[110] K. Kokkonen and M. Kaivola. „Scanning heterodyne laser interferometer for phase-sensitive absolute-amplitude measurements of surface vibrations“. In: *Applied Physics Letters* 92.6 (Feb. 2008), p. 063502. ISSN: 0003-6951. URL: https://doi.org/10.1063/1.2840183.

[111] P. J. de Groot. „Vibration in phase-shifting interferometry“. In: *J. Opt. Soc. Am. A* 12.2 (1995), pp. 354–365. URL: https://opg.optica.org/josaa/abstract.cfm?URI=josaa-12-2-354.

[112] *M23R*. Earthworks Audio. Sept. 23, 2025.

[113] *Si5350/51 EVALUATION BOARD USER'S GUIDE*. Skyworks Solutions, Inc. Dec. 2021.

[114] *DC-3GHZ/DC-6GHZ 90DB programmable RF-attenuator*. Shenzhen Tianzhongtian Trading Co., Ltd. No.1706, Block B, Seven Star Commercial Plaza, Shenzhen, Guangdong, China.

[115] CTA. *TargetLibraries*. The website is not public. A copy can be provided on request. Aug. 18, 2024. URL: https://gitlab.cta-observatory.org/cta-array-elements/common/targetlibraries.

[116] F. Meylahn, N. Knust, and B. Willke. „Stabilized laser system at 1550 nm wavelength for future gravitational-wave detectors“. In: *Phys. Rev. D* 105 (12 2022), p. 122004. URL: https://link.aps.org/doi/10.1103/PhysRevD.105.122004.

[117] J. S. Elise Van den Bossche and M. Vardaro. *IMC test set-up update*. ET Pathfinder Labbook - The website is not public. Sept. 21, 2025. URL: https://etpathfinder.maastrichtuniversity.nl/imc-test-set-up-update/.

[118] Y. G. Marco Vardaro Elise Van den Bossche and L. Kranzhoff. *Planned Experiments on BST Bench*. ETpathfinder Workshop. June 3, 2025. URL: https://indico.nikhef.nl/event/6624/.

[119] A. Franzen. *ComponentLibrary*. May 2006. URL: https://www.gwoptics.org/ComponentLibrary/.

[120] D. Bose, V. R. Chitnis, P. Majumdar, and B. S. Acharya. „Ground-based gamma-ray astronomy: history and development of techniques". In: *The European Physical Journal Special Topics* 231.1 (Jan. 2022). arXiv:2201.04719 [astro-ph], pp. 3–26. ISSN: 1951-6355, 1951-6401. URL: http://arxiv.org/abs/2201.04719 (visited on 09/24/2025).

[121] A. M. Hillas. „Evolution of ground-based gamma-ray astronomy from the early days to the Cherenkov Telescope Arrays". In: *Astroparticle Physics* 43 (2013), pp. 19–43. ISSN: 0927-6505. URL: https://www.sciencedirect.com/science/article/pii/S0927650512001326.

[122] NASA/GSFC. *Multiwavelength Milky Way*. Sept. 24, 2025. URL: https://ecuip.lib.uchicago.edu/multiwavelength-astronomy/gamma-ray/science/04.html.

[123] T. C. Weekes, M. F. Cawley, D. J. Fegan, K. G. Gibbs, et al. „Observation of TeV Gamma Rays from the Crab Nebula Using the Atmospheric Cerenkov Imaging Technique". In: 342 (July 1989), p. 379. DOI: 10.1086/167599.

[124] G. Pühlhofer, F. Leuschner, and H. Salzmann. „H.E.S.S.: The High Energy Stereoscopic System". In: *Handbook of X-ray and Gamma-ray Astrophysics*. Springer Nature Singapore, Dec. 2023, 1–41. ISBN: 9789811645440. URL: http://dx.doi.org/10.1007/978-981-16-4544-0_69-2.

[125] D. Hanna and R. Mukherjee. „The Very Energetic Radiation Imaging Telescope Array System (VERITAS)". In: *Handbook of X-ray and Gamma-ray Astrophysics*. Springer Nature Singapore, 2024, 2703–2743. ISBN: 9789811969607. URL: http://dx.doi.org/10.1007/978-981-19-6960-7_68.

[126] O. Blanch and J. Sitarek. „The Major Gamma-Ray Imaging Cherenkov Telescopes (MAGIC)". In: *Handbook of X-ray and Gamma-ray Astrophysics*. Springer Nature Singapore, 2024, 2667–2701. ISBN: 9789811969607. URL: http://dx.doi.org/10.1007/978-981-19-6960-7_67.

[127] S. P. Wakely and D. Horan. „TeVCat: An online catalog for Very High Energy Gamma-Ray Astronomy“. In: *International Cosmic Ray Conference* 3 (2008), pp. 1341–1344.

[128] *Science with the Cherenkov Telescope Array*. WORLD SCIENTIFIC, Feb. 2018. ISBN: 9789813270091. URL: http://dx.doi.org/10.1142/10986.

[129] T. C. Consortium and R. A. Ong. „The Cherenkov Telescope Array Science Goals and Current Status“. In: *EPJ Web of Conferences* 209 (2019). Ed. by M. De Vincenzi, A. Capone, and A. Morselli, p. 01038. ISSN: 2100-014X. URL: http://dx.doi.org/10.1051/epjconf/201920901038.

[130] V. Hess. *On the Observations of the Penetrating Radiation during Seven Balloon Flights*. 2018. arXiv: 1808.02927 [physics.hist-ph]. URL: https://arxiv.org/abs/1808.02927.

[131] A. Goldstein, P. Veres, E. Burns, M. S. Briggs, et al. „An Ordinary Short Gamma-Ray Burst with Extraordinary Implications: Fermi-GBM Detection of GRB 170817A“. In: *The Astrophysical Journal Letters* 848.2 (Oct. 2017), p. L14. ISSN: 2041-8213. URL: http://dx.doi.org/10.3847/2041-8213/aa8f41.

[132] J. G. Green, A. Carosi, L. Nava, B. Patricelli, et al. *Chasing Gravitational Waves with the Cherenkov Telescope Array*. 2024. arXiv: 2310.07413 [astro-ph.HE]. URL: https://arxiv.org/abs/2310.07413.

[133] H. Abdalla, H. Abe, F. Acero, A. Acharyya, et al. „Sensitivity of the Cherenkov Telescope Array for probing cosmology and fundamental physics with gamma-ray propagation“. In: *Journal of Cosmology and Astroparticle Physics* 2021.02 (Feb. 2021), 048–048. ISSN: 1475-7516. URL: http://dx.doi.org/10.1088/1475-7516/2021/02/048.

[134] R. G. Lang, H. Martínez-Huerta, and V. de Souza. „Improved limits on Lorentz invariance violation from astrophysical gamma-ray sources“. In: *Phys. Rev. D* 99 (4 2019), p. 043015. URL: https://link.aps.org/doi/10.1103/PhysRevD.99.043015.

[135] V. C. Rubin, W. K. Ford Jr., and N. Thonnard. „Rotational properties of 21 SC galaxies with a large range of luminosities and radii, from NGC 4605 (R=4kpc) to UGC 2885 (R=122kpc).“ In: 238 (June 1980), pp. 471–487. DOI: 10.1086/158003.

[136] D. Clowe, A. Gonzalez, and M. Markevitch. „Weak-Lensing Mass Reconstruction of the Interacting Cluster 1E 0657558: Direct Evidence for the

Existence of Dark Matter“. In: *The Astrophysical Journal* 604.2 (Apr. 2004), 596–603. ISSN: 1538-4357. URL: http://dx.doi.org/10.1086/381970.

[137] G. R. Blumenthal, S. M. Faber, J. R. Primack, and M. J. Rees. „Formation of galaxies and large-scale structure with cold dark matter“. In: *Nature* 311.5986 (Oct. 1984), pp. 517–525. ISSN: 1476-4687. URL: https://doi.org/10.1038/311517a0.

[138] J. Matthews. „A Heitler model of extensive air showers“. In: *Astroparticle Physics* 22.5 (2005), pp. 387–397. ISSN: 0927-6505. URL: https://www.sciencedirect.com/science/article/pii/S0927650504001598.

[139] W. Heitler. *The quantum theory of radiation*. Vol. 5. International Series of Monographs on Physics. Oxford: Oxford University Press, 1936.

[140] M. S. Longair. *High Energy Astrophysics*. 2011.

[141] R. Ulrich, R. Engel, and M. Unger. „Hadronic multiparticle production at ultrahigh energies and extensive air showers“. In: *Phys. Rev. D* 83 (5 2011), p. 054026. URL: https://link.aps.org/doi/10.1103/PhysRevD.83.054026.

[142] C. Bambi and A. Sangangelo. *Handbook of X-ray and Gamma-ray Astrophysics*. 2022.

[143] T. K. Gaisser. *Cosmic rays and particle physics.* 1990.

[144] M. Spurio. *Particles and Astrophysics: A Multi-Messenger Approach*. Astronomy and Astrophysics Library. Springer International Publishing, 2014. ISBN: 9783319080512. URL: https://books.google.de/books?id=4P67BAAAQBAJ.

[145] M. Barrantes, J. Valdes, O Musalem, A Hurtado, et al. „Atmospheric corrections of the cosmic ray fluxes detected by the Solar Neutron Telescope at the Summit of the Sierra Negra Volcano in Mexico“. In: *Geofísica Internacional* 57 (Oct. 2018), pp. 253–275. DOI: 10.22201/igeof.00167169p.2018.57.4.2105.

[146] P. A. Cerenkov. „Visible Radiation Produced by Electrons Moving in a Medium with Velocities Exceeding that of Light“. In: *Phys. Rev.* 52 (4 1937), pp. 378–379. URL: https://link.aps.org/doi/10.1103/PhysRev.52.378.

[147] M. de Naurois and D. Mazin. „Ground-based detectors in very-high-energy gamma-ray astronomy“. In: *Comptes Rendus Physique* 16.6 (2015). Gamma-ray astronomy / Astronomie des rayons gamma, pp. 610–627. ISSN: 1631-

0705. URL: https://www.sciencedirect.com/science/article/pii/S1631070515001462.

[148] P. Grieder. *Extensive air showers. High energy phenomena and astrophysical aspects. A tutorial, reference manual and data book. Vol. I and II.* Vol. 1. Jan. 2010. ISBN: 978-3-540-76940-8. DOI: 10.1007/978-3-540-76941-5.

[149] I. Frank and I. Tamm. „Coherent Visible Radiation of Fast Electrons Passing Through Matter". In: *Selected Papers*. Ed. by B. M. Bolotovskii, V. Y. Frenkel, and R. Peierls. Berlin, Heidelberg: Springer Berlin Heidelberg, 1991, pp. 29–35. ISBN: 978-3-642-74626-0. URL: https://doi.org/10.1007/978-3-642-74626-0_2.

[150] J. Schäfer. *ShowerPy: v0.1.1*. Version v0.1.1. May 2025. URL: https://doi.org/10.5281/zenodo.15342222.

[151] H. J. Völk and K. Bernlöhr. „Imaging very high energy gamma-ray telescopes". In: *Experimental Astronomy* 25.1–3 (Mar. 2009), 173–191. ISSN: 1572-9508. URL: http://dx.doi.org/10.1007/s10686-009-9151-z.

[152] G. Roellinghoff, S. T. Spencer, and S. Funk. „Advanced modelling of the night sky background light for imaging atmospheric Cherenkov telescopes". In: *Astronomy amp; Astrophysics* 698 (June 2025), A212. ISSN: 1432-0746. URL: http://dx.doi.org/10.1051/0004-6361/202554532.

[153] H. Anderhub, M. Backes, A. Biland, V. Boccone, et al. „Design and operation of FACT – the first G-APD Cherenkov telescope". In: *Journal of Instrumentation* 8.06 (2013), P06008. URL: https://dx.doi.org/10.1088/1748-0221/8/06/P06008.

[154] C. Fruck. „The galactic center resolved with MAGIC and a new technique for atmospheric calibration". PhD thesis. Munich University of Technology, Germany, Jan. 2015.

[155] A. M. Hillas. „Cerenkov Light Images of EAS Produced by Primary Gamma Rays and by Nuclei". In: *19th International Cosmic Ray Conference, Volume 3*. Ed. by F. C. Jones. Vol. 3. International Cosmic Ray Conference. Aug. 1985, p. 445.

[156] R. Parsons and J. Hinton. „A Monte Carlo template based analysis for air-Cherenkov arrays". In: *Astroparticle Physics* 56 (Apr. 2014), 26–34. ISSN: 0927-6505. URL: http://dx.doi.org/10.1016/j.astropartphys.2014.03.002.

[157] URL: https://www.ctao.org/. (accessed: 20.06.2025).

[158] W. B. Atwood, A. A. Abdo, M. Ackermann, W. Althouse, et al. „THE LARGE AREA TELESCOPE ON THE FERMI GAMMA-RAY SPACE TELESCOPEMISSION“. In: *The Astrophysical Journal* 697.2 (May 2009), 1071–1102. ISSN: 1538-4357. URL: http://dx.doi.org/10.1088/0004-637X/697/2/1071.

[159] H. Schoorlemmer. *A next-generation ground-based wide field-of-view gamma-ray observatory in the southern hemisphere*. 2019. arXiv: 1908.08858 [astro-ph.HE]. URL: https://arxiv.org/abs/1908.08858.

[160] Z. Cao, D. della Volpe, S. Liu, Editors, et al. *The Large High Altitude Air Shower Observatory (LHAASO) Science Book (2021 Edition)*. 2022. arXiv: 1905.02773 [astro-ph.HE]. URL: https://arxiv.org/abs/1905.02773.

[161] K. Abe, S. Abe, A. Aguasca-Cabot, I. Agudo, et al. „Performance of the Large-Sized Telescope prototype of the Cherenkov Telescope Array“. In: *PoS* ICRC2023 (2023), p. 594. DOI: 10.22323/1.444.0594.

[162] K. Abe, S. Abe, A. Abhishek, F. Acero, et al. „A new method of reconstructing images of gamma-ray telescopes applied to the LST-1 of CTAO“. In: *Astronomy amp; Astrophysics* 691 (Nov. 2024), A328. ISSN: 1432-0746. URL: http://dx.doi.org/10.1051/0004-6361/202450889.

[163] J.-F. Glicenstein, O. Abril, J.-A. Barrio, O. B. Bigas, et al. *NectarCAM : a camera for the medium size telescopes of the Cherenkov Telescope Array*. 2015. arXiv: 1508.06555 [astro-ph.IM]. URL: https://arxiv.org/abs/1508.06555.

[164] G. Pühlhofer, C. Bauer, S. Bernhard, M. Capasso, et al. *FlashCam: a fully-digital camera for the medium-sized telescopes of the Cherenkov Telescope Array*. 2015. arXiv: 1509.02434 [astro-ph.IM]. URL: https://arxiv.org/abs/1509.02434.

[165] V. Vassiliev, S. Fegan, and P. Brousseau. „Wide field aplanatic two-mirror telescopes for ground-based -ray astronomy“. In: *Astroparticle Physics* 28.1 (Sept. 2007), 10–27. ISSN: 0927-6505. URL: http://dx.doi.org/10.1016/j.astropartphys.2007.04.002.

[166] E. Giro, R. Canestrari, G. Sironi, E. Antolini, et al. „First optical validation of a Schwarzschild Couder telescope: the ASTRI SST-2M Cherenkov telescope“. In: *AA* 608 (2017), A86. URL: https://doi.org/10.1051/0004-6361/201731602.

[167] K. Schwarzschild. *Untersuchungen zur geometrischen Optik I*. Astronomische Mitteilungen der Universitäts-Sternwarte zu Göttingen, 1905.

[168] A. Couder. „Sur un type nouveau de télescope photographique“. In: *Comptes Rendus* 183.45 (1926), pp. 1276–1279.

[169] G. Sironi. „Aplanatic telescopes based on Schwarzschild optical configuration: from grazing incidence Wolter-like x-ray optics to Cherenkov two-mirror normal incidence telescopes“. In: *Optics for EUV, X-Ray, and Gamma-Ray Astronomy VIII*. Ed. by S. L. O'Dell and G. Pareschi. Vol. 10399. International Society for Optics and Photonics. SPIE, 2017, p. 1039903. URL: https://doi.org/10.1117/12.2275422.

[170] R. White, J. Amans, D. Berge, G. Bonanno, et al. „The Small-Sized Telescopes for the Southern Site of the Cherenkov Telescope Array“. In: *Proceedings of 37th International Cosmic Ray Conference — PoS(ICRC2021)*. ICRC2021. Sissa Medialab, July 2021, p. 728. URL: http://dx.doi.org/10.22323/1.395.0728.

[171] C. Adams, R. Alfaro, G. Ambrosi, M. Ambrosio, et al. „Detection of the Crab Nebula with the 9.7 m prototype Schwarzschild-Couder telescope“. In: *Astroparticle Physics* 128 (2021), p. 102562. ISSN: 0927-6505. DOI: https://doi.org/10.1016/j.astropartphys.2021.102562.

[172] D. Depaoli. *Status of the SST Camera for the Cherenkov Telescope Array*. 2023. arXiv: 2310.01183 [astro-ph.IM]. URL: https://arxiv.org/abs/2310.01183.

[173] G. Tagliaferri, A. Antonelli, T. Arnesen, J. Aschersleben, et al. „The small-sized telescope of CTAO“. In: *Ground-based and Airborne Telescopes IX*. Ed. by H. K. Marshall, J. Spyromilio, and T. Usuda. Vol. 12182. International Society for Optics and Photonics. SPIE, 2022, 121820K. URL: https://doi.org/10.1117/12.2627956.

[174] R. White. *SST Camera Design Report SST-CAM-DSR-001 Version 3.a*. This document is not public. 2024.

[175] S. Funk, D. Jankowsky, H. Katagiri, M. Kraus, et al. „TARGET: A digitizing and trigger ASIC for the Cherenkov telescope array“. In: *AIP Conference Proceedings* 1792.1 (Jan. 2017), p. 080012. ISSN: 0094-243X. eprint: https://pubs.aip.org/aip/acp/article-pdf/doi/10.1063/1.4969033/13735526/080012_1_online.pdf. URL: https://doi.org/10.1063/1.4969033.

[176] L. Tibaldo, J. A. Vandenbroucke, A. M. Albert, S. Funk, et al. *TARGET: toward a solution for the readout electronics of the Cherenkov Telescope Array*. 2015. URL: https://arxiv.org/abs/1508.06296.

[177] A. Albert, S. Funk, H. Katagiri, T. Kawashima, et al. „TARGET 5: A new multi-channel digitizer with triggering capabilities for gamma-ray atmospheric Cherenkov telescopes“. In: *Astroparticle Physics* 92 (2017), pp. 49–61. ISSN: 0927-6505. DOI: https://doi.org/10.1016/j.astropartphys.2017.05.003.

[178] D. Stricker-Shaver, S. Ritt, and B. J. Pichler. „Novel Calibration Method for Switched Capacitor Arrays Enables Time Measurements With Sub-Picosecond Resolution“. In: *IEEE Transactions on Nuclear Science* 61.6 (2014), pp. 3607–3617. DOI: 10.1109/TNS.2014.2366071.

[179] CTA. *CTA Requirements - Product Requirements Level B*. The website is not public. Oct. 16, 2025. URL: https://jama.cta-observatory.org/perspective.req#/items/28780?projectId=11.

[180] B. Schwab. *About Temperature Dependence of TARGET C and CTC Calibration*. Master's thesis. 2021.

[181] A. Zink. personal correspondence. 2024.

[182] M. Able. *On Front-End Electronics for the SST Camera: Timebase Calibration and Wilkinson Comparator Tuning of the Digitiser ASIC CTC*. Master's thesis. 2024.

[183] A. Chapyzhenka and J. Probell. „Wavedrom: Rendering beautiful waveforms from plain text“. In: *Synopsys User Group* (2016).

[184] CTA. *CTA Requirements - Product Requirements Level B*. The website is not public. Jan. 19, 2024. URL: https://jama.cta-observatory.org/perspective.req#/containers/26364?projectId=11.

[185] J. Dutka. „On the early history of Bessel functions“. In: *Archive for History of Exact Sciences* 49.2 (June 1995), pp. 105–134. ISSN: 1432-0657. URL: https://doi.org/10.1007/BF00376544.

[186] B. Schwab. *ETscripts*. The website is not public. A copy can be provided on request. Oct. 26, 2025. URL: https://git.ecap.work/bschwab/et_scripts.

Acknowledgements

On this part I would like to thank everybody that joined or helped me on this adventure of pursuing my PhD. Getting to this point was not easy and is most likely impossible without your support. First and foremost, I would like to thank my lovely wife Stefanie Schwab for supporting me all along. I would be nothing without her.
Then, of course, Stefan Funk, my supervisor, for trusting me with this project, which also somehow is the first tipping toe of the Erlangen Centre of Astroparticle Physics in the landscape of gravitational wave detection. I had a lot of freedoms to decide in which direction to develop this project and I am very thankfully for that as this also taught one things or another about project management.
I would like to thank Adrian Zink for basically mentoring me. I learned from him more than any other person and that pragmatism in problem solving is often king. Gisela Anton for here advice and enthusiasm for physics that is just contagious. Martin van Beuzekom for introducing me to everything revolving around the optical setup of the phase camera. In a three days trip to NIKHEF he guided me on how to set up such system in the laboratory. Martin van Beuzekom, Matteo Tacca and Paul Kuijer and the rest of the phase camera working group we formed together. I am really thankful for sharing their of knowledge with us, which is not taken for granted. Stefan Hild, Marco Vardaro and Elise Van den Bossche and the rest of the ET Pathfinder crew for making the measurement campaign of the phase camera reality. Everything was exceptional from the organisation to the preparation and communication. We were warmly welcomed by everyone and had a great time with great results there. Andreas Zmija for joining the measurement campaign in Maastricht. Exploring the city together was pretty cool and I think we had a pretty good time there! Also, the spareribs and DeRuijters are not gonna eat themselves! The SST Camera Working, which was always fun to be around. Adrian Zink, Johannes Schäfer, Rodrigo Guedes Lang, Jonas Glombitza, Stefanie Schwab, and Stefan Funk for proof reading all or some part of this thesis. Gabriela Eckner, which had always an open ear for my stupid questions and for her support in all kinds of paper work. The gamma-group for the nice working atmosphere and also outside activities. There is always a helping hand if needed. The corner office for all the fun we had and the nice themed decorations, especially around Christmas. The 305 office of the old building, where the memes flowed like whine and work tasted like honey? or whatever... And of course, my family and all my friends that supported me all along!